Compensation engineering for silicon solar cells

Maxime Forster

Numéro d'Ordre : 2012ISAL0139 Année 2012

Thèse

Compensation engineering for silicon solar cells

présentée devant

L'Institut National des Sciences Appliquées de Lyon

et The Australian National University

pour obtenir le grade de

Docteur

Ecole Doctorale : Electronique Electrotechnique Automatique

Spécialité : Micro et Nanotechnologies

par

Maxime FORSTER

soutenue le 17 décembre 2012 devant la commission d'examen

Jury

LEMITI Mustapha	Professeur	Directeur
FOURMOND Erwann	Maître de Conférences	Directeur
CUEVAS Andres	Professeur	Directeur
EINHAUS Roland	Ingénieur de Recherche	Encadrant
PALAIS Olivier	Professeur	Rapporteur
ALTERMATT Pietro	Directeur de Recherche	Rapporteur
HAHN Giso	Professeur	Examinateur
SLAOUI Abdelilah	Directeur de Recherche	Examinateur
DUBOIS Sébastien	Ingénieur de Recherche	Invité
DURAND Yvonnick	Ingénieur	Invité
MARTINUZZI Santo	Professeur	Invité

Cette thèse a été préparée à l'Institut des Nanotechnologies de Lyon (INSA de Lyon)
Et à la Research School of Engineering (The Australian National University)

Liste des écoles doctorales

SIGLE	ÉCOLE DOCTORALE	NOM ET COORDONNÉES DU RESPONSABLE
CHIMIE	**CHIMIE DE LYON** http://edchimie-lyon.fr Insa : R. GOURDON	**M. Jean Marc LANCELIN** Université de Lyon - Collège doctorale Bâtiment ESCPE 43 bd du 11 novembre 1918 69622 VILLEURBANNE Cedex Tél: 04.72.43.13.95 directeur@edchimie-lyon.fr
E.E.A.	**ÉLECTRONIQUE, ÉLECTROTECHNIQUE, AUTOMATIQUE** http://edeea.ec-lyon.fr Secrétariat : M.C. HAVGOUDOUKIAN ede2a@insa-lyon.fr	**M. Gérard SCORLETTI** École Centrale de Lyon 36 avenue Guy de Collongue 69134 ECULLY Tél: 04.72.18.60.97 gerard.scorletti@ec-lyon.fr
E2M2	**ÉVOLUTION, ÉCOSYSTÈME, MICROBIOLOGIE, MODÉLISATION** http://e2m2.universite-lyon.fr Insa : H. CHARLES	**Mme Gudrun BORNETTE** CNRS UMR 5023 Université Claude Bernard Lyon 1 Bâtiment Forel 43 bd du 11 novembre 1918 69622 VILLEURBANNE Cedex Tél: 04.72.43.12.94 e2m2@biomserv.univ-lyon1.fr
EDISS	**INTERDISCIPLINAIRE SCIENCES-SANTÉ** Sec : Safia AIT CHALAL Insa : M. LAGARDE	**M. Didier REVEL** Hôpital Louis Pradel Bâtiment Central 28 Avenue Doyen Lépine 69500 BRON Tél: 04.72.68.49.09 didier.revel@creatis.uni-lyon1.fr
INFOMATHS	**INFORMATIQUE ET MATHÉMATIQUES** http://infomaths.univ-lyon1.fr	**M. Johannes KELLENDONK** Université Claude Bernard Lyon 1 INFOMATHS Bâtiment Braconnier 43 bd du 11 novembre 1918 69622 VILLEURBANNE Cedex Tél: 04.72.44.82.94 infomaths@univ-lyon1.fr

SIGLE	ÉCOLE DOCTORALE	NOM ET COORDONNÉES DU RESPONSABLE
Matériaux	**MATÉRIAUX DE LYON** Secrétariat : M. LABOUNE PM : 71.70 – Fax : 87.12	**M. Jean-Yves BUFFIERE** INSA de Lyon MATEIS Bâtiment Blaise Pascal 7 avenue Jean Capelle 69621 VILLEURBANNE Cedex Tél: 04.72.43.83.18 jean-yves.buffiere@insa-lyon.fr
MEGA	**MÉCANIQUE, ÉNERGÉTIQUE, GÉNIE CIVIL, ACOUSTIQUE** Secrétariat : M. LABOUNE PM : 71.70 – Fax : 87.12	**M. Philippe BOISSE** INSA de Lyon Laboratoire LAMCOS Bâtiment Jacquard 25 bis avenue Jean Capelle 69621 VILLEURBANNE Cedex Tél: 04.72.43.71.70 philippe.boisse@insa-lyon.fr
ScSo	**ScSo**[1] Insa : J.Y. TOUSSAINT	**M. OBADIA Lionel** Université Lyon 2 86 rue Pasteur 69365 LYON Cedex 07 Tél: 04.78.69.72.76 Lionel.Obadia@univ-lyon2.fr

[1]Histoire, Géographie, Aménagement, Urbanisme, Archéologie, Science politique, Sociologie, Anthropologie

Declaration

I certifiy that this thesis does not incorporate, without acknowldgement, any material previously submitted for a degree or a diploma in any university, and that, to the best of my knowledge it does not contain any material previously published or written by another person except where due reference is made in the text. The work in this thesis is my own, except for the contributions made by others as described in the Acknowledgements.

Maxime Forster

January 2013

Acknowledgments

My PhD took place in two different universities – INSA de Lyon and the Australian National University – and a company – Apollon Solar. I am deeply grateful to my supervisors from all three parties – Erwann Fourmond and Mustapha Lemiti (INSA de Lyon), Andrés Cuevas (ANU) and Roland Einhaus (Apollon Solar) – for the trust, support and encouragements they gave me and for the foolproof enthusiasm for research they shared with me.

I also thank Pietro Altermatt and Olivier Palais for the time they spent to review my thesis, as well as Giso Hahn, Abdellilah Slaoui, Santo Martinuzzi, Yvonnick Durand and Sébastien Dubois for accepting to be part of my defense panel.

At INSA de Lyon, I wish to thank Gérard Guillot and Catherine Bru-Chevalier for welcoming me to the Nanotechnology Institute of Lyon (INL) and for giving access to the NanoLyon technology platform. I also thank all the technical staff running this platform for their daily support – Philippe Girard, Robert Perrin, Khaled Ayadi, Joëlle Grégoire and Andreï Sabac. In the Photovoltaic group, I thank Mustapha Lemiti, Erwann Fourmond, Anne Kaminsky, Danièle Blanc-Pélissier, Alain Fave and Tetyana Nychyporuk for their help and sympathy. I also thank all PhD students, postdocs and fixed-term employees from INL for many helping hands and good laughs, especially Barbara Bazer-Bachi, Caroline Boulord, Maïlys Grau, Romain Couderc, Romain Mailhes, Hubert Hody, Manu Gerelli, José Almeyda, Abdou Harouri, Louardi Remache, Gilles Poulain, Pierre Béllanger, Walf Chikhaoui, Alvaro Francisco, Mouna Zouaoui, Hassan Chamas, Alexandru Focsa and Keith Fraser. I also thank all the interns that have helped me throughout my PhD and who have greatly contributed to the work presented here – Maxime Levaslot, Aude Sautel, Audoin Hamon, Bastien Dehestru and Antoine Thomas.

At the ANU, I give a huge thanks to Fiacre Rougieux for helping me to settle in Canberra and for offering me a roof during the first few weeks I spent there. I also thank Fiacre for many inspiring discussions and for his invaluable contribution to the work presented in this thesis. I thank Chris Samundsett, Erin Davis, Maureen Brauers, Theng Kho for helping me so many times in the lab as well as all the technical staff – Nina De Caritat, James Costel, Bruce Gordon, Glen Cecil and Mark Saunders. I warmly thank everyone from the Semicondutor and Solar Cells' group – Andrés Cuevas, Daniel Macdonald, Fiacre Rougieux, Pheng Phang, , Siew Lim, An Liu, James Bullock, Xinyu Zhang, Kelvin Sio – or adopted by the group – Simeon Baker-Finch, Lachlan Black, Nick Grant, Tom Ratcliff,

Yimao Wan, Andrew Thomson – for fruitful and friendly exchanges during meetings, in the labs or in the tea room. I thank all the other PhD students, postdocs and interns from CECS for the very pleasant time spent with them at the ANU, especially Arnold McKinley, Kean Chern Fong, Matthieu Erbert, Rémi Chauvin, Wensheng Liang, Azul Osorio Mayon, Lujia Xu, Chog Barugkin, Jeff Cumpston, José Zapata, Rebecca Dunn, Leonie Fierz, Marta Vivar and Manuel Fuentes.

I also thank all my colleagues from Apollon Solar – Roland Einhaus, Jed Kraiem, Julien Degoulange, Hubert Lauvray, Oleksiy Nichiporuk, Frédéric Madon, Robert De Franclieu, Julien Dupuis, Etienne Saint-Sernin and Klaus Bamberg – for their massive intellectual and material support and contribution to the work presented in this thesis and for fitting me in as a regular member of the team during my PhD.

I also thank FerroPem and especially François Cocco and Delphine Grosset-Bourbange for letting me use some of the silicon they produce for my experiments. I would also like to thank Jacky Stadler from Siltronix for making his pullers available for my co-doping experiments at Siltronix and Eric and Patrice for growing and shaping our ingots and for sharing some of their longstanding experience in silicon crystal growth. I also thank Giuseppe Galbiati from ISC Konstanz for making solar cells with our material. I would also like to thank Jordi Veirman and Sébastien Dubois from CEA-INES for many discussions on compensated material and for letting me use their Hall setup at the beginning of my PhD.

Finally, I thank all my family for their support and in particular my dad for correcting the English of my introduction.

Abstract

This thesis focuses on the effects of dopant compensation on the electrical properties of crystalline silicon relevant to the operation of solar cells. We show that the control of the net dopant density, which is essential to the fabrication of high-efficiency solar cells, is very challenging in ingots crystallized with silicon feedstock containing both boron and phosphorus such as upgraded metallurgical-grade silicon. This is because of the strong segregation of phosphorus which induces large net dopant density variations along directionally solidified silicon crystals. To overcome this issue, we propose to use gallium co-doping during crystallization, and demonstrate its potential to control the net dopant density along p-type and n-type silicon ingots grown with silicon containing boron and phosphorus. The characteristics of the resulting highly-compensated material are identified to be: a strong impact of incomplete ionization of dopants on the majority carrier density, an important reduction of the mobility compared to theoretical models and a recombination lifetime which is determined by the net dopant density and dominated after long-term illumination by the boron-oxygen recombination centre. To allow accurate modelling of upgraded-metallurgical silicon solar cells, we propose a parameterization of these fundamental properties of compensated silicon. We study the light-induced lifetime degradation in p-type and n-type Si with a wide range of dopant concentrations and compensation levels and show that the boron-oxygen defect is a grown-in complex involving substitutional boron and is rendered electrically active upon injection of carriers through a charge-driven reconfiguration of the defect. Finally, we apply gallium co-doping to the crystallization of upgraded-metallurgical silicon and demonstrate that it allows to significantly increase the tolerance to phosphorus without compromising neither the ingot yield nor the solar cells performance before light-induced degradation.

Résumé

Ingénierie de compensation pour cellules solaires en silicium

Cette thèse s'intéresse aux effets de la compensation des dopants sur les propriétés électriques du silicium cristallin. Nous montrons que le contrôle du dopage net, qui est indispensable à la réalisation de cellules solaires à haut rendement, s'avère difficile dans les lingots cristallisés à partir de silicium contenant à la fois du bore et du phosphore. Cette difficulté s'explique par la forte ségrégation du phosphore durant la cristallisation, qui donne lieu à d'importantes variations de dopage net le long des lingots de silicium solidifés de façon directionelle. Pour résoudre ce problème, nous proposons le co-dopage au gallium pendant la cristallisation et prouvons l'efficacité de cette technique pour contrôler le dopage net le long de lingots de type p ou n fabriqués à partir d'une charge de silicium contenant du bore et du phosphore. Nous identifions les spécificités du matériau fortement compensé ainsi obtenu comme étant: une forte sensibilité de la densité de porteurs majoritaires à l'ionisation incomplète des dopants, une réduction importante de la mobilité comparée aux modèles théoriques et une durée de vie des porteurs qui est déterminée par la densité de porteurs majoritaires et dominée après éclairement prolongé par les centres de recombinaison liés aux complexes de bore et d'oxygène. Pour permettre la modélisation de cellules solaires à base de silicium purifié par voie métallurgique, nous proposons une paramétrisation des propriétés fondamentales du silicium compensé mentionnées ci-dessus. Nous étudions également la dégradation de la durée de vie des porteurs sous éclairement dans des échantillons de silicium de type p et n présentant une large gamme de niveaux de dopage et de compensation. Nous montrons que le défaut bore-oxygène est issu d'un complexe formé à partir de bore substitutionnel pendant la fabrication des lingots et activé sous injection de porteurs par une reconfiguration du défaut assistée par des charges positives. Finalement, nous appliquons le co-dopage au gallium pour la cristallisation de silicium purifié par voie métallurgique et démontrons que cette technique permet d'augmenter sensiblement la tolérance au phosphore sans compromettre le rendement matière de l'étape de cristallisation ou la performance des cellules solaires avant dégradation sous éclairement.

Contents

Acknowledgements **7**

Abstract **9**

Résumé **11**

Contents **15**

Introduction **17**

1 Review of the electrical properties of compensated silicon for solar cells **23**

1.1 Definitions . . . 23

1.1.1 Compensated silicon . . . 23

1.1.2 Majority carrier density and net doping . . . 24

1.1.3 Compensation ratios . . . 24

1.2 Recombination in compensated silicon . . . 26

1.2.1 Experimental observations . . . 27

1.2.2 Intrinsic recombination . . . 28

1.2.3 Recombination through defects . . . 30

1.2.4 The boron-oxygen defect . . . 35

1.2.5 Summary . . . 37

1.3 Carrier transport in compensated silicon . . . 37

1.3.1 Scattering mechanisms . . . 37

1.3.2 Resistivity-to-doping relation . . . 38

1.3.3 Deviation from mobility models . . . 41

1.4 Compensated silicon solar cells . . . 42

1.4.1 Open-circuit voltage . . . 43

1.4.2 Short-circuit current . . . 43

1.4.3 Fill factor . . . 44

1.4.4 Efficiency . . . 45

1.4.5 Breakdown voltage . . . 46

1.4.6 Temperature coefficients . . . 47

1.5 Conclusion . . . 48

2 Compensation engineering to control the net doping along silicon ingots 49

2.1 Theory . . . 49

2.1.1 Crystallization techniques . . . 49

2.1.2 Distribution of impurities in silicon crystals . . . 52

2.1.3 Dopant distribution in compensated silicon ingots . . . 56

2.2 Experimental procedure . . . 61

2.2.1 Material preparation . . . 61

2.2.2 Characterization . . . 62

2.3 Results . . . 63

2.3.1 Resistivity profiles . . . 63

2.3.2 SIMS profiles . . . 64

2.3.3 Majority carrier density profiles . . . 65

2.3.4 Majority carrier mobility profiles . . . 67

2.4 Conclusion . . . 68

3 Carrier concentration, transport and recombination in compensated silicon 69

3.1 Characterization . . . 70

3.1.1 Majority carrier density and mobility measurements . . . 70

3.1.2 Minority carrier mobility measurements . . . 71

3.1.3 Lifetime measurements . . . 71

3.2 Majority carrier density in compensated silicon . . . 72

3.2.1 Calculating incomplete ionization . . . 72

3.2.2 Incomplete ionization at room-temperature . . . 74

3.2.3 Temperature dependence of the majority carrier density . . . 77

3.3 Carrier mobility in compensated silicon . . . 80

3.3.1 Reduction compared to models at room-temperature . . . 80

3.3.2 Temperature-dependence . . . 82

3.3.3 Mobility correction . . . 85

3.4 Recombination in compensated silicon . . . 86

3.4.1 *p*-type Si . . . 87

3.4.2 *n*-type Si . . . 90

3.5 Conclusion . . . 92

4 The boron-oxygen defect 95

4.1 Experimental procedure . . . 97

4.2 Defect density . . . 97

4.2.1 Effective defect density . . . 97

4.2.2 Defect density in *p*-type Si . . . 99

4.2.3 *n*-type Si co-doped with B, P and Ga . . . 104
4.2.4 Summary . . . 104
4.3 Degradation kinetics . . . 105
4.3.1 Degradation in *p*-type silicon . . . 105
4.3.2 Degradation in *n*-type silicon . . . 108
4.4 Shockley-Read-Hall characteristics . . . 110
4.5 Conclusion . . . 112

5 Application of compensation engineering to UMG-Si solar cells 115
5.1 Experimental procedure . . . 116
5.1.1 Purification . . . 116
5.1.2 Crystallization . . . 116
5.1.3 Solar cells fabrication . . . 118
5.2 Modelling . . . 118
5.3 Results . . . 119
5.3.1 Recombination lifetime . . . 119
5.3.2 Open-circuit voltage . . . 120
5.3.3 Short-circuit current density . . . 121
5.3.4 Efficiency . . . 122
5.4 Conclusion . . . 124

Conclusions and Outlook 127

Appendix 131

Bibliography 147

List of publications 149

Résumé étendu 153

Introduction

Motivation

Photovoltaic (PV) technology is expected to play an important role in helping countries meet their targets for CO2 abatement and the share of electricity consumption supplied by renewable-energy resources [1]. The International Energy Agency (IEA) is forecasting that penetration of the global electricity supply by solar power will reach 5% by 2030, with a cumulative installed PV worldwide capacity just below 1TWp [2]. Such a forecast implies steady growth of the PV market by about 15% per year on average (although such growth would be much slower than the continuous 30% to 50% annual growth seen over the past decade) reaching 105GWp/year by 2030.

On the other hand, the PV market is largely dominated by solar modules made of crystalline silicon (c-Si), with a share historically oscillating from 80 to 90%. Considering the advantages of this technology – its simplicity, relatively high achievable efficiency, abundance of Si (nearly 30% of the earth's crust) and the huge accumulated knowledge stemming from long-standing use of c-Si in the semiconductor industry – it is likely to dominate the market for the next decade, perhaps longer. This means that the expected growth of the PV market will most probably entail a significant increase in worldwide production capacity for solar grade (SoG)-Si[2] in the years to come.

SoG-Si is traditionally obtained by purifying cheap and abundant metallurgical-grade Si (MG-Si, itself directly obtained by carbothermal reduction of silica), using the Siemens gas-phase distillation process. The Siemens process, which yields very pure Si (electronic-grade (EG)-Si), is expensive, with high energy consumption (~ 200Wh/kg), and involves the use – and in some cases release – of toxic substances. Moreover, increments in the production capacity are limited by the long construction lead-time for Siemens purification plants (circa three years) and by the large investment entailed, with typical capital expenditure (Capex) of 100$ per kg of extended annual production capacity. Figure 1 shows the pay-off time as a function of the Si selling price, assuming 15$/kg operational expenditure (Opex). Large

[2]In this work, we use the term SoG-Si to refer to Si used to fabricate solar cells, irrespectively of its degree of purity or of the purification techniques used to produce it. Other terms will be introduced, such as MG-Si, UMG-Si or EG-Si, which we use to refer to the kind of manufacturing processes which the designated Si has been subjected to.

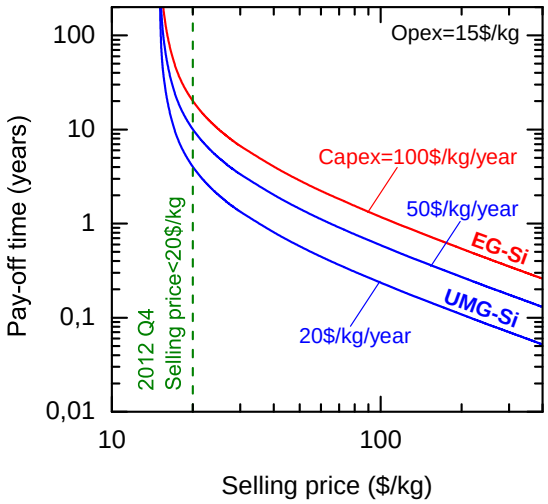

Figure 1: Pay-off time of a Si purification plant as a function of the selling price.

oversupply has recently pushed the price of EG-Si down below 20$/kg, thereby contributing to the substantial reduction in the price of solar modules, reaching an average of 0.7$/Wp in the last quarter of 2012. However Figure 1 clearly shows that such a low selling price does not allow EG-Si manufacturers to make any short-term profits that could in turn feed future investments to increase their production capacity. To further expand, the EG-Si market is therefore likely to go through a period of shortage before prices go up again, yielding the profits needed for investment in production capacity. The EG-Si industry has behaved in this way for the past 35 years, going through alternating cycles of shortage and oversupply, which have fuelled major price fluctuations. These price fluctuations have had little impact on the semiconductor industry, historical consumer of EG-Si, because Si represents only a very small fraction of the cost of integrated circuits. In the PV industry, however, Si is an important component in the cost of solar modules. Sudden variations in the price of EG-Si may consequently limit efforts to drive down module costs for PV to compete with conventional energy resources.

Upgraded metallurgical-grade (UMG)-Si is an interesting alternative, which could secure the availability of SoG-Si at a low price. It is obtained using improved metallurgical refinement techniques [3, 4, 5, 6] which are generally less energy-consuming (20 – 40kWh/kg), have a lower impact on the environment and require moderate investments (Capex typically of 20 – 50$/kg). These metallurgical refinement techniques are, however, less efficient than the Siemens process and therefore UMG-Si usually contains more impurities than EG-Si. Such impurities may alter the performance of PV modules in different ways, depending on their nature and concentration. The cost of PV electricity depends on the total system cost, of which Si feedstock is only one component. Because the efficiency of PV modules affects the costs of every part of a PV system (in $/Wp), substantially lower performance is unacceptable for UMG-Si solar cells, even associated with a substantial cut in feedstock costs. The challenge for UMG-Si is thus to make solar cells with comparable efficiency to EG-Si solar cells despite the presence of more impurities. The most important of these impurities are transition metals (Fe, Cu, Zn, etc.), light elements (C, N, O) and dopants (B, P, Al).

Metallic impurities are known to act as strong recombination centres in Si, limiting the conversion efficiency of solar cells. They can, however, be effectively removed by segregation during directional solidification and rendered inactive by efficient gettering processes during solar cell fabrication.

Light elements are usually electrically inactive in the dissolved state. However, in supersaturation, their presence can lead to the formation of precipitates and inclusions (SiC and SiN) which can shunt solar cells and affect the mechanical properties of Si, potentially leading to greater wafer-breakage inline. Light elements can also form complexes (oxygen-related thermal donors, boron-oxygen defect, etc.) which cause recombination in Si. However, much as metallic impurities, light elements can be reduced – by segregation (in the case of C) or evaporation from the melt (in the case O) – down to levels similar to the background contamination of standard ingot crystallization techniques.

The electrical properties of Si, like any other semiconductor, depend critically on the presence of dopants. The latter determine the polarity of conduction (n-type or p-type) and the concentration of free charge-carriers, which in turn influence carrier recombination and transport properties, essential components of PV conversion. Contrary to other impurities, B and P cannot be easily removed by segregation. Their elimination through plasma purification [6], slag treatment [4] or advanced evaporation techniques [3] thus represents the major cost element of UMG-Si purification. Both B and P are therefore usually present in UMG-Si in larger concentrations than is optimal for use as the base of a solar cell. However, because dopants of opposite types tend to cancel each other out, it is theoretically possible to tolerate higher dopant concentrations, provided the net difference between acceptors and donors is kept in a reasonable range for solar cells. This phenomenon is called compensation.

In the present thesis, we aim to improve the understanding of the physics of compensation, in order to precisely assess its impact on solar cells. The ultimate goal is to control the electrical properties of Si, by «compensation engineering», in order to achieve performance in UMG-Si solar cells equivalent to that of EG-Si, while increasing their tolerance to high dopant concentrations.

Outline

In Chapter 1, we introduce the key properties of Si which are relevant to the operation of a solar cell and can be altered by dopant compensation: charge-carrier recombination and transport. We review the literature dealing with the impact of compensation on these fundamental properties and link them to the characteristics of solar cells. This review shows that high-efficiency solar cells can be fabricated with Si containing both B and P in larger concentrations than in standard EG-Si solar cells, provided net doping is well controlled by compensation.

In Chapter 2, after reviewing the most common crystallization techniques and the theory of impurity segregation, we show that in practice controlling the net doping by compensation is very challenging at ingot-level. This is due to the different distributions of B and P during directional solidification, which cause substantial variation in the net doping along the length of compensated Si ingots. As a solution, we introduce a compensation-engineering technique which consists in co-doping the Si melt before crystallization with an acceptor dopant with a low segregation coefficient, for example gallium (Ga). We demonstrate experimentally that, by counterbalancing the increase in P concentration throughout crystallization, uniform net doping can be maintained along directionally solidified p-type and n-type Si ingots, even when the Si melt contains high concentrations of both B and P.

In Chapter 3, we examine the electrical properties of p-type and n-type Si samples with a wide range of dopant concentrations and compensation levels and for the first time co-doped with B, P and Ga. We identify and discuss the particularities of compensated Si: powerful impact of incomplete ionization on the majority carrier-density; lower carrier mobility than predicted by standard models; carrier lifetime before degradation highly correlated to majority carrier density; and carrier lifetime after degradation entirely dominated by the boron-oxygen (BO) recombination centre, but with less dependence on majority carrier-density. We demonstrate that before light-induced degradation, the beneficial effect of compensation on carrier lifetime outweighs the reduction in mobility and that the outcome of compensation on the minority carrier diffusion length is consequently positive. We also introduce a method for calculating incomplete ionization, and establish a parametrization of both carrier mobility and lifetime in compensated Si.

In Chapter 4, we concentrate on evaluating the BO defect density, formation or activation kinetics, and recombination activity, in order to assess the structure of the defect as well as the degradation mechanism. We find the effective defect density in p-type Si to be proportional to the total substitutional boron concentration. It also displays poor correlation with the majority carrier density. This strongly vouches for the involvement of substitutional boron against interstitial boron in the defect complex. On the other hand, the degradation rate constant is found to be proportional to the hole density squared in both p-type and n-type Si. By confronting this result with previously proposed defect models, we show that it implies that degradation proceeds through the reconfiguration of a latent defect from an inactive state to a highly-recombinant form. Lastly we analyse the characteristics of the boron-oxygen recombination centre using the Schockley-Read-Hall (SRH) statistics. We find that the SRH parameters of the BO recombination centre cannot be accurately determined using either injection-dependent or temperature-dependent lifetime spectroscopy. We suggest that further work should be devoted to dispelling lingering doubts about the SRH parameters, which would in turn boost confidence in the widely used method for estimating BO defect density.

In Chapter 5, we apply what we have learned in the previous chapters to improving the quality and yield of UMG-Si ingots, and to modelling solar cells made with this material. We experimentally show that industrial-type solar cells with efficiencies exceeding 18% before light-induced degradation can be manufactured with UMG-Si and that Ga co-doping allows higher P concentrations to be tolerated in the feedstock without compromising either ingot yield or solar cell performance. The good agreement between the modelled and experimental characteristics of both UMG-Si and EG-Si solar cells attests to the validity of the parametrization of carrier lifetime and mobility introduced in chapter 3. After activation of the BO defect, we show that performance-degradation is stronger in UMG-Si than in EG-Si solar cells. We also show that compensation does not allow to reduce light-induced degradation. These results call for more intensive efforts to mitigate the BO defect, in order to make UMG-Si competitive with EG-Si.

Chapter 1

Review of the electrical properties of compensated silicon for solar cells

The effects of dopant compensation in Si have been the subject of many studies for a wide variety of applications. Because the intended application of this thesis is photovoltaics, we focus in this chapter on the review of the fundamental properties of compensated Si that are relevant to the well-functioning of a solar cell. These fundamental properties are charge carrier recombination and transport.

In section 1.1, we start by defining the quantities that are essential for the discussion of dopant compensation.

In section 1.2, after reviewing the different recombination mechanisms, we assess the impact of compensation on the recombination lifetime.

In section 1.3, similarly to section 1.3, we review the different scattering mechanisms and describe the particular behaviour of the carrier mobility in compensated Si.

In section 1.4, we use the physical background covered in section 1.3 and 1.4 to understand the effects of compensation on the characteristics of solar cells and hence on their performance and reliability.

In section 1.5, we conclude the chapter and open the scope for compensation engineering.

1.1 Definitions

1.1.1 Compensated silicon

Compensated Si is characterized by the presence of both donor and acceptor dopants in similar concentrations (respectively N_{D} and N_{A}). Because Si inevitably contains electrically active species, originating from the feedstock or introduced during crystal growth, there

is a residual amount of both donors and acceptors in all Si devices. In very pure EG-Si devices, these species are, however, present in concentrations several orders of magnitude lower than the intentional doping. In this work, we restrict the definition of compensation to Si in which the majority carrier concentration is detectably affected by the presence of a compensating dopant. We thus define compensated Si as containing a concentration of minority dopant or compensating dopant (N_{min}) of at least 3% of that of the majority dopant (N_{maj}). This corresponds to the resolution of most of the conductance measurement techniques.

1.1.2 Majority carrier density and net doping

In compensated Si, the type of majority carrier (electron or hole) is defined by the nature of the majority dopant (donor or acceptor). If donors outnumber acceptors ($N_{\mathrm{D}} > N_{\mathrm{A}}$), Si is n-type and electron is the majority carrier. Alternatively, if acceptors are more numerous than donors ($N_{\mathrm{A}} > N_{\mathrm{D}}$), Si is p-type and hole is the majority carrier. It is generally considered that the majority carrier density (noted n_{maj}) equals, at equilibrium, the net dopant concentration $N_{\mathrm{maj}} - N_{\mathrm{min}}$, assuming that all dopants are ionized at room-temperature. As we will show in chapter 3, this assumption might lead to some errors, depending on the nature of the majority dopant, on its concentration and on how strong compensation is. In this review chapter, however, we will assume, as did previous authors, complete ionization of dopants. This enables us to explain in a more straightforward manner the impact of dopant compensation on the electrical properties of Si. It reads:

$$n_{\mathrm{maj}} = n_0 = N_{\mathrm{D}}^{+} - N_{\mathrm{A}}^{-} \approx N_{\mathrm{D}} - N_{\mathrm{A}} \tag{1.1}$$

in n-type Si, and

$$n_{\mathrm{maj}} = p_0 = N_{\mathrm{A}}^{-} - N_{\mathrm{D}}^{+} \approx N_{\mathrm{A}} - N_{\mathrm{D}} \tag{1.2}$$

in p-type Si. In Equations 1.1 and 1.2, n_0 and p_0 are respectively the equilibrium electron and hole densities. N_{D} and N_{A} represent respectively the concentrations of *substitutional* donor and acceptor dopants while N_{D}^{+} and N_{A}^{-} are the concentrations of ionized dopants. As a result, for a given majority dopant concentration, the equilibrium majority carrier density is reduced by the presence of compensating dopants. Figure 1.1 summarizes this sub-section, by drawing the iso-carrier density lines and the doping range corresponding to compensated Si.

1.1.3 Compensation ratios

It is often useful when studying the electrical properties of compensated Si to be able to quantify compensation i.e. how close to each other the concentrations of donors and acceptors are. Over the years, various ratios have been used for that purpose. The most widely

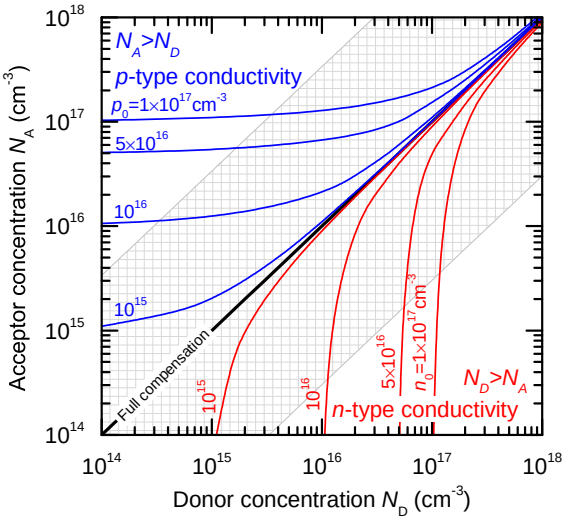

Figure 1.1: Delimitation of the doping ranges for n-type and p-type Si and lines of isocarrier density. The hatched zone represents the doping range in which Si is considered as compensated, according to the definition given in the present section.

spread in literature is the ratio of the minority dopant concentration to the majority dopant concentration noted R_C (equation 1.3) [7, 8, 9]:

$$R_C = \frac{N_{min}}{N_{maj}} \tag{1.3}$$

This ratio, comprised between 0 for uncompensated Si and 1 for full compensation, is convenient to use because of its simplicity and the fact that it does not diverge. In the rest of this thesis, we will thus use R_C in most cases, especially when studying moderate compensation ($R_C < 0.9$). The disadvantage of this ratio, however, is that it does not allow a readable distinction between very high degrees of compensation.

To study variations of the electrical properties at extreme compensation, it may be more appropriate to use diverging ratios, such as those defined by Libal *et al.* [10] or Dubois *et al.* [11], since these ratios enable a stretched representation of the range of very high compensation. In the present work, we use the compensation ratio defined by Libal *et al.* (Equation 1.4), and noted K_C in the rest of this manuscript, when dealing with the effects of extreme compensation.

$$K_C = \frac{N_{maj} + N_{min}}{N_{maj} - N_{min}} \tag{1.4}$$

This ratio varies from 1 in uncompensated Si to $+\infty$ at full compensation. Note that easy conversion between R_C and K_C is possible using equations 1.5 and 1.6:

$$R_C = \frac{K_C - 1}{K_C + 1} \tag{1.5}$$

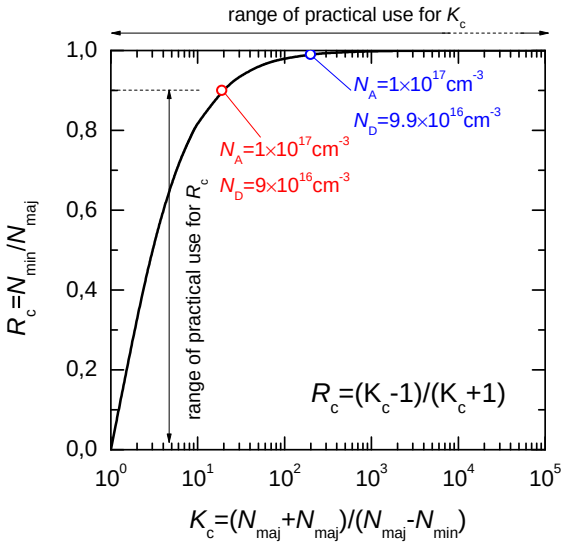

Figure 1.2: Relation between compensation ratios R_C and K_C. The small variation of R_C at extreme compensation indicates that it is not appropriate for studying effects that might arise at very high compensation.

$$K_C = \frac{1+R_C}{1-R_C} \tag{1.6}$$

Figure 1.2 illustrates the range of practical use of each compensation ratio. It shows that, while K_C keeps up increasing at extreme compensation, R_C saturates around 1 and does not permit to describe the increase of compensation after a certain limit. Let us consider the example of Si doped with an acceptor density of $N_A = 10^{17}cm^{-3}$ and a donor density of $N_D = 9\times10^{16}cm^{-3}$ (blue dot on Fig.2). Such a Si is p-type, with a net doping of $N_A - N_D = 1\times10^{16}cm^{-3}$ and compensation ratios are respectively $R_C = 0.9$ and $K_C = 19$. If compensation is now increased by rising the donor concentration up to $9.9\times10^{16}cm^{-3}$, the net doping is reduced by one order of magnitude, down to $10^{15}cm^{-3}$ and the electrical properties will be changed substantially. This increase in compensation is well represented by the large increase of K_C, by about one order of magnitude, up to 199. In the mean time, R_C undergoes a small variation, by only 10%, which may not be representative of the actual change in electrical properties in this range of compensation.

1.2 Recombination in compensated silicon

As put forward by Swanson and Sinton, "*the operation of a well-designed solar cell is controlled by generation and recombination*" [12]. One of the main challenges of using low-cost UMG-Si for high-efficiency solar cells is to maintain sufficiently low recombination in the bulk of the device, despite the presence of a higher concentration of dopants and recombination-active impurities. In this section, we review previous work studying recombination in compensated Si. The first sub-section 1.2.1 focuses on experimental evidence of the increase of the effective recombination lifetime with compensation. The following three

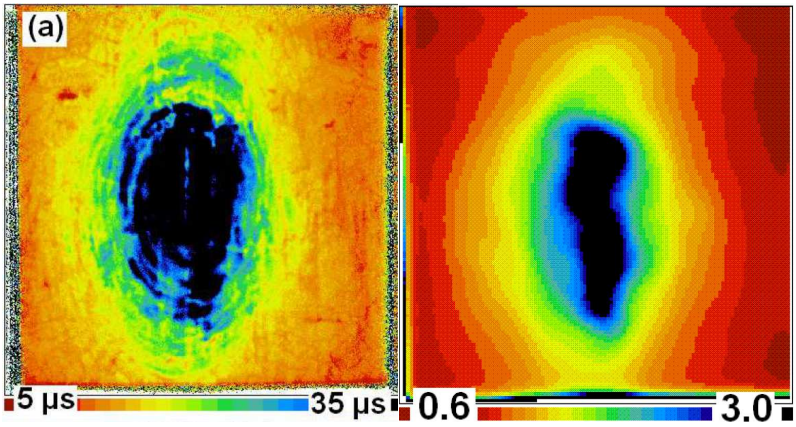

(a) (b)

Figure 1.3: (a) Lifetime mapping of a heterogeneously-doped multi-crystalline compensated Si wafer. (b) resistivity mapping of a neighbouring wafer in the ingot. Both figures are reprinted from [17].

sub-sections 1.2.2, 1.2.3 and 1.2.4 examine the different recombination mechanisms in Si in order to provide a theoretical explanation for this observed behaviour. Finally, the last sub-section 1.2.5 summarizes and concludes on the impact of compensation on the effective carrier lifetime.

1.2.1 Experimental observations

Over the last decade, several groups have reported an increase of the effective recombination lifetime τ_{eff} in highly-compensated regions of mono- and multi-crystalline Si ingots [10, 13, 14, 15, 16] and wafers [17] made with UMG-Si.

One striking and visual example recently came out of a study by Veirman *et al.* [17]. They reported an increase of τ_{eff} in the highly-compensated centre region of a heterogeneous multi-crystalline Si wafer, doped with boron and phosphorus (Figure 1.3). In this wafer, the concentration of boron is uniform ($[\text{B}] = 2.6 \times 10^{17}\text{cm}^{-3}$) across the wafer's surface whereas that of phosphorus increases from $[\text{P}] = 1.6 \times 10^{17}\text{cm}^{-3}$ around the edges to $[\text{P}] = 2.1 \times 10^{17}\text{cm}^{-3}$ in the centre. As a consequence, compensation is stronger in the centre ($R_{\text{C}} = 0.81$) of the wafer than on the edges ($R_{\text{C}} = 0.71$). As attested by the comparison between lifetime and resistivity maps, the lifetime increase coincides perfectly with the increase in compensation. It is remarkable that the highest lifetime is measured in the most compensated region of the wafer, despite the fact that this region also contains the highest total concentration of dopants.

To comprehend this observation, it is central to understand that the strength of most recombination mechanisms increases with the equilibrium majority carrier concentration, as will be shown theoretically in the next three sections. If we consider the majority carrier concentration as equal to the net doping, it appears from equations 1.1 and 1.2 that it is reduced when the compensating dopant concentration increases. The raise of τ_{eff} with compensation can thus be explained in terms of this majority carrier density reduction. A good

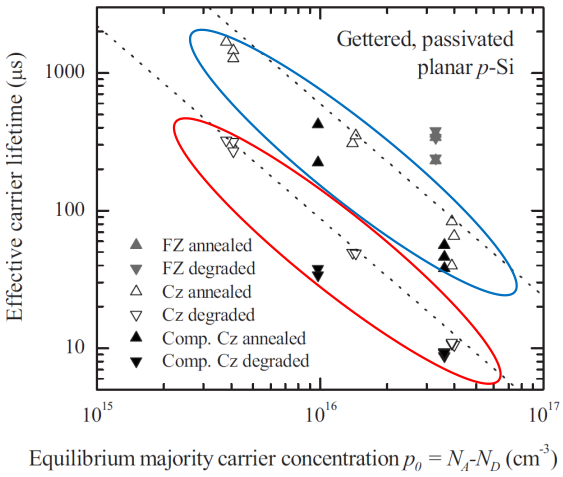

Figure 1.4: Variation of the effective recombination lifetime with the equilibrium majority carrier density in uncompensated and compensated Si. The measured lifetime in compensated Cz-Si scales with the lifetime in uncompensated Cz-Si, showing that the majority carrier density is the dominant parameter that determines recombination. The blue circle indicates the data points in Cz-Si before light-induced degradation while the red circle indicates data points in degraded Cz-Si i.e. after activation of the boron-oxygen defect (see Sub-section 1.2.4). Reprinted from [18].

experimental illustration of the role of the majority carrier density in recombination can be found in a recent contribution by Macdonald *et al.* [18]. On a set of p-type Czochralski-Si wafers, they found that τ_{eff} measured before and after light-induced degradation (see Subsection 1.2.4 and Chapter 4 for more details on the light-induced degradation), followed the same inverse relation to p_0 in compensated as in uncompensated Si (Figure 1.4). The slightly lower τ_{eff} in the compensated samples, compared to uncompensated Si with the same p_0, suggests that the additional dopants present in compensated Si are responsible for very little, if at all, recombination.

On the other hand, Veirman *et al.* [14] found that the bulk lifetime measured in highly-doped ([B] = $2.5 - 5 \times 10^{17}\text{cm}^{-3}$) and highly-compensated Si could be dominated by recombination through the energy level introduced by boron atoms. This study was, however, done on multi-crystalline Si, presumably containing crystallographic defects that may vary one sample to another in nature and abundance, and thus in recombination activity. Recombination at extended crystal defects was however not mentioned in their paper. To clarify that point, the question of recombination through dopants will be addressed in chapter 2 in which original lifetime data in highly-doped and highly-compensated mono-crystalline Si will be presented.

1.2.2 Intrinsic recombination

Radiative and Auger recombination mechanisms both consist of a direct transition by an electron from a given state in the conduction band to a vacant state in the valence band. They differ by the way the excess energy released by the transition is dissipated.

In radiative recombination, the excess energy is released through the emission of a photon. The radiative recombination rate depends on both the concentrations of electron and holes, as expressed by:

$$U_{\mathrm{rad}} = Bpn \tag{1.7}$$

where B is the coefficient of radiative recombination, equal to $9.5 \times 10^{-15}\mathrm{cm}^3\mathrm{s}^{-1}$ at 300K [19]. In an indirect band-gap semiconductor such as Si, this type of recombination has to be accompanied by the emission or absorption of a phonon, in addition to the photon emission, in order to conserve both energy and momentum. As a result, the radiative recombination rate is low compared to that of other recombination mechanisms and is therefore usually considered negligible.

In Auger recombination, the excess energy released by the electron-hole recombination is transferred to a third free carrier, electron or hole. A simple model for the description of Auger recombination considers the charge carriers to be non-interacting quasi-free particles [20]. This results in a simple expression for the Auger recombination rate:

$$U_{\mathrm{Auger}} = C_{\mathrm{n}} n^2 p + C_{\mathrm{p}} n p^2 \tag{1.8}$$

where C_{n} and C_{p} are the Auger coefficient, respectively equal to $2.8\times10^{-31}\mathrm{cm}^6\mathrm{s}^{-1}$ and $0.99\times10^{-31}\mathrm{cm}^6\mathrm{s}^{-1}$ [21]. Although this model fails to accurately reproduce experimental values for the Auger recombination lifetime [22, 23], it enables one to easily grasp its dependence on the carrier concentrations. Equation 1.8 shows that the Auger recombination rate is proportional to the carrier density squared, which makes this mechanism dominant at high injection or high dopant concentration.

The recombination lifetime is expressed as the ratio of the excess carrier density Δn to the recombination rate U:

$$\tau = \frac{\Delta n}{U} \tag{1.9}$$

An accurate parametrization of the intrinsic recombination lifetime, accounting for radiative and Auger recombination, has been given by Kerr and Cuevas [24]:

$$\tau_{\mathrm{intrinsic}} = \frac{1}{(n_0 + p_0 + \Delta n)(1.8 \times 10^{-24} n_0^{0.65} + 6 \times 10^{-25} p_0^{0.65} + 3 \times 10^{-27} \Delta n^{0.8} + 9 \times 10^{-15})} \tag{1.10}$$

which simplifies to:

$$\tau_{\mathrm{intrinsic}} = \frac{1}{(n_0 + \Delta n)(1.8 \times 10^{-24} n_0^{0.65} + 3 \times 10^{-27} \Delta n^{0.8} + 9 \times 10^{-15})} \tag{1.11}$$

in n-type Si, and:

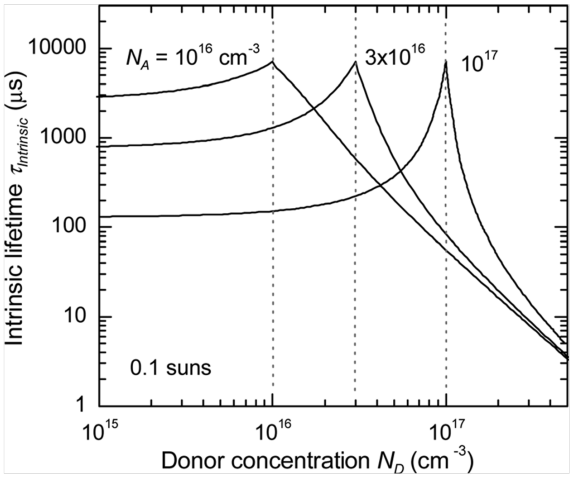

Figure 1.5: Variation of the intrinsic recombination lifetime with the donor concentration for fixed acceptor concentrations of 10^{16}, 3×10^{16} and 1×10^{17}cm^{-3}. $\tau_{\text{intrinsic}}$ clearly increases with compensation, due to the reduction of n_{maj}. Reprinted from [25].

$$\tau_{\text{intrinsic}} = \frac{1}{(p_0+\Delta n)(6\times10^{-25}p_0^{0.65}+3\times10^{-27}\Delta n^{0.8}+9\times10^{-15})} \tag{1.12}$$

in p-type Si.

As inferred by equations 1.11 and 1.12, the intrinsic recombination lifetime increases with decreasing majority carrier concentration ($n_{\text{maj}} = n_0$ or p_0) and decreasing excess carrier density Δn. As shown by equations 1.1 and 1.2, for a given majority dopant concentration N_{maj}, it is possible to reduce the majority carrier density n_{maj} by adding compensating dopants. Hence, the intrinsic recombination lifetime can be increased by compensation. This was shown by Macdonald and Cuevas [25], who calculated $\tau_{\text{intrinsic}}$ for constant acceptor concentrations and variable donor concentrations under a fixed generation rate of 0.1suns (Figure 1.5).

1.2.3 Recombination through defects

All commercially available crystalline Si substrates contain both impurities and intrinsic crystal defects (even in mono-crystalline Si with the presence of self-interstitials and/or vacancies) which vary in nature and density depending on the feedstock and crystallization process used. Some of these impurities and crystal defects induce energy levels in the band gap which may successively trap one electron and one hole, hence acting as a channel for recombination of excess free carriers.

The statistics of recombination through defects were established independently by Shockley and Read [26] and by Hall [27] and is known as the Shockley-Read-Hall (SRH) statistics. The recombination lifetime can be expressed for a given defect with the simplified SRH equation:

$$\tau_{\text{SRH}} = \frac{\tau_{\text{n0}}(p_0+p_1+\Delta n)+\tau_{\text{p0}}(n_0+n_1+\Delta n)}{(n_0+p_0+\Delta n)} \tag{1.13}$$

in which n_1 and p_1 are respectively the electron and hole densities when the Fermi level coincides with the defect energy level E_T:

$$n_1 = N_C \exp\left(-\frac{E_C - E_T}{kT}\right) \tag{1.14}$$

$$p_1 = N_V \exp\left(-\frac{E_T - E_V}{kT}\right) \tag{1.15}$$

In equation 1.13, τ_{n0} and τ_{p0} are respectively the fundamental electron and hole lifetimes, defined as:

$$\tau_{n0} = \frac{1}{N_T v_{th} \sigma_n} \tag{1.16}$$

$$\tau_{p0} = \frac{1}{N_T v_{th} \sigma_p} \tag{1.17}$$

in which N_T is the defect concentration, v_{th} the carrier thermal velocity and σ_n and σ_p are the capture-cross sections of the specific recombination centres, respectively for electrons and holes.

Note that the simplified SRH equation can be used only if the defect density is lower than a certain critical value, in order to avoid excessive trapping effects. For a given defect, the applicability of the simplified SRH equation can be verified using the expression of the critical defect density as a function of the doping given by Macdonald and Cuevas [28]. According to this expression, the defects that will be studied in this work are usually present in a concentration that falls into the range of applicability of the simplified SRH statistics, for the dopant density range relevant to solar cells.

To study the impact of the equilibrium majority carrier density, and ergo compensation, on recombination through defects, it is convenient to study separately defects introducing an energy level close to mid-gap from those with an energy level near the edge of the valence or the conduction band [29].

Mid-gap levels:

Typical defects introducing a deep energy level close to mid-gap are dissolved transition metals such as *interstitial* iron (Fe_i) [30, 31], manganese (Mn_i) [32] or vanadium (V_i) [30] and *substitutional* gold (Au_s) [33] or zinc (Zn_s) [34].

In the case of an energy level close to mid-gap, the SRH equation (Equation 1.13) can be transformed into very simple expressions for the low-injection ($\Delta n \ll n_{maj}$) lifetime τ_{LI}:

$$\tau_{LI} \approx \tau_{p0} \tag{1.18}$$

in n-type Si, and

$$\tau_{\mathrm{LI}} \approx \tau_{\mathrm{n0}} \tag{1.19}$$

in p-type Si, and for the high-injection ($\Delta n \gg n_{\mathrm{maj}}$) lifetime τ_{HI}:

$$\tau_{\mathrm{HI}} \approx \tau_{\mathrm{n0}} + \tau_{\mathrm{p0}} \tag{1.20}$$

In other words, the SRH lifetime is equal to the fundamental lifetime of the minority carrier (τ_{p0} in n-type or τ_{n0} in p-type) at low-injection and to the sum of the fundamental lifetimes ($\tau_{\mathrm{n0}}+\tau_{\mathrm{p0}}$) at high-injection. Because these fundamental lifetimes τ_{n0} and τ_{p0} are constants, the low- and high-injection lifetimes are independent of the majority carrier density n_{maj}. The transition between the two, however, logically depends on n_{maj}. If the high-injection lifetime τ_{HI} is higher than the low-injection lifetime τ_{LI}, the SRH recombination lifetime under a given generation rate may hence be influenced by n_{maj}.

The injection-dependent character of the SRH lifetime depends on the capture cross section ratio $k = \sigma_{\mathrm{n}}/\sigma_{\mathrm{p}}$ of the defect and on the polarity of the material (n-type or p-type). When a defect has a larger capture cross section for the minority carrier than for the majority carrier ($k < 1$ in n-type Si or $k > 1$ in p-type Si), τ_{LI} is smaller than τ_{HI}. In that case, the SRH lifetime exhibits a dependence on the excess carrier density Δn with a transition from low- to high-injection around $\Delta n = n_{\mathrm{maj}}$.

This was illustrated by Macdonald and Cuevas [25] for the case of $\mathrm{Fe_i}$ in p-type Si. Figure 1.6a, from [25], shows for a fixed $\mathrm{Fe_i}$ concentration $5 \times 10^{11}\mathrm{cm}^{-3}$ the SRH lifetime dependence on Δn, for different equilibrium hole concentrations p_0. One can see that due to the much larger capture cross section for electrons than for holes (k = 700) the SRH lifetime is greatly increased from low- to high-injection. As p_0 decreases, the transition from low-injection to high-injection is shifted towards the lower excess carrier concentrations (Figure 1.6a). For a fixed generation of 0.1suns, the SRH lifetime thus increases from 13μs for $p_0 = 10^{17}\mathrm{cm}^{-3}$ up to 2.3ms for $p_0 = 10^{14}\mathrm{cm}^{-3}$. This shows in the overall lifetime, calculated at 0.1suns, which is, for a fixed acceptor concentration, greatly improved when p_0 is reduced by compensation (Figure 1.6b). This effect is referred to as the "injection-level effect" leading to an increase of τ_{SRH} with compensation.

Note that the capture cross section ratio usually depends on the donor or acceptor nature of the defect. Donors ($\mathrm{Fe_i}$, $\mathrm{Mn_i}$, $\mathrm{V_i}$), the charge state of which alternates between positive and neutral, are generally more attractive for electrons than for holes ($k > 1$). They hence display an injection-level effect resulting in an increase of τ_{SRH} with compensation in p-type Si but not in n-type Si. Conversely, acceptors ($\mathrm{Au_s}$, $\mathrm{Zn_s}$) alternate between negative and neutral and are thus more attractive for holes ($k < 1$) and show an injection-level effect in n-type Si only.

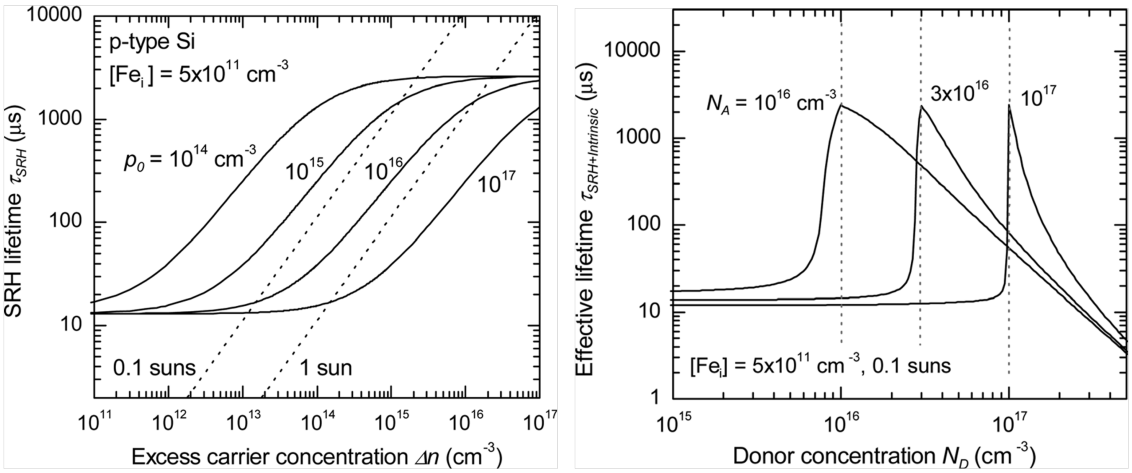

(a) (b)

Figure 1.6: Left: Dependence of the calculated SRH lifetime of Fe_i on the excess carrier density for different equilibrium hole density p_0. Right: Variation with the donor concentration of the calculated effective lifetime under a generation of 0.1 suns, for fixed acceptor concentrations. The effective lifetime shows a strong improvement close to full compensation. Both figures are reprinted from [25].

Shallow levels ($E_C - E_T < 0.3eV$ or $E_T - E_V < 0.3eV$):

Shallow levels are typically introduced by dissolved metals such as Ti, Cr or Mo or by complexes such as CrB or Fe-acceptor (FeB, FeGa, FeIn...) pairs. For a shallow level in p-type Si, the simplified expressions of Equation 1.13 for the low-injection and high-injection lifetimes τ_{LI} and τ_{HI} are:

$$\tau_{\mathrm{LI}} \approx \tau_{\mathrm{n0}} + \tau_{\mathrm{p0}} \times \frac{n_1}{p_0} \tag{1.21}$$

$$\tau_{\mathrm{HI}} \approx \tau_{\mathrm{n0}} + \tau_{\mathrm{p0}} \times \frac{n_1 + \Delta n}{\Delta n} \tag{1.22}$$

for an energy level close to the conduction band, and:

$$\tau_{\mathrm{LI}} \approx \tau_{\mathrm{n0}} \times \frac{p_0 + p_1}{p_0} \tag{1.23}$$

$$\tau_{\mathrm{HI}} \approx \tau_{\mathrm{n0}} \times \frac{p_1 + \Delta n}{\Delta n} + \tau_{\mathrm{p0}} \tag{1.24}$$

for an energy level close to the valence band.

Equations are not shown for n-type Si because they are strictly symmetrical to equations 1.21, 1.22, 1.23 and 1.24. One can deduce from these equations that:

- As for deep-levels, the SRH lifetime of shallow levels is in general different at low-injection than at high-injection. It may thus show a similar "injection-level effect" to that observed

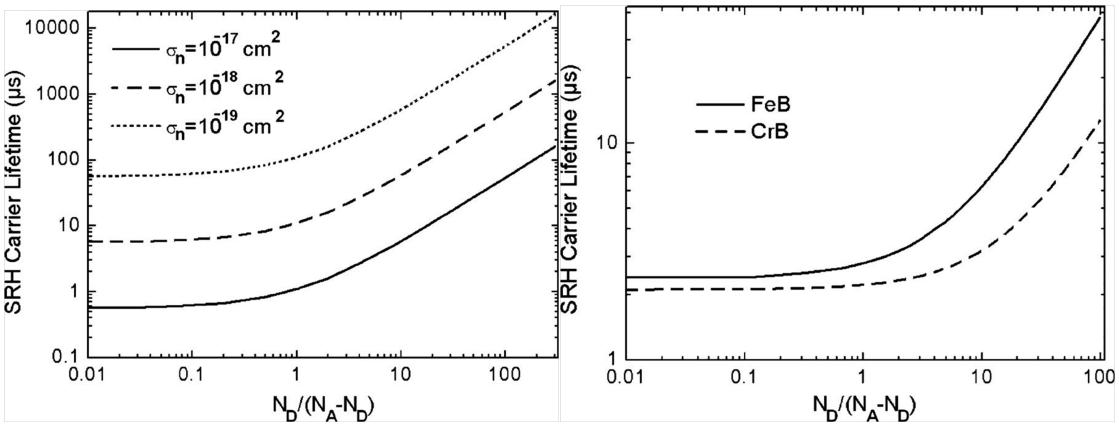

Figure 1.7: Calculated SRH lifetime of B atoms (Left) and FeB and CrB pairs (Right) in p-type Si as a function of the compensation level. Above a certain threshold, the SRH lifetime increases with compensation. Reprinted from [11].

for deep-levels, in the case of a significantly higher capture cross section for the majority carrier than for the minority carrier.

- The low-injection SRH lifetime τ_{LI} is in general dependent on the equilibrium majority carrier density n_{maj}. The lower n_{maj} is, the higher τ_{LI} will be.

Dubois *et al.* [11] explained the experimentally observed increase in lifetime with compensation by this variation of the low-injection SRH lifetime of shallow levels with the majority carrier density. They calculated the SRH lifetime in p-type Si of B atoms (Figure 1.7a) as well as CrB and FeB pairs (Figure 1.7b) to increase noticeably with the compensation level (in their work defined as $N_{\mathrm{D}}/(N_{\mathrm{A}}-N_{\mathrm{D}})$).

Dubois *et al.* argued that this increase of τ_{SRH} with compensation was to be attributed to a "Fermi-level effect". They explained that as compensation increases, E_{F} shifts towards mid-gap, inducing a change of the charge state of shallow acceptors, from neutral to negatively charged, rendering them less attractive for minority carrier electrons. While this analysis may hold true for B atoms, CrB pairs (Figure 1.8) and other defects with a level located near the top of the valence band, it can be shown (Figure 1.8b) that the charge state of FeB pairs, the energy level of which is located close to the bottom of the conduction band, remains unaffected by compensation in p-type Si.

Instead, the improvement of τ as E_{F} moves towards mid-gap, according to equation 1.21, can be attributed to electrons trapped by FeB defects having a larger probability to be re-emitted into the conduction band than to recombine with a hole in the valence band, as the population of holes decreases.

In general, one can say that the Fermi-level effect is observed when E_{F} gets close to the defect's energy level or to its mirror image in the other half of the band gap. In other words when the majority carrier density becomes comparable to n_1 or p_1, the Fermi-level effect leads to an increase of the low-injection SRH lifetime [25]. For example, Macdonald and Cuevas recently showed that almost no improvement of τ_{SRH} of the FeB pair was to be

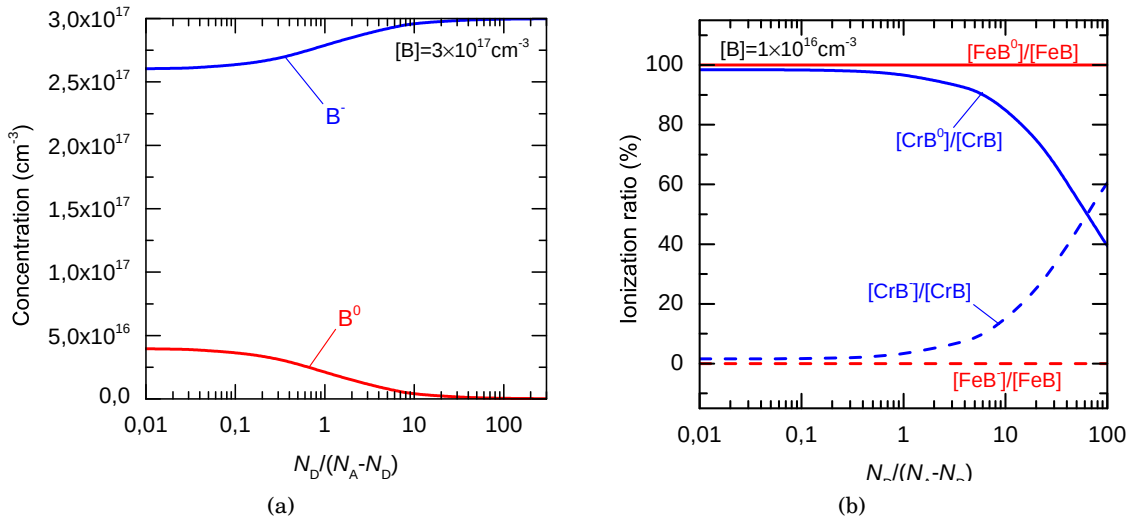

Figure 1.8: Variation of the fraction of ionized B atoms (Left) and FeB and CrB pairs (Right) in p-type Si with the compensation level. While the ionization of B and CrB is affected by compensation, FeB pairs remain in p-type completely neutral.

expected when p_0 was decreased from 10^{17}cm^{-3} to 10^{16}cm^{-3}, while they calculated a strong increase when p_0 was decreased below n_1 ($3 \times 10^{15}\text{cm}^{-3}$), from 10^{16}cm^{-3} to 10^{15}cm^{-3}.

Note that FeB pairs have in practical no impact on the field operation of solar modules because they dissociate within a few seconds under illumination. Nevertheless, their study is essential to understand the minority carrier lifetime or the characteristics of solar cells which are usually measured without preillumination sufficient to break FeB pairs. They also constitute a convenient case of study to illustrate the impact of compensation on the recombination through shallow levels, because their SRH parameters have been extensively [35, 36, 37, 38] studied and are thus fairly well-known. With respect to compensation, what is important to remember from the investigation of the SRH lifetime of FeB pairs is that the recombination strength of shallow levels generally weakens as n_{maj} decreases below a certain threshold, due to a Fermi level effect.

1.2.4 The boron-oxygen defect

A degradation of the recombination lifetime is known to occur in boron-doped and oxygen-containing crystalline Si under illumination or carrier injection [39]. This degradation is thought to result from the formation or activation of a boron-oxygen (BO) complex of which the electrical characteristics have been extensively studied over the years in uncompensated B-doped Cz-Si. Its SRH parameters were determined by Rein and Glunz [40] through a combination of temperature- and injection-dependent lifetime spectroscopy to be $E_C - E_{T,BO} = 0.41\text{eV}$ and $k = 9.3$. It thus falls into the category of defects with an energy level close to mid-gap and a moderately asymmetrical capture cross section ratio. Due to its larger capture cross section for electrons than for holes, the SRH lifetime of the BO defect should thus display a moderate increase in p-type Si, when p_0 is reduced by compensation, because of the previously described injection-level effect.

First studies on uncompensated B-doped Cz Si also measured the BO defect density $N_{T,BO}$ to be proportional to the *substitutionnal* boron (B_s) concentration [41] and to the square of the *interstitial* oxygen (O_i) concentration [42]. This enabled to draw a picture of the defect which depicted it as made up of one *substitutionnal* boron atom and one *interstitial* oxygen dimer. The proportionality of $N_{T,BO}$ to $[B_s]$ and on $[O_i]^2$ results in a recombination lifetime in the degraded state τ_{deg} that can be described at an injection of $\Delta n = 0.1 \times p_0$ by the following empirical parametrization, built up by Bothe *et al.* [43]:

$$\tau_{deg} = 7.675 \times 10^{45} \times [B_s]^{-0.824} \times [O_i]^{-1.748} \tag{1.25}$$

In compensated p-type Si, however, Kopecek *et al.* [44] found that $N_{T,BO}$ was actually proportional to the majority carrier density p_0 instead of the total *substitutionnal* boron concentration $[B_s]$. Note that this finding was made possible in compensated Si by the fact that p_0 is lower than $[B_s]$, while both are almost equal in uncompensated Si. This surprising result was soon after confirmed by similar experiments made by independent groups [45, 46, 47, 48]. Since then, authors have strived to explain it, either by the existence of boron-phosphorus pairs [45, 44], or by building new defect models from which the participation of *substitutionnal* boron is excluded [49]. The aim of this review chapter is not to provide a detailed discussion of the possible reasons for the observed dependence of $N_{T,BO}$ on p_0, which will be discussed in chapter 4. This result is, in itself, enough to show the particularity of the BO defect, for which not only the recombination activity can be reduced by compensation, but also the density of recombination active defect. Considering this linear dependence of $N_{T,BO}$ on p_0 instead of $[B_s]$, the empirical formula 1.25 given by Bothe *et al.* should be usable in the case of compensated Si if one replaces $[B_s]$ by p_0. This reads:

$$\tau_{deg} = 7.675 \times 10^{45} \times [p_0]^{-0.824} \times [O_i]^{-1.748} \tag{1.26}$$

By combining this parametrization to the SRH constants determined by Rein and Glunz [34], it is possible to calculate the injection-dependent SRH lifetime for the BO defect. We did so, using the same conditions as in [19] and for an *interstitial* oxygen concentration of $[O_i] = 7 \times 10^{17} cm^{-3}$ which is a common value for Cz-Si. We chose different fixed concentrations of $[B_s] = 1 \times 10^{16}$, 3×10^{16} and $1 \times 10^{17} cm^{-3}$ and increased compensation by varying the phosphorus concentration. The results (Figure 1.9) show that for the chosen values of $[B_s]$, the effective lifetime τ_{eff} at a fixed generation of 0.1suns is very low ($\tau_{eff} = 2 - 17 \mu s$) in absence of compensation ($R_C = 0$). This suggests that in UMG-Si containing high concentrations of B, τ_{eff} might be almost entirely limited by recombination through the BO defect. However, τ_{eff} is calculated to be greatly improved by compensation, due to the reduction of the BO defect density as p_0 decreases.

Note that light-induced degradation was recently also observed in n-type Si compensated with boron [50]. The formation, and the electrical activity of the defect are, however, more complex in n-type than in p-type and many aspects are yet to be understood in the former material [46, 51, 52, 53]. One point that seems to be generally observed in n-type com-

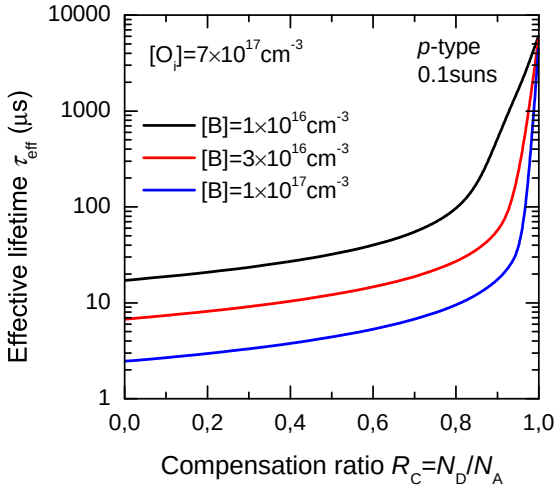

Figure 1.9: Variation of the effective lifetime with compensation in the presence of the boron-oxygen defect in p-type Si. τ_{eff} increases strongly with compensation due to the reduction of the BO defect density with decreasing p_0.

pensated Si is that the BO defect density does not decrease, as it does in p-type Si, when the majority carrier density n_0 is reduced by compensation.

1.2.5 Summary

To summarize this section, we have seen that irrespectively of what mechanism dominates recombination, its strength is determined by the equilibrium majority carrier density. In addition, the only available unambiguous lifetime data on compensated mono-crystalline Si suggest that dopants themselves do not act as important recombination centres. Recombination is therefore identical in compensated Si as in uncompensated Si with the same net doping. It can thus be effectively minimized by reducing the majority carrier density, either by a lower majority dopant concentration or by compensation.

1.3 Carrier transport in compensated silicon

The transport of a charge carrier in a semiconductor is altered by its interaction with local perturbations of the electrical potential in the crystal. Such interaction decreases the excess velocity of a carrier, through the dissipation of part of its energy and/or momentum, and hence reduces its ability (mobility μ or diffusivity D) to move under the influence of an electric field or a concentration gradient. This dissipation of the energy and/or momentum of a charge carrier is called scattering.

1.3.1 Scattering mechanisms

Typical scattering centres in Si are phonons, ionized and neutral impurities, charge carriers and dipoles. In the present section, we restrict our description to the main scattering mechanisms that have been identified [54] as relevant to the study of compensated Si for the

dopant concentration range found in UMG-Si. These scattering mechanisms are phonon scattering, ionized impurity scattering and carrier-carrier scattering.

Phonon scattering Phonon scattering is caused by lattice vibrations, that cause variations of the electrical potential. Phonon scattering can lead to a dissipation of both energy and momentum of a charge carrier. Its importance increases with the concentration of phonons as the temperature (T) is raised. Therefore, the mobility μ_{L} resulting from lattice scattering generally follows an inverse power dependence on T [55, 56] :

$$\mu_{\mathrm{L}} = \frac{1}{T^{\alpha}} \tag{1.27}$$

with α a constant depending on the type of carrier.

Ionized impurity scattering Ionized impurity scattering occurs when a charge carrier encounters the Coulomb field of a fixed ionized impurity. The carrier is deflected from its original trajectory and part of its momentum is dissipated. In doped Si, ionized impurity scattering centres are mainly dopants which are usually present in concentrations far above that of other charged impurities. The strength of ionized impurity scattering increases with the concentrations of ionized dopants (N_{maj}, N_{min}) and decreases with T. The mobility μ_{I} due to ionized impurity scattering hence follows a function of N and T which decreases with N and increases with T.

Carrier-carrier scattering Carrier-carrier scattering works essentially in the same way as ionized impurity scattering. The only difference arises from the fact that the charge carrier is deflected by the Coulomb field of a mobile charge instead of fixed one. Only scattering with carriers of opposite charge is considered to have a significant impact on the mobility [57]. Scattering between carriers of the same charge is only a second order mechanism and does not lead to a loss of momentum but only to its redistribution among carriers of the same type.

To include multiple scattering mechanisms in the calculation of the carrier mobility μ, it is possible to sum their contributions μ_i using Mathiessen's rule:

$$\frac{1}{\mu} = \sum \frac{1}{\mu_i} \tag{1.28}$$

1.3.2 Resistivity-to-doping relation

Uncompensated silicon

In uncompensated Si, the mobility μ of a given type of carrier (electron or hole) is fixed by the temperature T and the concentration of the majority dopant N_{maj}. For a given T, the carrier mobility decreases monotonically with N_{maj}, due to the increasing ionized

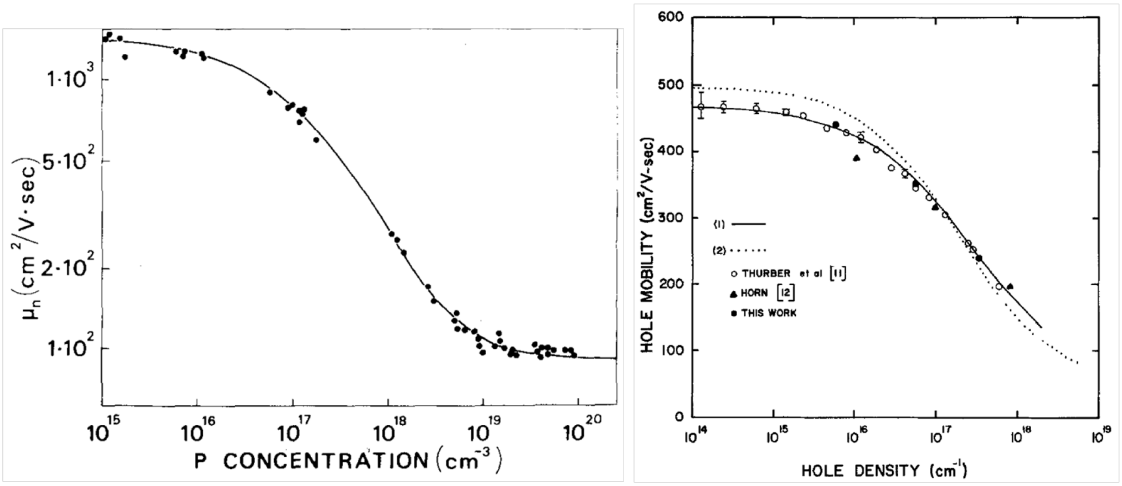

(a) (b)

Figure 1.10: (a) Variation of the electron mobility with the phosphorus concentration in uncompensated n-type Si at room-temperature. Reprinted from [58]. (b) Variation of the hole mobility with the hole density in uncompensated p-type Si at room-temperature. Reprinted from [59].

impurity scattering (Figure 1.10). Note that the electron mobility is in general higher than the hole mobility. This is due to the indirect nature of the motion of a hole, which involves a step-by-step displacement of a large number of electrons, from one occupied orbital to the neighbouring vacant one.

The majority carrier mobility μ_{maj} directly relates the resistivity ρ, which is easily measurable, to the majority carrier density n_{maj} and hence the doping, through the relation:

$$\rho = \frac{1}{n_{\text{maj}} \times q \times \mu_{\text{maj}}} = \frac{1}{N_{\text{maj}} \times q \times \mu_{\text{maj}}(N_{\text{maj}})} \tag{1.29}$$

in which q is the elementary charge of an electron. Because the variation of μ_{maj} with N_{maj} is weak, the evolution of ρ with N_{maj} is dominated by the inverse component $1/N_{\text{maj}}$. The resistivity ρ therefore decreases monotonically with the majority dopant concentration N_{maj} (Figure 1.11). For a given value of ρ, there is thus only one possible corresponding value of N_{maj}. As a fortunate consequence, the majority carrier density, or the majority dopant concentration, can be unambiguously determined by a simple ρ measurement in uncompensated Si. This is, however, not the case in compensated Si.

Compensated silicon

In compensated Si, the majority carrier density does not anymore depend only on the majority dopant concentration N_{maj} but on both N_{maj} and N_{min}, through equations 1.1 and 1.2. In addition, μ is affected by carrier scattering on both the majority- and the minority dopant. For a given majority carrier density n_{maj}, or net doping $N_{\text{maj}} - N_{\text{min}}$, the total concentration of ionized dopant scattering centres is larger in compensated Si than in uncompensated Si

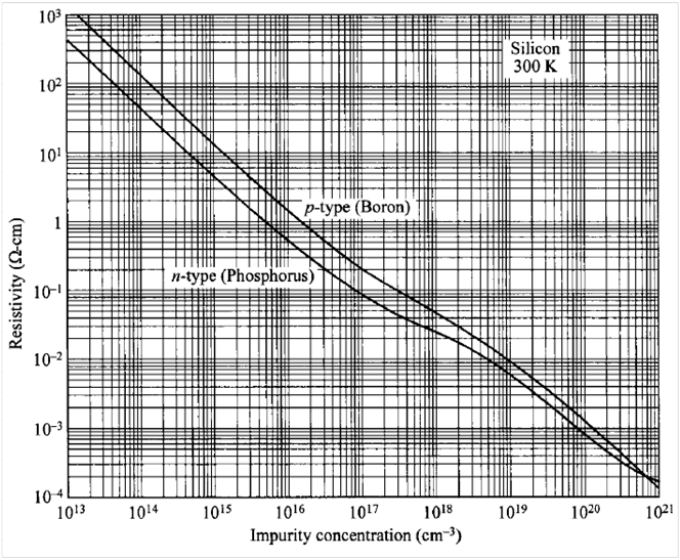

Figure 1.11: Variation of the resistivity in uncompensated n-type Si doped with phosphorus and p-type Si doped with boron as a function of the dopant concentration. Reprinted from [55].

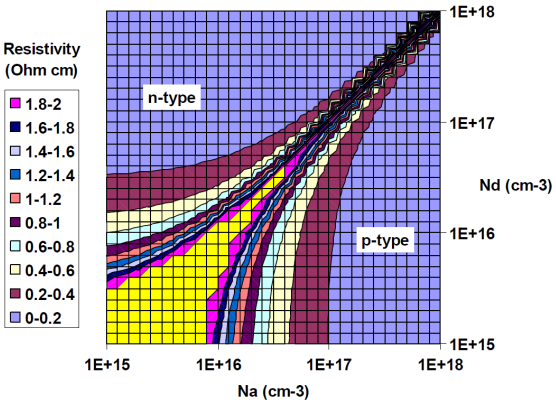

Figure 1.12: Resistivity as a function of the acceptor and donor concentrations in compensated Si using the model of Thurber [61] and Arora [62]. Reprinted from [60].

and μ is therefore lower. As a result, the resistivity, which is expressed below, does not exhibit an unambiguous relation to the individual dopant concentrations N_{maj} and N_{min} or even to the net dopant density $N_{\mathrm{maj}} - N_{\mathrm{min}}$:

$$\rho = \frac{1}{n_{\mathrm{maj}} \times q \times \mu_{\mathrm{maj}}} = \frac{1}{(N_{\mathrm{maj}} - N_{\mathrm{min}}) \times q \times \mu_{\mathrm{maj}}(N_{\mathrm{maj}}, N_{\mathrm{min}})} \tag{1.30}$$

Cuevas [60] calculated the resistivity of compensated Si, as a function of the concentrations of acceptor and donor dopants, using for μ_{maj} the model of Thurber [61] and Arora [62] which assumes that μ depends on the total dopant concentration $N_{\mathrm{maj}} + N_{\mathrm{min}}$. The result, displayed on Figure 1.12, shows that for a given value of ρ, there is an infinity of possible donor and acceptor concentration $(N_{\mathrm{A}}, N_{\mathrm{D}})$ couples and values for the net doping $N_{\mathrm{A}} - N_{\mathrm{D}}$.

This shows that ρ measurements cannot be used in compensated Si, as in uncompensated Si, to deduce the dopant concentrations or the majority carrier density. This fact forces

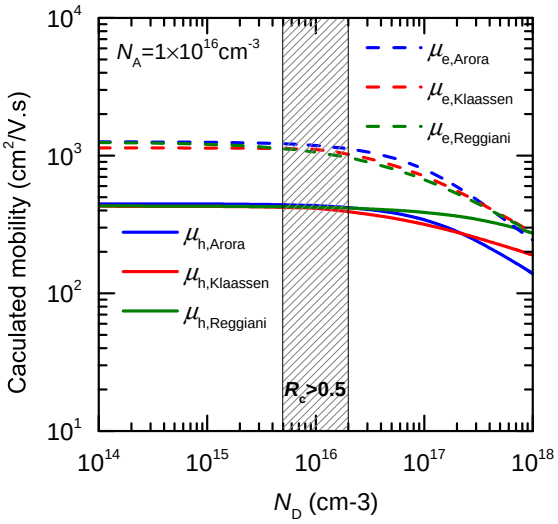

Figure 1.13: Variation of the electron and hole mobility with the donor concentration, in Si containing an acceptor concentration of 1×10^{16}cm^{-3} calculated with Arora's, Klaassen's and Reggiani's model. The hashed zone represent highly-compensated Si with $R_C > 0.5$.

authors dealing with compensated Si to use techniques that measure directly the majority carrier density, such as Hall effect, capacitance-voltage or free-carrier absorption measurements, and to develop new characterization techniques [63, 64] to estimate the individual concentrations of dopants in compensated Si.

1.3.3 Deviation from mobility models

Modelling the mobility is essential to predict the performance of solar cells. In particular, the minority carrier mobility $\mu_{\min}$ affects the minority carrier diffusion length $L_{\min}$, which is a central parameter for the suitability of a material for solar cells, as it directly controls the electrical current that can be generated. In addition, the knowledge of the mobility can be necessary for Si wafers and solar cells characterization, for example for photoconductance based lifetime measurements [65] or for *interstitial* oxygen mapping [66].

Most mobility models are entirely empirical [62, 67, 68, 69], and were constructed to fit experimental data on uncompensated Si. Most of these models hence consider μ to depend only on the dopant sum $N_A + N_D$, thereby assuming that ionized dopants act as identical scattering centres, irrespectively of their type and of the considered carrier. Only Klaassen's model [57, 56] is semi-empirical, and separates the different scattering mechanisms, i.e. lattice scattering, ionized donor scattering, ionized acceptor scattering and carrier-carrier scattering. It also includes the screening of scattering centres by other surrounding charges. A quick glimpse at the comparison between Klaassen's model and other purely empirical models (Figure 1.13), however, shows that they do not yield significantly different values in the concentration range of interest for solar cells, even in compensated Si.

Over the last five years, many studies have confronted mobility models to experimental data in compensated Si [10, 46, 70, 71, 14, 72, 73, 74, 75, 76, 77]. They all come to the same conclusions, that can be summarized as follows:

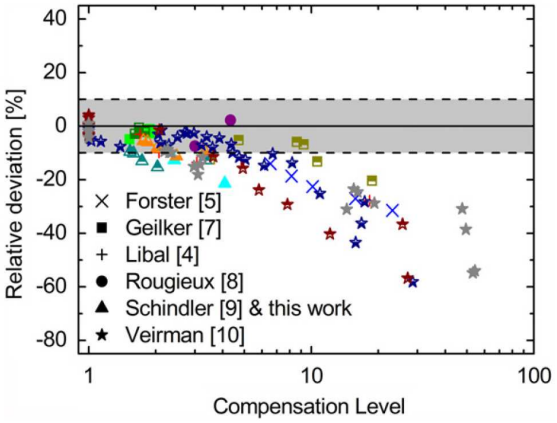

Figure 1.14: Relative deviation of the measured majority carrier mobility compared to Klaassen's model. This figure presents mobility data from 6 different research groups. Reprinted from [77].

- In lightly compensated Si, the measured μ can be accurately described by the available models.

- At higher compensation levels, models overestimate μ. The deviation from the models increases with the compensation level (Figure 1.14).

- The deviation from Klaassen's model, in highly-compensated Si, is in general stronger for the minority carrier than it is for the majority carrier. This is despite Klaassen's model reproduces the minority carrier mobility in uncompensated Si with greater accuracy than other models.

Different explanations have been proposed to explain this reduction of the measured mobility in compensated Si compared to models. Veirman *et al.* have suggested the existence of a compensation-specific scattering mechanism [70] or the presence of local net doping non uniformities acting either as scattering centres or as sources of errors for the mobility measurements [71]. Lim *et al.* [46, 74] and more recently Schindler *et al.* [77] have proposed that the mobility could be lower due to the reduction of the screening of scattering centres by free carriers of which the concentration is reduced by compensation. These propositions will be discussed in chapter 3, in the light of our measurements of the temperature-dependence of the majority carrier mobility in compensated Si.

1.4 Compensated silicon solar cells

In the previous sections, we have analysed how dopant compensation influences recombination and carrier mobility in Si. This lays the fundamentals that are necessary to understand the impact of compensation on the performance of solar cells. The first following 4 sub-sections (5.3.2,5.3.3,1.4.3 and 5.3.4) deal with the influence of compensation on the basic characteristics of solar cells i.e. the open-circuit voltage, the short-circuit current, the fill factor and as a result the efficiency. The next 2 sub-sections (1.4.5 and 1.4.6) deal with issues related to the field operation of solar modules, through the study of how compensa-

tion acts upon the reverse breakdown voltage of solar cells and the temperature coefficients of their characteristics.

1.4.1 Open-circuit voltage

The open-circuit voltage (V_{oc}) of a solar cell is defined by the following expression:

$$V_{oc} = kT \times \ln\left(\frac{(n_0 + \Delta n) \times (p_0 + \Delta n)}{n_i^2}\right) \approx kT \times \ln\left(\frac{(n_{maj} + \Delta n) \times \Delta n}{n_i^2}\right) \tag{1.31}$$

This expression shows that there are two competing effects of n_{maj}, and thus of compensation, on the open-circuit-voltage. On one hand, n_{maj} is directly involved in the expression of the open-circuit voltage and, at equal Δn, V_{oc} decreases as n_{maj} is reduced. On the other hand, the reduction of n_{maj} increases Δn, through the improved effective recombination lifetime τ_{eff}. Macdonald and Cuevas [25] theoretically showed that at moderate doping ([B] = $1-3\times10^{16}$cm^{-3}), the latter effect dominates, and that V_{oc} increases monotonically as τ_{eff} is improved with decreasing n_{maj} by compensation. At higher doping ([B] = 10^{17}cm^{-3}), V_{oc} initially decreases with compensation, due to the reduction in n_{maj}, until very strong compensation is reached and above which the voltage starts increasing again, due to the enhancement of τ_{eff} (see Figure 1.15a).

This theoretical finding was confirmed by Veirman *et al.* [14] who measured V_{oc} to decrease with the height of two p-type multi-crystalline Si ingots made with UMG-Si (Figure 1.15b) which contained very large boron concentrations ($2-4\times10^{17}$cm^{-3}). In those ingots, compensation increases along the ingot height due to phosphorus segregation being stronger than that of boron (see chapter 2).

Note, however, that both the modelling from [25] and the experimental data from [14] neglect the influence of the BO defect (in [14], V_{oc} was measured before light-induced degradation). Due to the strong dependence of τ_{eff} on p_0 in the presence of the BO defect (Figure 1.9), the lifetime effect of compensation on the voltage might dominate even at high doping, which would lead to a monotonic increase of V_{oc} with compensation.

In any case, the optimization of the open-circuit voltage requires a precise control of the majority carrier density. The optimum n_{maj} depends on the mechanisms that dominate recombination and is hence to be determined for each particular material and solar cell structure of interest. It is also worth noting that, if neglecting the impact of μ on the excess carrier distribution across the thickness of a solar cell, the open-circuit voltage depends, for a given structure, only on n_{maj} and should thus not be different in compensated Si from in uncompensated Si with the same net doping.

1.4.2 Short-circuit current

The quality of the material used for the base of a solar cell determines the short-circuit current J_{sc} of the device through the minority carrier diffusion length, defined by:

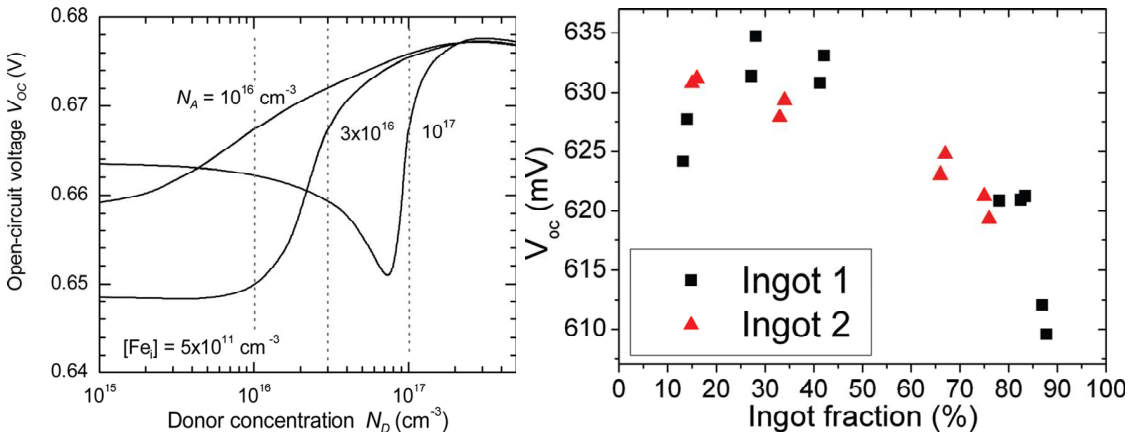

Figure 1.15: (a): Calculated open-circuit voltage as a function of the donor concentration for fixed acceptor concentrations. Reprinted from [25]. (b): Measured V_{oc} along the height of two highly-doped and compensated multi-crystalline UMG-Si ingots. Reprinted from [14].

$$L_{\min} = \sqrt{\tau_{\text{eff}} \times D_{\min}} = \sqrt{\tau_{\text{eff}} \times \mu_{\min} \times \frac{kT}{q}} \tag{1.32}$$

Again, the effect of compensation on J_{sc} is subjected to a compromise, this time between the increase of the recombination lifetime τ_{eff} and the reduction of the minority carrier mobility $\mu_{\min}$. Theoretical evaluation of the trade-off between the opposite trends of these two parameters is made difficult by the inaccuracy of mobility models for compensated Si. Previous workers [25, 78] have calculated J_{sc} to increase monotonically with compensation, but their modelling can be regarded as optimistic, since they used Klaassen's model which is known to overestimate $\mu_{\min}$ in highly-compensated Si.

While theoretical studies do not allow to conclude on the outcome of the competition between τ_{eff} and $\mu_{\min}$, some experimental studies [11, 79] have reported $L_{\min}$ to increase significantly with compensation. This suggests that the mobility reduction is largely outweighed by the increase in τ_{eff}. For example, Dubois *et al.* [11] measured a larger $L_{\min}$ in the highly-compensated centre region of a solar cell made with a neighbouring wafer to those of which the resistivity and lifetime are shown in Figure 1.3.

Due to this enhancement of $L_{\min}$ with compensation, J_{sc} have been measured by different groups to increase monotonically with compensation, as reported in [13, 80, 81].

1.4.3 Fill factor

The fill factor (FF) encompasses all the losses that reduce the voltage or the current of a solar cell at maximum power point below their values in open-circuit and short-circuit conditions. FF can be influenced by n_{maj} in two ways [25]:

- The base conductivity decreases with decreasing n_{maj}, inducing an increase of resistive losses. These resistive losses reduce the voltage at maximum power point (V_{mpp}) compared

to the voltage in open-circuit condition.

- Due to carrier collection, the excess carrier density is lower at maximum power point than it is in open-circuit conditions. This also induces V_{mpp} to be lower than V_{oc}. When the recombination lifetime exhibits a strong excess carrier density dependence (see Figure 1.6), it might decrease from its high injection value to its low injection value as the cell is shifted from open-circuit to maximum power point. As a result, the decrease in excess carrier density is even stronger, leading to a reduced V_{mpp} and hence a lower FF. Since the Δn transition from low to high injection depends on n_{maj}, compensation may affect FF through a lifetime injection-dependence effect.

As a result, FF generally decreases as n_{maj} is reduced by compensation, due to the lifetime injection-level effect and, to a lesser extent, due to the resistive losses. This is until extreme compensation is reached, for which the injection-level effect ceases (the base is in high injection at maximum power point as in open-circuit) and FF increases with compensation back to a stable value.

1.4.4 Efficiency

The conversion efficiency (η) of a solar cell is the fraction of incident light power (P_{incident}) which is converted into usable electrical power. It can be expressed by:

$$\eta = \frac{J_{\mathrm{sc}} \times V_{\mathrm{oc}} \times FF}{P_{\mathrm{incident}}} \tag{1.33}$$

To maximize η, it is thus necessary to optimize the product of the 3 parameters on which we have discussed the impact of compensation in the previous sub-sections. As we have shown, these 3 parameters are strongly dependent on the equilibrium majority carrier density n_{maj} in the base of solar cells which can be adjusted by compensation. So far, the only limitation of compensation arises from the reduction of mobility which makes the short-circuit current lower for a compensated solar cell than for an uncompensated one with the same n_{maj}. The study of J_{sc}, however, showed that the reduction of μ_{min} is largely counterbalanced by the increase of τ_{eff} with compensation and should thus not impose a drastic penalty on the device performance. Experimental results on the efficiency of compensated UMG-Si solar cells confirm this analysis.

The first experimental observation [82] showing that η could be improved by compensation was made during the early phase of the Photosil project, with a measured jump of 3.5% absolute in the highly-compensated top region of an ingot made with purified MG-Si. The efficiency was then still relatively low (12.5% maximum), due to the large concentrations of dopants and metal contaminants. Since then, repeatable η of above 15% on average [14, 83] have been achieved on multi-crystalline UMG-Si ingots despite large concentrations of B and P (on the order of [B] = 1 – 3ppmw/1.3 – 3.9×10^{17}cm^{-3} and [P] = 6 – 8ppmw/2.7 – 3.6×10^{17}cm^{-3}). With purer UMG-Si material ([B] < 0.5ppmw/6.5×10^{16}cm^{-3} and [P] < 1ppmw/4.5×10^{16}cm^{-3} comparable η to uncompensated EG-Si have been obtained, with typical values above 16%

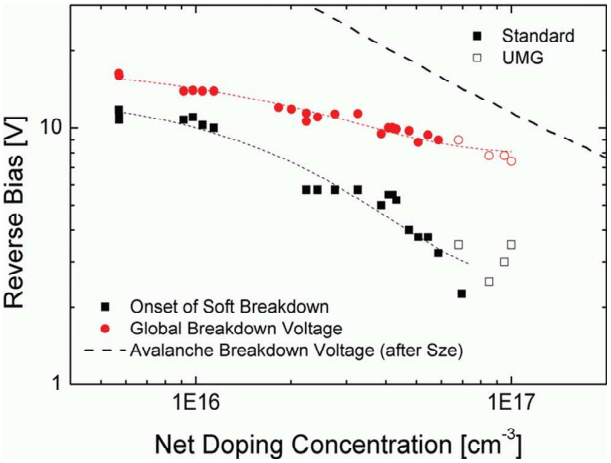

Figure 1.16: Variation of the global breakdown voltage and the voltage at which onset of breakdown appears, as a function of the net doping. For both the global breakdown and the onset of breakdown, compensated cells scale very well with uncompensated cells, indicating that the dominant parameter for breakdown is the majority carrier density. Reprinted from [92].

for multi-crystalline [84, 85, 86, 87] and reaching up to 19% for mono-crystalline Si solar cells [47, 85, 88]. These results clearly prove that compensated Si can be an appropriate material for making high-efficiency solar cells.

1.4.5 Breakdown voltage

A shaded solar cell might, when connected in strings inside a module in operation, be reversed-biased by the other cells. When this results in a large reverse current, especially if the latter is localized, the module can be damaged by the resulting excessive heat generation. The phenomenon of junction breakdown under a reverse bias is thus a serious reliability issue for modules which has to be treated at the cell level. The physical mechanisms of junction breakdown have been reviewed in detail in the case of mono-crystalline Si by Mahadevan *et al.* [89] and more recently for multi-crystalline Si by Breitenstein *et al.* [90]. Although different types of breakdown have been identified to occur in mono- and in multi-crystalline Si solar cells, it was shown that the breakdown voltage (V_B) decreases in both cases with the base doping, presumably due to the reduction of the space charge region of the junction [91].

In compensated UMG-Si, Kwapil *et al.* [92] measured the breakdown voltage V_B to follow the same dependence on the net doping $N_{maj} - N_{min}$ as in uncompensated EG-Si. This is despite the larger concentration of metals in UMG-Si that are known to enhance junction breakdown [90]. Such result indicates that the influence of the net doping is dominant over that of other contaminants. Recently, a similar dependence of V_B on $N_{maj} - N_{min}$ was also reported by Veirman *et al.* [80]. Those results show that the severity of junction breakdown can be mitigated by keeping $N_{maj} - N_{min}$ low i.e. by a tight control of compensation in the case of UMG-Si.

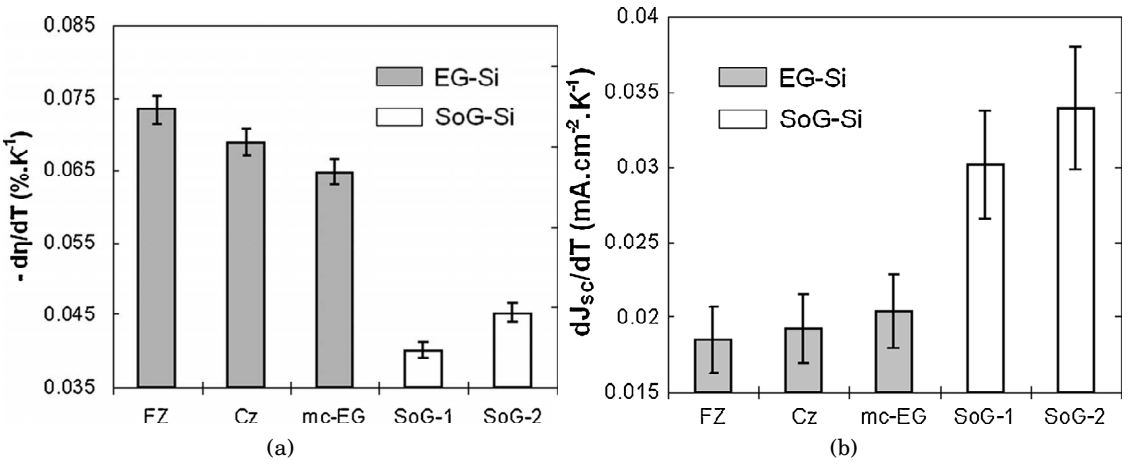

Figure 1.17: Comparison of the efficiency (a) and short-circuit current (b) temperature coefficients of compensated UMG-Si (referred to as SoG-Si in the graphics) solar cells with uncompensated EG-Si solar cells. Reprinted from [93].

1.4.6 Temperature coefficients

In a recent study, Tanay *et al.* [93] have reported a weaker degradation with increasing temperature of the conversion efficiency of solar cells made with compensated UMG-Si, compared to those made with uncompensated EG-Si. This improved temperature-dependence was shown to result from a larger increase of the short-circuit current in compensated UMG-Si solar cells than in the EG-Si control solar cells.

In the same study, the authors showed that this behaviour could be explained by two characteristics of compensated UMG-Si:

1. The weaker dependence of the minority carrier mobility on temperature in compensated Si.

2. The larger concentration of recombination-active defects in UMG-Si, limiting the minority carrier diffusion length, and of which the capture cross sections decrease quadratically with T.

These better temperature coefficients for modules made with compensated UMG-Si solar cells should yield a better field power output per installed peak power than standard modules made with EG-Si solar cells, since the operation temperature is usually higher than the standard testing temperature. This was shown in an experiment conducted by Peter *et al.* [94] who compared over 20 months the performance ratio of systems with UMG-Si modules to systems with standard EG-Si modules. The results clearly show that UMG-Si modules perform better than EG-Si modules during the hot season and slightly worse during cold months.

1.5 Conclusion

In this chapter, we have reviewed the fundamental electrical properties of compensated Si. The analysis of recombination in Si shows that it is determined by the majority carrier density and can thus be lowered by compensation. On the other hand, the mobility of both the majority and the minority carrier is shown to decrease with compensation, due to the additional ionized dopants scattering centres and to a mechanism of which the origin is not yet clearly identified.

Investigations of the basic characteristics of solar cells show that the improvement of the recombination lifetime largely overweights the minority carrier mobility reduction, driving the diffusion length, and hence the short-circuit current of a solar cell, to increase monotonically with compensation. Other cell characteristics, such as the open-circuit voltage, the fill-factor or the reverse breakdown voltage are also strongly depending on the majority carrier density but are only weakly affected by the carrier mobility. These characteristics are thus almost identical in compensated Si as in uncompensated Si with the same net doping.

As a consequence, the optimal majority carrier density should be very similar for compensated Si as for uncompensated Si solar cells with the only additional losses in compensated Si being due to the lower carrier mobility. As we saw in the last sub-section, these losses become less important as the temperature increases, which suggest that their influence is minimized in field operation conditions compared to room-temperature.

These findings open the discussion for “compensation engineering” which consists in, when the majority carrier concentration differs from its optimal value, adjusting it by the addition of either compensating dopant or majority dopant. In UMG-Si, the majority dopant concentration is usually much higher than the optimal majority carrier density and compensation engineering is therefore essential to achieve the best possible cell performance. The next chapter will focus on the practical challenges that such an approach implies when it has to be employed at the ingot level and will demonstrate the potential of gallium co-doping to control the net doping along UMG-Si ingots.

Chapter 2

Compensation engineering to control the net doping along silicon ingots

In the end of chapter 1, we came to the conclusion that good performance solar cells could be made with compensated Si, upon condition that the net dopant density was well-controlled. While this means for the solar cell manufacturer that a careful selection of the incoming wafers in a production line is required, it implies for the ingot grower the necessity to be able to fabricate ingots with a well-targetted and uniform net doping, in order to deliver the largest possible fraction of the crystallized material.

As we show in this chapter, a tight control of the net doping along directionally solidified compensated Si ingots may, however, prove very challenging, due to the strong segregation of phosphorus. To overcome this issue, we propose to use gallium co-doping and demonstrate its potential to control the net doping along p-type and n-type crystals grown with Si initially containing both boron and phosphorus.

- In section 2.1, we briefly describe the most widely used crystallization techniques for solar cell production and provide the theoretical background necessary to understand the problematic of segregation of dopants in compensated Si ingots. We also explain in detail the principle of gallium co-doping to obtain Si crystals with uniform net doping.

- In sections 2.2 and 2.3 we present the experiments that we have conducted, by growing Czochralski Si crystals, to demonstrate the effectiveness of gallium co-doping to control the net doping along p-type and n-type Si ingots.

2.1 Theory

2.1.1 Crystallization techniques

In 2010, about 83% of the world production of solar modules was based on crystalline Si, almost entirely obtained by either the Czochralski technique (44%) or by ingot casting (55%).

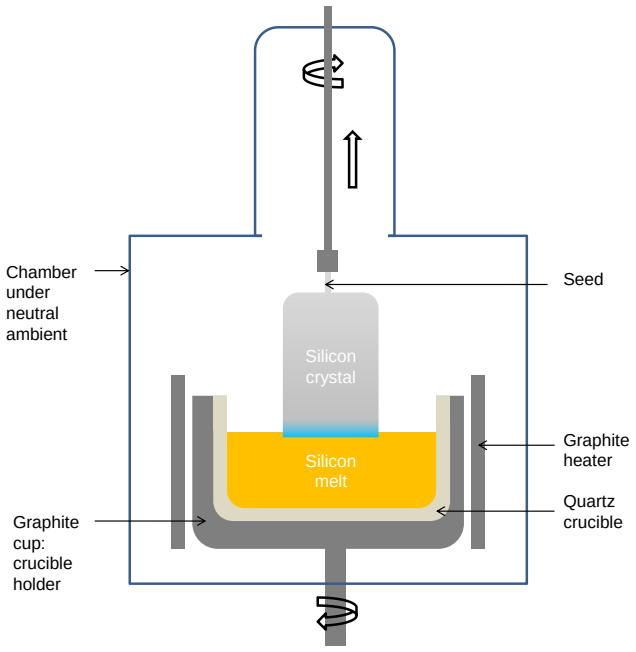

Figure 2.1: Schematic of a typical Czochralski crystal pulling system.

In this sub-section, we describe these two major crystallization techniques.

2.1.1.1 Czochralski growth

The Czochralski (Cz) crystallization technique was discovered in 1916 and first published in 1918 [95]. This technique was for the first time applied to the growth of Si crystals in 1952 and it was not until 1958 [96] that the achievement of dislocation-free Si crystals was reported.

A schema of a Cz pulling system in operation is drawn in Figure 2.1. Si is first molten in a quartz crucible and maintained at a temperature just above the melting point. A mono-crystalline Si seed with the desired crystal orientation is then brought into contact with the surface of the Si melt. The crystal is then grown by pulling the seed from the melt and decreasing temperature below the melting point, while the seed and the crucible are rotating in opposite directions. The diameter of the crystal is controlled during the process by adjusting the pulling rate v and the temperature. Typical industrial Cz-Si crystals for PV are currently of $200-300$mm in diameter and up to 2m in length.

The resulting material is mono-crystalline and free of dislocations. It, however, contains point defects of which the nature (vacancies or self-interstitials) and the concentration depend on the growing conditions [97] and have a critical influence on the quality of the material. In addition, Cz-Si contains large concentrations of oxygen (O), due to the dissolution of the quartz crucible, and carbon (C), due to the contamination by the graphite heating elements of the system. While neither of them is electrically active in its dissolved state, both are undesirable in Si. Indeed, oxygen forms complexes (BO defect, thermal donors) and precipitates that affect the doping and significantly enhance recombination, while carbon induces mechanical stresses and promotes oxygen precipitation. Typical O concentrations

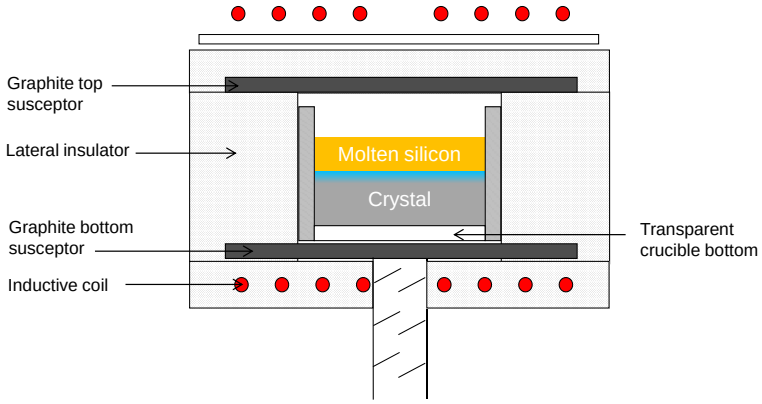

Figure 2.2: Schematic of the ingot casting system developed by Cyberstar and Apollon Solar. Details can be found in [99].

in Cz-Si are in the range $5-10\times10^{17}\text{cm}^{-3}$ while the C concentration can be kept below $1\times10^{17}\text{cm}^{-3}$.

Note that it was shown that the oxygen contamination can be significantly reduced by the application of a transverse magnetic field [98], which suppresses turbulent convection in the case of small diameter crystals. The potential and cost-effectiveness of magnetic-Cz (MCz) is, however, yet to be proven for large diameter crystals.

Another possible improvement of the standard Cz-growth process that has to be mentioned here is the possibility to reload the crucible with Si during crystallization, in order to make continuous or semi-continuous growth. This possibility will show of particular interest as we address the phenomenon of impurity segregation in section 2.1.2.

2.1.1.2 Ingot casting

In the casting technique, Si is molten and crystallized inside the crucible. The ingot is directionally solidified, from bottom to top, by extracting the heat from the bottom of the system. When a seed is put in the bottom of the crucible, this technique enables to obtain mono-crystalline or quasi-mono-crystalline Si ingots. In the absence of a seed, the ingot is multi-crystalline. A schematic of the crystallization system developed by Cyberstar and Apollon Solar [99] is given in Figure 2.4, as an example of an ingot casting process.

The main advantage of this technique over the Cz method is that it enables to crystallize much larger ingots with a higher throughput and hence a lower cost. Also, crucibles used for ingot casting are coated with Si nitride, acting as a barrier against the diffusion of oxygen from the crucible into the Si. As a consequence, the O concentration is usually lower in cast ingots than in Cz crystals, typically in the order of $1-5\times10^{17}\text{cm}^{-3}$.

On the other hand, although this technique was initially developed for making single crystals [100], it has mostly been used for the growth of multi-crystalline Si ingots which, by definition, contain grain boundaries and dislocations acting as nucleation sites for the precipitation of impurities and as strong recombination centres. Even when single crystals are grown by the seed-assisted casting method, high dislocation densities are difficult to

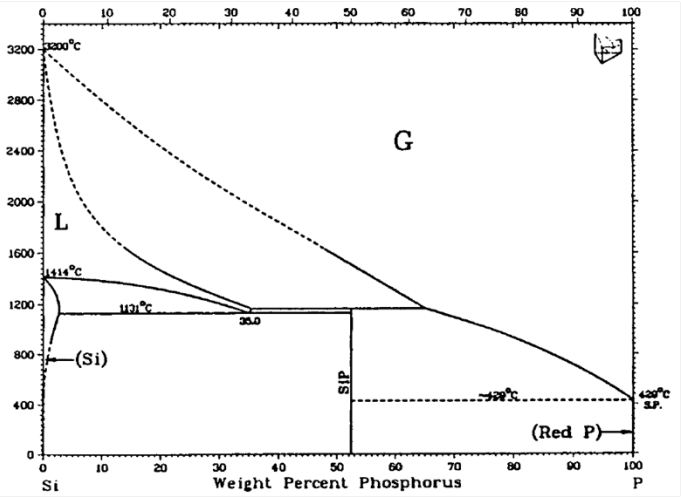

Figure 2.3: Phase diagram of the binary alloy Si-P. Reprinted from [101].

avoid in the entire ingot, due to residual stresses occurring during crystallization and ingot cooling. In addition, cast ingots are usually more strongly contaminated in C, due to the proximity of the heating elements to the Si melt, and in metallic impurities that are thought to originate from the Si nitride coating. Overall, cast Si usually displays lower recombination lifetime than Cz-Si and thus yields lower efficiencies, especially in the case of advanced solar cell devices.

2.1.2 Distribution of impurities in silicon crystals

As we have seen in the previous sub-sections, the two major crystallization techniques that are used to for the production of Si wafers for the photovoltaic industry are both directional. This has consequences in terms of impurity distribution along crystals, due to the phenomenon of segregation. In this sub-section, we describe segregation and analyse its impact on the doping variation in directionally solidified Si crystals.

2.1.2.1 Segregation

A given solute does not usually have the same solubility in the liquid phase of a given substance than in its solid phase. This leads to the phenomenon of segregation when both the solid and the liquid phase of an alloy coexist, as during crystallization of doped Si. This phenomenon can be illustrated with the example of the Si-P alloy, the phase diagram of which is shown in Figure 2.3.

Let us imagine for example an alloy of 10% of P and 90% of Si. The phase diagram of the Si-P system indicates that, at 1500°C, this alloy is present in the form of one liquid solution. If the alloy is progressively cooled down, a solid phase appears as the temperature of the system reaches that of the liquidus (~ 1390°C). This solid phase has a P concentration which is, as determined by the solidus curve, much lower (~ 1%) than the total P concentration of the alloy. As a consequence, a large part of the P contained in the volume of the alloy which

is solidified is rejected into the liquid phase. The liquid phase is therefore enriched in P, following the liquidus curve as the fraction of solidified compound increases with decreasing T.

This phenomenon is called segregation and can be represented at a given T by the ratio of the solute concentration of the solidus curve $C_S(T)$ to that of the liquidus curve $C_L(T)$ (Equation 2.1). This ratio is called the segregation or partition coefficient.

$$k = \frac{C_S(T)}{C_L(T)} \tag{2.1}$$

In doped Si, the impurity concentration is much lower than 10%, usually in the order of 0.01 to 1ppma. In that case, the solidus and liquidus curves can be approximated by straight lines, of which the slopes m_S and m_L define the equilibrium segregation coefficient k_0 of a given impurity in Si:

$$k_0 = \frac{m_L}{m_S} \tag{2.2}$$

Experimental values for the equilibrium segregation coefficients of most impurities in Si have been gathered in an exhaustive review by Trumbore [102]. We report in table 2.1 the segregation coefficients for the main dopants in Si.

Element	k_0
Boron	0.8
Gallium	0.008
Aluminium	0.002
Indium	4×10^{-4}
Phosphorus	0.35
Arsenic	0.3
Antimony	0.023

Table 2.1: Equilibrium segregation coefficients of the main dopants in Si.

One can notice that all the major dopants have in Si an equilibrium segregation coefficient which is lower than unity. As a result, dopants are rejected during crystallization into the liquid phase and their concentration along directionally solidified crystals increases with the solidified fraction, as will be shown using Scheil's equation in the next sub-section.

2.1.2.2 Scheil's equation

Let us now apply segregation to the distribution of an impurity along a Si crystal solidified along one direction. We consider for that a constant volume of Si contained in a bar with a length L and a cross section A, the solidification front progressing at a distance l from the seed (Figure 2.4).

The conservation of the total amount of solute when an element of volume $\mathrm{d}l \times S$ is solidified reads:

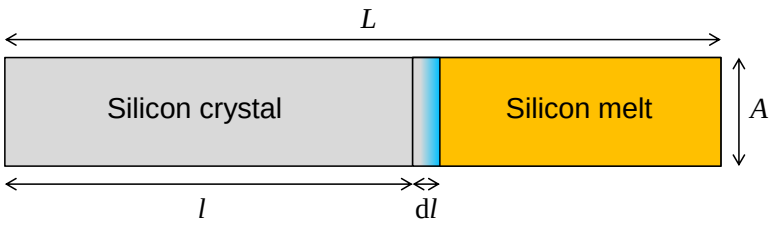

Figure 2.4: Schematic of the directional solidification of a Si crystal.

$$A \times (L - l) \times \mathrm{d}C_\mathrm{L} = (C_\mathrm{L} - C_\mathrm{S}) \times \mathrm{A} \times \mathrm{d}l \tag{2.3}$$

With C_L the impurity concentration in the Si melt, which is considered as perfectly homogeneous[1], and C_S the concentration incorporated into the solidified element of volume $\mathrm{d}l \times A$. By using $C_\mathrm{S} = k_0 \times C_\mathrm{L}$, and introducing the solidified fraction $f_\mathrm{S} = l/L$, equation 2.3 becomes:

$$\frac{\mathrm{d}C_\mathrm{L}}{C_\mathrm{L}} = (1 - k_0) \times \frac{df_S}{1 - f_S} \tag{2.4}$$

By integrating this equation, using C_0, the initial impurity concentration in the Si melt as a boundary condition, we obtain:

$$C_\mathrm{L} = C_0 \times (1 - f_S)^{k_0 - 1} \tag{2.5}$$

This leads to Scheil's equation [103] for the distribution of an impurity along a directionally solidified crystal:

$$C_\mathrm{S} = k_0 \times C_0 \times (1 - f_S)^{k_0 - 1} \tag{2.6}$$

Note that this equation is only valid in the case of a conservative system, in which there is no addition or loss of Si or impurity after the beginning of crystallization. Two particular cases can be mentioned as departing from those conditions:

1. The first one is the case of continuous growth, mentioned before, in which the crucible is replenished with Si during crystallization. The impurity in the Si melt is in this case diluted by the addition of Si. If the reloading is appropriately optimized, the impurity concentration can thus be kept almost constant along the length of crystals obtained by continuous Cz-growth.

2. The second one is the case of an impurity being added into the melt or evaporated from the free surface of the Si melt during crystallization. This is for example the case of oxygen, which is both added into the melt, through the dissolution of the crucible,

[1] This either assumes a perfectly stirred Si melt or an infinite diffusion coefficient for the considered impurity in liquid Si. This will be discussed in Sub-section 2.1.2.3.

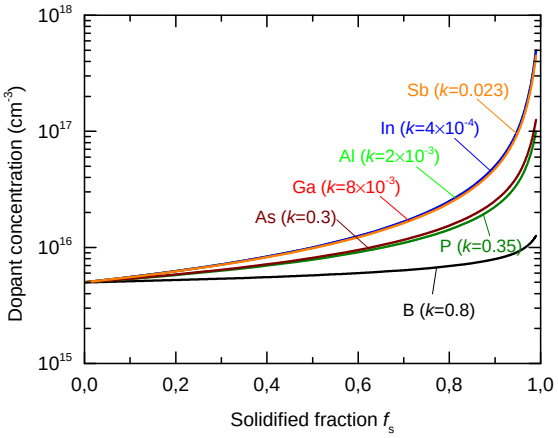

Figure 2.5: Variation of the concentration of most common dopants with the solidified fraction along directionally solidified Si crystals.

and evaporated from the free surface of the melt. Scheil's equation hence cannot be applied to the calculation of the oxygen distribution in Si ingots [104].

In the rest of this thesis, we consider the assumption of a conservative system to be a good approximation for the dopants that are investigated (boron, phosphorus and gallium) and for standard Cz-growth and ingot casting techniques that are the most widely used in wafer production for solar cells.

Figure 2.5 shows, for common dopants, the calculated impurity distribution as a function of the solidified fraction, using Scheil's equation. The initial concentrations in the melt C_0 were adjusted for each dopant to yield a doping of $5 \times 10^{15}\text{cm}^{-3}$ at the beginning of crystallization. Because all of these dopants have a segregation coefficient below 1, they are progressively rejected in the liquid phase during crystallization, and their concentration thus increases with the solidified fraction. As can be seen, the lower the segregation coefficient, the stronger the doping variation along the ingot height. Boron, of which the segregation coefficient is very close to unity, shows a very uniform distribution. P and As, with lower segregation coefficients (0.35 and 0.3 respectively) display a larger variation but still not as strong as Sb, Ga, Al and In with segregation below 0.1. This highlights one of the major motivation for the choice of B and P as the dopants used for most of the Si devices.

Interestingly, Sb, Ga, Al and In show exactly the same variation along the ingot height despite their k_0 being significantly different. This shows that, below a certain threshold for k_0, the variation of the impurity concentration does not depend anymore on k_0. According to Scheil's equation (equation 2.6), the impurity concentration cannot increase by more than a factor of 10 along the first 90% of an ingot, even at extremely low k_0.

2.1.2.3 Effective segregation coefficient

To derive Scheil's equation, we have considered that the Si melt is perfectly homogeneous. Although the melt is effectively homogenized by thermal convection and by the rotation of the crucible, the impurity concentration usually varies in the vicinity of the solid/liquid

interface at which impurities are rejected into the melt ($k_0 < 1$) or depleted from the melt ($k_0 > 1$). To take this into account, Burton, Prim and Schlichter [105] considered the existence of a diffusion layer in the Si melt at the solid/liquid interface, of which the thickness δ can be calculated as a function of the growth conditions:

$$\delta = 1.6 \times D^{\frac{1}{3}} \times K_v^{\frac{1}{6}} \times \omega^{-\frac{1}{2}} \tag{2.7}$$

in which D is the diffusion coefficient of impurity in liquid Si, K_v is the kinematic viscosity of the Si melt [106, 107], and ω is the crystal rotation rate. They also showed that this diffusion layer could be accounted for in the calculation of the impurity distribution, by simply using in Scheil's equation an effective segregation coefficient k_{eff}, defined by equation 2.8. This derivation of the effective segregation coefficient is commonly referred to as the BPS theory for the initials of its inventors.

$$k_{\text{eff}} = \frac{k_0}{1 + (1 - k_0)\exp\left(-\frac{v\delta}{D}\right)} \tag{2.8}$$

2.1.3 Dopant distribution in compensated silicon ingots

2.1.3.1 Net doping variations

As we have seen in chapter 1, controlling the net doping is of paramount importance for the performance of compensated Si solar cells. The following paragraphs aim at showing the difficulty to do so when growing crystals with Si containing both boron and phosphorus. We chose to study separately the case of p-type and n-type compensated Si ingots.

***p*-type compensated Si ingots** Let us imagine a relatively impure UMG-Si, containing 0.8ppmw ($1.04 \times 10^{17}\text{cm}^{-3}$) of B and 3ppmw ($1.36 \times 10^{17}\text{cm}^{-3}$) of P. The B and P distribution along an ingot grown with such a Si feedstock, without the addition of dopant, is shown in Figure 2.14. Because of the smaller segregation coefficient of P compared to B, its concentration increases more strongly along the ingot height. Therefore, the net doping $N_{\text{A}} - N_{\text{D}}$, which starts at a value of $3.5 \times 10^{16}\text{cm}^{-3}$ decreases with the solidified fraction, until the P concentration exceeds that of B and the Si switches from p-type to n-type at about 70% of the crystal length.

If the optimum majority carrier density is lower than $3.5 \times 10^{16}\text{cm}^{-3}$ for a particular cell process, one might be tempted to add P into the Si melt in order to reduce the maximum net doping in the crystal. It is, however, obvious from figure 2.14 that doing so would result in a shift of the type inversion towards the beginning of crystallization and thus in a decrease of the maximum usable fraction of the ingot. If, on the other hand, one wants to push the type inversion towards the end of crystallization, they can add boron into the melt but knowing that this will result in an undesirable increase of the net doping at the beginning of crystallization.

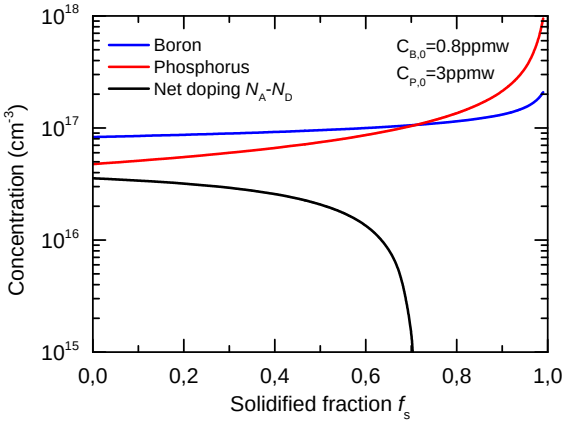

Figure 2.6: B, P and net doping distribution along a ingot crystallized with 0.8ppmw of B and 3ppmw of P.

Figure 2.7 illustrates the trade-off that a would-be compensation engineer has to face if trying to control the net doping along a p-type Si ingot co-doped with B and P. If specifying that at least 90% of the ingot has to be p-type, the maximum acceptable P concentration, for an initial B concentration of 1×10^{17}cm^{-3}, is 8×10^{16}cm^{-3}. In that case the minimum value for the net doping at the beginning of crystallization is 5×10^{16}cm^{-3}. This highlights the limits of compensation engineering at the ingot level when using only B and P as dopants, since the net doping at the beginning of crystallization can only be reduced to about half of the total boron concentration, without compromising too much the maximum ingot yield.

If now specifying a maximum net doping of for example 1×10^{16}cm^{-3}, in addition to the requirement of having 90% of p-type Si, the intersection of the 1×10^{16}cm^{-3} iso-net doping line with the 90% iso-type inversion line (indicated with an orange dot on figure 2.7) gives the maximum concentrations of B and P that can be tolerated in the Si melt. These maximum concentrations are respectively $[B]_0 = 1.9 \times 10^{16}$cm^{-3} (0.15ppmw) and $[P]_0 = 1.5 \times 10^{16}$cm^{-3} (0.33ppmw). Such drastic specifications put a high pressure on the purification of UMG-Si and limit its potential cost advantage over the Siemens process.

Note that a similar approach to define the B and P specifications in UMG-Si was presented by Enebakk *et al.* [108]. They, however, based their approach on setting a target for the resistivity at $f_S = 0\%$ instead of the net doping. As we have shown in chapter 1, the relevant parameter for solar cells is the net doping and the lower mobility in compensated Si makes the resistivity a misleading indicator of the net doping.

***n*-type compensated Si ingots** In n-type compensated Si ingots, the origin of the problem is identical to p-type compensated Si, except for this time, the stronger segregation of P compared to B leads to a strong increase of the net doping with the solidified fraction. Figure 2.8 shows the variation of the net doping along an n-type uncompensated P-doped Si ingot, and n-type compensated Si ingots with different initial concentrations of B ($[B]_0$ =0.3, 0.5 and 1ppmw or 3.9×10^{16}, 6.5×10^{16} and 1.3×10^{17}cm^{-3}). For each of them, the P concentration $[P]_0$ in the Si melt is adjusted to yield a net doping equal to 5×10^{15}cm^{-3} at the

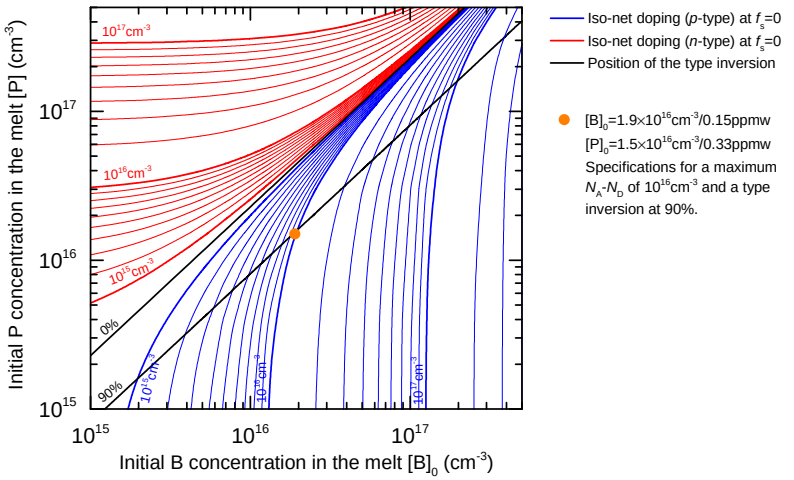

Figure 2.7: Iso-net doping at the beginning of crystallization $f_S = 0\%$ and solidified fraction at which the switch from p-type to n-type occurs, in a directionally solidified Si crystal, as a function of the initial B and P concentrations in the melt.

beginning of crystallization. For comparison, we also show the doping variation in an uncompensated B-doped with the same target for the doping at $f_S = 0\%$. The concentrations of B and P in the Si melt for each of those ingots are reported in table 2.2

As can be seen on figure 2.8, the net doping varies over a much wider range in compensated n-type Si ingots than in uncompensated ingots doped with only P. One can also see that the higher the initial B concentration $[B]_0$ is, the stronger the net doping variation will be. Indeed, because of the presence of compensating B atoms, it is necessary that the Si melt initially contains a relatively high concentration of P for the entire ingot to be n-type i.e. for the concentration of P to be higher than the B concentration at the beginning of crystallization. For example, if the Si melt contains 0.5ppmw of B (6.5×10^{16}cm^{-3}), it is necessary that it is also doped with at least 3.54ppmw (1.6×10^{17}cm^{-3}) of P (already in the Si feedstock or added before crystallization) for the net doping ($N_D - N_A = [P] - [B]$) to be higher than 5×10^{15}cm^{-3} in the first solidified part of the ingot. Under such conditions, because the P concentration increases along the ingot whereas the B concentration remains almost constant, the net doping rises up to very high values (1.7×10^{17}cm^{-3} at $f_S = 90\%$) in the last solidified fraction of the ingot. This corresponds to a variation of the net doping along the first 90% of the ingot by a factor of 34!

Assuming that an acceptable net doping range is $5 - 20 \times 10^{15}$cm^{-3} (as delimited by two dashed lines in figure 2.8) for a given solar cell process, one can calculate the ingot yield for all the ingots considered above (reported in Table 2.2). Note that because of the wide net doping variation, the ingot yield is systematically very small in n-type ingots grown from a compensated Si melt. Even when the initial B concentration is as low as 0.3ppmw, which corresponds to commercial UMG-Si, the ingot yield does not exceed 50%. Such a low material yield is not economically viable and penalizes the competitiveness of n-type UMG-Si.

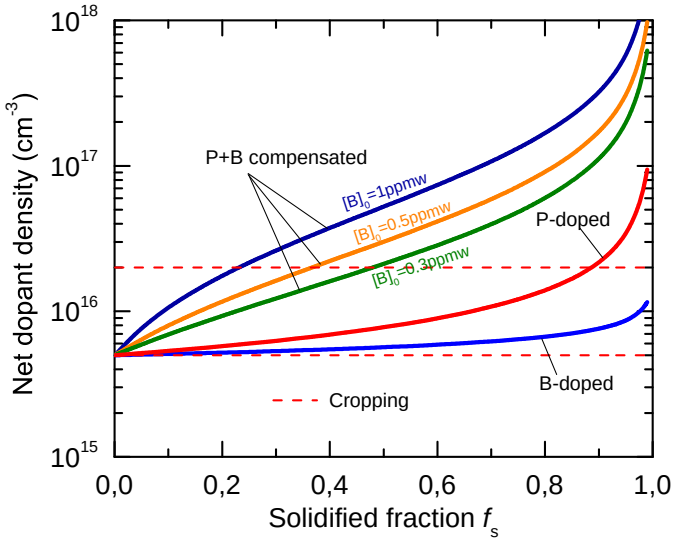

Figure 2.8: Calculated net doping profile along a p-type uncompensated B-doped Si ingot, an n-type uncompensated P-doped Si ingot and compensated n-type ingots co-doped with P and B.

$[B]_0$ (ppmw/cm^{-3})	$[P]_0$ (ppmw/cm^{-3})	Conductivity type	Ingot yield (%)
$0.047/6.1\times10^{15}$	...	p-type	100%
...	$0.304/1.38\times10^{16}$	n-type	88%
$0.3/3.9\times10^{16}$	$2.24/1.02\times10^{17}$	n-type	48%
$0.5/6.5\times10^{16}$	$3.54/1.60\times10^{17}$	n-type	36%
$1/1.30\times10^{17}$	$6.77/3.07\times10^{17}$	n-type	24%

Table 2.2: Initial dopant concentrations in the Si melt and calculated material yield for the ingots represented in figure 2.8. The material yield is calculated considering that an acceptable range for the net doping is $5-20\times10^{15}$cm^{-3}.

2.1.3.2 Gallium co-doping

Gallium is an acceptor dopant and has, as reported in table 2.1, a very low segregation coefficient $k_{Ga}=0.008$. We propose to use these advantageous properties to counterbalance the increase of P along the length of directionally solidified crystals. The idea of Ga co-doping can be illustrated with the previous examples taken for p-type and n-type compensated Si ingots.

***p*-type co-doped Si ingots** As we have seen on figure 2.10, an ingot grown with a Si feedstock containing 0.8ppmw of B and 3ppmw of P should display, according to Scheil's equation, a net doping of 3.5×10^{16}cm^{-3} at $f_S=0\%$ and an inversion from p-type to n-type at $f_S=70\%$. It can be shown, using Scheil's equation, that by adding 70ppmw of Ga, this type inversion can be completely avoided. Because of the very low segregation of Ga, its concentration is low in the beginning of the ingot and its addition to the melt hence only result in a small increase of the net doping at $f_S=0\%$, up to 4.7×10^{16}cm^{-3}. In contrast, to push the type inversion to $f_S=90\%$ without using Ga, one would have to increase the initial B concentration in the melt up to 1.3ppmw, which would lead to a net doping of

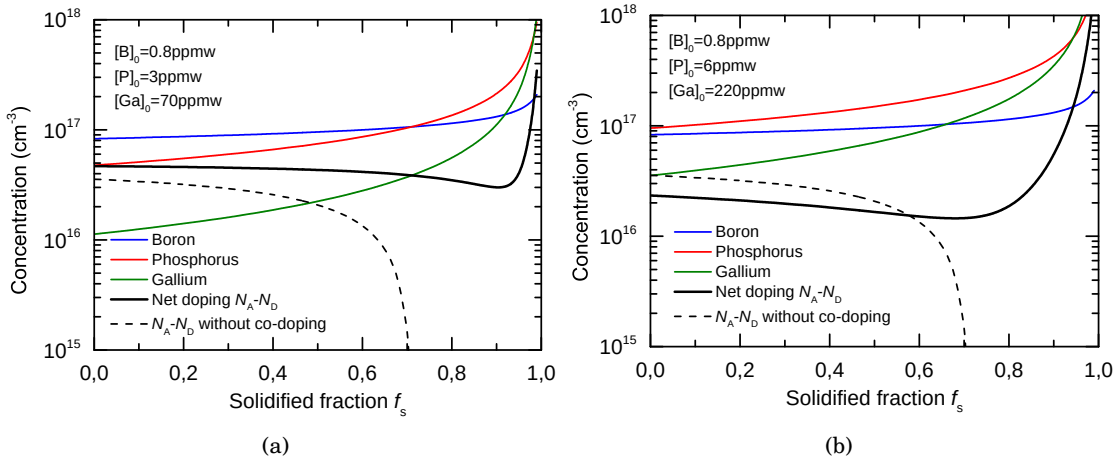

Figure 2.9: Dopants distribution along p-type Si ingots co-doped with B, P and Ga. Relatively low net doping and completely p-type Si ingots can be achieved by the addition of Ga.

$8.8 \times 10^{16}\text{cm}^{-3}$ at $f_S = 0\%$. Also note that due to Ga co-doping, the net doping is very uniform ($3.0 - 4.7 \times 10^{16}\text{cm}^{-3}$) along 95% of the ingot.

Now, if a given solar cell process requires a lower net doping than $4.7 \times 10^{16}\text{cm}^{-3}$, it is possible to reduce it by adding P, while maintaining an entirely p-type ingot with the addition of Ga. For example, if $[\text{P}]_0$ is increased up to 6ppmw and $[\text{Ga}]_0$ to 220ppmw, it is possible to maintain a uniform net doping comprised in the range $1.4 - 2.5 \times 10^{16}\text{cm}^{-3}$ over 85% of the ingot. The net doping then increases abruptly due to the strong accumulation of Ga in the very last fraction of the ingot.

***n*-type co-doped Si ingots** Similarly to the growth of p-type ingots, Ga can be used for n-type ingots to counterbalance the increase of P towards the end of crystallization. In that case, the aim is not to avoid a type inversion but to minimize the increase of the net doping $N_D - N_A$ with the solidified fraction. An example is shown in figure 2.10 for an ingot grown with Si containing 0.5ppmw of B. Scheil's equation shows that, by adjusting adequately the P and Ga concentrations in the Si melt before crystallization, the net doping can be kept in the range we previously defined ($5 - 20 \times 10^{15}\text{cm}^{-3}$) over 85% of the ingot.

Note that an important advantage of Ga co-doping over other proposed solution to control the net doping along Si ingots is that Ga is added with the Si and other dopants into the crucible before melting and that there is no reloading of Si or impurity during crystallization. This technique can thus be used with the most basic Cz and casting furnaces and do not require an additional reloading system.

One could also remark that two other p-type dopants, Al and In, have been identified as displaying the same distribution as Ga along directionally solidified Si ingots. Al, however, is known for forming highly recombination active complexes with O [109] and is thus not desirable in Si for solar cells. Because of the very small segregation coefficient of In (4×10^{-4}), larger quantities should be added in the melt to yield the same concentration in the

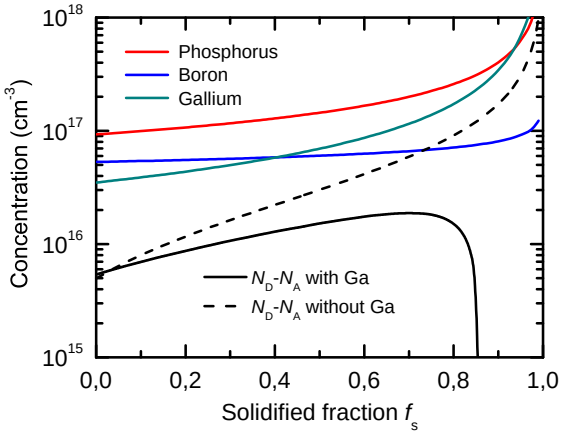

Figure 2.10: P, B, Ga and net doping distribution along an n-type ingot grown from a melt containing [B]=0.5ppmw, [P]=5.62ppmw and [Ga]=202ppmw. The net doping is compared to what it would be without the use of Ga co-doping.

crystal as with Ga. Taking those considerations into account, Ga thus appears to be the best candidate to apply compensation engineering at the ingot level.

2.2 Experimental procedure

In the previous section, we have shown that strong net doping variations were to be expected in compensated ingots grown with Si containing both boron and phosphorus. We proposed, based on calculations using Scheil's equation, that these net doping variations could be suppressed by gallium co-doping. In this section, we report an experimental investigation of the effectiveness of Ga co-doping in controlling the doping variations along p-type and n-type compensated Si ingots.

2.2.1 Material preparation

For this study, four <100>-oriented Si ingots of about 160mm in diameter was crystallized using the Czochralski technique. The crystals were pulled with an average rate of v = 0.7mm/min, a crystal rotation rate of w_{cryst} = 1.26rad.s^{-1} and an inverse rotation of the crucible with a rate of w_{cruc} = 0.84rad.s^{-1} under an Ar pressure of 20torr. For these crystal growth conditions, the effective segregation coefficient of each impurity can be calculated from the equilibrium segregation coefficient presented in table 2.1, using the BPS theory (equation 2.8). These effective segregation coefficients are reported in table 2.3.

Dopant	k_{eff}
Boron	0.818
Phosphorus	0.365
Gallium	8.6×10^{-3}

Table 2.3: Effective segregation coefficients of B, P and Ga for the specific growth conditions used in this work.

Each crystal was pulled from a Si melt made of 10 to 15kg of intrinsic EG-Si to which precisely weighed quantities of P, B and Ga were added (Table 2.4). B and P were introduced under the form of highly-doped Si wafers in which the dopant concentration was determined by four-point probe resistivity measurements. Ga was added as high-purity pellets. For this study, we chose to use intrinsic EG-Si and to add B, P and Ga, instead of starting with a UMG-Si already containing B and P. This was in order to study the impact of dopants only and to separate out the influence of other impurities, that may be found in UMG-Si, on the electrical properties of the material.

Ingot	Type	Mass (kg)	$[B]_0$ (ppmw/cm^{-3})	$[P]_0$ (ppmw/cm^{-3})	$[Ga]_0$ (ppmw/cm^{-3})
Cz#1	p-type	15	$0.21/2.7\times10^{16}$	$3.93/1.8\times10^{17}$	$288/5.8\times10^{18}$
Cz#2	p-type	15	$1.5/2.0\times10^{17}$	$7.0/3.7\times10^{17}$	$180/3.6\times10^{18}$
Cz#3	p-type	10	$1.5/2.0\times10^{17}$	$10/4.5\times10^{17}$	$300/6.0\times10^{18}$
Cz#4	n-type	10	$0.50/6.5\times10^{16}$	$5.6/2.6\times10^{17}$	$202/4.1\times10^{18}$

Table 2.4: Initial concentrations in the Si melt for the 4 Cz-Si ingots co-doped with B, P and Ga that were grown in this work.

For the p-type ingots, the concentrations of B and P were chosen to be representative of extreme cases of UMG-Si. The Ga concentration was adjusted using Scheil's equation in order to yield fully p-type Si ingots with a relatively low net doping. In Cz#1, the B concentration is low while the P concentration is very high. For this ingot, we aim at showing that even when the feedstock contains a much higher concentration of P than of B, it is still possible to obtain, by Ga co-doping, a fully p-type ingot with a net doping compatible with the fabrication of good performance solar cells. In Cz#2 and Cz#3, we start with a high concentration of B, *a priori* unsuitable for the fabrication of high-efficiency solar cells. We then try to reduce the net doping by adding P while maintaining fully p-type ingots with the addition of Ga. The concentrations of P and Ga were chosen for Cz#2 to be moderately compensated ($R_C = 0.60 - 0.90$) and Cz#3 highly compensated ($R_C = 0.77 - 0.97$).

For the n-type ingot, the B concentration (0.5ppmw/6.5×10^{16}cm^{-3}) was chosen to be slightly above the current specification for p-type UMG-Si ingots. The P and Ga concentrations were calculated using Scheil's equation to obtain n-type Si with a net doping comprised in the range $5 - 20\times10^{15}$cm^{-3} over 85% of the ingot.

After crystallization, all ingots were shaped into 125×125mm^2 pseudo-square bricks and sliced by wire sawing into wafers with a thickness of $200-240\mu$m. Note that, for each ingot, about 15-25% of the initial Si mass remained in the crucible at the end of crystallization or was cut off with the ingot tail. Unfortunately, ingot Cz#2 broke during wire sawing and only wafers from two heights ($f_S = 4\%$ and $f_S = 32\%$) could be used for the characterization at the wafer level.

2.2.2 Characterization

After crystallization, the conductivity type was checked along the length of each ingot with a Semilab PN-100 surface photovoltage tester. After shaping into 125×125mm^2 pseudo-

square bricks, the resistivity was measured by Eddy current along the length of the crystals on one of the flat edges of the brick.

After wire sawing, wafers from various ingot heights were cut into $20 \times 20\text{mm}^2$ samples. These samples were annealed under nitrogen ambient for 1h at 600°C to dissociate oxygen-related thermal donors [110]. The resistivity ρ and the Hall carrier density n_{H} were then measured at 300K using an Ecopia HMS-5000 Hall effect device. For the measurement, good ohmic contacts were achieved using an indium gallium eutectic alloy paste. The actual majority carrier density n_{maj} was deduced from the measured Hall carrier density n_{H} with the relation:

$$n_{\text{maj}} = r_{\text{H}} \times n_{\text{H}} \tag{2.9}$$

using for the Hall factor r_{H} the values determined by Szmulowicz [111] for p-type and by Ohta *et al.* [112] for n-type.

To check the distribution of B, P and Ga, their concentrations were also measured by secondary-ion mass spectroscopy (SIMS) on samples from different heights along ingots Cz#1 and Cz#3. The provider of the SIMS analysis gave the error of the measurement to be 10% and the accuracy to be 5% for B and P and 20% for Ga.

As mentioned previously, only two heights of ingot Cz#2 were usable for Hall effect measurements. Because this chapter aims at studying the doping uniformity along the full usable length of Si crystals, we only present for Cz#2 its resistivity profile and we keep the Hall effect measurements for the study of the electrical properties of co-doped Si that will be presented in chapter 3.

2.3 Results

2.3.1 Resistivity profiles

The polarity of the material is measured to be p-type along the entire length of ingots Cz#1, Cz#2 and Cz#3 and n-type along Cz#4. The p-type conductivity of ingots Cz#1, Cz#2 and Cz#3 can be attributed to the addition of Ga since, according to Scheil's law, the concentrations of B and P are so that Cz#1 and Cz#3 would be entirely n-type and Cz#2 only 60% p-type without the presence of Ga.

The resistivity profiles, measured along the length of these co-doped ingots are given in figure 2.11. As can be seen on figure 2.11a, the resistivity is measured to be higher than 0.4Ω.cm in all p-type ingots (Cz#1, Cz#2 and Cz#3), which suggests that Ga co-doping was efficient in keeping a moderate net doping, in addition to maintaining the Si p-type. The resistivity along the n-type ingot (Cz#4) is measured to be very uniform and comprised in a range ($1.1 - 1.4\Omega$.cm) which is *a priori* suitable for the fabrication of high-efficiency solar cells.

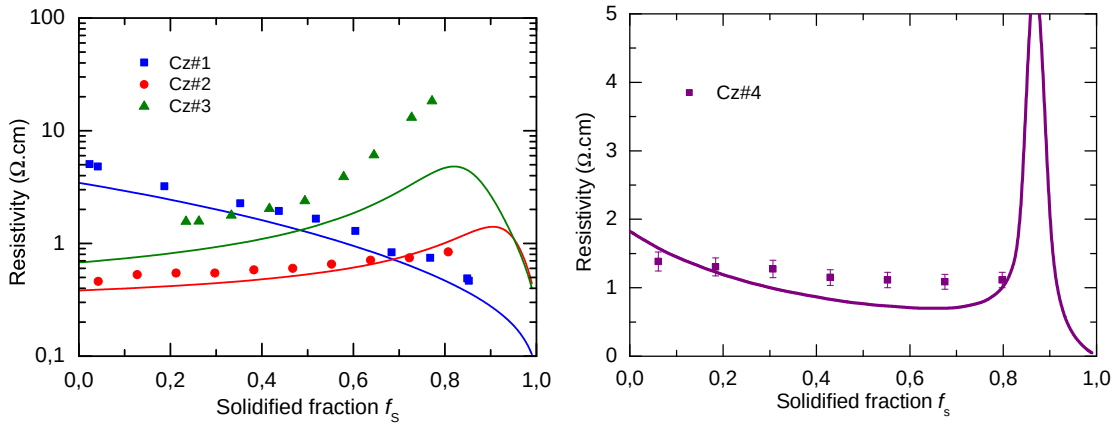

Figure 2.11: Resistivity profiles measured and calculated along the co-doped ingots grown in this work.

However, as discussed in section 1.3.2 of chapter 1, because of the presence of dopants of both types, there is no unambiguous relation between the resistivity and the majority carrier density in compensated Si. Due to the higher concentration of ionized dopant scattering centres, the majority carrier mobility is lower in compensated Si than it is in uncompensated Si with the same net doping. At equal resistivity ρ, the majority carrier density n_{maj} will generally be higher in compensated Si than in uncompensated Si. As a result, since it is n_{maj} which determines most of the electrical properties of Si and the performance of solar cells, resistivity specifications defined for uncompensated electronic-grade Si should not be applied to judge the suitability of compensated Si material.

Also plotted on figure 2.11 are the theoretical ρ profiles calculated using Scheil's law for the dopants distribution, Klaassen's model for the mobility and by taking into account incomplete ionization (see Chapter 3) in the evaluation of n_{maj}. Note that the measured ρ is systematically higher than calculated. The reasons for that discrepancy will be discussed in the following sub-sections.

2.3.2 SIMS profiles

B, P and Ga concentrations measured by SIMS are plotted for ingots Cz#1 and Cz#3 in figure 2.12 and compared to the profiles expected by Scheil's equation. Although the measured concentrations of B and Ga are systematically below the theoretical values, one can observe a good qualitative agreement between SIMS measurements and Scheil's equation suggesting that k_{eff} values from table 2.3 are correct. These two plots illustrate well the idea of Ga co-doping, of which the concentration is measured to follow almost perfectly the increase of P concentration. This shows how appropriate Ga is to compensate the inhomogeneous distribution of P.

We have mentioned previously that the measured resistivity was systematically higher than predicted. The lower concentrations measured for B and Ga in ingots Cz#1 and Cz#3

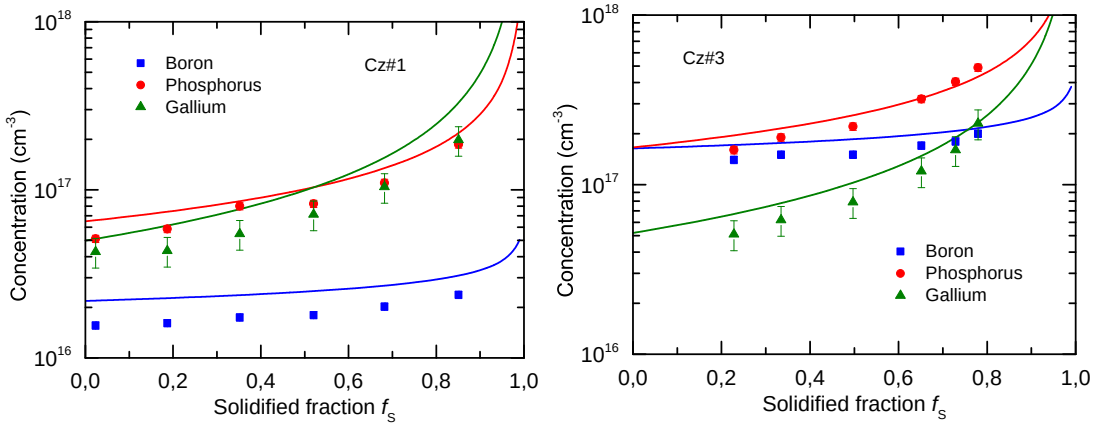

Figure 2.12: SIMS profiles along ingots Cz#1 (a) and Cz#3 (b). Solid lines are the profiles calculated with Scheil's equation.

could potentially explain this higher resistivity in the p-type ingots. Such lower concentrations could be due to errors in the evaluation of the initial concentrations added into the melt or to evaporation of part of the dopants before the beginning of crystallization.

Note, however, that the impurity profiles measured by SIMS do not show a better consistency with resistivity measurements than calculations using Scheil's law. Indeed, fitting the SIMS measurements and using the values obtained to calculate the resistivity yields a ρ of 12Ω.cm at the beginning of ingot Cz#1, which is far higher than the measured value of 5Ω.cm. Similarly, fitting SIMS measurements for ingot Cz#3 yields a type inversion at $f_S = 54\%$ which is also in strong disagreement with type and resistivity measurements carried out along this brick.

2.3.3 Majority carrier density profiles

Figures 2.13 and 2.14 show the majority carrier density deduced from the measured Hall carrier density along ingots Cz#1, Cz#3 and Cz#4. Also shown is the net doping $N_{maj} - N_{min}$ and majority carrier density n_{maj}, calculated using Scheil's law for the dopants distribution and taking incomplete ionization (see chapter 3) into account for the evaluation of n_{maj}. For ingots Cz#1 and Cz#3, we also plot the calculated n_{maj}, using this time the B, P and Ga concentrations given by the fit to SIMS measurements.

The experimental n_{maj} is very well matched by calculations when using the B, P and Ga concentrations directly determined by Scheil's equation. Only along ingot Cz#3 is p_0 slightly lower than calculated. The difference can, however, be regarded as small considering that p_0 is much lower than [B], [P] and [Ga] and a small relative error on one or several of these concentrations could thus lead to a strong relative error on p_0.

On the other hand there is a poor agreement between the measured n_{maj} and that deduced from the fit to SIMS data in ingots Cz#1 and Cz#3. The discrepancy between calculated and measured concentrations revealed in sub-section 2.3.2 might thus be due to a systematic

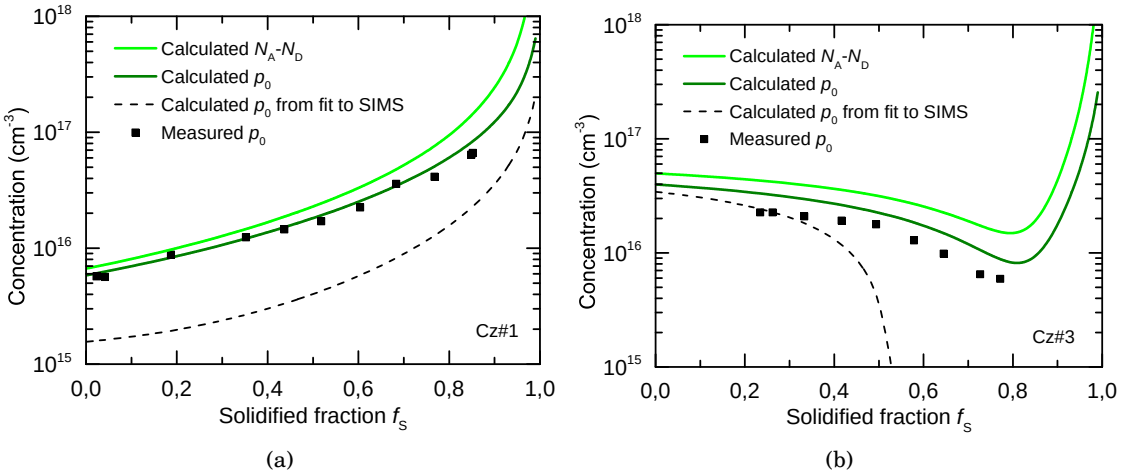

Figure 2.13: Measured and calculated majority carrier density p_0 along p-type ingots Cz#1 (a) and Cz#3 (b).

inaccuracy in the SIMS determination of B and Ga concentrations, rather than to an error in the initial concentrations introduced into the Si melt. In the rest of this thesis, we consider the concentrations of B, P and Ga to be equal to the values given by Scheil's equation. A good agreement between experimental and theoretical temperature-dependencies of the majority carrier density presented in chapter 3 will give even more confidence in the accuracy of the concentrations given by Scheil's equation.

Gratefully to compensation, one can see that n_{maj} is significantly lower than the boron concentration in p-type ingots and than the phosphorus concentration in the n-type ingot. This high degree of compensation enables to have the majority carrier density in a reasonable range for the fabrication of high-efficiency solar cells, i.e. $5.6{\times}10^{15} - 6.6 \times 10^{16}\mathrm{cm}^{-3}$ in ingot Cz#1, $5.9{\times}10^{15} - 2.3 \times 10^{16}\mathrm{cm}^{-3}$ in ingot Cz#3 and $0.8{\times}10^{16} - 1.4 \times 10^{16}\mathrm{cm}^{-3}$ in Cz#4, despite high initial majority dopant concentrations.

Note the particularly uniform majority carrier density measured along the n-type ingot Cz#4, especially compared to the net doping distribution shown in figure 2.8 for a P and B compensated Si ingot with the same B concentration. It can be anticipated from Scheil's equation that the Si should, in ingot Cz#4, turn p-type at about $f_S = 85\%$, due to the strong accumulation of Ga in the last solidified part of the crystal. This is yet a much larger usable fraction than what would be the ingot yield (36%, see table 2.2) without the addition of Ga. In that respect, there is a clear improvement of the material yield of n-type compensated Si ingots due to Ga co-doping.

It is also worth it to remark that in the p-type ingots studied in this work, the majority carrier density n_{maj} is calculated to differ significantly from the net dopant density $N_{\mathrm{maj}} - N_{\mathrm{min}}$, due to the incomplete ionization of dopants. This behaviour will be analysed in greater details in chapter 3.

In view of the good agreement between the measured and the calculated n_{maj}, the only parameter left to explain the resistivity being higher than expected is the majority carrier mobility μ_{maj}. We will show in sub-section 2.3.4 that, as observed by previous authors, μ_{maj}

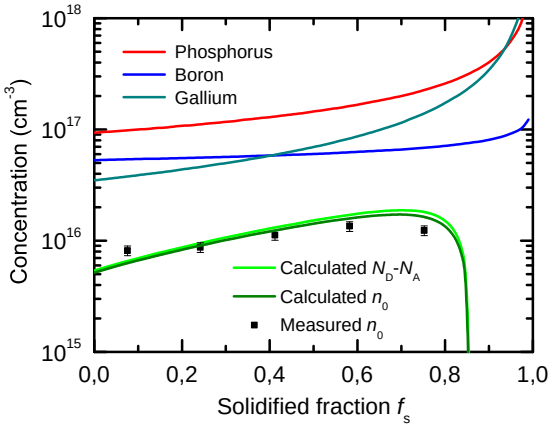

Figure 2.14: B, P and Ga distribution and measured and calculated majority carrier density along n-type ingot Cz#4

is along these compensated Si ingots much lower than the values given by Klaassen's model which we have used to calculate ρ.

2.3.4 Majority carrier mobility profiles

The experimental majority carrier mobility μ_{maj} can be calculated from the resistivity ρ and the majority carrier density n_{maj}, both measured by Hall effect, using:

$$\mu_{\text{maj}} = \frac{1}{n_{\text{maj}} \times q \times \rho} \tag{2.10}$$

As shown in figures 2.15 and 2.16, there is a systematic reduction of μ_{maj} compared to Klaassen's model by up to 30% in Cz#1, 47% in Cz#3 and 50% in ingot Cz#4.

This deviation also seems to be more important in the most compensated regions of those ingots, in good agreement with previous findings made by other research groups and mentioned in Sub-section1.3.3.

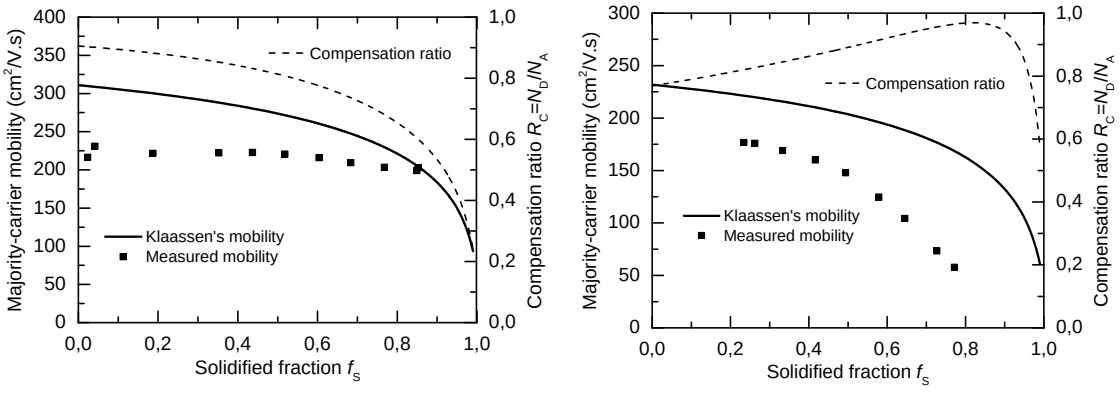

Figure 2.15: Measured majority carrier mobility along ingots Cz#1 (a) and Cz#3 (b) compared with Klaassen's model.

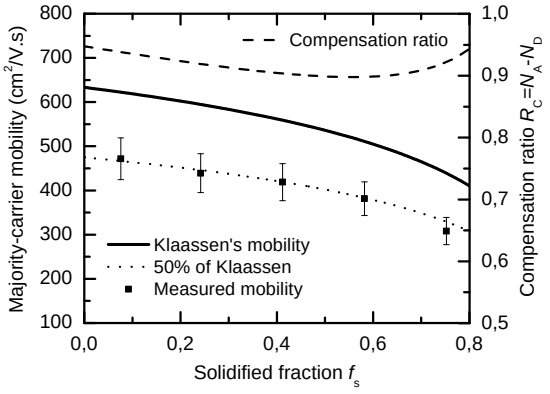

Figure 2.16: Measured majority carrier mobility along ingot Cz#4 and compared with Klaassen's model.

This reduction of the majority carrier mobility compared with Klaassen's model can alone explain the higher experimental values for ρ than expected by our calculations. In the next chapter, we will focus on the reasons for this reduction and develop a parametrization to accurately predict the carrier mobility in compensated Si.

2.4 Conclusion

In this chapter, we have analysed the phenomenon of impurity segregation and shown that it yields strong net doping variation in directionally solidified ingots grown with Si containing both B and P. To solve this issue, we have demonstrated that Ga co-doping can be used efficiently to control the net doping along compensated Si crystals. We have shown that, thanks to the addition of gallium, it is possible to obtain fully p-type Si ingots with a relatively low net doping, despite unfavourable initial boron and phosphorus concentrations (phosphorus concentration much higher than boron concentration or very high initial boron concentration). In n-type Si ingots, Ga co-doping also enables to obtain a very uniform net doping, suitable to the fabrication of high-efficiency solar cells, over a large fraction of the ingot and despite the presence of high concentrations of B and P. Ga co-doping is hence a compensation engineering technique which should allow to improve the quality and material yield of ingots made with UMG-Si and enable to tolerate higher concentrations of B and P, thereby releasing the pressure on purification.

In this chapter, however, we have so far only judged the suitability of crystalline Si merely based on its net doping. To confirm that co-doped Si is appropriate for making high-efficiency solar cells, due to the low net doping and in spite of the high total dopant concentration, it is necessary to carry out a complete assessment of carrier transport and recombination in this material. This will be done in chapter 3. In addition, we have observed or mentioned particular characteristics of compensated Si, such as the mobility reduction or the strong incomplete ionization of dopants, without explaining them. The following chapter also aims at improving the understanding of those phenomena.

Chapter 3

Carrier concentration, transport and recombination in compensated silicon

We have seen in Chapter 1 that both the majority carrier density (p_0 in p-type or n_0 in n-type) and the mobility of majority and minority carriers have a critical influence on the electrical properties of crystalline Si and on the performance of solar cells. For modelling, characterization or simply to understand the physics of Si material, it is often required to know theses quantities. In commonly used uncompensated Si, they can usually be deduced directly from the dopant concentration. In compensated Si, such as upgraded metallurgical-grade Si, the prediction of these quantities is, however, not as straightforward.

For example, it is common practice when dealing with compensated Si to consider the majority carrier density as equal to the net doping, which is equivalent to considering all dopants to be ionized at room temperature. While neglecting incomplete ionization (i.i.) is usually a fair assumption for devices made of uncompensated electronic-grade Si with relatively low doping ($< 10^{16}\text{cm}^{-3}$), it becomes questionable for the higher dopant concentrations that might be encountered in compensated UMG-Si. In addition, we have proposed in Chapter 2 to use Ga as a third compensating dopant to control the net doping along Si ingots. In that case, due to the higher ionization energy of Ga in Si compared to B, it is necessary to treat the matter of i.i. with even more attention.

Chapter 1 mentions that a reduction of the mobilities of both majority and minority carriers has been reported by several groups. This reduction was confirmed in Chapter 2 to affect the majority carrier mobility in our samples. Such a discrepancy between conventional theory and experimental data calls for an investigation of its physical origin and for a modification of mobility models, in order to predict accurately the mobility in compensated Si.

In Chapter 1, we have also seen that contradictory propositions had been made regarding recombination in compensated Si. While some authors claim that the lifetime is limited by recombination through boron atoms [14] in highly-doped and compensated Si, others suggest that the recombination lifetime is entirely determined by the majority carrier density

[25], irrespectively of the total boron concentration. Since the main motivation for controlling the majority carrier density by compensation engineering is to minimize recombination, such a contradiction has to be resolved.

In this chapter, we first aim at assessing the impact of i.i. on the equilibrium carrier density in compensated Si. After describing our experimental setup in Section 3.1, we show in Section 3.2, through both theoretical calculations and experiment, that room-T i.i. is more important in compensated Si than in uncompensated Si. We also draw the main factors contributing to incomplete ionization, which are the majority dopant concentration, its activation energy, the conductivity type and the compensation ratio.

In Section 3.3 we confirm in our compensated Si samples the reduction of the mobilities of both majority and minority carriers compared to Klaassen's model. By studying the T-dependence of the majority carrier mobility in compensated Si, we provide new data which enable to discard the existence of a compensation-specific scattering mechanism and to show that the previously proposed reduction of the screening of ionized impurities by free carriers cannot alone explain the observed mobility reduction in compensated Si. We then propose a simple empirical correction of Klaassen's model which enables to accurately predict the mobility in compensated Si around room-T.

In Section 3.4, we measure the recombination lifetime in compensated Si with a wide doping range and show that, while it displays a clear correlation with the majority carrier density before degradation, this correlation surprisingly tends to disappear after the activation of the BO defect.

3.1 Characterization

3.1.1 Majority carrier density and mobility measurements

To study the carrier concentration and mobility in compensated Si, samples of $2 \times 2\text{cm}^2$ in dimension were cut from wafers selected at different heights of ingots Cz#1, Cz#2, Cz#3, Cz#4 and of an uncompensated B-doped control Si ingot grown in the same conditions. All, samples were subjected to a 1h annealing at 600°C under nitrogen ambient to dissolve oxygen-related thermal donors that might have formed during ingot cooling. Temperature (T)-dependent Hall-effect measurements were then carried out using an Ecopia HMS-5000 device equipped with a T control system cooled with liquid nitrogen. The resistivity (ρ) and the Hall carrier density (n_{H}) were measured on a Van Der Pauw configuration between 80K and 350K. The conductivity majority carrier density p_0 or n_0 was deduced from n_{H} using for the Hall factor r_{H} the values given at each T by Szmulowicz [111] for p-type Si and Ohta and Sakata [112] for n-type Si. μ_{maj} was then deduced from the measured ρ and majority carrier density.

To verify the validity of these r_{H} values for compensated Si, we have also measured p_0 by free carrier absorption (FCA) on a set of neighbouring samples from ingots Cz#1 and Cz#2. We used a Fourier transform infrared spectrophotometer (FTIR) and analysed the spectra

according to the method described in [75]. The absorption coefficient due to free carriers α_{FC} is given in p-type Si by:

$$\alpha_{\mathrm{FC}}(p_0, \lambda) = c_{\mathrm{FCA}} \times q \times \rho \times p_0^2 \times \lambda^2 \tag{3.1}$$

in which λ is the incident wavelength and c_{FCA} is a constant. This c_{FCA} constant was determined to be equal to $5.5 \times 10^{-12} \mathrm{m}^2 \cdot \mathrm{V}^{-1} \cdot \mathrm{s}^{-1}$ by calibrating our FTIR spectrophotometer with uncompensated B-doped float-zone (Fz) and Cz wafers with a wide doping range (from 3×10^{15} to $1.5 \times 10^{17} \mathrm{cm}^{-3}$). Absorption measurements were fitted in the middle infrared range ($\lambda = 2 - 8 \mu m$) for this analysis. Wafers were mechanically polished on both sides to obtain a mirror-like surface. Undoped ($10^4 \Omega \cdot \mathrm{cm}$) Fz-Si was used as a reference for the measurement.

3.1.2 Minority carrier mobility measurements

The minority carrier mobility was measured on $6 \times 6 \mathrm{cm}^2$ samples from neighbouring wafers, using the method developed by Sproul *et al.* [113, 114]. In this technique, the mobility is deduced from the effective minority carrier lifetime in Si samples with infinite surface recombination velocity (SRV). Under such conditions, the measured photoconductance decay time τ_{eff} can be expressed by:

$$\frac{1}{\tau_{\mathrm{eff}}} = \frac{1}{\tau_{\mathrm{b}}} + \left(\frac{\pi}{W}\right)^2 D_{\mathrm{min}} \tag{3.2}$$

in which τ_{b} is the bulk lifetime, W is the sample's thickness and D_{min} is the minority carrier diffusion coefficient. By thinning the samples by acid etch, one can measure τ_{eff} at different thicknesses and extract D_{min}, which equals the slope of the linear regression of the plot of $1/\tau_{eff}$ as a function of $(\pi/W)^2$. In our experiment the minority carrier lifetime was measured by microwave photo-conductance decay (μW – PCD) with a Semilab WT2000PV and infinite SRV was ensured by degrading the surface using laser ablation.

3.1.3 Lifetime measurements

Samples from neighbouring wafers, together with uncompensated P-doped and B-doped controls as well as samples from a Cz ingot grown with UMG-Si [85], were subsequently acid etched to remove saw damage, RCA cleaned, and underwent a phosphorus diffusion gettering at 820°C to dissolve oxygen-related thermal donors and eliminate metallic impurities. This ensures that there is no or very little impact of FeB and FeGa pairs during the degradation experiment. Diffused regions were then removed by an additional acid etch and samples were RCA cleaned before being coated on both sides by hydrogenated Si nitride $\mathrm{SiN_x}:\mathrm{H}$ at 235°C, using plasma-enhanced chemical vapour deposition (PECVD).

After deposition, samples were annealed in the dark at 200˚C under air ambient in order to annihilate the boron-oxygen defect. The annihilation kinetic is known to be much

slower in n-type than in p-type Si [46, 51]. To ensure complete annihilation of the BO defect, n-type samples were thus annealed for a much longer time (100h) than p-type samples (30min). The recombination lifetime was then measured using inductively-coupled photoconductance decay [65], immediately after annealing and after different times t of illumination under a 10mW/cm^2 halogen lamp at $25-27$°C. The effective recombination lifetime degraded under illumination in all the samples except for those which did not contain B, in which it remained stable. This proves that the surface passivation quality of the $SiN_x:H$ layer did not change throughout the experiment. The observed degradation in samples containing B can thus be attributed to a decrease of the bulk lifetime.

3.2 Majority carrier density in compensated silicon

3.2.1 Calculating incomplete ionization

The ionization of a dopant located in a *substitutional* position of the Si lattice is governed by the occupancy of its energy ground state. Under equilibrium, this occupancy depends on the position of the Fermi energy level (E_F) with respect to the dopant energy level (E_{dop}), according to the Fermi-Dirac statistics:

$$\frac{N_D^-}{N_D} = \frac{1}{1+g\times\exp\left(\frac{E_F-E_{dop}}{kT}\right)} \tag{3.3}$$

for donors, and:

$$\frac{N_A^-}{N_A} = \frac{1}{1+g\times\exp\left(\frac{E_{dop}-E_F}{kT}\right)} \tag{3.4}$$

for acceptors. Since each donor level is able to accept one electron of either spin, donor ground states in Si are twofold degenerate and the degeneracy factor g used in equation 3.3 is equal to 2. Similarly, because each acceptor level is able to accept one hole of either spin together with the fact that there are two degenerate valence bands, acceptor ground states in Si are fourfold degenerate and the degeneracy factor g is hence taken as equal to 4 for acceptors 3.4. The equilibrium electron and hole densities n_0 and p_0 can also be expressed in a simple manner as a function of E_F using Boltzmann statistics (equations 3.5 and 3.6) which applies to non-degenerate semiconductors considered in this work. In equations 3.5 and 3.6, the effective densities of states N_C and N_V, respectively in the conduction and in the valence bands are calculated using the parametrization derived by Green [115].

$$n_0 = N_C\exp\left(-\frac{E_C-E_F}{kT}\right) \tag{3.5}$$

$$p_0 = N_V\exp\left(-\frac{E_F-E_V}{kT}\right) \tag{3.6}$$

By numerically solving the Poisson equation, which simplifies to:

$$p_0 + \sum N_D^+ = n_0 + \sum N_{\mathrm{A}}^- \tag{3.7}$$

in the case of uniform bulk doping, we determine the only E_{F} that allows the neutrality condition to be satisfied and deduce all the relevant parameters to study incomplete ionization (i.i.) of dopants.

E_{dop}varies with the dopant concentration as the Metal-Non Metal (MNM) or Mott transition [116] is approached. The mechanisms occurring near the Mott transition have been well explained by Altermatt *et al.* [117, 118] who derived a parametrization for most commonly used dopants. In the present work, we use this parametrization (Equation 3.8), of which the constants $E_{\mathrm{dop},0}$, N_{ref} and c are reported in Table 3.2, to account for the variation of the energy level of B and P (Figure 3.1). Since no parametrization was found in the literature for Ga-doping, we use a fit of equation 3.8 to experimental data [119, 120] on Ga-doped Si (Figure 3.1). Constants used for this fit are also given in Table 3.2. By using this parametrization, we assume E_{dop} not to be affected by compensation. The validity of this assumption will be discussed later in this chapter by contrasting calculations to experimental data. It is also worth noting that this parametrization may not be valid for gallium concentrations higher than $3\times10^{18}\mathrm{cm}^{-3}$ for which there are no experimental data available. For that reason, we represent E_{dop} above $3\times10^{18}\mathrm{cm}^{-3}$ with a dotted line, to indicate that our parametrization is likely not to be valid in this concentration range.

$$E_{\mathrm{dop}} = \frac{E_{\mathrm{dop},0}}{1+(N_{\mathrm{dop}}/N_{\mathrm{ref}})^c} \tag{3.8}$$

Dopant	$E_{\mathrm{dop},0}$(meV)	$N_{\mathrm{ref}}(\mathrm{cm}^{-3})$	c
B	44.4	1.3×10^{18}	1.4
P	45.5	2.2×10^{18}	2
Ga	72.0	5.0×10^{18}	0.75

Table 3.1: Constants used for the calculation of E_{dop} for B, P and Ga.

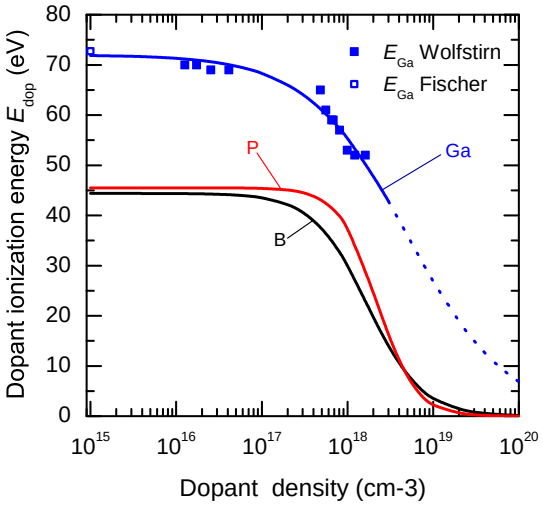

Figure 3.1: Evolution of the activation energy of B, P and Ga as a function of dopant concentration.

To consider i.i. in compensated Si, one can either look at the fraction of ionized majority dopant (N_D^+/N_D for donors and N_A^+/N_A for acceptors) or at the ratio of the majority carrier density to the net doping $n_{maj}/(N_{maj}-N_{min})$. Unlike in uncompensated Si, these two ratios differ in compensated Si. In this section, we intend to assess the impact of i.i. on n_{maj} which, as mentioned previously, has a great influence on the electrical properties of Si materials and solar cells. For that purpose, the most relevant parameter to focus on in order to assess the impact of i.i. and the error that is made when neglecting it (i.e. assuming $n_{maj} = N_{maj} - N_{min}$) is therefore $n_{maj}/(N_{maj}-N_{min})$. This ratio is referred to as the ionization ratio in the rest of the chapter.

3.2.2 Incomplete ionization at room-temperature

Figure 3.2 shows the result of our calculations at 300K for [B] ranging from $1\times10^{16}\text{cm}^{-3}$ to $5\times10^{17}\text{cm}^{-3}$ compensated with various amounts of P. In uncompensated Si ($R_C = 0$), E_F gets closer to the top of the valence band with increasing [B] (Figure 3.2 (a)). As a consequence, it also approaches the B energy level E_B, leading to a partial inoccupation of the B states (equation 3.4) and therefore to a reduced fraction of ionized B atoms (Figure 3.2 (b)). At concentrations above $5\times10^{16}\text{cm}^{-3}$ the amount of unionised B atoms starts to exceed 3%. When B is compensated with P, E_F is shifted towards the middle of the gap (Figure 3.2 (a)) and moves away from E_B. This causes the fraction of ionized B to increase up to nearly 100% as the compensation ratio $R_C = N_A/N_D$ increases from 0 to 1 (Figure 3.2 (b)). Surprisingly, this increase of the amount of ionized B atoms does not result in an increase of the ionization ratio $p_0/(N_A-N_D)$ which remains nearly constant in the case of low [B] and slightly decreases with compensation for high [B] (Figure 3.2 (c)). This is so because, as compensation increases, the net doping becomes smaller compared to [B] and thus a small amount of unionised B leads to a relatively strong effect on the carrier density. This observation shows that in p-type compensated Si containing [B] $> 5\times10^{16}\text{cm}^{-3}$ as can

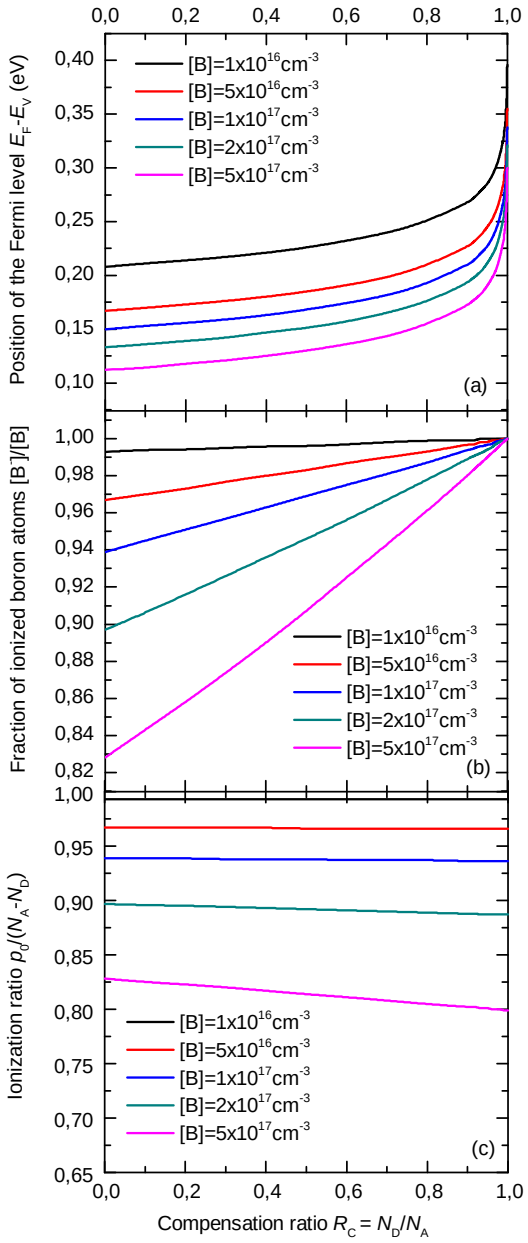

Figure 3.2: Calculation of the evolution of (a) the position of the Fermi level, (b) the fraction of ionized boron atoms and (c) the ionization ratio $p_0/(N_A - N_D)$ with the compensation ratio R_C at 300K in B and P p-type compensated Si.

be the case of UMG-Si, i.i. has to be taken into account to estimate p_0, no matter what the net doping is and even if the latter would be low enough to consider full ionization in the case of uncompensated Si.

Figure 3.3 shows the evolution of the ionization ratio as a function of the majority dopant concentration, calculated at 300K respectively for n-type (a) and p-type (b) Si. These two plots highlight the main factors influencing incomplete ionization in Si: they are (1) the majority dopant concentration, (2) its ionization energy, (3) the type of majority dopant and (4) the compensation ratio.

1. In the $10^{15} - 10^{18}\text{cm}^{-3}$ doping range, i.e. for concentrations below the Mott transition, the impact of i.i. on the carrier density increases with the concentration of majority dopant.

2. The higher the ionization energy of the majority dopant is, the stronger the impact of i.i. on the majority carrier density will be. This is revealed by the lower ionization ratio in the case of Ga ($E_{\text{Ga,0}} = 72\text{meV}$) doping compared to B ($E_{\text{B,0}} = 44.4\text{meV}$) doping.

3. i.i. is calculated to be stronger in B-doped Si than in P-doped Si, despite the slightly lower ionization energy for B ($E_{\text{B,0}} = 44.4\text{meV}$) than for P ($E_{\text{P,0}} = 45.5\text{meV}$). This is due to the fact that acceptors are fourfold degenerate (each acceptor level is able to accept one hole of either spin together with the fact that there are two degenerate valence bands) in contrast with donors that are only twofold degenerate (each donor level can accept one electron of either spin). For a given ionization energy and majority dopant concentration, i.i. is therefore stronger in p-type than in n-type Si.

4. Lastly, one can see that the ionization ratio is, in compensated Si, lower than in uncompensated Si, showing that compensation enhances the importance of i.i.. This is so because as compensation increases, the net doping is reduced compared to the majority dopant concentration. As a consequence, a given fraction of non ionized majority dopants leads to a stronger relative impact on the carrier density.

One general rule that can be deduced from the way these four factors influence i.i. is that for a given net doping, the carrier density will be more strongly affected in compensated than in uncompensated Si.

From figure 3.3, one can infer if a Si sample with a given doping will be affected by i.i. or not. As the range of dopant concentrations found in compensated UMG-Si is as broad as $10^{16} - 5 \times 10^{17}\text{cm}^{-3}$, the influence of i.i. on the carrier density might be negligible (<1% in p-type Si with $N_{\text{A}} = [\text{B}] = 1 \times 10^{16}\text{cm}^{-3}$) or on the contrary very important (40% for p-type Si with $[\text{Ga}] = 5 \times 10^{17}\text{cm}^{-3}$), depending on the quality of the material. In general, i.i. becomes important (>3%) in p-type Si containing more than $5 \times 10^{16}\text{cm}^{-3}$ of B or $2 \times 10^{16}\text{cm}^{-3}$ of Ga or in n-type Si containing more than $1 \times 10^{17}\text{cm}^{-3}$ of P.

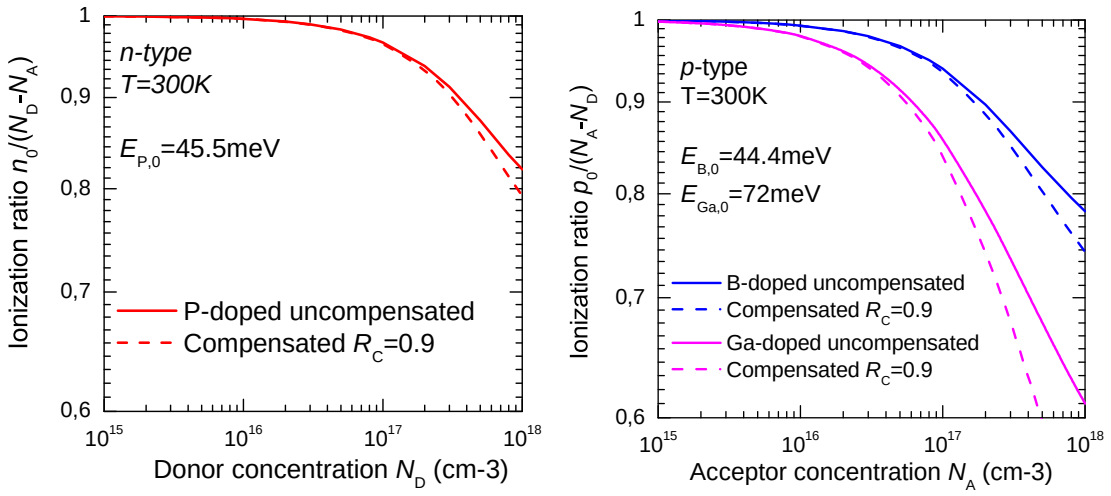

(a) (b)

Figure 3.3: Ionization ratio calculated as a function of the majority dopant concentration in n-type (a) and p-type (b) Si for different dopants and compensation levels. The 4 factors influencing incomplete ionization are highlighted in these two graphs, i.e. the majority dopant concentration, its ionization energy, its type (n- or p-type) and the compensation ratio.

3.2.3 Temperature dependence of the majority carrier density

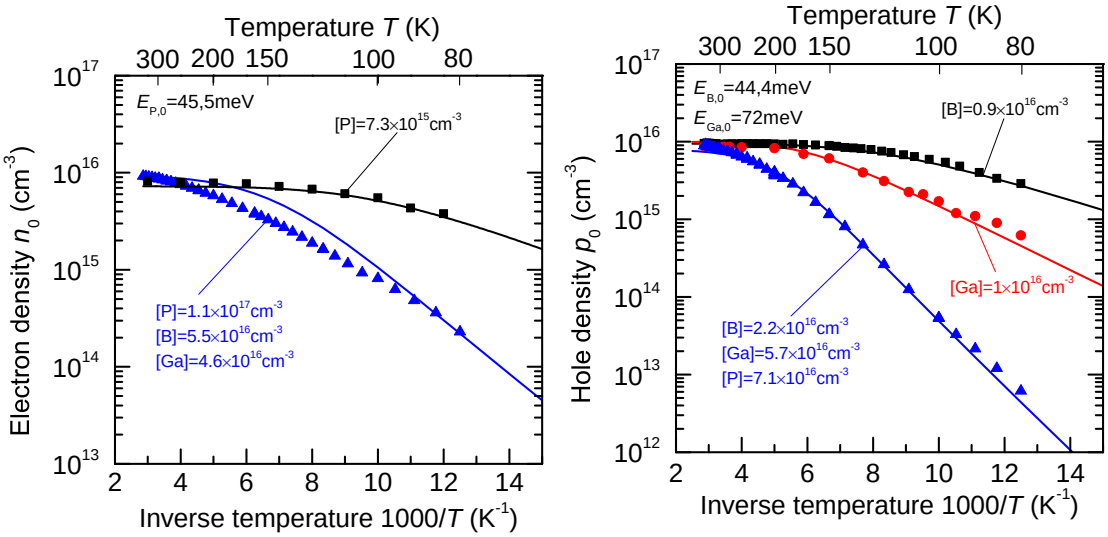

(a) (b)

Figure 3.4: T-dependence of the measured carrier density in uncompensated and compensated n-type (a) and p-type (b) Si samples. The Hall data in Ga-doped Si and in P-doped Si are respectively taken from [121] and [112]. Solid lines are obtained by calculated the carrier density as described in sub-section 3.2.1.

Figure 3.4 shows p_0 and n_0, deduced from Hall effect measurements, as a function of T in one uncompensated B-doped Si sample and both in n-type and p-type Si samples co-doped with B, P and Ga. Samples were chosen to have a similar net doping in the range

$(8-9)\times10^{15}\text{cm}^{-3}$. For comparison, we have added to the plot published Hall data on uncompensated P-doped [112] and Ga-doped Si [121] with similar net doping (respectively $7.3\times10^{15}\text{cm}^{-3}$ and $1\times10^{16}\text{cm}^{-3}$). Also shown is the carrier density calculated for each sample using the method described in sub-section 3.2.1. For the co-doped samples, the dopants concentrations were estimated from the position of the wafer in the ingot using Scheil's equation.

One can see that, due to i.i., the majority carrier density decreases with T in all samples. In the compensated samples shown here, it decreases by about 2 or 3 orders of magnitude between 350K and 80K while it only does so by a factor of 5, 20 or 2 in uncompensated B-, Ga- or P-doped Si, respectively. This illustrates the generally stronger importance of incomplete ionization in compensated than in uncompensated Si.

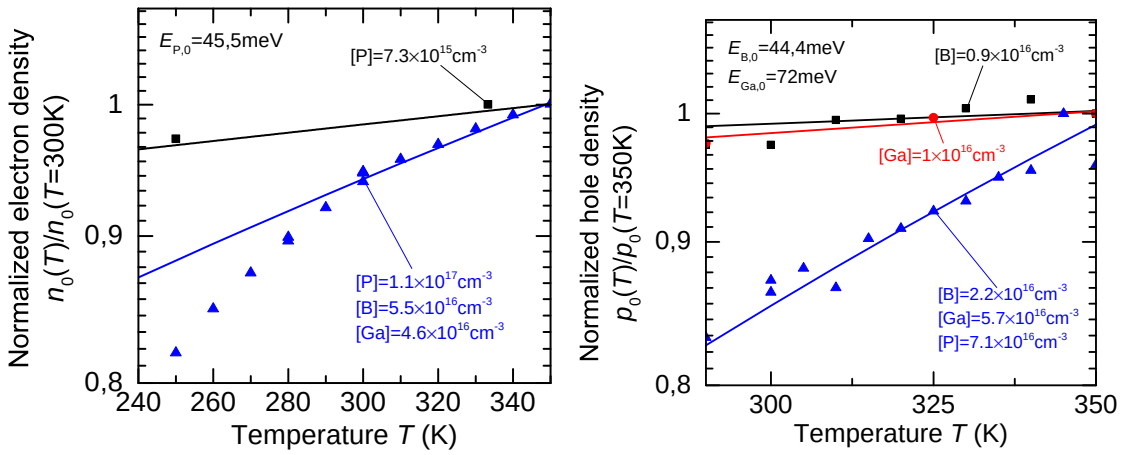

Figure 3.5: Variation of the measured majority carrier density around room-T. The Hall data in Ga-doped Si and in P-doped Si are respectively taken from [121] and [112]. Solid lines are guides for the eye.

A closer look at the variation of the carrier density around room-T (Figure 3.5) also reveals that in uncompensated B-, Ga- or P-doped Si, the carrier density is stable between 300K and 350K, indicating that, in these samples, the saturation range is already reached at 300K, i.e. there is virtually no i.i. at room-T. In compensated samples, however, the carrier density keeps increasing between 300K and 350K by about 15% in the p-type sample (Figure 3.5b) and 6% in the n-type sample (Figure 3.5a), which shows that there is significant i.i. at room-T. This confirms our previous theoretical finding of sub-section 3.2.2 that room-T i.i. is stronger in compensated Si than in uncompensated Si with equivalent net doping.

As can be seen on figure 3.4b, the experimental p_0 agrees very well with the calculated one, including in compensated Si, over the entire studied T range. This good agreement gives confidence regarding the validity of the procedure we used to evaluate the position of the Fermi level in p-type Si.

In contrast, there is a noticeable discrepancy between the experimental and the calculated n_0 in the n-type compensated sample (Figure 3.4a). The weaker slope of the measured

carrier density dependence with 1000/T in the lower T range indicates that the ionization energy of P (E_P) might be lower than what we used in our calculation. Note that the parametrization that we chose to account for the variation of E_P [118] with P concentration was established for uncompensated Si. Photoluminescence analyses have previously shown that E_P could be affected by compensation for dopant concentrations close to the Mott transition [9]. A recent study of the donor-acceptor pair luminescence [64] in B and P compensated Si with [B] and [P] lower than $1 \times 10^{17}\text{cm}^{-3}$, however, indicates that there is no change of the E_P and E_B compared to the commonly accepted values. The scarcity of the data found in the literature for compensated Si in the $10^{17} - 10^{18}\text{cm}^{-3}$ doping range leaves us with no other option than to use the available parametrization given by Altermatt *et al.* for uncompensated Si [118]. Note that we were not able to achieve a better fit by adjusting E_P.

Another possible source of error might arise from the Hall factor r_H that was used to convert n_H into n_0. Again, r_H was determined for mildly compensated Si and might not be valid for the higher compensation levels encountered in our samples. Further work is needed to assess the T-dependence of r_H in compensated Si, for example by comparing Hall effect measurements to carrier density data collected with alternative techniques such as capacitance-voltage measurements. It is worth noting that although there is a visible discrepancy between the experimental and the calculated n_0, the relative error on the ionized P concentration should be very small. Indeed, the maximum difference between the measured and the calculated n_0 is of $2.3 \times 10^{15}\text{cm}^{-3}$ at 160K which represents only 2% of the expected ionized P concentration ($1.07 \times 10^{17}\text{cm}^{-3}$) at that T. Hence, the calculated ionized dopant concentrations can still be considered appropriate input parameters in Klaassen's model, when calculating the dependence of μ_{maj} with T as will be done in the next section.

Because the only possible E_F solution to the Poisson equation systematically lies in the lower half of the band gap in p-type Si and in the upper half in n-type Si, compensating dopants (shallow donors in p-type Si and shallow acceptors in n-type Si) remain always completely ionized, independently of T. As a result, the concentration of ionized majority dopants cannot decrease below the total concentration of compensating dopants but can only get closer to it as T decreases. In that respect, reducing T is equivalent to increasing the compensation ($R_C \to 1$ and $K_C \to \infty$ as T decreases), since it effectively closes the gap between the concentrations of ionized majority and compensating dopants.

For example, calculation shows that, in the co-doped sample shown in figure 3.4b, R_C increases from 0.91 to practically 1 and K_C from 21 up to 3×10^4 as T decreases from 300K to 80K (Figure 3.6). This increase of compensation, due to i.i. of majority dopants at low T will enable us, in the next section, to rule out the existence of a compensation-specific scattering mechanism.

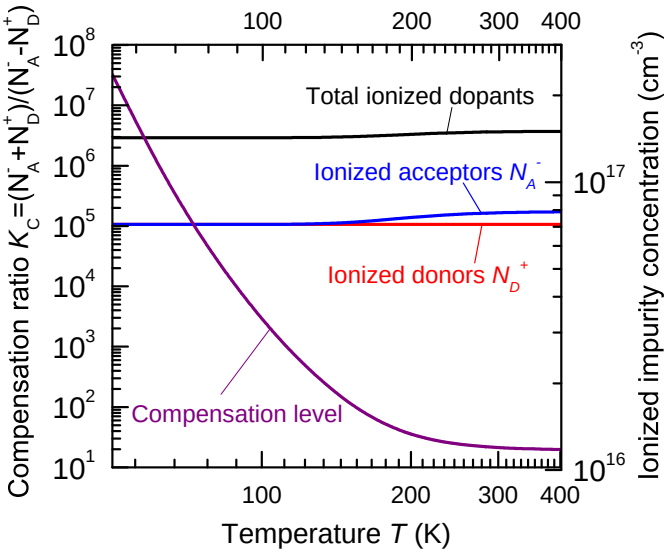

Figure 3.6: T-dependence of the calculated ionized dopant concentrations and of the compensation ratio K_C. The total ionized dopant concentration remains almost constant with decreasing T, while the carrier density decreases, leading to a strong increase of the compensation level.

3.3 Carrier mobility in compensated silicon

3.3.1 Reduction compared to models at room-temperature

It appears from our measurements that Klaassen's model describes accurately the experimental data in uncompensated Si but systematically overestimates the mobility in compensated Si. The relative reduction of μ_{maj} and μ_{min} measured at 300K compared to Klaassen's model [57], is plotted as a function of K_{C} in figure 3.7. Absolute values for μ_{maj} and μ_{min} are given in the Appendix 5.4.

Note that the relative deviation from Klaassen is measured to increase with compensation and to be independent of the total dopant concentration and on the type of conductivity, p- or n-type. In addition, one can observe that μ_{min} is in general more strongly affected than μ_{maj}. As mentioned in chapter 1, similar discrepancy between theoretical and experimental mobility was independently observed by different authors [10, 70, 71, 14, 72, 73, 46, 74, 75, 76, 77] and is similar if using other available mobility models [62, 67, 68, 69]. This section discusses the possible reasons for this observed discrepancy.

Klaassen's model takes into account 3 different scattering mechanisms that are relevant to the study of compensated Si: lattice scattering, ionized impurity scattering and electron-hole scattering. In addition, it incorporates the screening of scattering centres by free carriers and differentiates the collision cross-section of scattering centres with attractive from those with a repulsive potential. There are three possibilities to explain why Klaassen's model fails to match the measured mobility in compensated Si.

The first possibility that could explain the reduction of the measured μ_{maj} would be that the actual Hall factor differs in compensated Si from the values that were established for un-

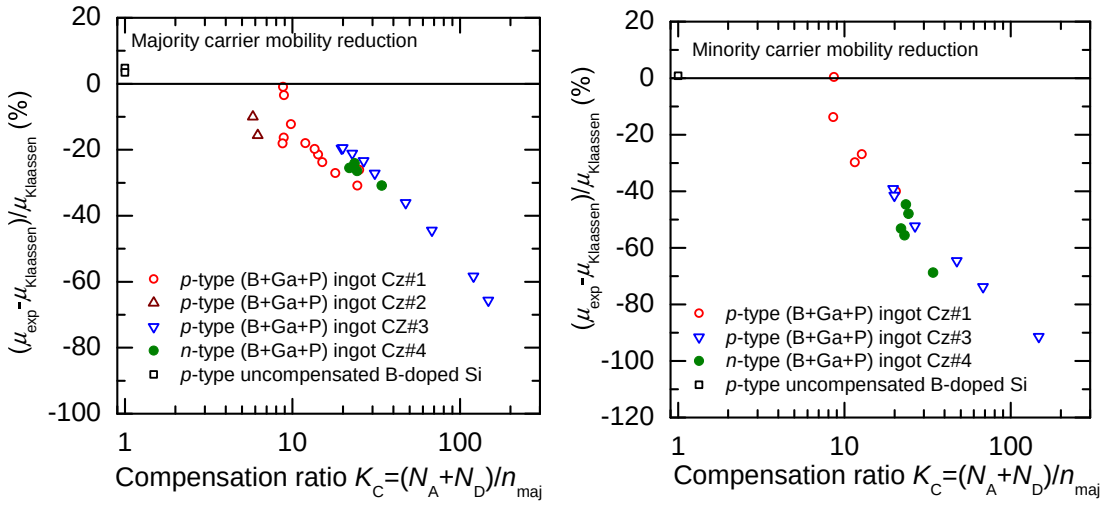

(a) (b)

Figure 3.7: Relative reduction of the measured majority carrier mobility (a) and minority carrier mobility (b) compared to Klaassen's model at 300K. The deviation increases with the compensation ratio K_C for both majority and minority carriers.

compensated or weakly compensated Si [111, 112]. The Hall factor depends on the relative weight of the different scattering mechanisms at play. There is hence *a priori* no reason for its value to be the same in compensated Si as in uncompensated Si. A lower r_H could lead in compensated Si to an apparent reduction of the mobility deduced from Hall effect measurements. Comparing p_0 values measured at 300K by FCA to p_H values on samples from ingots Cz#1 and Cz#2, however, gives an average Hall factor of $r_H = \frac{p_0}{p_H} = 0.73 \pm 0.08$ (Figure 3.8), in good agreement with $r_H = 0.75$ calculated by Szmulowicz [111]. Other groups have also found the Hall factor at room-T to be similar in p-type [51, 70] and n-type [70] compensated Si to the values previously reported for uncompensated Si. As a consequence, the observed reduction can safely be attributed to an actual conductivity mobility reduction rather than to a variation of r_H. Also note that the measurement of the minority carrier mobility, which is also found to be reduced in compensated Si, is completely independent of the Hall factor.

Another explanation which was proposed involves the existence of an additional scattering mechanism in compensated Si which Klaassen's model would not account for, i.e. a compensation-specific scattering mechanism [70]. The fact that the difference between theoretical and experimental mobility increases with R_C at room-T supports this explanation. In the next sub-section, however, we will show that it is not consistent with the T-dependence of the majority carrier mobility.

The third proposition that was put forward attributed the mobility reduction to the reduction of the screening of ionized impurities by free carriers, because of their lower relative concentration. This would lead to an increase of the scattering cross section of ionized impurities, as the free carrier concentration is reduced by compensation, that Klaassen's model considers inconsequential in this doping range. In the next sub-section, we will also

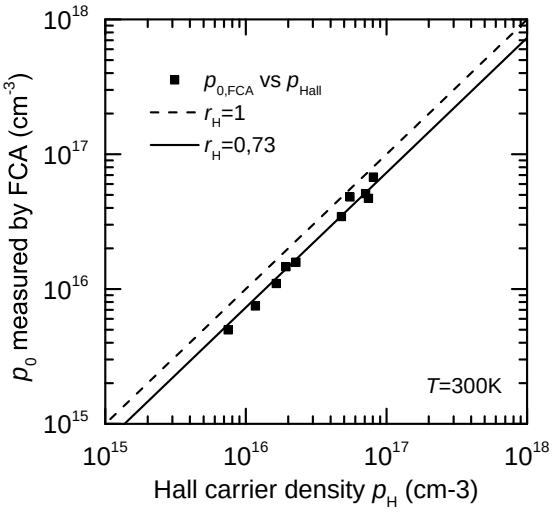

Figure 3.8: Carrier density p_0 measured by FCA at 300K against the Hall carrier density p_H.

show that the T-dependence of the measured majority carrier mobility suggests that this proposition cannot alone explain the observed discrepancy between experiment and theory.

3.3.2 Temperature-dependence

The majority carrier mobility as a function of T is shown in figure 3.9 for the same samples as shown in figure 3.4b. Figure 3.9 also displays for each sample the carrier mobility calculated with Klaassen's model [57, 56] using either the total dopant densities (dashed lines) or the calculated ionized dopant concentrations (solid lines) as input parameters.

In uncompensated B- and Ga-doped Si, the experimental μ_{maj} shows a perfect agreement with Klaassen's model around room-T. At lower T, experimental data agrees relatively well with the model when accounting for i.i. while it shows significant discrepancy if i.i. is neglected. It is worth noting that μ_{maj} is measured to be the same in Ga-doped Si as in B-doped Si over the almost entire T range. This shows that ionized Ga atoms act as equivalent scattering centres to ionized B atoms. The only difference between μ_{maj} in Ga- and in B-doped Si appears below 150K, where i.i. starts to be important in Ga-doped Si, B-doped Si being still in the saturation range (Figure 3.4b). Although Klaassen's model has been developed for B-doped Si, it reproduces with equal accuracy μ_{maj} in Ga-doped Si between 80K and 350K if i.i. of dopants is accounted for. It is therefore not necessary to distinguish between the two impurities when modelling μ_{maj} in Si co-doped with B and Ga and the sum of both ionized concentrations can be used as a single input for the ionized acceptor density in Klaassen's model.

On the other hand, the mobility measured in the co-doped sample is lower than the calculated mobility over the entire T range. Several remarks can be made concerning the T-dependence of the majority carrier mobility in compensated Si.

As we have seen, compensating dopants (in this case P atoms) are always completely ionized ($[P^+] = [P]$) and the concentration of ionized acceptor dopants cannot decrease below

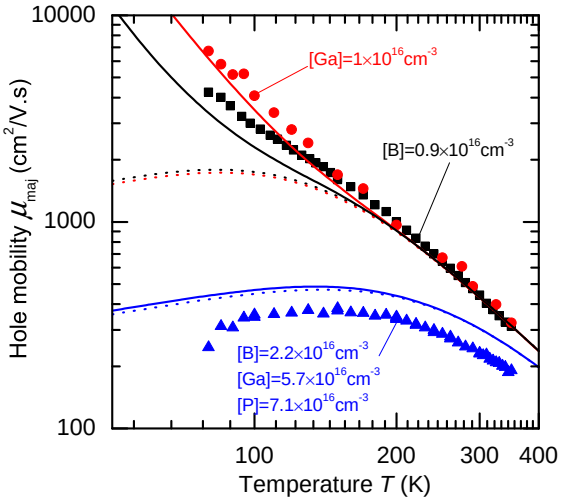

Figure 3.9: T-dependence of the measured hole mobility in B-doped, Ga-doped and B, P and Ga co-doped Si. The mobility calculated with Klaassen's model is represented by solid lines (incomplete ionization) and dotted lines (complete ionization).

their concentration ($N_A^- > [P]$) but can only approach it as T reduces. Consequently, the total density of ionized dopants cannot decrease below $2 \times [P]$. This means that in highly-compensated Si, in which the concentration of acceptor dopants is only slightly above [P], the total density of ionized impurities will remain almost unchanged with decreasing T. For example, in the co-doped sample studied here, the minimum value for the total concentration of ionized dopants is $14.2 \times 10^{16}\text{cm}^{-3}$ which is very close (94.7%) to the total dopant concentration $15.0 \times 10^{16}\text{cm}^{-3}$. This fact is evidenced in figure 3.6 in which the calculated concentration of ionized dopant appears to be almost constant with T.

As a consequence, incomplete ionization has only a weak influence on the dopant concentration used as input when calculating the carrier mobility. Since ionized acceptor and donor concentrations remain almost constant with T, the modelled mobility is essentially the same whether taking i.i. into account or not, even at low T (Figure 3.9).

In addition, it is well-known that ionized impurity scattering is more important at low T due to the increasing collision cross-section of fixed charges whereas lattice scattering is dominant at high T because of stronger phonons. In uncompensated Si, the increasing collision cross-section of ionized impurities is counterbalanced by the reduction of their concentration and therefore μ_{maj} remains limited by lattice scattering over the entire T range studied (keeps up increasing with decreasing T). In compensated Si, however, since the concentration of ionized impurities remains constant with reducing T while their collision cross-section simultaneously increases, μ_{maj} is dominated by ionized impurity scattering at low T, up to a relatively high T (140-150K in the co-doped samples shown in figure 3.9), at which it reaches its maximum. As a consequence, μ_{maj} varies with T within a much narrower range in compensated Si than in uncompensated Si.

One last observation that has to be made is that, as we have seen in Figure 3.6, the compensation ratio is hugely increased by decreasing T up to extreme values (here 3×10^4 at 80K) far higher than any compensation ratios that have been reported previously in com-

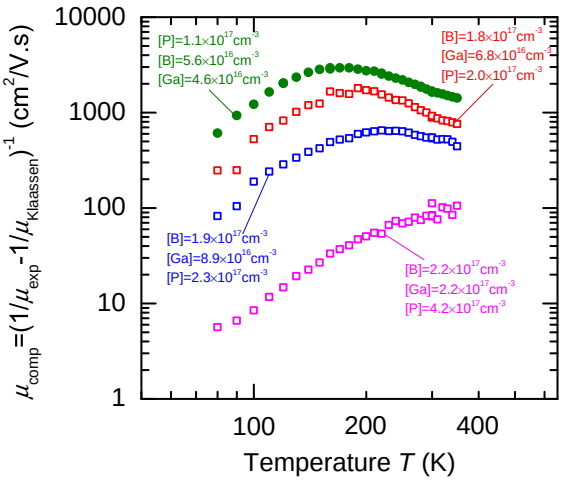

Figure 3.10: T-dependence of the calculated mobility component responsible for the discrepancy between Klaassen's model and the measured mobility in compensated Si.

pensated Si measured at room-T. No μ_{maj} drop is, however, observed at these low T which disqualifies the potential existence of a compensation-specific scattering mechanism. On the contrary, the deviation of the measured μ_{maj} from Klaassen's model seems to be independent of T.

A way to assess the nature of the scattering mechanisms that are not well described by Klaassen's model in compensated Si is to use Mathiessen's rule (Equation 1.28) to isolate the mobility component μ_{comp} responsible for the discrepancy.

$$\frac{1}{\mu_{\text{comp}}} = \frac{1}{\mu_{\text{exp}}} - \frac{1}{\mu_{\text{Klaassen}}} \tag{3.9}$$

This mobility component, plotted for different samples in figure 3.10, appears not to have, in general, a monotonic dependence on T. In most samples, μ_{comp} increases with T at low T and decreases with T in the higher T range. This suggests that the deviation from Klaassen's model is not due to the underestimation of a single scattering mechanism or mobility component. For example, it was suggested that the underestimation by Klaassen's model of the reduction of the screening of ionized impurities by free carriers with increasing compensation could explain the observed discrepancy. If such was the case, it should lead to a monotonic decrease of μ_{comp} with T, due to the decrease of the collision cross-section of ionized impurities with increasing T. In contrast, a monotonic increase of μ_{comp} with T should be observed if the only miscalculated mobility component was lattice scattering. The non-monotonic T-dependence of μ_{comp} therefore seems to indicate that the error made by Klaassen's model concerns more than one scattering mechanism.

It should be noted here that Klaassen's model relies on a substantial amount of fitting of calculated and experimental data, in particular to derive the screening, the collision cross-section ratio of repulsive to attractive scattering centres, and the collision cross-section ratio of mobile to immobile scattering centres. Fitting of experimental data was also done to define the constants used for the variation of the mobility with T.

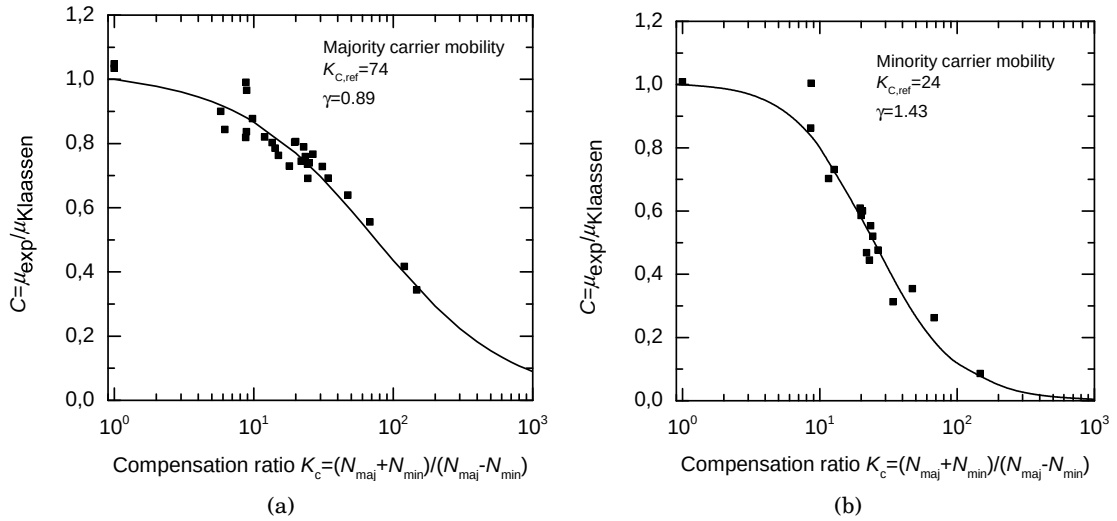

Figure 3.11: Correction factor for the mobility of majority carriers (a) and minority carriers (b) in compensated Si.

Since all these fits were achieved on uncompensated Si, it is not utterly surprising that Klaassen's model fails to describe μ in compensated Si in which the different sources of scattering are present in different proportions. The discrepancy between experimental and theoretical μ in compensated Si highlights the non-physical character of Klaassen's model rather than an actual mobility reduction due to compensation. A complete re-assessment of all the fitting parameters is needed to establish a model that would successfully reproduce the mobility in compensated Si as accurately as in uncompensated Si.

3.3.3 Mobility correction

As mentioned in chapter 1, it is essential for accurate modelling of solar cells or for several characterization techniques to be able to calculate the mobilities of majority and minority carriers in compensated Si. For that purpose, we have previously proposed to correct Klaassen's model using an additional mobility component, depending on the compensation ratio K_C, based on a fit to experimental data [122].

As recently argued by Schindler *et al.* [77], such an approach can only be valid in the eventuality of the existence of a compensation-specific scattering mechanism. They, instead, proposed to introduce a compensation-dependent term in the Caughey-Thomas expression used as a starting point to derive Klaassen's model. This term is meant to represent the reduction of the screening resulting from compensation. There is, however, no explanation in their paper on how this empirical term is meant to give a better description of the screening than is already done by Klaassen's model. In addition we have shown that the T-dependence of the majority carrier mobility indicates that the reduction of the screening cannot alone explain the deviation from Klaassen.

Hence, both approaches are purely empirical. While using a purely empirical correction, it is worth making it as simple as possible, in order to facilitate its implementation in model-

Type of carrier	$K_{C,ref}$	γ
Majority	74	0.89
Minority	24	1.43

Table 3.2: Constants used for the mobility correction.

ling computer programs. As we have seen, the magnitude of the deviation from Klaassen's model only depends at room-T on the compensation ratio and on the type of carrier, majority or minority. This means that the mobility can simply be corrected, for each type of carriers, by a prefactor C placed in front of the value calculated by Klaassen and depending solely on the compensation ratio. Figure 3.11 plots the ratio of the measured mobility to that calculated with Klaassen's model. One can see that this ratio can be fitted for both majority and minority carriers, using an expression of the form:

$$C = \frac{1}{1 + \left[(K_C - 1)/K_{C,ref}\right]^{\gamma}} \tag{3.10}$$

of which the fitting constants $K_{C,ref}$ and γ are reported in table 3.2.

This empirical correction prefactor can be used to predict more accurately the mobility at 300K in compensated Si. Note that C is equal to unity for uncompensated Si ($K_C = 1$) for which Klaassen's describes well experimental data with no correction.

Figure 3.12 shows some examples of the measured T-dependence of the majority carrier mobility in our samples, compared to Klaassen's model with (solid lines) and without (dashed lines) using the correction. The prefactor C is taken as independent of T and calculated using the compensation ratio at 300K. One can see that around room-T, the corrected Klaassen's model agrees very well with the measured mobility. In addition, although the correction factor C was obtained by fitting experimental data at 300K, the measured mobility shows a satisfactory agreement with the corrected model over the entire 80-350K T range in most samples, except in the case of extreme compensation for which μ_{maj} shows a stronger decrease with reducing T.

3.4 Recombination in compensated silicon

In this section, we study the effective recombination lifetime in compensated Si. As we have seen in Chapter 1, the BO defect is an important source of recombination. It has been shown that this defect can be permanently suppressed by simultaneous annealing and light soaking [123]. The cost effectiveness of such a permanent deactivation process in an industrial production is, however, yet to be proven. For that reason, we show separately the measured τ_{eff} before and after activation of the BO defect. The lifetime before degradation is meant to represent the optimistic case of solar cell manufacturers being able to eliminate the BO defect in the near future, while the lifetime after degradation is more representative of the current status.

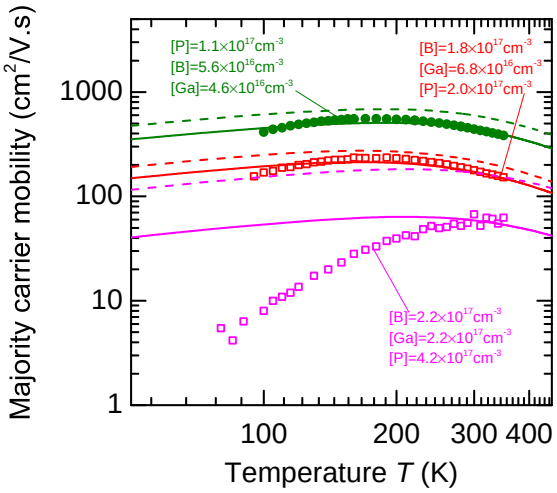

Figure 3.12: Majority carrier mobility variation with T in 3 different compensated samples and compared to Klaassen's model with (solid line) and without (dashed line) the correction prefactor C.

A fit to Dannhauser and Krause's mobility sum measurements [124, 125, 126] is commonly used to convert photo-conductance data into excess carrier density for injection-dependent lifetime measurements [65]:

$$\mu_{\min} + \mu_{\mathrm{maj}} = 1800 \frac{1 + \exp\left[0.8431 \ln\left(\frac{\Delta n + N_{\mathrm{dop}}}{N_{\mathrm{ref}}}\right)\right]}{1 + 8.36 \exp\left[0.8431 \ln\left(\frac{\Delta n + N_{\mathrm{dop}}}{N_{\mathrm{ref}}}\right)\right]} \tag{3.11}$$

This fit was recently confirmed to be valid for uncompensated Si [127]. In compensated Si, however, it overestimates the mobility sum in the same manner as we showed Klaassen's model does. To account for that lower mobility in our samples, we adjust the doping used as input in the fit to Dannhauser and Krause's mobility so that it yields the same low-injection mobility sum as we previously measured.

Because of trapping effect occurring at low injection, we could not measure accurately τ_{eff} at 0.1suns in all of our samples. As a consequence, we report the lifetime values at a constant excess carrier density $\Delta n = 5 \times 10^{14} \mathrm{cm}^{-3}$.

3.4.1 *p*-type Si

Figure 3.13 shows the measured lifetime before and after prolonged illumination in co-doped ingots Cz#1, Cz#2 and Cz#3, in B-doped Cz-Si controls and in samples taken from different heights of a B and P compensated Cz ingot grown with UMG-Si [85].

Before degradation Several features can be pointed out for τ_{eff} before activation of the BO defect (Figure 3.13a). First, there is a strong correlation between τ_{eff} and p_0, in good agreement with the conclusion drawn in Chapter 1 that recombination is determined by the majority carrier density.

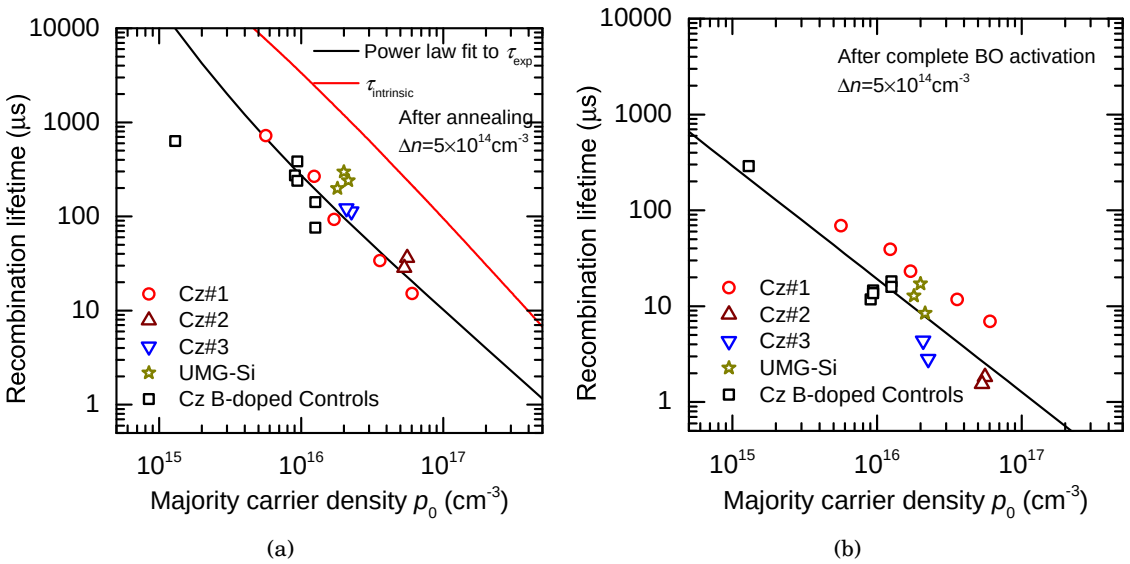

Figure 3.13: Measured recombination lifetime at an excess carrier density $\Delta n = 5 \times 10^{14}\text{cm}^{-3}$ after annealing (a) and after complete degradation under illumination (b).

Note that samples co-doped with Ga scale well with B-doped controls, showing that there is no additional recombination due to the presence of Ga. This result is not surprising considering the high lifetimes previously reported in Ga-doped Si [128, 129, 130]. It, however, indicates that there is no recombination active defect resulting from the interaction of Ga with B or P. This result also shows that there is very little iron in the co-doped samples studied here, due to the use of EG-Si and to the efficient phosphorus diffusion gettering. Indeed, the lifetime measurements were done prior to any illumination and iron should thus be present in its associated state with acceptors. As FeGa pairs have been shown to be stronger recombination centres than FeB pairs [131], a lower lifetime should hence be measured in the samples containing Ga, if we were in presence of significant iron concentrations.

It also has to be observed that samples from ingots Cz#2 and Cz#3, containing large concentrations of B ($1 - 2 \times 10^{17}\text{cm}^{-3}$), scale well with uncompensated B-doped controls and samples from ingot Cz#1 with low B concentrations. This indicates that recombination through B atoms does not, in these samples, severely impact on the overall recombination lifetime, contrarily to the proposition made by Veirman *et al.* [14]. Note that the majority carrier density was much higher in their study, which enhances the recombination activity of shallow levels and may have made recombination through B atoms dominant. In any case, our results show that if the majority carrier density is significantly reduced by compensation, the impact of recombination through B atoms is negligible, even when they are present in large concentrations.

Finally, one can see that the lifetime measured in UMG-Si samples follows the same dependence on p_0 as other samples made with EG-Si. This shows that the additional recombination active impurities present in UMG-Si can be effectively removed by a standard phosphorus diffusion gettering step. The lifetime in the resulting Si is governed, as in the

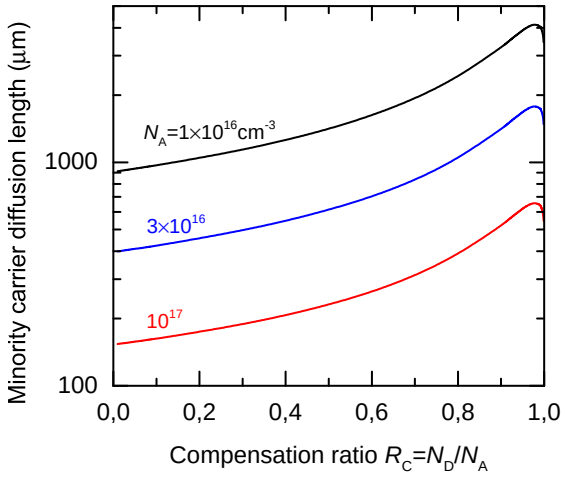

Figure 3.14: Calculated evolution of the minority carrier diffusion length with compensation in Si before BO defect activation.

other samples, by the majority carrier density.

Note that τ_{eff} is measured to be considerably lower than the intrinsic lifetime reported for very pure Fz-Si of equivalent net doping. This indicates that recombination due to imperfect surface passivation and possibly O-related recombination centres (precipitates) have a significant impact in our samples.

As we saw in section 3.3, the minority carrier mobility is reduced by compensation. To estimate the impact of compensation on the electrical current flowing through a solar cell under operation, it is therefore more relevant to focus on the minority carrier diffusion length L_{min} rather than on the lifetime. From the measured dependence of τ_{eff} on p_0 and the variation of the minority carrier mobility with compensation, established in Section 3.3, we can infer the outcome of the trade-off between lifetime improvement and mobility reduction with compensation, on the minority carrier diffusion length. For that purpose, we use a SRH parametrization of the recombination lifetime fitted on our experimental data (Figure 3.13a):

$$\tau_{\text{n0}} = 6 \times 10^{23} \times p_0^{-1.34} \tag{3.12}$$

$$\tau_{\text{p0}} = 5 \times \tau_{\text{n0}} \tag{3.13}$$

Note that this parametrization yields values close to the parametrization recently given by Schmidt *et al.* [132] for the effective recombination lifetime after permanent deactivation of the BO defect.

Figure 3.14, shows the evolution of the minority carrier diffusion length (Equation 1.32) calculated with this parametrization for τ_{eff} and Klaassen's model with the correction proposed in Sub-section 3.3.3 for the minority carrier mobility. L_{D} is calculated to increase with compensation, due to the increasing τ_{eff} until it reaches a maximum at extreme com-

pensation ($R_C = 0.98$) and starts decreasing due to the strong reduction of μ_{min}. This is in good agreement with previous experimental findings, presented in Chapter 1, showing a monotonic increase of the minority carrier diffusion length and of the short-circuit current of solar cells with compensation.

Degraded lifetime After complete degradation under illumination (Figure 3.13b), τ_{eff} is reduced in all samples by a factor ranging from 2 to 40. Therefore, it is clear that the BO defect is the dominant recombination mechanism after degradation. The measured lifetime still seems to decrease with increasing p_0 but the data points are more strongly scattered than before degradation. This result is rather bewildering if one remembers the literature results presented in Chapter 1. Indeed, because of the particular behaviour of the density of the BO defect, which was found in p-type Si to be proportional to the majority carrier density, τ_{eff} should show an even stronger correlation with p_0 after degradation than before. Note that, however, other factors than the doping may affect the concentration of the BO defect, such as the oxygen concentration which may vary strongly from one sample to another. A more in-depth study of the BO defect, which will be presented in Chapter 4, is hence required to understand the present results.

3.4.2 *n*-type Si

Before degradation Figure 3.15 shows the measured lifetime before degradation in samples taken from various heights along the n-type co-doped ingot Cz#4, together with one P-doped Cz control. High τ_{eff} values are measured in these samples, up to about 1ms and just below the reported intrinsic lifetime. The measured lifetime of 1.2ms in the 0.7Ω.cm P-doped Cz control, for which the intrinsic lifetime is expected to be 2.7ms, suggests that the lifetime may also be partially limited by surface recombination or residual O-related bulk recombination centres.

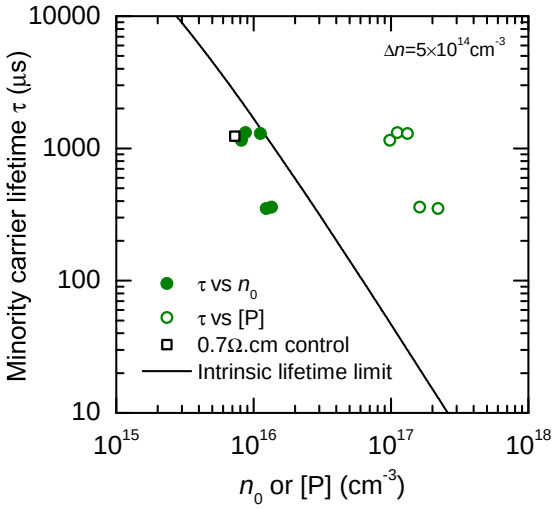

Figure 3.15: Recombination lifetime measured before degradation at various height of the n-type ingot Cz#4. Lifetime values are plotted as a function of n_0 or [P] and compared to the intrinsic lifetime limit calculated with Equation 1.12.

It is worth noting that the high minority carrier lifetime measured in samples from ingot Cz#4 is only possible due to compensation of P atoms by B and Ga. As shown in Figure 3.15, the measured lifetime is far above (two orders of magnitude) the theoretical intrinsic lifetime that would be expected if n_0 was equal to [P], that is to say if P atoms were not compensated by B and Ga. As noted in Chapter 2, because of strong compensation, n_0 is in these samples much lower than [P], which allows the high lifetime that we observe. If this lifetime is plotted as a function of the measured n_0, it falls just below the theoretical intrinsic lifetime.

Lower lifetimes, around $300\mu s$, are measured in samples close to the tail end of the ingot despite these samples having similar majority carrier density as the high lifetime ones. This may be explained by the multiplication of crystal defects, such as dislocations, in this region of the ingot. The multiplication of dislocation near the tail end of the ingot is hence attested by the disappearance of the four facets on the edge of the crystal that are characteristics of a <100>-oriented single crystalline structure.

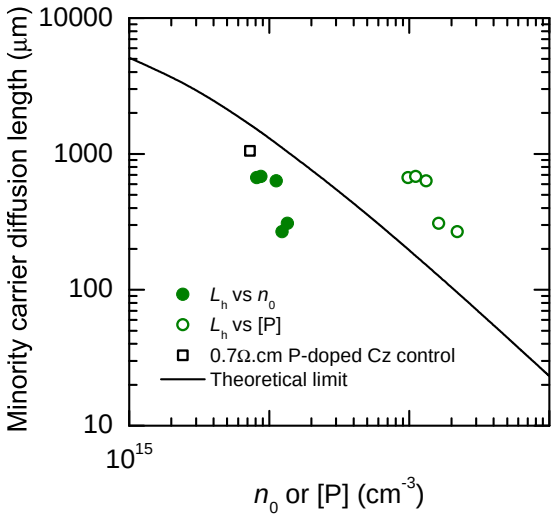

Figure 3.16: Calculated minority carrier diffusion length using the lifetime measured at an injection of 0.1suns and the measured minority carrier mobility. $L_{\min}$ is plotted as a function of n_0 and [P] and compared to the theoretical limit calculated using Klaassen's model for the minority carrier mobility.

Similarly to what we previously did for p-type compensated Si, we evaluate the minority diffusion length by using the measured τ_{eff} (at 0.1suns) and $\mu_{\min}$ in Equation 1.32. As can be seen on Figure 3.16, due to the mobility reduction, $L_{\min}$ is decreased compared to the theoretical uncompensated Si limit, when plotted against n_0. It is, however, still well above the theoretical limit when plotted against [P] i.e. above the maximum possible diffusion length if n_0 was equal to [P] (without compensation). This demonstrates that the increase in minority carrier lifetime due to compensation overweights the decrease in minority carrier mobility.

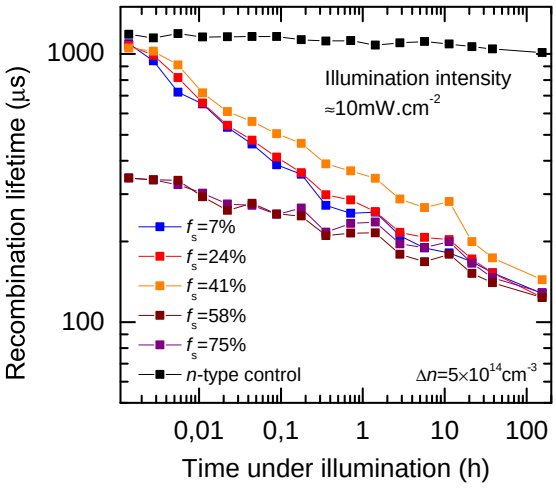

Figure 3.17: Evolution of the measured recombination lifetime in samples from different heights of ingot Cz#4.

Lifetime degradation Prolonged illumination leads to a slow but strong minority carrier lifetime degradation down to about $120-150\mu s$ after 155h under light-soaking (Figure 3.1). Because of the extremely slow degradation kinetics in n-type Si, the lifetime does not saturate, even after 155h illumination and the final degraded lifetime is hence likely to be even lower. In any case, $120\mu s$ is already below the lifetime that is usually required for high-efficiency n-type Si solar cells.

To produce n-type Si wafers with a stable minority carrier lifetime above 1ms from Si feedstock containing B, it is therefore essential to find solutions to mitigate the BO defect. One route may be the usage of alternative crystallization techniques with lower oxygen contamination such as magnetic-Cz, mono-cast or float-zone. Another solution might be to work on the permanent deactivation of the BO defect, as was shown to be possible in p-type Si [123], although first attempts have been unsuccessful in n-type compensated Si [133].

Note that because the net doping does not vary strongly along ingot Cz#4, we cannot draw any conclusion regarding the dependence of the degraded lifetime on n_0. Previous studies [51, 53], as will be discussed in Chapter 4, suggest that the BO defect density is proportional, in n-type compensated Si, to the total boron concentration.

3.5 Conclusion

Both calculations and Hall effect measurements presented in this chapter show that i.i. has a stronger influence on the majority carrier density in compensated Si than in uncompensated Si with the same net doping. This is despite the fact that the total concentration of ionized dopants is almost unaffected by i.i. in compensated Si, even at low T. In general, room-temperature i.i. impacts significantly on the carrier density in p-type Si when [B] is higher than $5\times10^{16}\text{cm}^{-3}$ or [Ga] higher than $2\times10^{16}\text{cm}^{-3}$, and in n-type Si when [P] is higher than $1\times10^{17}\text{cm}^{-3}$.

The previously reported discrepancy between theoretical and experimental μ was confirmed on a wide range of samples of both p-type and n-type. It is shown that this deviation depends only on the type of carrier (majority and minority) and on the compensation ratio. The T-dependence of μ_{maj} shows that there is no compensation-specific scattering mechanism and that the reduction of the screening is alone not sufficient to explain the observed deviation. We propose a correction of Klaassen's model by means of a simple prefactor, determined for a given carrier by the compensation ratio. This correction enables an accurate prediction of the mobility in highly-compensated Si around room-T and in moderately-compensated Si over the entire $80-350$K temperature range.

Finally, we have shown that the effective recombination lifetime is determined before degradation by the majority carrier density, irrespectively of the total dopant concentration. In contrast, the lifetime after degradation is much more scattered, which seems to disagree with the previously reported linear dependence of the BO defect density on the majority carrier density and hence with the calculations we did in Chapter 1. To understand this unexpected behaviour, we will focus in Chapter 4 on the characteristics of the BO defect in our material.

Chapter 4

The boron-oxygen defect

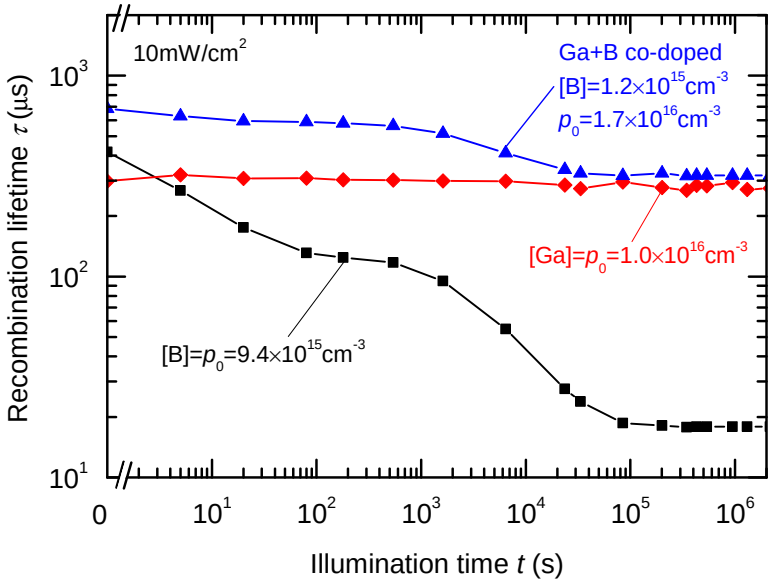

Figure 4.1: Evolution of the measured recombination lifetime, reported at $\Delta n = 0.1 \times p_0$, in p-type Si samples under illumination. Lines are guides to the eye.

We have observed in the previous chapter a strong degradation of the recombination lifetime under prolonged illumination in all of our samples containing B. Figure 4.1 displays examples of how this degradation proceeds in p-type Si. As can be seen, in Si containing B, two distinct degradations can identified: a fast but moderate degradation followed by a slow but strong degradation. Since 2004 [42] and until very recently, both degradations were believed to be due to the formation of a complex made up of one *substitutional* B atom (B_s) and one *interstitial* O dimer (O_{2i}). This defect model was proposed after the observation that only Si containing both B and O degrades, and that the saturated (i.e. after complete degradation) effective defect density $N^*_{t,sat}$ (see Sub-section 4.2.1 for the definition of $N^*_{t,sat}$) exhibits a linear dependence on B_s concentration [B] and a quadratic dependence on the *interstitial* O concentration [O_i].

However, recent measurements made on B and P co-doped p-type Si [44, 18, 46, 48] found that $N^*_{t,sat}$ was proportional to the hole density p_0 (i.e. to the net dopant density $N_A - N_D$)

rather than to the total boron concentration [B]. Note that this observation was made possible in Si co-doped with B and P because p_0 is, in such material, systematically below [B] whereas it is almost equal to [B] in uncompensated B-doped Si. This finding was initially explained by the existence of BP pairs in compensated Si resulting in a decrease of available B_s atoms for B_sO_{2i} complex formation [44, 18]. However, the existence of such BP pairs in large proportion was later shown to be very doubtful [50, 134, 45] and thus unable to explain the observed reduction of $N^*_{t,sat}$ in compensated p-type Si.

In the light of those observations, Voronkov and Falster [49] proposed a new model consisting of a latent defect made of one *interstitial* boron atom B_i and one oxygen dimer O_{2i}. The linear dependence of $N^*_{t,sat}$ on p_0 was thereby explained by the proportionality of the solubility N_{Bi} of positively charged B_i^+ in p-type Si to the free hole density, during the last stage of crystal cooling.

Another recently debated issue is how the degradation itself proceeds. While some previous works [135, 136, 42] have proposed the degradation to result from the formation of the defect, through a defect reaction, others [49, 53] pictured it as a change in the configuration of a grown-in defect, from a latent inactive state to a recombination active form.

As we have seen in Figure 3.13, the recombination lifetime in Si containing B is largely dominated by the BO defect, even in lowly-doped uncompensated Si. This means that the reduction of its effect represents a challenge of paramount importance, not only for UMG-Si, but for industrial p-type Si solar cells in general, since they are almost entirely based on B-doped and O-containing cast or Cz substrates. A fine understanding of the physics of the BO defect, i.e. of its composition and genesis, should be very useful to develop new strategies to suppress it. One point which particularly needs clarification, especially with respect to compensation engineering, is the dependence of the BO defect density on either [B] or p_0. A dependence on p_0, found in several papers [44, 18, 46, 48], would mean that the BO defect can be completely suppressed by extreme compensation as modelled in Chapter 1, Figure 1.9. The lifetime measurements we presented in Figure 3.13, however, suggest that this may not be the case, since there is a clear loss of correlation between τ_{eff} and p_0 from the annealed to the degraded state. Our lifetime data add up to recent results presented by Bernardini *et al.* [137] who found the strength of the degradation in p-type compensated Si solar cells to correlate with [B] instead of p_0. This controversy justifies a more detailed analysis of the variation of the defect density with doping.

For that purpose, we present in this chapter a systematic study of the effective defect density (Section 4.2) and formation kinetics (Section 4.3) on a set of samples with original doping (for example with $p_0 > [B]$) and wide variations in dopant concentration and compensation level. These new data, confronted to previous measurements, enable to clearly establish the dependence of the BO defect density on [B], which unambiguously demonstrates the involvement of B_s in the complex. The degradation kinetics also prove the degradation not to result from the complex formation but rather indicates it to proceed through the reconfiguration of a latent defect. In Section 4.4, we finally analyse the SRH parameters of the BO defect and cast doubts on their commonly accepted values.

4.1 Experimental procedure

The experimental procedure that we followed to study the characteristics of the BO-related lifetime degradation is the same as that already presented in sub-section 3.1.3 of the previous chapter i.e. measurements of the recombination lifetime on gettered (to avoid the presence of bistable FeB and FeGa pairs and to annihilate thermal donors) and passivated samples immediately after annealing and after different times under illumination.

In addition to the samples presented in Chapter 3, we also processed and measured Si samples that were selected at different heights (20%, 30%, and 40%) of a Cz-Si crystal of 50–70mm in diameter, grown from a melt doped with $1.47 \times 10^{15}\text{cm}^{-3}$ of B and $1.67 \times 10^{18}\text{cm}^{-3}$ of Ga. These samples present the advantage for this study that they contain more Ga than B and therefore p_0 is about 10 times higher than [B]. This will enable us to clearly establish if the defect density's linear dependence on p_0, previously observed in compensated Si in which $p_0 < [\text{B}]$, is still valid when $p_0 > [\text{B}]$. In these samples, p_0 was deduced from the resistivity measured with a four-points probe while [B] was calculated from the sample's position in the crystal and the initial concentrations in the Si melt using Scheil's equation. It lies in the range $[\text{B}] = (1.2 \pm 0.5) \times 10^{15}\text{cm}^{-3}$ to $[\text{B}] = (1.3 \pm 0.9) \times 10^{15}\text{cm}^{-3}$.

The magnitude of the lifetime degradation is known to depend critically on the *interstitial* oxygen concentration $[\text{O}_\text{i}]$ [138]. An experimental measurement of $[\text{O}_\text{i}]$ is therefore essential in any light-induced degradation experiments. For that purpose, we measured $[\text{O}_\text{i}]$ in all samples by Fourier transform infrared spectroscopy (FTIR). We found $[\text{O}_\text{i}]$ to be in the range $[\text{O}_\text{i}] = (6 \pm 1) \times 10^{17}\text{cm}^{-3}$ to $(11 \pm 2) \times 10^{17}\text{cm}^{-3}$.

4.2 Defect density

4.2.1 Effective defect density

Attempts to detect the BO defect by deep-level transient spectroscopy (DLTS) have so far been unsuccessful, presumably because of its very low concentration. As a result, most of the data that have yet been published on the defect density were obtained by lifetime spectroscopy.

The recombination lifetime due to the BO defect can be calculated by subtracting the inverse lifetime measured in the annealed state from that in the degraded state, assuming that no other recombination channels are affected by the annealing/illumination cycle:

$$Y = \frac{1}{\tau_{\text{BO}}} = \frac{1}{\tau_{\text{deg}}} - \frac{1}{\tau_0} \tag{4.1}$$

A common approach is to consider the defect density to be proportional in p-type Si to the reciprocal lifetime of the BO defect Y taken at an excess carrier density equal to 10% of the equilibrium majority carrier density [42]. This stands from the assumption that the BO defect introduces a deep level, as proposed by Schmidt and Cuevas [41] and confirmed by

Rein and Glunz [40], and that the inverse SRH lifetime (Equation 1.13) of the BO defect N_t^* can thus simplify at $\Delta n = 0.1 \times p_0$ to:

$$N_t^* = Y(\Delta n = 0.1 \times p_0) \approx \frac{1}{\tau_{n0} + 0.09 \times \tau_{p0}} = N_t \times v_{th} \left(\frac{1}{\sigma_n} + \frac{0.09}{\sigma_p} \right)^{-1} \tag{4.2}$$

Since v_{th}, σ_n and σ_p are constants, N_t^* is proportional to the BO defect density N_t and can thus be used to compare samples with different doping concentrations. We thus call N_t^* the effective defect density. A similar expression can be obtained for the inverse SRH lifetime in n-type Si at $\Delta n = 0.1 \times n_0$:

$$N_t^* = Y(\Delta n = 0.1 \times n_0) \approx \frac{1}{\tau_{p0} + 0.09 \times \tau_{n0}} = N_t \times v_{th} \left(\frac{1}{\sigma_p} + \frac{0.09}{\sigma_n} \right)^{-1} \tag{4.3}$$

We shall insist here on the fact that this method for the evaluation of the BO defect density is only valid if recombination through this defect is dominated by a single deep level and if N_t^* is used to compare samples of the same conductivity type. We will discuss the former assumption in Sections 4.2.3 and 4.4.

It is well known that the effective defect density after complete degradation $N_{t,sat}^*$ displays a quadratic dependence on $[O_i]$. This dependence is thought to be due to the participation of oxygen dimers [42] which are themselves present in a concentration proportional to $[O_i]$ squared [139]. Hence, small variations in $[O_i]$ from one sample to another can lead to significant variations in $N_{t,sat}^*$ even for equal doping levels. Since we intend to study the impact of dopant concentration on the defect density and the nature of the B atom involved in the complex, a more relevant parameter to focus on is:

$$N_{BC} = \frac{N_{t,sat}^*}{[O_i]^2} \tag{4.4}$$

This oxygen-normalized parameter reflects the influence of defect components (such as [B] or p_0) not directly related to $[O_i]$.

4.2.2 Defect density in *p*-type Si

4.2.2.1 Si co-doped with Ga and B

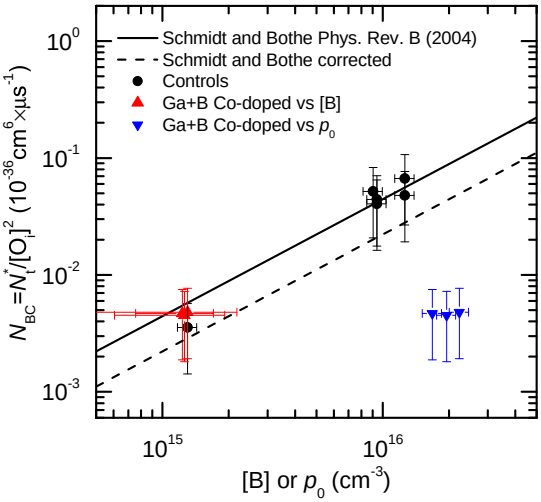

Figure 4.2: Normalized effective defect density in B-doped controls and in Si co-doped with B and Ga plotted as a function of the B concentration or the carrier density. Solid line is a fit to experimental data on B-doped Si from [42]. Dashed line corresponds to the same fit divided by a correction factor of 2 to account for the defect density reduction expected in P-diffused Si.

The normalized effective defect density N_{BC} measured for samples co-doped with Ga and B and for B-doped controls is plotted in Figure 4.2 as a function of p_0 and [B]. For comparison, we have also plotted a linear regression of experimental data points from Schmidt and Bothe [42] obtained on uncompensated B-doped Cz Si samples. A reduction of the BO defect density by about a factor of 2 was found by the same authors in P-diffused Si as compared to as-cut Si [43], presumably because of the reduction of the concentration of oxygen dimers. Since our samples underwent a phosphorus-diffusion, whereas the samples from [42] did not, we have corrected the linear fit from [42] by dividing the effective defect density by 2, in order to be able to compare it with our measurements.

As can be read on Figure 4.2, B-doped controls measured in the present work agree well with the previously measured defect density, which supports the validity of our experimental setup. In samples co-doped with Ga and B, however, N_{BC} is reduced by more than one order of magnitude compared to B-doped Si when plotted against p_0. On the other hand, it scales well with B-doped Si when plotted as a function of [B]. Note that the drastic reduction of N_{BC} compared to the linear dependence on p_0 is only observable in these samples because [B] is about 10 times lower than p_0 due to the high concentration of Ga. We conclude from this result that in Si co-doped with B and Ga, the defect density is not related to p_0 but is, instead, proportional to [B].

Voronkov and Falster's model [49] fails to describe the present result, since the concentration of dissolved *interstitial* $\mathrm{B_i}$ involved in that defect model is believed to be proportional to p_0 and independent of [B]. Instead, the proportionality to [B], found in our experiment,

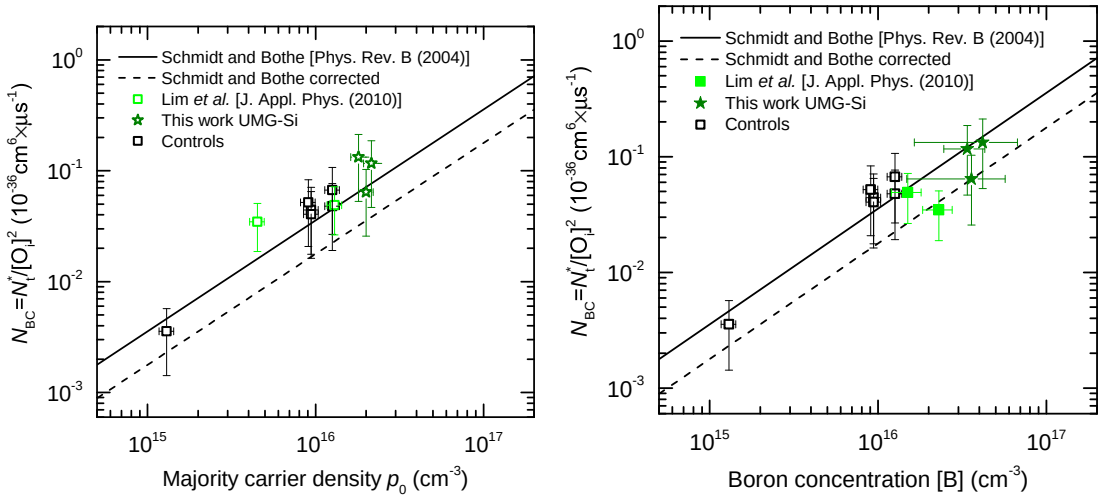

(a) (b)

Figure 4.3: Normalized effective defect density in B and P compensated UMG-Si plotted as a function of p_0 (a) or [B] (b). Our results are compared to B-doped controls, to a fit to experimental data on B-doped Si from [42] and to experimental data on B and P compensated Si from Lim *et al.* [46].

indicates the participation of *substitutional* B_s in the defect formation. As discussed in this chapter's introduction, the involvement of B_s in the BO defect is, however, difficult to reconcile with previous findings that the defect density is proportional to p_0 in B and P compensated Si in which $p_0 <$ [B].

One could also imagine that the defect is made of B_i, according to Voronkov and Falster's model, but that either one of the two densities of B_i or O_{2i} is strongly affected by the presence of Ga. For example, the formation of B_iGa_s or Ga_sO_{2i} pairs during the cooling of samples after phosphorus-diffusion is conceivable. No indication of the existence of such complexes has, however, been reported yet. Further investigation would be necessary to assess if they would be stable enough to reduce either concentrations of B_i or O_{2i} to such an extent that the BO defect density would decrease by more than one order of magnitude, as it is observed in this work.

4.2.2.2 *p*-type Si co-doped with B and P

Figure 4.3 shows the normalized effective defect density in our B and P compensated UMG-Si samples, together with previously published data from Lim *et al.* [46] on B and P compensated Cz-Si samples that were gettered at a similar T to our samples (847°C in [46] against 820°C in our experiment). We only plot the samples from the seed and tail ends of the ingot presented in [46] for which $[O_i]$ was reported. N_{BC} is plotted for each sample either as a function of p_0 (Figure 4.3a) or as a function of [B] (Figure 4.3b) and compared, in the same fashion as in Figure 4.2, to uncompensated B-doped controls as well as to a linear fit to previously published data from [42].

Note that other data have been published for the effective BO defect density in B and P

compensated Si by Macdonald *et al.* [18] and by Geilker *et al.* [48]. We, however, did not include those results in Figure 4.3 because the values for $[O_i]$ were not reported for each of the samples presented in their papers and N_{BC} could thus not be calculated. In addition, measurements presented by Geilker *et al.* were made on ungettered samples. Since high-T annealing was shown to strongly affect the BO defect concentration [140, 141, 51], it is essential for a valid comparison that all samples have gone through a similar thermal history. We therefore discuss the results of references [18] and [48] separately.

In our UMG-Si samples and in samples from [46], the small difference between p_0 and [B], together with the large uncertainties, arising mainly from the oxygen concentration measurement, make it very difficult to establish if N_{BC} is proportional to p_0 or to [B].

Lim *et al.* [46] concluded from their measurements that the BO defect density was proportional to p_0 rather than to [B]. This conclusion was based on the observation that $N^*_{t,sat}$ and p_0 vary in the same direction in their samples while $N^*_{t,sat}$ and [B] vary in opposite directions. Taking into account the variation of $[O_i]$ by plotting N_{BC} instead of $N^*_{t,sat}$ shows that such tendencies are not utterly obvious, since the variation of N_{BC} along the ingot presented in [46] remains smaller than the experimental error (Figure 4.2.2.14.3.

None of the samples presented in Figure 4.3 are very strongly compensated, which otherwise would have enabled an easier distinction between a linear dependence on p_0 or on [B]. Moreover, [B] is kept in a narrow range. A larger set of data with wider variations of [B] and compensation should enable to conclude with more confidence.

Such a set of data was presented by Geilker *et al.*, who measured $N^*_{t,sat}$ in samples with a wide range of dopant concentrations, comprising samples with high [B] and strong compensation. They, however, showed samples with low [B] or weak compensation in one graphic (Fig 3 of [48]) and samples with high [B] and strong compensation in a separate graphic (Fig 4 of [48]) plotted in a peculiar manner together with n-type Si samples. Reporting the data points corresponding to the p-type samples with high [B] and strong compensation from Fig 4 to Fig 3 of [48] shows that these points do not scale with the linear dependence on p_0 expected from the measurements made on samples with low [B] or light compensation. $N^*_{t,sat}$ in samples with high [B] and strong compensation is on the contrary found to be more than one order of magnitude higher than the expected dependence on p_0. This result strongly challenges the proposition that the BO defect density is in general proportional to p_0 in compensated Si.

In the work by Macdonald *et al.* [18], the reduction of $N^*_{t,sat}$ in compensated samples was quite important and those samples were carefully compared to uncompensated B-doped controls which had undergone the same process. Nevertheless, because compensated Si samples with only two different dopants concentrations were presented and considering the fact that [B] and p_0 vary between these samples in the same direction, one cannot conclude with absolute certainty in favour of a linear relation between $N^*_{t,sat}$ and p_0.

4.2.2.3 *p*-type Si co-doped with B, P and Ga

Figure 4.4 shows the normalized effective defect density in our samples co-doped with B, P and Ga plotted as a function of p_0 or [B]. These samples present the advantage to display a large variation in [B], p_0 and in the degree of compensation.

When plotted against p_0, the measured N_{BC} does not agree well with the fit to Schmidt and Bothe's measurements. If one looks at each group of samples separately, N_{BC} seems to increase with p_0 in each ingot. If looking at all samples together, there is, however, a poor consistency between different ingots. When plotted against [B], however, although there is still a significant scatter of the data points, there is a much better consistency between different groups of samples, with a general tendency for N_{BC} to increase with [B], following the fit to Schmidt and Bothe's measurements.

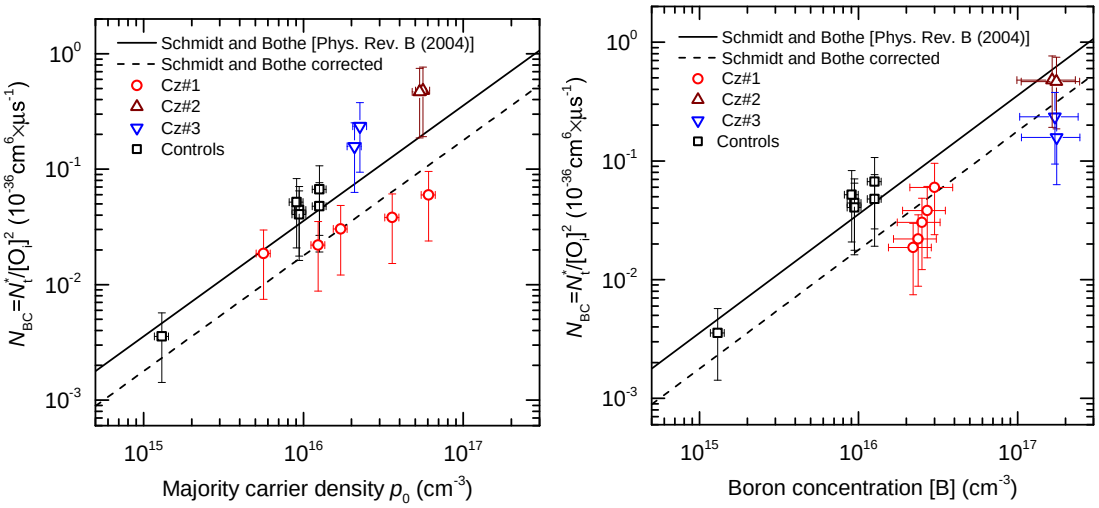

(a) (b)

Figure 4.4: Normalized effective defect density in Si co-doped with B, P and Ga, plotted as a function of p_0 (a) or [B] (b). Our results are compared to B-doped controls and to a fit to experimental data on B-doped Si from [42].

4.2.2.4 Combined data for the defect density in *p*-type Si

To observe separately the potential influences of [B] or p_0 on N_{BC}, we look in our entire set of data for groups of samples with equal p_0 and for other groups with equal [B]. To study the influence of [B], we found two groups of iso-p_0: one with 7 samples having $p_0 = 2.0 \pm 0.3 \times 10^{16}\text{cm}^{-3}$ and one with 3 samples with $p_0 = 5.7 \pm 0.4 \times 10^{16}\text{cm}^{-3}$. Plotting N_{BC} against [B] in these two groups (Figure 4.5a) clearly shows that there is a correlation between them. To study the influence of p_0, we found two groups of 4 samples, the first one with $[B] = 1.7 \pm 0.06 \times 10^{17}\text{cm}^{-3}$ and the second one with $[B] = 3.6 \pm 0.6 \times 10^{17}\text{cm}^{-3}$. In Figure 4.5b, we see an increase of N_{BC} with p_0 in samples with $[B] = 1.7 \pm 0.06 \times 10^{17}\text{cm}^{-3}$ and no clear trend in samples with $[B] = 3.6 \pm 0.6 \times 10^{17}\text{cm}^{-3}$.

The clear correlation between N_{BC} and [B] unambiguously indicates the participation of

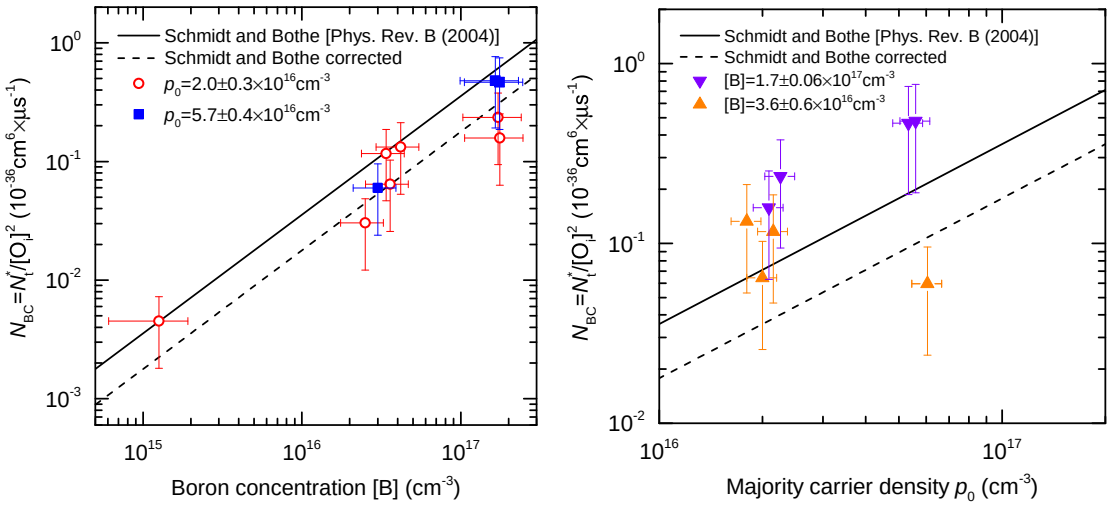

Figure 4.5: Normalized effective defect density in p-type Si with iso-p_0 or iso-[B], as a function of [B] (a) or p_0 (b). Our results are compared to a fit to experimental data on B-doped Si from [42].

substitutional boron B_s in the complex, since there is no other means through which [B] can influence N_{BC}. We have proposed in Sub-section 4.2.2.1, as an alternative explanation to the involvement of B_s in the complex, that [B_i] or [O_{2i}] could be reduced due to the presence of Ga. This could have justified, keeping B_iO_{2i} as the defect complex, the lower values for N_{BC} in Si co-doped with Ga and B than in uncompensated B-doped Si with the same p_0. Such a proposition can be discarded in the views of the present results, since in some of the samples co-doped with B, P and Ga, N_{BC} is measured to be higher than in uncompensated Si with the same p_0. The only remaining plausible interpretation for the variation of N_{BC} with [B] is hence the participation of B_s in the BO complex. Note that this conclusion is supported by a recent study [142] which showed, by density functional theory, that the concentration of B_i was too low to explain the lifetime degradation and that the calculated characteristics of the B_iO_{2i} complex were inconsistent with those measured by lifetime spectroscopy for the BO defect.

The variation of N_{BC} with p_0 is less obvious in our samples, but cannot be completely invalidated, especially considering the previously published data that we have mentioned. However, while the variation of N_{BC} with [B] can only be attributed to a change of the actual BO defect density, there are many ways to explain a variation of N_{BC} with p_0. For example, we will see in Section 4.3 that one model proposes the degradation to result from a charge-driven reconfiguration of a latent inactive defect, into a highly-recombination active form. We can imagine with such a model that the fraction of the defect concentration which is turned into the recombination active configuration may depend on p_0. A variation of N_{BC} with p_0 could also arise from a change in the recombination activity of the defect. This could, however, only be the case if recombination through the BO defect was not dominated, as assumed in the derivation of Equation 4.2, by a single deep level. For example, we have seen in Section 1.2.3 that the low-injection lifetime of a shallow level can decrease with the

equilibrium majority carrier density p_0. The eventuality of the commonly accepted SRH parameters of the BO defect being mistaken will be discussed in Section 4.4.

4.2.3 *n*-type Si co-doped with B, P and Ga

As we have seen in Chapter 2, n_0 is almost constant along the entire height of the n-type co-doped Si ingot (Cz#4) studied in this work. The B concentration does not vary much either along this ingot, due to the segregation coefficient of B being very close to unity ($k_B = 0.8$). An investigation of the defect density on samples from this ingot only, with the hope to understand the effect of compensation on the BO defect in n-type Si, would therefore be vain. It is, however, worth reporting here some of the important results that have been published by other authors studying the lifetime degradation in n-type compensated Si [51, 52, 53]:

1. It was shown that the BO defect recombination lifetime could not be fitted in n-type Si by the SRH equations with one single deep energy level. Rougieux *et al.* [52] managed to fit their data with two independent levels (one deep and one shallow) while Voronkov *et al.* [53] considered two dependent levels. In any case, this means that the effective defect density in n-type Si cannot be deduced directly from the inverse lifetime taken at a fixed injection level $\Delta n = 0.1 \times n_0$. A fit of the entire injection level dependence of the BO recombination lifetime is, as a matter of fact, necessary to evaluate the effective defect density in n-type Si.

2. Neither Rougieux *et al.* [52, 51] nor Voronkov *et al.* [53] observed a dependence of the effective defect density on the majority carrier density. The latter authors came to the conclusion that the BO defect density is proportional in n-type Si to [B], inferring the participation of *substitutional* boron in the complex responsible for the degradation. This seems to corroborate our conclusions from Sub-sections 4.2.2.1, 4.2.2.2 and 4.2.2.3. Voronkov *et al.* argued that the defect responsible for the degradation observed in n-type Si corresponds to the fast degradation observed in p-type Si (see the following Section 4.3) and can thus be made of B_s without being in contradiction with the B_iO_{2i} complex that they propose for the slow degradation in p-type Si. It would, however, appear as a curious coincidence if the fast and slow degradations observed in B-doped p-type Si, these two degradations showing numerous similarities, were to be attributed to two completely unrelated complexes with entirely different precursors.

4.2.4 Summary

We have shown in this section that in p-type Si, the effective defect density, deduced from the inverse BO recombination lifetime assuming it to be dominated by a single deep level, correlates well with a linear dependence on the total boron concentration [B] and shows no obvious correlation with the majority carrier density p_0. The dependence on [B] can only be explained by the participation of *substitutional* boron in the BO complex. On the other

hand, the dependence on p_0 observed by other research groups could be explained either by an actual variation of the BO defect density in its active state or by an alteration of its recombination activity, in case it is not, as commonly assumed, dominated by a single deep level.

The participation of *substitutional* boron in the BO complex is supported by other works reporting the BO defect density to be proportional to the total B concentration in n-type compensated Si.

4.3 Degradation kinetics

4.3.1 Degradation in p-type silicon

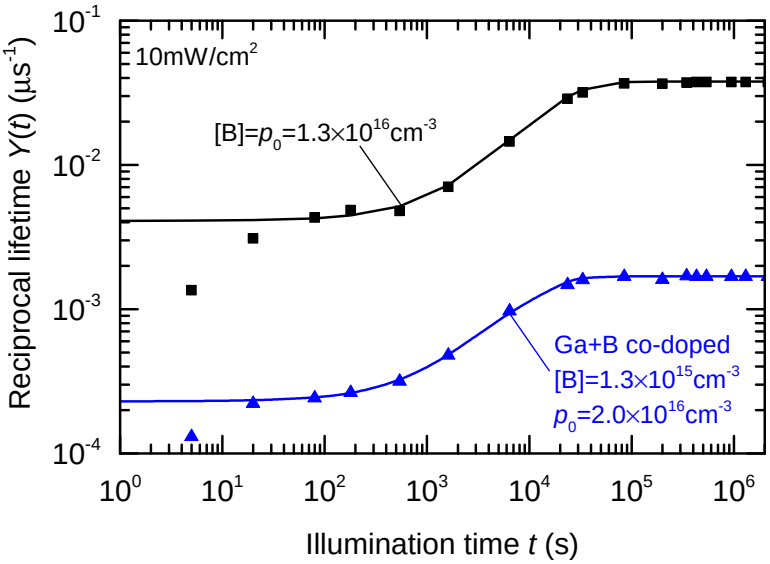

Figure 4.6: Evolution of the measured (dots) and calculated (lines) reciprocal lifetimes, at $\Delta n = 0.1 \times p_0$, in p-type samples under illumination.

The evolution of the measured effective defect density $N_t^*(t)$ with the illumination time t can be fitted (Figure 4.6), as previously reported [18], with an expression of the form:

$$N_t^*(t) = N_{\text{fast}} + N_{\text{slow}} \times \left(1 - \exp\left(-R_{\text{gen}} \times t\right)\right) \tag{4.5}$$

in which N_{fast} accounts for a fast initial degradation occurring during the first few seconds of light exposure (Figure 4.1), N_{slow} represents the magnitude of the slow degradation and R_{gen} is the formation or activation rate constant of the slow-forming defect. In this work, we only focus on the slow-forming defect which dominates in p-type the overall recombination lifetime. Note that because the degradation kinetic was found to be independent of $[O_i]$ [41], we do not need to normalize $N_t^*(t)$ to extract R_{gen} which enables to separate out of the error caused by $[O_i]$ measurement.

Two different models have been proposed for the slow degradation mechanism. The first one [135, 136, 42], which we refer to as the defect reaction model, considers the degradation to result from the formation of the BO complex, through the diffusion of oxygen dimers O_{2i} until they get trapped by fixed boron atoms. In this model, O_{2i} diffuses via a Bourgoin-Corbett recombination-enhanced mechanism [143, 144] limited by the capture of holes. The diffusivity of O_{2i} is hence proportional to the hole density p_0. On the other hand, the capture process depends on the mean distance that O_{2i} has to diffuse before it encounters a fixed B atom. The larger the concentration of the B-related component of the defect (B_i if the complex is B_iO_{2i} and B_s if the complex is B_sO_{2i}), the shorter the distance that O_{2i} has to diffuse before it gets trapped will be. Therefore, the formation rate constant R_{gen} is proposed in this model (see details in [135]) to be proportional to the product of the hole density p_0 (for the diffusivity of O_{2i}) by the concentration of the B-related component of the defect (for the distance that has to be crossed by O_{2i} to be captured by B atoms), itself proportional to N_{BC}.

The second model [49] proposes the complex to be already formed before degradation. The degradation is thereby thought to result from the rearrangement of the grown-in defect, from its latent configuration, which has a low recombination activity, into a configuration with a strong recombination activity. The change of the defect's configuration is described by a complex mechanism, in which the free energy barrier for the reconfiguration can only be overcome if the defect is temporarily recharged to a double positive state. This yields R_{gen} to be proportional to the hole density squared p^2 (equal to the equilibrium hole density squared p_0^2 in p-type Si at low injection) and independent of N_{BC} (see details in [49]).

The formation rate constant R_{gen} of the slow forming BO defect, extracted from the fit of Equation 4.5 to the measured $N_t^*(t)$, is plotted in Figure 4.7 against p_0^2 and as a function of $N_{BC} \times p_0$. Figure 4.7a also depicts R_{gen} calculated with Palmer's model, which fits previous experimental data in uncompensated B-doped Si [135]. As can be seen, R_{gen} measured in B-doped controls agrees well with Palmer's model, which again proves the validity of our experimental setup.

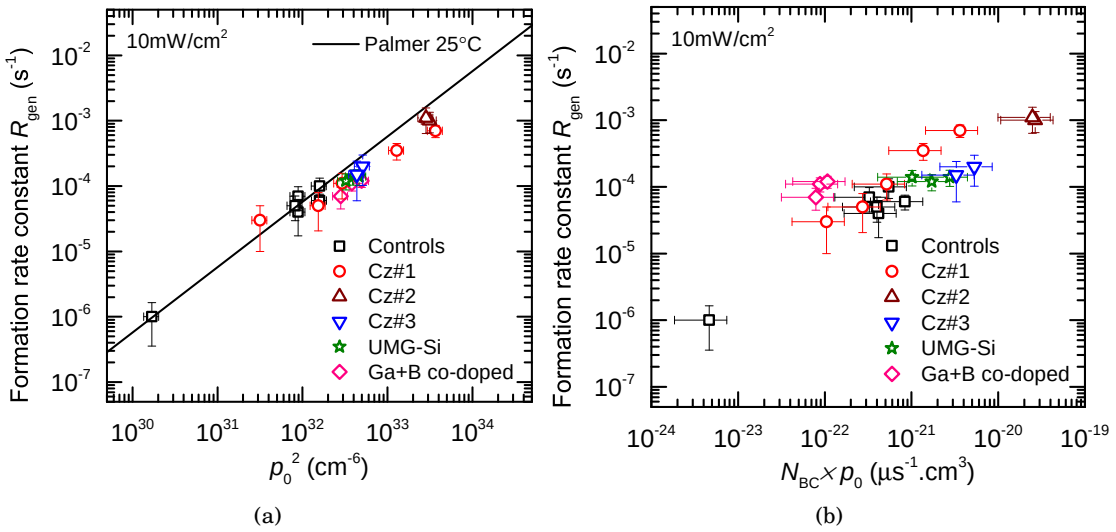

Figure 4.7: Variation of the defect formation rate constant with the majority carrier density p_0 (a) and with the product of the majority carrier density by the boron-related component of the defect $p_0 \times [B]$ (b).

Figure 4.7a shows that there is a clear linear relation between R_{gen} and p_0^2, which supports the latent defect model. Note that previous measurements of the degradation kinetics in uncompensated Si could not allow to lean toward one model or the other for the obvious reason that $N_{BC} \times p_0$ and p_0^2 were proportional ($N_{BC} \propto [B] \approx p_0$ in uncompensated Si). Similarly, previous measurements in compensated Si found the B-related component of the BO defect was proportional to p_0. In that case, both the defect reaction model and the latent defect model should also yield the same linear dependence on p_0^2 [134, 46]. In our samples, however, we have found that the concentration N_{BC} is not in general proportional to p_0. As a consequence, the defect reaction model would not expect R_{gen} to be proportional to p_0^2 in our samples but instead to $N_{BC} \times p_0$. If R_{gen} is plotted as a function of $N_{BC} \times p_0$ (Figure 4.7b), there is, however, a lower consistency between samples and a larger scattering of the data points. The distinct linear dependence of R_{gen} on p_0^2 thus enables to reject the defect reaction model proposed in [135].

Note that this observation adds up to two major deficiencies of the diffusion limited defect reaction model proposed by Palmer *et al.* [135]:

1. Firstly, the diffusion mechanism described in this model involves the participation of oxygen dimers with a double positive charge O_{2i}^{2+}. The existence of oxygen dimers in Si in another state than neutral was, however, recently shown to be very doubtful [145].

2. Secondly, the reaction is thought to stop when all the available oxygen dimers have been captured by B atoms. In such a defect reaction model, similar to the pairing reaction of the well-known FeB pairs, the final defect concentration depends only on the initial concentration of oxygen dimers and is completely independent of the B concentration [B] or of the majority carrier density p_0.

4.3.2 Degradation in *n*-type silicon

In *n*-type Si, the lifetime degradation is thought to proceed in the same manner as in *p*-type Si, i.e. by a change of the configuration of a pre-existing defect, requiring the capture of two holes [53]. The generation rate constant R_{gen} is therefore also proportional to the hole density squared p^2. However, in the case of *n*-type Si, p is not anymore equal to the equilibrium hole density p_0 but is instead equal to the excess-carrier density Δp. During illumination, Δp depends on the generation rate G and on the recombination lifetime τ, through:

$$p = \Delta p = G \times \tau \tag{4.6}$$

With G taken as equal to ϕ/d with the photon flux assumed to be $\phi = 2.5 \times 10^{16}\text{cm}^{-2}\text{s}^{-1}$ for the illumination intensity of 10mW/cm^2 we used in our experiment and with d the sample's thickness. We assume the distribution of excess carriers across the thickness of the wafer to be uniform. This assumption stands from the very fast diffusion of excess carriers compared to the bulk lifetime and enables to strongly simplify the considerations developed further.

Two characteristics of the lifetime degradation in *n*-type Si can be deduced from Equation 4.6:

1. Firstly, for an illumination intensity $P = 10\text{mW/cm}^2$, p is generally much lower (in the range $5\times10^{13}-2\times10^{15}\text{cm}^{-3}$ in our samples) in *n*-type Si than p_0 usually is in *p*-type Si for solar cells. As a consequence, the degradation is generally much slower in *n*-type Si than in *p*-type, as can be seen on Figure 3.17 and as reported in previous works [46, 51, 52, 53]. According to our measurements and to those of Bothe *et al.* [39], R_{gen} is in *p*-type Si equal to $g_{\text{s}} \times p^2$ with $g_{\text{s}} = 5 \times 10^{-37}\text{cm}^6/\text{s}$ at 25°C. This gives for a hole density $p = 2 \times 10^{15}\text{cm}^{-3}$ a time constant of 10^6s (~ 280h) which is much longer than the observed degradation. We have, however, mentioned previously the existence of a fast degradation occurring within a few seconds in *p*-type Si. This degradation was found by Bothe *et al.* [39] to proceed with a formation rate constant $R_{\text{gen,f}}$ equal to $g_{\text{f}} \times p^2$ with $g_{\text{f}} = 5 \times 10^{-34}\text{cm}^6/\text{s}$ at 25°C. This yields for $p = 2 \times 10^{15}\text{cm}^{-3}$ a time constant of 10^3s (~ 0.28h) which is in better qualitative agreement with the onset of the observed degradation.

2. Secondly, in the course of the degradation, p is not anymore constant as in *p*-type Si but decreases with τ according to Equation 4.6. As a consequence, R_{gen} decreases during the degradation and the evolution of the defect density cannot anymore be fitted by a single exponential. The degradation can effectively be modelled in the manner described below and treated in [53].

To start with, we consider the lifetimes of the fast-forming defect $\tau_{\text{BO,f}}(t)$ and of the slow-forming defect $\tau_{\text{BO,s}}(t)$ to be both invariant with the injection level. The reciprocal lifetimes $Y_{\text{f}}(t) = 1/\tau_{\text{BO,f}}(t)$ and $Y_{\text{s}}(t) = 1/\tau_{\text{BO,s}}(t)$ are assumed to be proportional to the concentration

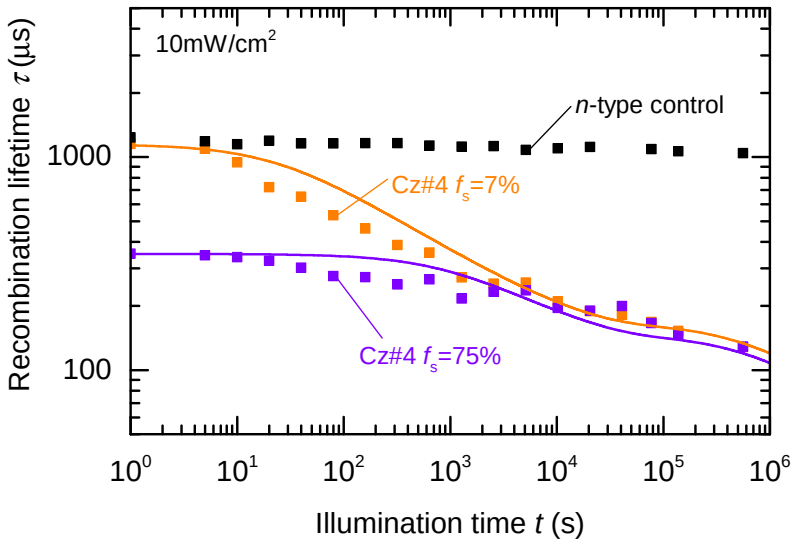

Figure 4.8: Evolution of the recombination lifetime with illumination time in co-doped n-type samples from ingot Cz#4. Dots are measured lifetime values and lines represent the modelled lifetime.

of their corresponding defect. From the exponential evolution of the effective defect density found in p-type Si, one can deduce that the variation of $Y_{\mathrm{f}}(t)$ and $Y_{\mathrm{s}}(t)$ can be expressed as follows:

$$\frac{\mathrm{d}Y_{\mathrm{f}}}{\mathrm{d}t} = R_{\mathrm{gen,f}} \times \left[Y_{\mathrm{f,sat}} - Y_{\mathrm{f}}(t)\right] = g_{\mathrm{f}} \times p^2 \times \left[Y_{\mathrm{f,sat}} - Y_{\mathrm{f}}(t)\right] \tag{4.7}$$

$$\frac{\mathrm{d}Y_{\mathrm{s}}}{\mathrm{d}t} = R_{\mathrm{gen,s}} \times \left[Y_{\mathrm{s,sat}} - Y_{\mathrm{s}}(t)\right] = g_{\mathrm{s}} \times p^2 \times \left[Y_{\mathrm{s,sat}} - Y_{\mathrm{s}}(t)\right] \tag{4.8}$$

With $Y_{\mathrm{f,sat}}$ and $Y_{\mathrm{s,sat}}$ the values taken by $Y_{\mathrm{f}}(t)$ and $Y_{\mathrm{s}}(t)$ after complete degradation. In Equations 4.7 and 4.8, p can be expressed by decomposing τ in Equation 4.6:

$$p = \frac{G}{Y_{\mathrm{f}}(t) + Y_{\mathrm{s}}(t) + 1/\tau_0} \tag{4.9}$$

in which τ_0 is the initial lifetime prior to degradation.

By numerically integrating Equations 4.7 and 4.8, combined with 4.9, we are able to model the lifetime degradation, with $Y_{\mathrm{f,sat}}$ and $Y_{\mathrm{s,sat}}$ as the only fitting parameters.

Figure 4.8 compares this modelling with our experimental values for the samples from both ends of ingot Cz#4. For more clarity, we do not plot the other measured samples, which display similar lifetime degradation curves (Figure 4.6). This plot shows a qualitative good agreement between theory and experiment. The fact that we obtain a reasonable fit of the experimental data with such a simplistic approach as the one we used, using the same formation rate constants as those determined in p-type Si, vividly confirms the dependence of R_{gen} on p^2. It constitutes a strong supportive element of the latent defect model proposed by Voronkov *et al.* [49, 53]. Note that this does not contradict our previous

conclusion (Section 4.2) that *substitutional* B is involved in the defect complex instead of the participation of *interstitial* B proposed by Voronkov and Falster in [49]. The latent character of the defect does not imply a specific composition; the existence of a latent B_sO_{2i} defect that would form during ingot cooling is possible.

4.4 Shockley-Read-Hall characteristics

To verify the validity of the assumption that we made in Section 4.2, to deduce the effective BO defect density from lifetime measurements, we study in this section the SRH characteristics of the BO recombination centre.

A traditional way of studying the injection-dependence of the recombination lifetime is to plot it as a function of the excess carrier concentration. As recently pointed out by Voronkov *et al.* [146, 53], a more convenient way to extract the SRH characteristics of a defect may be to plot τ as a function of the ratio of the minority carrier concentration to the majority carrier concentration ($n/p = \Delta n/(\Delta n + p)$ in p-type Si and $p/n = \Delta p/(\Delta p + n)$ in n-type Si). Indeed, τ_{SRH} can be expressed for a single level in p-type Si by:

$$\tau_{SRH} = \tau_{n0} \times \left(\frac{p_1}{p} + 1\right) + \tau_{p0} \times \left(\frac{n_1}{p}\right) + \tau_{p0} \times \left(\frac{n}{p}\right) \tag{4.10}$$

It can thus be shown that τ_{SRH} is a linear function of n/p, since $d\tau_{SRH}/d\left(\frac{n}{p}\right)$ does not depend on the injection level:

$$\frac{d\tau_{SRH}}{d\left(\frac{n}{p}\right)} = \tau_{p0} - \frac{\tau_{p0} \times n_1 + \tau_{n0} \times p_1}{p_0} \tag{4.11}$$

In the case of a deep level, Equation 4.10 can be reduced to a very simple linear function of n/p:

$$\tau_{SRH} = \tau_{n0} + \tau_{p0} \times \left(\frac{n}{p}\right) \tag{4.12}$$

Therefore, if recombination through the BO defect is dominated by a single deep level, τ_{BO} should thus be a linear function of n/p. Moreover, from the characteristics of this linear dependence, i.e. the intersection with the y-axis ($\tau\left(\frac{n}{p} = 0\right) = \tau_{n0}$) and the slope ($d\tau/d\left(\frac{n}{p}\right) = \tau_{p0}$) of the curve, it should be possible to extract the capture cross section ratio σ_n/σ_p:

$$k_{app} = \frac{\frac{d\tau}{d\left(\frac{n}{p}\right)}}{\tau\left(\frac{n}{p} = 0\right)} = \frac{\tau_{HI} - \tau_{LI}}{\tau_{LI}} = \frac{\tau_{p0}}{\tau_{n0}} = \frac{\sigma_n}{\sigma_p} \tag{4.13}$$

This capture cross section ratio is a characteristic of the trap and should hence be the same in every sample. On the other hand, in the case of shallow level, since τ_{LI} decreases with p_0 (Equation 1.21) while τ_{LI} remains constant, k_{app} should increase with p_0.

A linear relation is indeed found in all of our samples between τ_{BO} and n/p, in the range of n for which τ is not visibly affected by trapping (see the two examples in Figure 4.9a). The apparent capture cross section ratio (Equation 4.13), however, varies significantly from one sample to another in the range of 5 to 22. Such a variation of k_{app} could be explained if the energy level of the trap introduced by the BO defect was shallow instead of close to mid-gap as commonly assumed. However, the variation of k_{app} would in that case correlate with p_0, which is shown not to be the case in Figure 4.9b. Instead, the variation of k_{app} from one sample to another seems to be completely random.

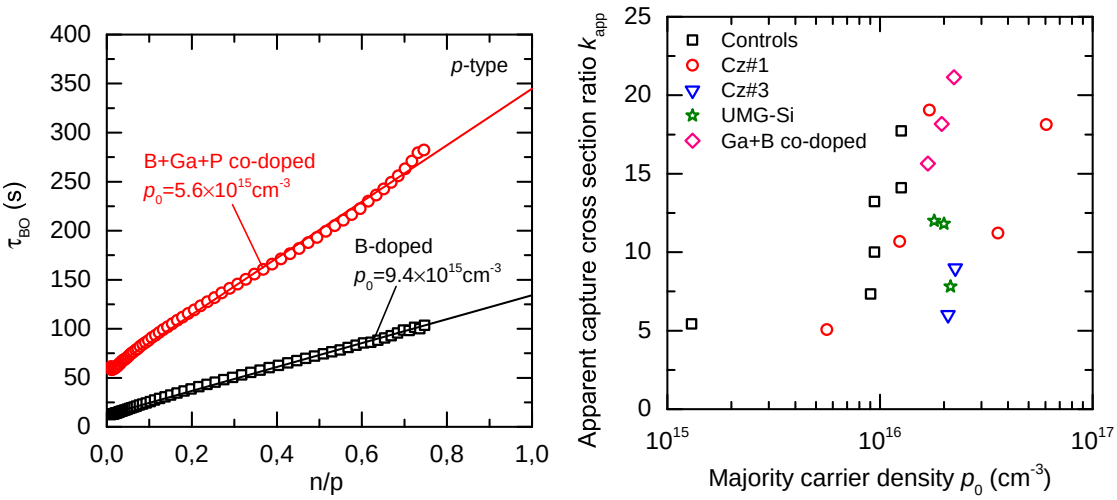

Figure 4.9: (a) Recombination lifetime of the BO defect τ_{BO} plotted as a function of n/p for two different p-type Si samples. (b) Apparent capture cross section ratio calculated from lifetime measurements in p-type Si samples using Equation as a function of the majority carrier density p_0.

Similar observations were made by Schmidt and Cuevas [41] as well as by Rein and Glunz [40]. They could only achieve a good fit of their injection-dependent lifetime data if a separate independent shallow level, in addition to the mid-gap level, was taken into account in the modelling of τ_{SRH}. Note that Schmidt and Cuevas [41] also found this shallow level to be present in some samples but not in others, independently of p_0. They proposed it to result from the activation of some form of thermal donors by illumination.

Whatever the origin of this additional shallow level, because it limits τ at high injection, it may lead to the variations we observe for the apparent capture cross section ratio k_{app}. Because it appears randomly in some samples but not in others, it may hide a potential dependence of k_{app} on p_0 and makes the interpretation of the injection-dependent lifetime data very ambiguous. For example, we can show that the same lifetime measurements can be fitted with equal accuracy using either a single deep level with a small σ_n/σ_p or a deep level with a large σ_n/σ_p and an additional shallow level located at 0.15eV below the bottom of the conduction band (Figure 4.10).

As a consequence, our experimental data do not allow to confirm if the BO defect introduces

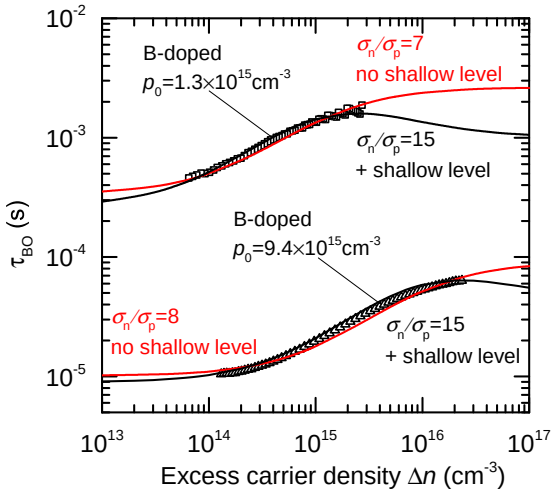

Figure 4.10: Variation of the recombination lifetime of the BO defect as a function of the excess carrier density. Dots are measured values while lines represent the modelled SRH lifetime either with a single mid-gap level (dark lines) or with a mid-gap level and a shallow level $E_C - E_{shallow} = 0.15$eV (red lines).

a deep level or a shallow level i.e. if the apparent capture cross section ratio is dependent or not on p_0. Our measurements hence do not enable to confirm or invalidate the assumption formulated in Section 4.2.1 that the defect density is in p-type Si proportional to the inverse lifetime given at a standard injection level $\Delta n = 0.1 \times p_0$.

Note that since this additional shallow level also affected the lifetime in the study of Rein and Glunz [40], the value of 9.3 for the capture cross section that they extracted from the injection-dependent lifetime can thus not be considered as certain. As for the position of the energy level of the BO defect, it was determined by a fit of the temperature dependence of the low-injection lifetime up to 250°C. To avoid annihilation of the defect at temperatures above 100°C, they illuminated their samples with a a strong light intensity. This procedure is now known to result in a permanent deactivation of the defect rather than in avoiding its annihilation [123, 147, 148, 149]. It is hence very likely that the slope of the Arrhenius increase of τ with T, from which the defect's energy level is calculated, was affected by the permanent deactivation of the BO defect.

4.5 Conclusion

In this chapter, we have analysed the phenomenon of the BO-related lifetime degradation on a wide set of p-type and n-type Si sample containing B.

We have shown that the effective BO defect density depends on the total B concentration, which proves the participation of B_s in the defect complex. The previously observed dependence on p_0 was not confirmed nor ruled out by our results. We suggest that if such a dependence exists between the BO defect density and p_0, it could be due either to a variation of the fraction of the defect which is rendered active upon degradation or to a change of its recombination activity.

Studying the kinetics of the lifetime degradation reveals the defect activation rate constant to be proportional in both p-type and n-type Si to the hole density squared. This invalidates the defect reaction model involving the diffusion of O dimers and their capture by B atoms. It instead indicates a charge-driven reconstruction of a grown-in defect, from a latent inactive configuration into a highly recombination active form.

Investigating the BO recombination lifetime using the SRH statistics reveals unfruitful for the determination of the SRH parameters. This is so because of a random variation of the ratio of the high-injection to the low-injection lifetime. For a better confidence in the SRH parameters of the BO defect, on which we rely for the determination of the defect density by lifetime measurements, further work should be dedicated to their determination. For that purpose, a better understanding of the origin of the observed independent shallow level is required. Alternative lifetime measurements, such as quasi-steady-state photoluminescence [150, 151], could also be helpful in order to collect accurate lifetime data over a wider range of injection levels.

Chapter 5

Application of compensation engineering to UMG-Si solar cells

We have shown in Chapters 2 and 3 that compensation engineering can be used to maintain *a priori* adequate carrier recombination and transport properties for high-efficiency solar cells over a large fraction of ingots made with Si containing B and P. However, this study was so far only carried out on EG-Si, while the final application which is foreseen is clearly UMG-Si. In addition, our investigation of the impact of compensation was merely done at the wafer level and we have not yet confirmed the beneficial effect of compensation on solar cells. A validation of our results on solar cells made with UMG-Si is hence necessary to confirm the benefits of Ga co-doping.

One particular issue that has been addressed in Chapter 4 concerns the BO recombination centre, of which the activation results in a lifetime degradation under illumination or carrier injection. We have shown, among others, that the BO defect density increases with [B] while it was formerly thought to depend only on p_0. This finding tends to challenge the legitimacy of compensation engineering, which is based on the idea that recombination depends only on the majority carrier density and can thus be diminished by compensation, no matter what the total boron concentration is. The consequence of such a result on the potential application of compensation engineering to UMG-Si solar cells thus has to be assessed.

In this chapter, we apply compensation engineering to the crystallization of UMG-Si and focus on its impact on the performance of solar cells made with a standard industrial-type process for *p*-type Si. We show that Ga co-doping enables to increase the ingot yield and to tolerate a significantly higher concentration of P in UMG-Si without compromising the solar cells performance before light-induced degradation. Using the parametrization established in Chapter 3, which we implement in QSS-MODEL [152], we model the I-V characteristics of those solar cells and find a good agreement with measured data. Using similar modelling, we simulate those same solar cells after activation of the BO recombination centre, in order to assess the impact of compensation on their performance.

The solar cells performance after light-induced degradation has not been measured yet at

the time of the submission of this manuscript. It will be duly included in its final version.

5.1 Experimental procedure

5.1.1 Purification

For this study, we used a UMG-Si of which the purification process flow is drawn in Figure 5.1. The starting metallurgical-grade Si was produced by FerroPEM. A careful selection of the raw materials, i.e. silica and carbon, from which MG-Si is made in electric arc furnaces by carbothermic reduction, enables to limit the initial impurity concentration. A first segregation treatment is applied during the solidification of this MG-Si, reducing the concentrations of phosphorus and metallic impurities. The resulting material is then transferred to the PHOTOSIL facilities. There, Si is then purified according to the standard PHOTOSIL process ([85, 6, 5]), involving a plasma treatment to remove B and segregations to remove P and metallic impurities.

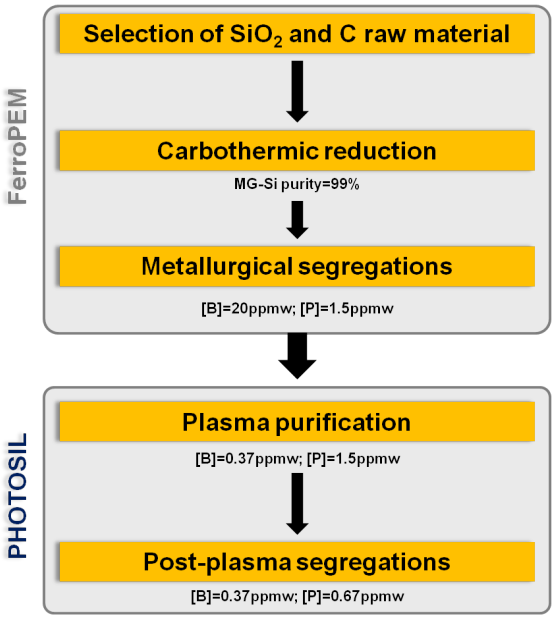

Figure 5.1: PHOTOSIL purification process flow.

At the end of the purification process, the average impurity content in the resulting UMG-Si batch is estimated from a local glow-discharge mass spectroscopy (GDMS) analysis to be $[B]_0 = 0.37$ppmw and $[P]_0 = 0.67$ppmw.

5.1.2 Crystallization

Two batches of 15kg, considered as identical in terms of impurities concentration, were selected from this UMG-Si to grow two different Cz ingots. The first one, which we will refer to as Cz#U1, was grown according to the process described in Chapter 2, without addition of any dopants aside from those already contained in the UMG-Si. After crystallization, the

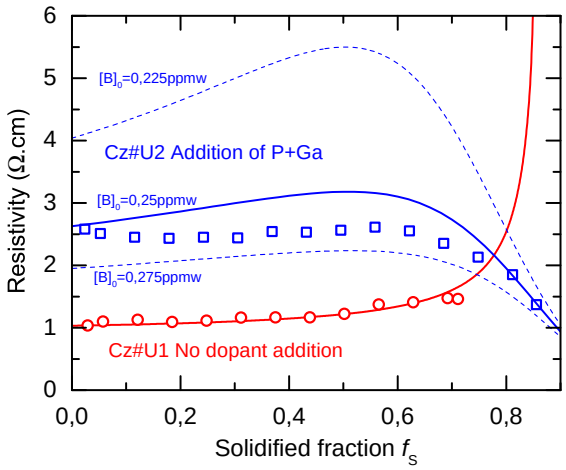

Figure 5.2: Resistivity profile of ingots Cz#U1 (red) and Cz#U2 (blue). Dots represent the resistivity measured by Eddy current along each ingot. Solid lines represent the calculated resistivity using Scheil's law for the dopants distribution and our corrected Klaassen's model (see Sub-section 3.3.3) for the majority carrier mobility.

ingot was shaped into a $125\times125\text{mm}^2$ pseudo-square brick and the resistivity was measured by Eddy current along the length of one of its edges (red dots in Figure 5.2). The recombination lifetime was also measured along the brick by μW – PCD, using a Freiberg instruments MDPingot characterization tool. To refine our evaluation of the initial concentrations $[B]_0$ and $[P]_0$ in this UMG-Si, we fitted the measured resistivity profile using Scheil's equation for the distribution of B and P and Klaassen's model with the correction presented in Section 3.3.3 for the majority carrier mobility. Varying $[B]_0$ and $[P]_0$ around the values determined by GDMS to achieve a good fit of the resistivity profile gives $[B]_0 = 0.25$ppmw and $[P]_0 = 0.60$ppmw. The average calculated p_0 is $1.5\times10^{16}\text{cm}^{-3}$ over 80% of the ingot height and a type changeover from p-type to n-type is expected at the solidified fraction 85%.

The second ingot, called Cz#U2, was grown using the same crystallization process. We, however, added 1.4ppmw of P and 85ppmw of Ga into the crucible before melting of the Si. The addition of P is meant to reduce the net doping to improve the recombination lifetime while the addition of Ga serves to avoid the type inversion. Note that without the addition of Ga, increasing the P concentration in the Si melt would reduce the p-type fraction of the ingot, which is low (85%) in Cz#U1. After crystallization, the ingot was shaped into a $125\times125\text{mm}^2$ pseudo-square brick, the resistivity was measured by Eddy current along the length of one of its edges (blue dots in Figure 5.2) and the recombination lifetime by μW – PCD. The ingot is 100% p-type and the resistivity is found to be relatively uniform and is, as expected, significantly increased compared to ingot Cz#U1. This shows that the majority carrier density has been effectively reduced by co-doping with P and Ga. Also note that the calculated ρ agrees reasonably well with measurements, which proves the robustness of our method to determine $[B]_0$ and $[P]_0$. Varying the initial B concentration $[B]_0$ by $\pm10\%$ in our calculations strongly modifies the modelled resistivity profile, which departs from the experimental one. This demonstrates the accuracy of the determined $[B]_0$ and $[P]_0$ in the Si feedstock and highlights the importance of a precise knowledge

of these values to apply compensation engineering successfully. Due to a higher degree of compensation (average $R_C = 0.85$ against 0.52 in Cz#U1), the average p_0 in Cz#U2 is calculated to be $0.8 \times 10^{16}\text{cm}^{-3}$.

5.1.3 Solar cells fabrication

Industrial type screen printed solar cells with full area Al back contact were fabricated at ISC Konstanz with wafers selected from different heights along ingots Cz#U1 and Cz#U2. Uncompensated B-doped EG-Si controls with a resistivity of 1.5Ω.cm and 3.5Ω.cm were processed together with wafers from Cz#U1 and Cz#U2. The process flow is drawn in Figure 5.3.

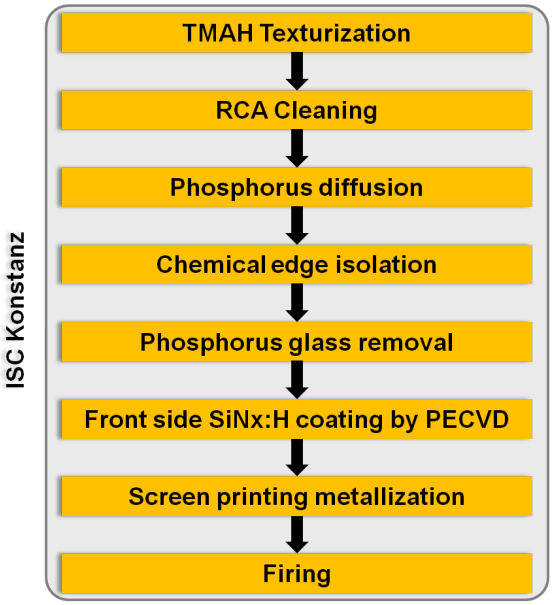

Figure 5.3: Solar cells fabrication process flow at ISC Konstanz.

Unfortunately, many wafers from all groups of wafers broke during the solar cell fabrication process and only 3 complete solar cells could be made with ingot Cz#U1. The origin of this large breakage remains unexplained. After processing, the I-V characteristics of each cell was measured under standard AM1.5G illumination conditions at 25°C. Cells were then completely degraded by illuminating them for 100h at 60°C under a 100mW/cm^2 halogen lamp and their I-V characteristics were then measured again at 25°C.

5.2 Modelling

To evaluate the impact of co-doping on solar cells, we also simulated their performance using the program QSS-MODEL [152]. This program allows to specify the ionized acceptor and donor concentrations in the base of the device. The recombination and transport properties can then be adjusted by setting the SRH parameters of up to two recombination centres

and by choosing the appropriate mobility model. In this work, we used Klaassen's model with the correction presented in Sub-section 3.3.3 for both minority and majority carrier mobilities.

For the recombination lifetime, we used the parametrization proposed in Sub-section 3.4.1 (Equations 3.12 and 3.13). This simulation represents the optimistic case of solar cells manufacturers being able to permanently deactivate the BO defect or ingot growers being able to avoid oxygen in Si crystals in a cost effective way. Our parametrization of the lifetime (Equations 3.12 and 3.13) already includes Auger and radiative recombination. Since those intrinsic components are automatically taken into account in QSS-MODEL, they have to be subtracted from the recombination current for an accurate simulation of the solar cells performance.

For the simulation of the devices that were fabricated, we assumed a fixed recombination in the front ($J_{0f} = 1 \times 10^{-12}$A/cm^2) and back ($J_{0b} = 2 \times 10^{-13}$A/cm^2) regions of the solar cells. For the optics, we considered a textured front surface coated with a 75nm thick $SiN_x:H$ layer and an optical shading of 7% by the metal grid on the front side. Solar cells were modelled under a standard illumination AM1.5G at 25°C.

To account for parasite shunts and resistive losses, we set the series resistance of the front and back regions at $R_s = 0.8\Omega{\cdot}$cm^2 and the shunt resistance at $R_{sh} = 5000\Omega \cdot$cm^2, representative of what was found for EG-Si solar cells.

5.3 Results

5.3.1 Recombination lifetime

Before degradation The recombination lifetime measured by $\mu W-PCD$ before light-induced degradation along both bricks is shown in Figure 5.4a and compared to that calculated at an injection of 0.1suns. Both calculations and measurements agree that τ is along most of the crystal length larger in co-doped ingot Cz#U2 than in ingot Cz#U1. As discussed above, this is due to the strong dependence of τ on the majority carrier density p_0 which is reduced from 1.5×10^{16}cm^{-3} on average in ingot Cz#U1 to 0.8×10^{16}cm^{-3} in Cz#U2.

One can see that the measured lifetime is lower, by almost one order of magnitude, than the values given by our parametrization. Note that this parametrization was based on lifetime measurements carried out on gettered and passivated samples. The lifetime measured along bricks may thus be lower because of recombination at the surface and because the Si has not been subjected to a phosphorus diffusion gettering which would have removed metal contaminants and dissolved oxygen-related thermal donors. Note, however, that the relative improvement of the recombination lifetime in the co-doped ingot Cz#U2 compared to ingot Cz#U1 is equivalent whether it is measured (average τ improved by a factor of 3.3) or calculated (average τ improved by a factor of 2.6).

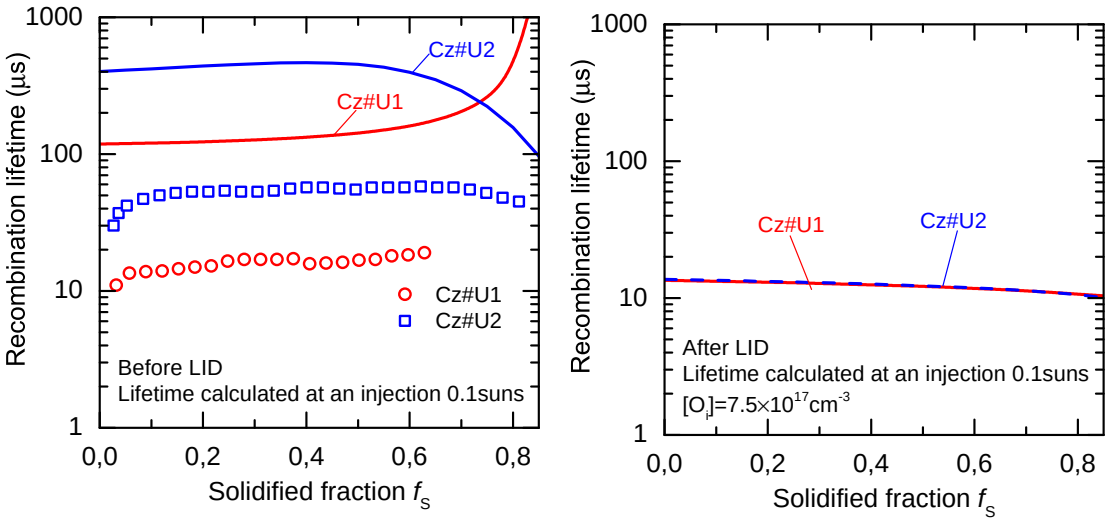

Figure 5.4: (a) Recombination lifetime measured by μW – PCD and modelled at an injection of 0.1suns before activation of the BO defect. (b) Recombination lifetime modelled at an injection of 0.1suns, after activation of the BO defect.

After degradation To calculate the lifetime after light-induced degradation, we used the parametrization of the degraded lifetime given by Bothe *et al.* [43] in combination with an assumed capture cross section ratio of $\sigma_n/\sigma_p = 9.3$. Following our findings from Chapter 4, showing that the BO-related lifetime degradation depends on [B] rather than on p_0, we used Bothe's parametrization in the form under which it was initially proposed (Equation 1.25), i.e. in which τ is a function of [B] and [O_i]. We assumed a constant $[O_i] = 7.5 \times 10^{17}\text{cm}^{-3}$ in both ingots which is a reasonable average value for Cz-Si. As can be seen on Figure 5.4b, the recombination lifetime is calculated to be significantly lower when considering the presence of the BO recombination centre. Because we consider that the BO defect introduces a deep energy level with a small capture cross section ratio $\sigma_n/\sigma_p = 9.3$ and that its density depends on [B] and [O_i], the recombination lifetime in the degraded state, modelled at an injection of 0.1suns, is only weakly dependent on p_0 and thus on compensation. Since we assume that [B] and [O_i] are the same in Cz#U1 as in Cz#U2, there is barely no difference in τ between those two ingots after activation of the BO defect. This indicates that the positive effect of compensation on τ, observed in Si before light-induced degradation, may completely disappear after activation of the BO defect.

5.3.2 Open-circuit voltage

The open-circuit voltage V_{oc}, measured and modelled for solar cells made with wafers originating from different heights along ingots Cz#U1 and Cz#U2 is shown in Figure 5.5.

Before degradation Both measurements and modelling indicate a very similar V_{oc} in ingots Cz#U1 and Cz#U2. This is because of the opposite effects of p_0 on the product $(p_0 + \Delta n)\times\Delta n$, in the expression of V_{oc} (1.31). As p_0 is reduced in Cz#U2 due to compensation, the

recombination lifetime increases (Figure 5.4a), leading to a larger Δn at a given injection. There is hence a small effect on V_{oc} of reducing p_0 by compensation, between ingot Cz#U1 and ingot Cz#U2. Note that V_{oc} is also measured and modelled to be equivalent in ingots Cz#U1 and Cz#U2 to EG-Si controls.

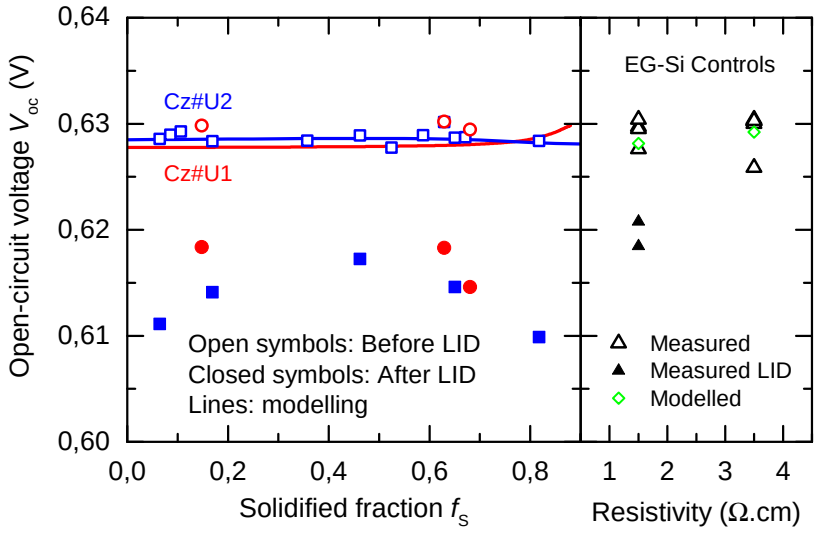

Figure 5.5: Left: Open-circuit voltage measured before activation of the BO defect (open symbols) and after degradation (closed symbols) and modelled before degradation (solid lines) along UMG-Si ingots Cz#U1 and Cz#U2. Right: Open-circuit voltage measured (open black triangles) and modelled before (green diamond-shaped) and after degradation (purple square) in EG-Si controls.

After degradation Figure 5.5 shows that a degradation of V_{oc} by $10-20$mV results from the activation of the BO defect under prolonged illumination. As we have seen in Subsection 5.3.1, the recombination lifetime is the same after light-induced degradation in ingots Cz#U1 and Cz#U2. In such case, V_{oc} decreases with reducing p_0, leading to lower values in ingot Cz#U2 than in ingot Cz#U1. In that respect, there is thus a negative impact of compensation on the magnitude of light-induced degradation of V_{oc}.

Also note that the degradation of V_{oc} is stronger in UMG-Si solar cells from ingots Cz#U1 and Cz#U2 than in EG-Si controls, due to the larger concentration of B in UMG-Si.

5.3.3 Short-circuit current density

Before degradation As can be seen in Figure 5.6, the short-circuit current density is measured to be slightly larger in ingot Cz#U2 than in ingot Cz#U1, in good accordance with simulation. This improvement in J_{sc} shows that the minority carrier diffusion length is improved in ingot Cz#U2 due to the reduction of p_0 by compensation. This confirms that before light-induced degradation, the positive impact of compensation on the recombination lifetime outweighs the minority carrier mobility reduction.

Note that J_{sc} in UMG-Si solar cells from ingot Cz#U2 is similar to EG-Si controls with similar p_0 (1.5Ω·cm controls for which $p_0 = 1 \times 10^{16}\text{cm}^{-3}$) and slightly lower than EG-Si controls with lower p_0. This proves that similar performance to EG-Si can be achieved in compensated Si with a good control of the net doping, even when the total dopant concentration is high (up to $2.15 \times 10^{17}\text{cm}^{-3}$ in the cells from Cz#U2).

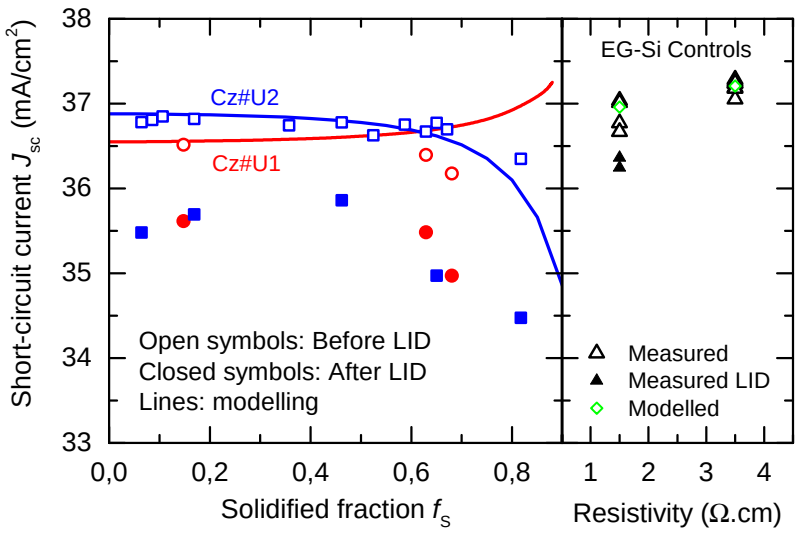

Figure 5.6: Left: Short-circuit current density measured before activation of the BO defect (open symbols) and after degradation (closed symbols) and modelled before degradation (solid lines) along ingots Cz#U1 and Cz#U2. Right: Short-circuit current density measured (open triangles) and modelled before (green diamond shape) and after degradation (purple square) in EG-Si controls.

After degradation Prolonged illumination leads to a drop of J_{sc} by $1-3\text{mA/cm}^2$ in cells from ingots Cz#U1 and Cz#U2 (Figure 5.6). After degradation, the recombination lifetime is expected to be the same in both ingots (Figure 5.4b) while the minority carrier mobility is lower in ingot Cz#U2, due to the larger concentration of dopants and the stronger compensation. One should thus expect a shorter minority carrier diffusion length in ingot Cz#U2 and thus a lower J_{sc} for solar cells made with wafers from this ingot. However, measured J_{sc} is similar in both ingots after light-induced degradation. This may be due to small differences in $[O_i]$ between the two ingots. In any cases, our results clearly show that compensation does not reduce the degradation of J_{sc} under illumination.

Similarly to V_{oc}, the degradation of J_{sc} is much stronger in solar cells made with UMG-Si than in EG-Si controls (about 0.5mA/cm^2) due to the larger B concentration in the former.

5.3.4 Efficiency

Before degradation The conversion efficiency η is measured and modelled before degradation to be similar in ingots Cz#U1 and Cz#U2. This is despite the much larger initial P concentration in the Si melt used to crystallize Cz#U2. This result demonstrates that it is

possible to tolerate a much higher P concentration in UMG-Si, by co-doping the Si melt with Ga, without compromising the final solar cells performance. Such a finding is very positive because it releases the specifications for P concentration, of which the reduction represents an important cost element of UMG-Si purification.

In addition, η is very similar in UMG-Si solar cells as in EG-Si controls. This indicates that UMG-Si can be an appropriate base material for making high-efficiency solar cells. Such encouraging results line up with the fast improvement of the performance of UMG-Si solar cells over the last few years [47, 85, 88], which has strongly narrowed the gap between UMG-Si and EG-Si.

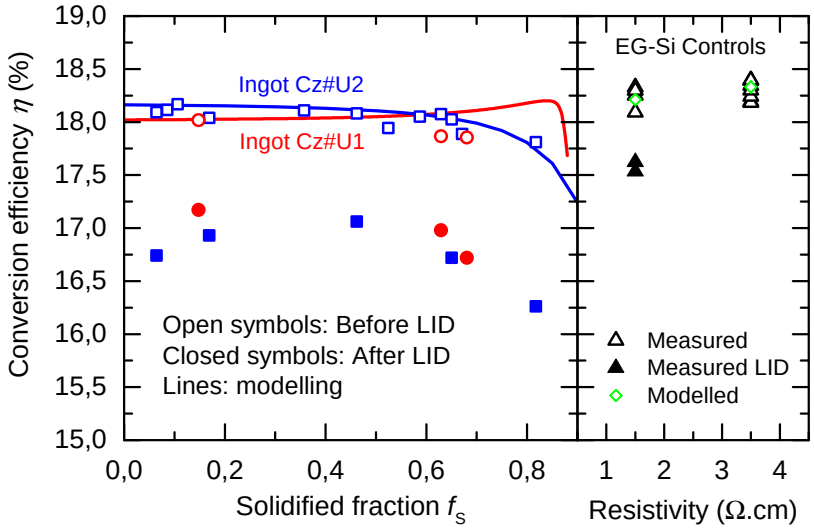

Figure 5.7: Left: Conversion efficiency measured before activation of the BO defect (open symbols) and after degradation (closed symbols) and modelled before degradation (solid lines) along ingots Cz#U1 and Cz#U2. Right: Conversion efficiency measured (open triangles) and modelled before (green diamond shape) and after degradation (purple square) in EG-Si controls.

After degradation A loss by up to about $1-2\%$ absolute in η results from light-induced degradation in ingots Cz#U1 and Cz#U2. As we have discussed in Sub-sections 5.3.1, 5.3.2 and 5.3.3 the improvement of τ due to compensation observed before degradation disappears after activation of the BO recombination centre. As a consequence, the overall conversion efficiency is lower in the highly-compensated ingot Cz#U2 than in Cz#U1. This shows that compensation engineering cannot be applied in the presence of the BO defect without suffering from a significant loss in solar cell performance.

Again, although the efficiency degradation expected in EG-Si controls is significant ($0.5-0.6\%$ absolute), it is much less severe than in UMG-Si solar cells. This highlights the importance of the challenge that represents the suppression of the BO defect for UMG-Si to be competitive with EG-Si. As lately pointed out by Schmidt *et al.* [132], several companies have recently reported efficiencies exceeding 20% for solar cells made with standard p-type Cz-Si substrates [153, 154] which suggests that these companies have already developed

effective strategies to suppress the BO defect. Such kind of BO defect suppression, either by reducing the oxygen content or by some form of permanent defect deactivation, should in theory be applicable to UMG-Si. This would make UMG-Si competitive with EG-Si, according to the results we presented before degradation.

Table 5.1 summarizes the experimental and modelled characteristics of solar cells made with UMG-Si ingots Cz#U1, Cz#U2 and with EG-Si control wafers.

5.4 Conclusion

In this chapter, we have studied the characteristics of solar cells made with wafers coming from two different *p*-type Cz-Si ingots grown with the same UMG-Si feedstock. In one of these two ingots, we have applied compensation engineering and demonstrated that it is possible to simultaneously decrease the majority carrier density and increase the *p*-type fraction by adding P and Ga into the Si melt before crystallization.

Before light-induced degradation, solar cells display high conversion efficiency (maximum $\eta = 18.17\%$) which is similar in both ingots and close to EG-Si solar cells made with the same process ($\eta_{EG} - \eta_{UMG} = 0.2 - 0.4\%$). This indicates that UMG-Si can be an appropriate material for high-efficiency solar cells and that Ga co-doping enables to tolerate a much higher concentration of P in UMG-Si without sacrificing the ingot yield or the solar cell performance. Modelling those solar cells using QSS-MODEL, in which we implement our parametrization of the carrier recombination and transport properties in compensated Si enables to faithfully predict the solar cells characteristics in both UMG-Si and EG-Si solar cells. This gives credit to this parametrization of μ and τ we established in Chapter 3 for compensated Cz-Si before degradation.

After degradation, UMG-Si solar cells suffer from a strong performance degradation under illumination, which is more severe than in EG-Si. In the presence of the BO defect, because of the strong dependence of its density on [B], compensation is no more efficient in improving the recombination lifetime. As a consequence, the degradation is stronger in highly-compensated Si and compensation engineering can thus not be applied without downgrading the solar cells performance. Such a result highlights the necessity to develop cost-effective strategies to suppress the BO defect for UMG-Si to reach similar performance to EG-Si.

Ingot	amount of cells	average V_{oc}	max V_{oc}	average J_{sc}	max J_{sc}	average η	max η
Cz#U1	3	629.8mV	630.2mV	36.4mA·cm^2	36.8mA·cm^2	17.91%	18.02%
Cz#U2	12	628.7mV	630.1mV	36.7mA·cm^2	36.9mA·cm^2	18.03%	18.17%
Controls 1.5Ω.cm	4	629.3mV	630.4mV	36.9mA·cm^2	37.0mA·cm^2	18.24%	18.33%
Controls 3.5Ω.cm	7	629.6mV	630.4mV	37.2mA·cm^2	37.3mA·cm^2	18.29%	18.40%

(a)

Ingot	V_{oc}	J_{sc}	η
Cz#U1	628.1mV	36.7mA·cm^2	18.05%
Cz#U2	628.5mV	36.4mA·cm^2	18.09%
Controls 1.5Ω.cm	628.1mV	37.0mA·cm^2	18.21%
Controls 3.5Ω.cm	629.2mV	37.2mA·cm^2	18.33%

(b)

Table 5.1: (a) I-V characteristics of the solar cells fabricated with ingots Cz#U1 and Cz#U2 and with EG-Si control wafers before light-induced degradation. (b) Average modelled solar cells characteristics before light-induced degradation.

Conclusions and Outlook

In this thesis, we have examined the impact of dopant compensation on the electrical properties of bulk Si and Si solar cells. We have analysed the practical issues associated with the growth of compensated UMG-Si crystals for solar cells and proven the potential of Ga co-doping to solve those issues.

The main contributions of this thesis are summarised below and suggestions are made for further related work.

Carrier transport in compensated silicon

This thesis has confirmed on a wide set of samples the previously observed electron and hole mobility reduction compared to Klaassen's model and found that it could neither be explained by a compensation-specific scattering mechanism, nor by the reduction of screening effects alone. While the exact components responsible for this discrepancy remain undetermined, it seems to arise from the partially empirical character of Klaassen's model, of which the constants were fitted on mobility measurements in uncompensated Si. To enable an accurate prediction of the mobility in compensated Si around room-temperature and hence of the resistivity and of the characteristics of compensated Si solar cells, we have established a simple and easily implemented correction factor for Klaassen's model. To elaborate a universal mobility model, which would accurately predict the mobility in Si with any doping, compensated or not, and at any temperatures, it is necessary to re-examine the fundamental physics of carrier scattering and screening. Such an effort goes well beyond the scope of the present thesis.

Nature of the boron-oxygen recombination centre

By systematically measuring the effective BO defect density in Si samples with a wide range of dopants concentrations and compensation levels, we have shown that it is proportional to the total B concentration rather than to majority carrier density. This proves the involvement of *substitutional* B in the defect complex instead of the recently proposed participation of *interstitial* B. The degradation kinetics are found to depend in both p-type and n-type Si

on the hole density squared which attests to the degradation proceeding through the activation of a latent defect. Standard injection-dependent and temperature-dependent lifetime spectroscopy techniques are revealed insufficient to determine the SRH parameters of the BO recombination centre. To further improve the understanding of the BO-related lifetime degradation, we suggest that alternative characterization techniques to inductively-coupled photoconductance measurements should be sought. Photoluminescence is one of them and could offer some valuable information on the nature of the mechanisms at play for the observed degradation.

Recombination in compensated silicon

The outcomes of this thesis on the relation of carrier lifetime to compensation are mixed. On one hand, we have found that the recombination lifetime before activation of the BO defect follows the same strong dependence on the majority carrier density in compensated Si as in uncompensated Si. This very positive finding has allowed to measure high lifetimes, up to 1ms in compensated n-type Si and 0.7ms in compensated p-type Si, and to fabricate solar cells with high-efficiency despite high concentrations of both B and P. We have, among others, experimentally shown that the increase in recombination lifetime due to compensation largely outweighs the minority carrier mobility reduction. This proves the beneficial outcome of compensation on the minority carrier diffusion length and hence on the current of a solar cell. On the other hand, we have shown that the BO defect concentration is proportional to the total boron concentration instead of the majority carrier density. This, together with the mild asymmetry of the capture cross sections of the BO recombination centre, means that compensation has virtually no positive impact on the recombination lifetime in the presence of the BO defect. As a consequence, UMG-Si solar cells with high B content show after light-induced degradation a significantly lower performance than cells made with EG-Si. This performance cannot be improved by compensation engineering, against what was previously suggested. As a consequence, suppressing the BO defect remains the major technical and scientific challenge for UMG-Si to become competitive with EG-Si for high-efficiency solar cells. The two main routes that are currently investigated to achieve that goal are the fabrication of low-O Si crystals (MCz, shallow melt continuous Cz growth...) and the neutralisation of the BO defect by appropriate thermal and illumination treatments. It is worth it to note that the suppression of the BO defect is not critical only for UMG-Si but for high-efficiency p-type Si solar cells in general, which will undoubtedly require Si substrates with a very high stabilized lifetime in order to surpass 20% in efficiency in production.

Compensation engineering by gallium co-doping

This thesis has explored Ga co-doping as a mean to control the net doping during crystallization of ingots with Si containing both B and P. We have shown that it can effectively be

used to counterbalance the increase of P concentration and maintain a uniform net doping along directionally solidified p-type and n-type Si crystals. When the Si feedstock contains too much B, co-doping with P and Ga allows to lower the net doping along p-type Si ingots without reducing the material yield. When the Si feedstock contains too much P, it allows to avoid the type inversion in p-type Si ingots or to limit the increase of the net doping with the solidified fraction in n-type Si ingots. Overall, the addition of Ga to the Si melt before ingot crystallization enables to tolerate higher concentrations of B and P in UMG-Si and maintain acceptable material yield and solar cells performance. This has the potential to significantly reduce the cost of UMG-Si purification, upon condition that efficient strategies are developed to suppress the aforementioned BO defect. Our study has been based exclusively on Cz-grown mono-crystalline Si ingots because, as we already mentioned, we wanted seperate out of the influence of crystal defects and also because we wanted to assess the potential of co-doped UMG-Si for high-efficiency solar cells. Because multi-crystalline Si currently dominates the global PV market, it represents the main target for UMG-Si. Multi-crystalline ingot crystallization also presents the considerable advantage for UMG-Si that leads to lower O contamination compared to Cz-Si and therefore to less severe light-induced degradation. One important further step would hence be to validate Ga co-doping with multi-crystalline Si, in order to check for possible interactions between Ga, crystal defects and/or impurities originating from the feedstock or introduced during crystallization.

Appendix : Carrier mobility data

[B] (cm^{-3})	[P] (cm^{-3})	[Ga] (cm^{-3})	μ_{maj} (cm^2/V.s)
$2.2 \times 10^{16} cm^{-3}$	$6.6 \times 10^{16} cm^{-3}$	$5.1 \times 10^{16} cm^{-3}$	216
$2.2 \times 10^{16} cm^{-3}$	$6.7 \times 10^{16} cm^{-3}$	$5.2 \times 10^{16} cm^{-3}$	231
$2.3 \times 10^{16} cm^{-3}$	$7.4 \times 10^{16} cm^{-3}$	$6.1 \times 10^{16} cm^{-3}$	222
$2.4 \times 10^{16} cm^{-3}$	$8.6 \times 10^{16} cm^{-3}$	$7.7 \times 10^{16} cm^{-3}$	222
$2.4 \times 10^{16} cm^{-3}$	$9.4 \times 10^{16} cm^{-3}$	$8.8 \times 10^{16} cm^{-3}$	223
$2.5 \times 10^{16} cm^{-3}$	$1.0 \times 10^{17} cm^{-3}$	$1.0 \times 10^{17} cm^{-3}$	221
$2.6 \times 10^{16} cm^{-3}$	$1.2 \times 10^{17} cm^{-3}$	$1.2 \times 10^{17} cm^{-3}$	216
$2.7 \times 10^{16} cm^{-3}$	$1.4 \times 10^{17} cm^{-3}$	$1.6 \times 10^{17} cm^{-3}$	209
$2.8 \times 10^{16} cm^{-3}$	$1.6 \times 10^{17} cm^{-3}$	$2.1 \times 10^{17} cm^{-3}$	203
$3.0 \times 10^{16} cm^{-3}$	$2.0 \times 10^{17} cm^{-3}$	$3.0 \times 10^{17} cm^{-3}$	173
$3.1 \times 10^{16} cm^{-3}$	$2.2 \times 10^{17} cm^{-3}$	$3.2 \times 10^{17} cm^{-3}$	199
$3.1 \times 10^{16} cm^{-3}$	$2.2 \times 10^{17} cm^{-3}$	$3.2 \times 10^{17} cm^{-3}$	203
$1.4 \times 10^{17} cm^{-3}$	$1.2 \times 10^{17} cm^{-3}$	$2.9 \times 10^{16} cm^{-3}$	226
$1.5 \times 10^{17} cm^{-3}$	$1.3 \times 10^{17} cm^{-3}$	$3.3 \times 10^{16} cm^{-3}$	208
$1.7 \times 10^{17} cm^{-3}$	$2.0 \times 10^{17} cm^{-3}$	$6.8 \times 10^{16} cm^{-3}$	177
$1.7 \times 10^{17} cm^{-3}$	$2.0 \times 10^{17} cm^{-3}$	$7.0 \times 10^{16} cm^{-3}$	176
$1.8 \times 10^{17} cm^{-3}$	$2.2 \times 10^{17} cm^{-3}$	$7.8 \times 10^{16} cm^{-3}$	169
$1.8 \times 10^{17} cm^{-3}$	$2.3 \times 10^{17} cm^{-3}$	$8.9 \times 10^{16} cm^{-3}$	160
$1.9 \times 10^{17} cm^{-3}$	$2.6 \times 10^{17} cm^{-3}$	$1.0 \times 10^{16} cm^{-3}$	148
$1.9 \times 10^{17} cm^{-3}$	$2.9 \times 10^{17} cm^{-3}$	$1.2 \times 10^{16} cm^{-3}$	125
$2.0 \times 10^{17} cm^{-3}$	$3.2 \times 10^{17} cm^{-3}$	$1.5 \times 10^{16} cm^{-3}$	104
$2.1 \times 10^{17} cm^{-3}$	$3.8 \times 10^{17} cm^{-3}$	$1.9 \times 10^{16} cm^{-3}$	73
$2.1 \times 10^{17} cm^{-3}$	$4.2 \times 10^{17} cm^{-3}$	$2.2 \times 10^{16} cm^{-3}$	58
$9.4 \times 10^{15} cm^{-3}$			441
$1.3 \times 10^{16} cm^{-3}$			424

Table 5.2: B, P and Ga concentrations and majority carrier mobility in p-type Si samples studied in this thesis.

[B] (cm^{-3})	[P] (cm^{-3})	[Ga] (cm^{-3})	μ_{maj} (cm^2/V.s)
$5.4 \times 10^{16} cm^{-3}$	$9.9 \times 10^{16} cm^{-3}$	$3.8 \times 10^{16} cm^{-3}$	472
$5.6 \times 10^{16} cm^{-3}$	$1.1 \times 10^{17} cm^{-3}$	$4.6 \times 10^{16} cm^{-3}$	439
$5.8 \times 10^{16} cm^{-3}$	$1.3 \times 10^{17} cm^{-3}$	$5.8 \times 10^{16} cm^{-3}$	419
$6.2 \times 10^{16} cm^{-3}$	$1.6 \times 10^{17} cm^{-3}$	$8.4 \times 10^{16} cm^{-3}$	381
$6.8 \times 10^{16} cm^{-3}$	$2.2 \times 10^{17} cm^{-3}$	$1.3 \times 10^{17} cm^{-3}$	308

Table 5.3: B, P and Ga concentrations and majority carrier mobility in *n*-type Si samples studied in this thesis.

[B] (cm^{-3})	[P] (cm^{-3})	[Ga] (cm^{-3})	μ_{min} (cm^2/V.s)
$2.2 \times 10^{16} cm^{-3}$	$6.7 \times 10^{16} cm^{-3}$	$5.2 \times 10^{16} cm^{-3}$	452
$2.4 \times 10^{16} cm^{-3}$	$8.6 \times 10^{16} cm^{-3}$	$7.7 \times 10^{16} cm^{-3}$	499
$2.5 \times 10^{16} cm^{-3}$	$1.0 \times 10^{17} cm^{-3}$	$1.0 \times 10^{17} cm^{-3}$	441
$2.7 \times 10^{16} cm^{-3}$	$1.3 \times 10^{17} cm^{-3}$	$1.6 \times 10^{17} cm^{-3}$	475
$3.0 \times 10^{16} cm^{-3}$	$2.0 \times 10^{17} cm^{-3}$	$2.9 \times 10^{17} cm^{-3}$	444
$1.7 \times 10^{17} cm^{-3}$	$2.0 \times 10^{17} cm^{-3}$	$6.7 \times 10^{16} cm^{-3}$	270
$1.7 \times 10^{17} cm^{-3}$	$2.0 \times 10^{17} cm^{-3}$	$7.1 \times 10^{16} cm^{-3}$	257
$1.8 \times 10^{17} cm^{-3}$	$2.4 \times 10^{17} cm^{-3}$	$8.9 \times 10^{16} cm^{-3}$	198
$1.9 \times 10^{17} cm^{-3}$	$2.8 \times 10^{17} cm^{-3}$	$1.2 \times 10^{17} cm^{-3}$	146
$1.9 \times 10^{17} cm^{-3}$	$2.9 \times 10^{17} cm^{-3}$	$1.2 \times 10^{17} cm^{-3}$	135
$2.0 \times 10^{17} cm^{-3}$	$3.2 \times 10^{17} cm^{-3}$	$1.5 \times 10^{17} cm^{-3}$	95
$2.2 \times 10^{17} cm^{-3}$	$4.3 \times 10^{17} cm^{-3}$	$2.3 \times 10^{17} cm^{-3}$	27
$1.3 \times 10^{16} cm^{-3}$			1109

Table 5.4: B, P and Ga concentrations and minority carrier mobility in *p*-type Si samples studied in this thesis.

[B] (cm^{-3})	[P] (cm^{-3})	[Ga] (cm^{-3})	μ_{min} (cm^2/V.s)
$5.4 \times 10^{16} cm^{-3}$	$9.8 \times 10^{16} cm^{-3}$	$3.8 \times 10^{16} cm^{-3}$	193
$5.6 \times 10^{16} cm^{-3}$	$1.1 \times 10^{17} cm^{-3}$	$4.6 \times 10^{16} cm^{-3}$	187
$5.8 \times 10^{16} cm^{-3}$	$1.3 \times 10^{17} cm^{-3}$	$5.9 \times 10^{16} cm^{-3}$	153
$6.2 \times 10^{16} cm^{-3}$	$1.6 \times 10^{17} cm^{-3}$	$8.3 \times 10^{16} cm^{-3}$	136
$6.8 \times 10^{16} cm^{-3}$	$2.3 \times 10^{17} cm^{-3}$	$1.4 \times 10^{17} cm^{-3}$	95

Table 5.5: B, P and Ga concentrations and minority carrier mobility in *n*-type Si samples studied in this thesis.

Bibliography

[1] D. B. climate change advisors (Deutsche bank group), "Global climate change policy tracker: An investors assessment. detailed analysis of targets by region and country," 2009.

[2] I. energy agency, "Technology roadmap - solar photovoltaic energy," 2008.

[3] N. Yuge, M. Abe, K. Hanazawa, H. Baba, N. Nakamura, Y. Kato, Y. Sakaguchi, S. Hiwasa, and F. Aratani, "Purification of metallurgical-grade silicon up to solar grade," *Progress in Photovoltaics: Research and Applications*, vol. 9, no. 3, pp. 203–209, 2001. [Online]. Available: http://dx.doi.org/10.1002/pip.372

[4] E. Enebakk, K. Friestad, R. Tronstad, C. Zahedi, and C. Dethloff, "Silicon feedstock for solar cells," Patent US 2007/0 128 099 A1, 2008.

[5] R. Einhaus, J. Kraiem, F. Cocco, Y. Caratini, D. Bernou, D. Sarti, G. Rey, R. Monna, C. Trassy, J. Degoulange, Y. Delannoy, S. Martinuzzi, I. Périchaud, M. C. Record, and P. Rivat, "Photosil - simplified production of solar silicon from metallurgical silicon," in *Proceedings of the 21st European Photovoltaic Solar Energy Conference, Dresden, Germany, WIP, Munich*, 2006.

[6] D. Sarti and R. Einhaus, "Silicon feedstock for the multi-crystalline photovoltaic industry," *Solar Energy Materials and Solar Cells*, vol. 72, no. 1 - 4, pp. 27 – 40, 2002. [Online]. Available: http://www.sciencedirect.com/science/article/pii/S0927024801001477

[7] R. K. Ray and H. Y. Fan, "Impurity conduction in silicon," *Phys. Rev.*, vol. 121, pp. 768–779, Feb 1961. [Online]. Available: http://link.aps.org/doi/10.1103/PhysRev.121.768

[8] D. M. Luz, S. S. Makler, and E. V. Anda, "The compensation effect in the impurity band of doped semiconductors," *Journal of Physics C: Solid State Physics*, vol. 21, no. 29, p. 5149, 1988. [Online]. Available: http://stacks.iop.org/0022-3719/21/i=29/a=012

[9] M. Levy, P. Y. Yu, Y. Zhang, and M. P. Sarachik, "Photoluminescence of heavily doped, compensated si:p,b," *Phys. Rev. B*, vol. 49, no. 3, pp. 1677–1684, Jan 1994.

[10] J. Libal, S. Novaglia, M. Acciarri, S. Binetti, R. Petres, J. Arumughan, R. Kopecek, and A. Prokopenko, "Effect of compensation and of metallic

impurities on the electrical properties of cz-grown solar grade silicon," *Journal of Applied Physics*, vol. 104, no. 10, p. 104507, 2008. [Online]. Available: http://link.aip.org/link/?JAP/104/104507/1

[11] S. Dubois, N. Enjalbert, and J. P. Garandet, "Effects of the compensation level on the carrier lifetime of crystalline silicon," *Applied Physics Letters*, vol. 93, no. 3, p. 032114, 2008. [Online]. Available: http://link.aip.org/link/?APL/93/032114/1

[12] R. Swanson and R. Sinton, "High-efficiency silicon solar cells," in *Advances in solar energy*, B. C. Karl W. Boer, American solar energy society Inc., Ed., 1990, pp. 427–484.

[13] J. Kraiem, R. Einhaus, and H. Lauvray, "Doping engineering as a method to increase the performance of purified mg silicon during ingot crystallization," in *Proceedings of the 34th IEEE Photovoltaic Specialists Conference, Philadelphia*, 2009.

[14] J. Veirman, S. Dubois, N. Enjalbert, J.-P. Garandet, and M. Lemiti, "Electronic properties of highly-doped and compensated solar-grade silicon wafers and solar cells," *Journal of Applied Physics*, vol. 109, no. 10, p. 103711, 2011. [Online]. Available: http://link.aip.org/link/?JAP/109/103711/1

[15] J. Libal, M. Acciarri, S. Binetti, R. Kopecek, R. Petres, C. Knopf, and K. Wambach, "Effect of extended defects on the electrical properties of compensated solar grade multicrystalline silicon," in *Proceedings of the 23rd European Photovoltaic Solar Energy Conference, Valencia, Spain*, W. Munich, Ed., 2008.

[16] R. Søndenå, A. Holt, and A.-K. Søiland, "Electrical properties of compensated n- and p-type monocrystalline silicon," in *Proceedings of the 26th European Photovoltaic Solar Energy Conference, Hamburg, Germany, WIP Munich*, W. Munich, Ed., 2011.

[17] J. Veirman, S.Dubois, N.Enjalbert, J. Garandet, B.Martel, D.Heslinga, J.Kraiem, I.Périchaud, and S.Martinuzzi, "B-p compensation in sog silicon: Cure or curse?" in *Proceedings of the 24th European Photovoltaic Solar Energy Conference, Hamburg, Germany*, W. Munich, Ed., 2009.

[18] D. Macdonald, F. Rougieux, A. Cuevas, B. Lim, J. Schmidt, M. D. Sabatino, and L. J. Geerligs, "Light-induced boron-oxygen defect generation in compensated p-type czochralski silicon," *Journal of Applied Physics*, vol. 105, no. 9, p. 093704, 2009. [Online]. Available: http://link.aip.org/link/?JAP/105/093704/1

[19] H. Schlangenotto, H. Maeder, and W. Gerlach, "Temperature dependence of the radiative recombination coefficient in silicon," *physica status solidi (a)*, vol. 21, no. 1, pp. 357–367, 1974. [Online]. Available: http://dx.doi.org/10.1002/pssa.2210210140

[20] M. Tyagi and R. V. Overstraeten, "Minority carrier recombination in heavily-doped silicon," *Solid-State Electronics*, vol. 26, no. 6, pp. 577 – 597, 1983. [Online]. Available: http://www.sciencedirect.com/science/article/pii/0038110183901740

[21] J. Dziewior and W. Schmid, "Auger coefficients for highly doped and highly excited silicon," *Applied Physics Letters*, vol. 31, no. 5, pp. 346–348, 1977. [Online]. Available: http://link.aip.org/link/?APL/31/346/1

[22] R. Sinton and R. Swanson, "Recombination in highly injected silicon," *Electron Devices, IEEE Transactions on*, vol. 34, no. 6, pp. 1380 – 1389, jun 1987.

[23] P. P. Altermatt, J. Schmidt, G. Heiser, and A. G. Aberle, "Assessment and parameterisation of coulomb-enhanced auger recombination coefficients in lowly injected crystalline silicon," *Journal of Applied Physics*, vol. 82, no. 10, pp. 4938–4944, 1997. [Online]. Available: http://link.aip.org/link/?JAP/82/4938/1

[24] M. J. Kerr and A. Cuevas, "General parameterization of auger recombination in crystalline silicon," *Journal of Applied Physics*, vol. 91, no. 4, pp. 2473–2480, 2002. [Online]. Available: http://link.aip.org/link/?JAP/91/2473/1

[25] D. Macdonald and A. Cuevas, "Recombination in compensated crystalline silicon for solar cells," *Journal of Applied Physics*, vol. 109, no. 4, p. 043704, 2011. [Online]. Available: http://link.aip.org/link/?JAP/109/043704/1

[26] W. Shockley and W. T. Read, "Statistics of the recombinations of holes and electrons," *Phys. Rev.*, vol. 87, no. 5, pp. 835–842, Sep 1952.

[27] R. N. Hall, "Electron-hole recombination in germanium," *Phys. Rev.*, vol. 87, pp. 387–387, Jul 1952. [Online]. Available: http://link.aps.org/doi/10.1103/PhysRev.87.387

[28] D. Macdonald and A. Cuevas, "Validity of simplified shockley-read-hall statistics for modeling carrier lifetimes in crystalline silicon," *Phys. Rev. B*, vol. 67, p. 075203, Feb 2003. [Online]. Available: http://link.aps.org/doi/10.1103/PhysRevB.67.075203

[29] S. Dubois, "Influence des interactions impureté-défaut et impureté-impureté sur le rendement de conversion des cellules photovoltaïques au silicium cristallin," Ph.D. dissertation, Université Paul-Cézane, Aix-Marseille, 2007.

[30] E. R. Weber, "Transition metals in silicon," *Applied Physics A: Materials Science & Processing*, vol. 30, pp. 1–22, 1983, 10.1007/BF00617708. [Online]. Available: http://dx.doi.org/10.1007/BF00617708

[31] A. Istratov, H. Hieslmair, and E. Weber, "Iron and its complexes in silicon," *Applied Physics A: Materials Science & Processing*, vol. 69, pp. 13–44, 1999, 10.1007/s003390050968. [Online]. Available: http://dx.doi.org/10.1007/s003390050968

[32] D. Macdonald, P. Rosenits, and P. N. K. Deenapanray, "Recombination activity of manganese in p- and n-type crystalline silicon," *Semiconductor Science and Technology*, vol. 22, no. 2, p. 163, 2007. [Online]. Available: http://stacks.iop.org/0268-1242/22/i=2/a=028

[33] D. Macdonald and L. J. Geerligs, "Recombination activity of interstitial iron and other transition metal point defects in p- and n-article crystalline silicon," *Applied Physics Letters*, vol. 85, no. 18, pp. 4061–4063, 2004. [Online]. Available: http://dx.doi.org/10.1063/1.1812833

[34] C.-T. Sah, P. C. H. Chan, C.-K. Wang, R.-Y. Sah, K. Yamakawa, and R. Lutwack, "Effect of zinc impurity on silicon solar-cell efficiency," *Electron Devices, IEEE Transactions on*, vol. 28, no. 3, pp. 304 – 313, mar 1981.

[35] J. E. Birkholz, K. Bothe, D. Macdonald, and J. Schmidt, "Electronic properties of iron-boron pairs in crystalline silicon by temperature- and injection-level-dependent lifetime measurements," *Journal of Applied Physics*, vol. 97, no. 10, p. 103708, 2005. [Online]. Available: http://link.aip.org/link/?JAP/97/103708/1

[36] S. Rein and S. W. Glunz, "Electronic properties of interstitial iron and iron-boron pairs determined by means of advanced lifetime spectroscopy," *Journal of Applied Physics*, vol. 98, no. 11, p. 113711, 2005. [Online]. Available: http://link.aip.org/link/?JAP/98/113711/1

[37] D. Macdonald, A. Cuevas, and J. Wong-Leung, "Capture cross sections of the acceptor level of iron–boron pairs in p-type silicon by injection-level dependent lifetime measurements," *Journal of Applied Physics*, vol. 89, no. 12, pp. 7932–7939, 2001. [Online]. Available: http://link.aip.org/link/?JAP/89/7932/1

[38] D. Macdonald, T. Roth, P. N. K. Deenapanray, T. Trupke, and R. A. Bardos, "Doping dependence of the carrier lifetime crossover point upon dissociation of iron-boron pairs in crystalline silicon," *Applied Physics Letters*, vol. 89, no. 14, p. 142107, 2006. [Online]. Available: http://link.aip.org/link/?APL/89/142107/1

[39] K. Bothe and J. Schmidt, "Electronically activated boron-oxygen-related recombination centers in crystalline silicon," *Journal of Applied Physics*, vol. 99, no. 1, p. 013701, 2006. [Online]. Available: http://link.aip.org/link/?JAP/99/013701/1

[40] S. Rein and S. W. Glunz, "Electronic properties of the metastable defect in boron-doped czochralski silicon: Unambiguous determination by advanced lifetime spectroscopy," *Applied Physics Letters*, vol. 82, no. 7, pp. 1054–1056, 2003. [Online]. Available: http://link.aip.org/link/?APL/82/1054/1

[41] J. Schmidt and A. Cuevas, "Electronic properties of light-induced recombination centers in boron-doped czochralski silicon," *Journal of Applied Physics*, vol. 86, no. 6, pp. 3175–3180, 1999. [Online]. Available: http://link.aip.org/link/?JAP/86/3175/1

[42] J. Schmidt and K. Bothe, "Structure and transformation of the metastable boron- and oxygen-related defect center in crystalline silicon," *Phys. Rev. B*, vol. 69, no. 2, p. 024107, Jan 2004.

[43] K. Bothe, R. Sinton, and J. Schmidt, "Fundamental boron-oxygen-related carrier lifetime limit in mono- and multicrystalline silicon," *Progress in Photovoltaics:*

Research and Applications, vol. 13, no. 4, pp. 287–296, 2005. [Online]. Available: http://dx.doi.org/10.1002/pip.586

[44] R. Kopecek, J. Arumughan, K. Peter, E. A. Good, J. Libal, M. Acciarri, and S. Binetti, "Crystalline si solar cells from compensated material: behaviour of light-induced degradation," in *Proceedings of the 23rd European Photovoltaic Solar Energy Conference, Valencia, Spain*, W. Munich, Ed., 2008.

[45] D. Macdonald, A. Liu, F. Rougieux, A. Cuevas, B. Lim, J. Schmidt., M. D. Sabatino, and L. Geerligs, "Boron-oxygen defects in compensated p-type czochralski silicon," in *Proceedings of the 24th European Photovoltaic Solar Energy Conference, Hamburg, Germany, WIP, Munich*, 2009.

[46] B. Lim, F. Rougieux, D. Macdonald, K. Bothe, and J. Schmidt, "Generation and annihilation of boron–oxygen-related recombination centers in compensated p- and n-type silicon," *Journal of Applied Physics*, vol. 108, no. 10, p. 103722, 2010. [Online]. Available: http://link.aip.org/link/?JAP/108/103722/1

[47] S. Rein, W. Kwapil, J. Geilker, G. Emanuel, M. Spitz, I. Reis, A. Weil, D. Biro, M. Glatthaar, A.-K. Soiland, E. Enebakk, and R. Tronstad, "Impact of compensated solar-grade silicon on czochralski silicon wafers and solar cells," in *Proceedings of the 24th European Photovoltaic Solar Energy Conference, Hamburg, Germany*, W. Munich, Ed., 2009.

[48] J. Geilker, W. Kwapil, and S. Rein, "Light-induced degradation in compensated p- and n-type czochralski silicon wafers," *Journal of Applied Physics*, vol. 109, no. 5, p. 053718, 2011. [Online]. Available: http://link.aip.org/link/?JAP/109/053718/1

[49] V. V. Voronkov and R. Falster, "Latent complexes of interstitial boron and oxygen dimers as a reason for degradation of silicon-based solar cells," *Journal of Applied Physics*, vol. 107, no. 5, p. 053509, 2010. [Online]. Available: http://link.aip.org/link/?JAP/107/053509/1

[50] T. Schutz-Kuchly, J. Veirman, S. Dubois, and D. R. Heslinga, "Light-induced-degradation effects in boron–phosphorus compensated n-type czochralski silicon," *Applied Physics Letters*, vol. 96, no. 9, p. 093505, 2010. [Online]. Available: http://link.aip.org/link/?APL/96/093505/1

[51] F. E. Rougieux, B. Lim, J. Schmidt, M. Forster, D. Macdonald, and A. Cuevas, "Influence of net doping, excess carrier density and annealing on the boron oxygen related defect density in compensated n-article silicon," *Journal of Applied Physics*, vol. 110, no. 6, p. 063708, 2011. [Online]. Available: http://dx.doi.org/10.1063/1.3633492

[52] F. E. Rougieux, M. Forster, D. Macdonald, A. Cuevas, B. Lim, and J. Schmidt, "Recombination activity and impact of the boron-oxygen-related defect in compensated n-type silicon," *Photovoltaics, IEEE Journal of*, vol. 1, no. 1, pp. 54 –58, july 2011.

[53] V. V. Voronkov, R. Falster, K. Bothe, B. Lim, and J. Schmidt, "Lifetime-degrading boron-oxygen centres in p-type and n-type compensated silicon," *Journal of Applied Physics*, vol. 110, no. 6, p. 063515, 2011. [Online]. Available: http://link.aip.org/link/?JAP/110/063515/1

[54] F. Rougieux, "Impact of dopant compensation on the electrical properties of silicon for solar cell applications," Ph.D. dissertation, The Australian National University, Canberra, 2012.

[55] S. M. Sze and K. K. Ng, *Physics of Semiconductor devices*, 3rd ed. Wiley Interscience, 2007.

[56] D. B. M. Klaassen, "A unified mobility model for device simulation - ii. temperature dependence of carrier mobility and lifetime," *Solid-State Electronics*, vol. 35, no. 7, pp. 961 – 967, 1992. [Online]. Available: http://www.sciencedirect.com/science/article/B6TY5-46VMC8J-MM/2/a6af4e017a6529d011f3c7da987bb9be

[57] ——, "A unified mobility model for device simulation - i. model equations and concentration dependence," *Solid-State Electronics*, vol. 35, no. 7, pp. 953 – 959, 1992. [Online]. Available: http://www.sciencedirect.com/science/article/B6TY5-46VMC8J-MK/2/36b0b3c849509819d12e002d345d634b

[58] F. Mousty, P. Ostoja, and L. Passari, "Relationship between resistivity and phosphorus concentration in silicon," *Journal of Applied Physics*, vol. 45, no. 10, pp. 4576–4580, 1974. [Online]. Available: http://link.aip.org/link/?JAP/45/4576/1

[59] L. C. Linares and S. S. Li, "An improved model for analyzing hole mobility and resistivity in p-type silicon doped with boron, gallium, and indium," *Journal of The Electrochemical Society*, vol. 128, no. 3, pp. 601–608, 1981. [Online]. Available: http://jes.ecsdl.org/content/128/3/601.abstract

[60] A. Cuevas, "The paradox of compensated silicon," in *Proceedings of the Conference on Optoelectronic and Microelectronic Materials and Devices*, 2008.

[61] W. R. Thurber, R. L. Mattis, Y. M. Liu, and J. J. Filliben, "Resistivity-dopant density relationship for boron-doped silicon," *Journal of the Electrochemical Society*, vol. 127, p. 2291, 1980.

[62] N. D. Arora, J. R. Hauser, and D. J. Roulston, "Electron and hole mobilities in silicon as a function of concentration and temeperature," *IEEE Transactions on electron devices*, vol. 29, no. 2, pp. 292–295, February 1982.

[63] D. Macdonald, A. Cuevas, and L. J. Geerligs, "Measuring dopant concentrations in compensated p-type crystalline silicon via iron-acceptor pairing," *Applied Physics Letters*, vol. 92, no. 20, p. 202119, 2008. [Online]. Available: http://link.aip.org/link/?APL/92/202119/1

[64] M. Tajima, T. Iwai, H. Toyota, S. Binetti, and D. Macdonald, "Donor - acceptor pair luminescence in compensated si for solar cells," *Journal of Applied Physics*, vol. 110, no. 4, p. 043506, 2011. [Online]. Available: http://link.aip.org/link/?JAP/110/043506/1

[65] R. A. Sinton and A. Cuevas, "Contactless determination of current–voltage characteristics and minority-carrier lifetimes in semiconductors from quasi-steady-state photoconductance data," *Applied Physics Letters*, vol. 69, no. 17, pp. 2510–2512, 1996. [Online]. Available: http://link.aip.org/link/?APL/69/2510/1

[66] J. Veirman, S. Dubois, N. Enjalbert, and M. Lemiti, "A fast and easily implemented method for interstitial oxygen concentration mapping through the activation of thermal donors in silicon." *Energy Procedia*, vol. 8, no. 0, pp. 41 – 46, 2011, <ce:title>Proceedings of the SiliconPV 2011 Conference (1st International Conference on Crystalline Silicon Photovoltaics)</ce:title>. [Online]. Available: http://www.sciencedirect.com/science/article/pii/S1876610211016080

[67] S. Reggiani, M. Valdinoci, L. Colalongo, M. Rudan, G. Baccarani, A. Stricker, F. Illien, N. Felber, W. Fichtner, and L. Zullino, "Electron and hole mobility in silicon at large operating temperatures. i. bulk mobility," *Electron Devices, IEEE Transactions on*, vol. 49, no. 3, pp. 490 –499, mar 2002.

[68] G. Masetti, M. Severi, and S. Solmi, "Modeling of carrier mobility against carrier concentration in arsenic-, phosphorus-, and boron-doped silicon," *IEEE Transactions on electron devices*, vol. 30, no. 7, pp. 764–769, July 1983.

[69] D. Caughey and R. Thomas, "Carrier mobilities in silicon empirically related to doping and field," *Proceedings of the IEEE*, vol. 55, no. 12, pp. 2192 – 2193, dec. 1967.

[70] J. Veirman, S. Dubois, N. Enjalbert, J. Garandet, D. Heslinga, and M. Lemiti, "Hall mobility reduction in single-crystalline silicon gradually compensated by thermal donors activation," *Solid-State Electronics*, vol. 54, no. 6, pp. 671 – 674, 2010. [Online]. Available: http://www.sciencedirect.com/science/article/B6TY5-4YHSCM7-1/2/b9488d65cc90d555ca1eb10a917e1b41

[71] J. Veirman, S. Dubois, N. Enjalbert, J. P. Garandet, D. R. Heslinga, and M. Lemiti, "Hall mobility drops in disordered boron-doped czochralski silicon compensated by thermal donors activation," *physica status solidi (c)*, vol. 8, no. 3, pp. 729–732, 2011. [Online]. Available: http://dx.doi.org/10.1002/pssc.201000223

[72] F. E. Rougieux, D. Macdonald, A. Cuevas, S. Ruffell, J. Schmidt, B. Lim, and A. P. Knights, "Electron and hole mobility reduction and hall factor in phosphorus-compensated p-type silicon," *Journal of Applied Physics*, vol. 108, no. 1, p. 013706, 2010. [Online]. Available: http://link.aip.org/link/?JAP/108/013706/1

[73] F. Rougieux, D. Macdonald, and A. Cuevas, "Transport properties of p-type compensated silicon at room temperature," *Progress in Photovoltaics: Research*

and Applications, vol. 19, no. 7, pp. 787–793, 2011. [Online]. Available: http://dx.doi.org/10.1002/pip.1036

[74] B. Lim, M. Wolf, and J. Schmidt, "Carrier mobilities in multicrystalline silicon wafers made from umg-si," *physica status solidi (c)*, vol. 8, no. 3, pp. 835–838, 2011. [Online]. Available: http://dx.doi.org/10.1002/pssc.201000144

[75] J. Geilker, W. Kwapil, I. Reis, and S. Rein, "Doping concentration and mobility in compensated material: comparison of different determination methods," in *Proceedings of the 25th European Photovoltaic Solar Energy Conference, Valencia, Spain*, W. Munich, Ed., 2010.

[76] F. Schindler, J. Broisch, W. Kwapil, J. Giesecke, M. Schubert, and W. Warta, "Conductivity mobility and hall mobility in compensated multicrystalline silicon," in *Proceedings of the 25th European Photovoltaic Solar Energy Conference, Valencia*, W. Munich, Ed., 2010.

[77] F. Schindler, M. C. Schubert, A. Kimmerle, J. Broisch, S. Rein, W. Kwapil, and W. Warta, "Modeling majority carrier mobility in compensated crystalline silicon for solar cells," *Solar Energy Materials and Solar Cells*, no. 0, pp. –, 2012. [Online]. Available: http://www.sciencedirect.com/science/article/pii/S0927024812002966

[78] C. Xiao, D. Yang, X. Yu, X. Gu, and D. Que, "Influence of the compensation level on the performance of p-type crystalline silicon solar cells: Theoretical calculations and experimental study," *Solar Energy Materials and Solar Cells, In press*, 2012. [Online]. Available: http://www.sciencedirect.com/science/article/pii/S0927024812003492

[79] S. Pizzini and C. Calligarich, "On the effect of impurities on the photovoltaic behavior of solar-grade silicon," *Journal of the Electrochemical society*, vol. 131, p. 2128, september 1984.

[80] J. Veirman, S. Dubois, J. Stendera, B. Martel, N. Enjalbert, and T. Desrues, "Mapping of the dopant compensation effects on the reverse and forward characteristics of solar cells," in *Proceedings 38th IEEE Photovoltaic Specialists Conference, Austin, Texas*, 2012.

[81] D. Kohler, B. Raabe, S. Braun, S. Seren, and G. Hahn, "Upgraded metallurgical grade silicon solar cells: a detailed material analysis," in *Proceedings of the 24th European Photovoltaic Solar Energy Conference, Hamburg, Germany*, W. Munich, Ed., 2009.

[82] J. Kraiem, R. Einhaus, F. Lissalde, S. Dubois, N. Enjalbert, B. Drevet, F. Servant, and D. Camel, "Innovative crystallisation of multi-crystalline silicon ingots from different types of silicon feedstock," in *Proceedings of the 23rd European Photovoltaic Solar Energy Conference, Valencia, Spain*, W. Munich, Ed., 2008.

[83] B. Drevet, D. Camel, N. Enjalbert, J. Veirman, J. Kraiem, F. Cocco, E. Flahaut, B. Marie, and I. Périchaud, "Segregation and crystallization of purified metallurgical

grade silicon: influence of process parameters on yield and solar cell efficiency," in *Proceedings of the 25th European Photovoltaic Solar Energy Conference, Valencia, Spain*, W. Munich, Ed., 2010.

[84] K. Peter, R. Kopecek, E. Enebakk, A. Soiland, and S. Grandum, "Towards 17efficient multicrystalline solar grade silicon solar cells," in *Proceedings of the 25th European Photovoltaic Solar Energy Conference, Valencia*, W. Munich, Ed., 2010.

[85] J. Kraiem, B. Drevet, F. Cocco, N. Enjalbert, S. Dubois, D. Camel, D. Grosset-Bourbange, D. Pelletier, T. Margaria, and R. Einhaus, "High performance solar cells made from 100process," in *Proceedings of the 35th IEEE Photovoltaic Specialists Conference, Hawaï*, 2010.

[86] A. Halm, J. Jourdan, S. Nichol, B. Ryningen, H. Tathgar, and R. Kopecek, "Detailed study on large area 100efficiencies exceeding 16percent," in *Proceedings of the 25th European Photovoltaic Solar Energy Conference, Valencia, Spain*, W. Munich, Ed., 2010.

[87] P. Engelhart, J. Wendt, A. Schulze, C. Klenke, A. Mohr, K. Petter, F. Stenzel, S. Hörnlein, M. Kauert, M. Junghänel, B. Barkenfelt, S. Schmidt, D. Rychtarik, M. Fischer, J. Müller, and P. Wawer, "R&d pilot line production of multicrystalline si solar cells exceeding cell efficiencies of 18<ce:title>Proceedings of the SiliconPV 2011 Conference (1st International Conference on Crystalline Silicon Photovoltaics)</ce:title>. [Online]. Available: http://www.sciencedirect.com/science/article/pii/S1876610211016511

[88] R. Einhaus, J. Kraiem, J. Degoulange, O. Nichiporuk, M. Forster, P. Papet, Y. Andrault, D. Grosset-Bourbange, and F. Cocco, "19heterojunction solar cells on cz wafers from non-blended upgraded metallurgical silicon," in *Proceedings 38th IEEE Photovoltaic Specialists Conference, Austin, Texas*, 2012.

[89] S. Mahadevan, S. M. Hardas, and G. Suryan, "Electrical breakdown in semiconductors," *physica status solidi (a)*, vol. 8, no. 2, pp. 335–374, 1971. [Online]. Available: http://dx.doi.org/10.1002/pssa.2210080202

[90] O. Breitenstein, J. Bauer, K. Bothe, W. Kwapil, D. Lausch, U. Rau, J. Schmidt, M. Schneemann, M. C. Schubert, J.-M. Wagner, and W. Warta, "Understanding junction breakdown in multicrystalline solar cells," *Journal of Applied Physics*, vol. 109, no. 7, p. 071101, 2011. [Online]. Available: http://link.aip.org/link/?JAP/109/071101/1

[91] M. Wagner, B. Gründig-Wendrock, P. Palinginis, and C. Knopf, "Shunts, diode breakdown and high reverse currents in multicrystalline silicon solar cells," in *Proceedings of the 24th European Photovoltaic Solar Energy Conference, Hamburg, Germany*, 2009.

[92] W. Kwapil, M. Wagner, M. C. Schubert, and W. Warta, "High net doping concentration responsible for critical diode breakdown behavior of upgraded metallurgical grade multicrystalline silicon solar cells," *Journal of Applied Physics*, vol. 108, no. 2, p. 023708, 2010. [Online]. Available: http://link.aip.org/link/?JAP/108/023708/1

[93] F. Tanay, S. Dubois, N. Enjalbert, and J. Veirman, "Low temperature-coefficient for solar cells processed from solar-grade silicon purified by metallurgical route," *Progress in Photovoltaics: Research and Applications*, vol. 19, no. 8, pp. 966–972, 2011. [Online]. Available: http://dx.doi.org/10.1002/pip.1104

[94] K. Petter, M. Strobel, D. Buss, M. Mette, Y. Ludwig, S. Malik, S. Rupp, and P. Wawer, "Long term stability of solar modules made from compensated sog-si or umg-si solar cells," *Energy Procedia*, vol. 8, no. 0, pp. 365 – 370, 2011, <ce:title>Proceedings of the SiliconPV 2011 Conference (1st International Conference on Crystalline Silicon Photovoltaics)</ce:title>. [Online]. Available: http://www.sciencedirect.com/science/article/pii/S1876610211016602

[95] J. Czochralski, "Ein neues verfahren zur messung der kristallisations-geschwindigkeit der metalle," *Z. Phys. Chem.*, vol. 92, p. 219, 1918.

[96] W. C. Dash, "Silicon crystals free of dislocations," *Journal of Applied Physics*, vol. 29, no. 4, pp. 736–737, 1958. [Online]. Available: http://link.aip.org/link/?JAP/29/736/1

[97] V. V. Voronkov and R. Falster, "Vacancy and self-interstitial concentration incorporated into growing silicon crystals," *Journal of Applied Physics*, vol. 86, no. 11, pp. 5975–5982, 1999. [Online]. Available: http://link.aip.org/link/?JAP/86/5975/1

[98] K. Hoshi, N. Isawa, T. Suzuki, and Y. Ohkubo, "Czochralski silicon crystals grown in a transverse magnetic field," *Journal of The Electrochemical Society*, vol. 132, no. 3, pp. 693–700, 1985. [Online]. Available: http://jes.ecsdl.org/content/132/3/693.abstract

[99] R. Einhaus, J. Kraiem, F. Lissalde, and R. Monna, "Innovative crystallization of multi-crystalline silicon," in *Proceedings of the 17th Photovotaics Science and Engineering Conference, Japan*, 2007.

[100] D. Viechnicki and F. Schmid, "Growth of large monocrystals of al2o3 by a gradient furnace technique," *Journal of Crystal Growth*, vol. 11, no. 3, pp. 345 – 347, 1971. [Online]. Available: http://www.sciencedirect.com/science/article/pii/0022024871901072

[101] R. A. Seilheimer, "Silicon phase diagrams," in *Handbook of semiconductor silicon technology*, W. C. O'Mara, R. B. Herring, and N. J. Lee P. Hunt, Noyes publications, Eds., 1990.

[102] F. A. Trumbore, "Solid solubility of impurity elements in germanium and silicon," *Bell system technical journal*, vol. 39, p. 205, 1960.

[103] E. Scheil, "Bemerkungen zur schichtkristallbildung," *Z. metallk.*, vol. 34, p. 70, 1942.

[104] Z. Xi, J. Tang, H. Deng, D. Yang, and D. Que, "A model for distribution of oxygen in multicrystalline silicon ingot grown by directional solidification," *Solar Energy Materials and Solar Cells*, vol. 91, no. 18, pp. 1688 – 1691, 2007. [Online]. Available: http://www.sciencedirect.com/science/article/pii/S0927024807002231

[105] J. A. Burton, R. C. Prim, and W. P. Slichter, "The distribution of solute in crystals grown from the melt. part i. theoretical," *The Journal of Chemical Physics*, vol. 21, no. 11, pp. 1987–1991, 1953. [Online]. Available: http://link.aip.org/link/?JCP/21/1987/1

[106] Y. Sato, T. Nishizuka, K. Hara, T. Yamamura, and Y. Waseda, "Density measurement of molten silicon by a pycnometric method," *International Journal of Thermophysics*, vol. 21, pp. 1463–1471, 2000, 10.1023/A:1006661511770. [Online]. Available: http://dx.doi.org/10.1023/A:1006661511770

[107] H. Sasaki, E. Tokizaki, X. M. Huang, K. Terashima, and S. Kimura, "Temperature dependence of the viscosity of molten silicon measured by the oscillating cup method," *Japanese Journal of Applied Physics*, vol. 34, no. Part 1, No. 7A, pp. 3432–3436, 1995. [Online]. Available: http://jjap.ipap.jp/link?JJAP/34/3432/

[108] E. Enebakk, A. Soiland, J. Akedal, and R. Tronstad, "Dopant specification of compensated silicon for solar cells of equal efficiency and yield as standard solar cells," in *Proceedings of the 3rd Intenational Workshop on Crystalline Silicon Solar Cells, SINTEF/NTNU, Trondheim, Norway*, June 2009.

[109] S. Pizzini, L. Giarda, A. Parisi, A. Solmi, G. Soncini, and C. Calligarich, in *Proceedings of the 14th IEEE Photovoltaic Specialists Conference, San Diego*, 1980.

[110] P. Wagner and J. Hage, "Thermal double donors in silicon," *Applied Physics A: Materials Science & Processing*, vol. 49, pp. 123–138, 1989, 10.1007/BF00616290. [Online]. Available: http://dx.doi.org/10.1007/BF00616290

[111] F. Szmulowicz, "Calculation of the mobility and the hall factor for doped p-type silicon," *Phys. Rev. B*, vol. 34, no. 6, pp. 4031–4047, Sep 1986.

[112] E. Ohta and M. Sakata, "Temperature dependence of hall factor in low-compensated n-type silicon," *Japanese Journal of Applied Physics*, vol. 17, no. 10, pp. 1795–1804, 1978. [Online]. Available: http://jjap.jsap.jp/link?JJAP/17/1795/

[113] A. B. Sproul, M. A. Green, and A. W. Stephens, "Accurate determination of minority carrier- and lattice scattering-mobility in silicon from photoconductance decay," *Journal of Applied Physics*, vol. 72, no. 9, pp. 4161–4171, 1992. [Online]. Available: http://link.aip.org/link/?JAP/72/4161/1

[114] A. W. Stephens and M. A. Green, "Minority carrier mobility of czochralski-grown silicon by microwave-detected photoconductance decay," *Journal of Applied Physics*, vol. 74, no. 10, pp. 6212–6216, 1993. [Online]. Available: http://link.aip.org/link/?JAP/74/6212/1

[115] M. A. Green, “Intrinsic concentration, effective densities of states, and effective mass in silicon,” *Journal of Applied Physics*, vol. 67, no. 6, pp. 2944–2954, 1990. [Online]. Available: http://link.aip.org/link/?JAP/67/2944/1

[116] N. F. Mott, “Metal-insulator transition,” *Rev. Mod. Phys.*, vol. 40, no. 4, pp. 677–683, Oct 1968.

[117] P. P. Altermatt, A. Schenk, and G. Heiser, “A simulation model for the density of states and for incomplete ionization in crystalline silicon. i. establishing the model in si:p,” *Journal of Applied Physics*, vol. 100, no. 11, p. 113714, 2006. [Online]. Available: http://link.aip.org/link/?JAP/100/113714/1

[118] P. P. Altermatt, A. Schenk, B. Schmithüsen, and G. Heiser, “A simulation model for the density of states and for incomplete ionization in crystalline silicon. ii. investigation of si:as and si:b and usage in device simulation,” *Journal of Applied Physics*, vol. 100, no. 11, p. 113715, 2006. [Online]. Available: http://link.aip.org/link/?JAP/100/113715/1

[119] K. B. Wolfstirn, “Hole and electron mobilities in doped silicon from radiochemical and conductivity measurements,” *Journal of Physics and Chemistry of Solids*, vol. 16, no. 3-4, pp. 279 – 284, 1960. [Online]. Available: http://www.sciencedirect.com/science/article/B6TXR-46M72SS-5G/2/a1288159a11cdfbb366116c337bd4ce3

[120] D. W. Fischer and J. J. Rome, “Additional structure in infrared excitation spectra of group-iii acceptors in silicon,” *Phys. Rev. B*, vol. 27, no. 8, pp. 4826–4832, Apr 1983.

[121] T. Hoshikawa, T. Taishi, K. Hoshikawa, I. Yonenaga, and S. Uda, “Temperature dependences of acceptor concentration, conductivity mobility, and resistivity of ga-doped czochralski-si crystals,” *Japanese Journal of Applied Physics*, vol. 48, no. 3, p. 031102, 2009. [Online]. Available: http://jjap.jsap.jp/link?JJAP/48/031102/

[122] E. Fourmond, M. Forster, R. Einhaus, H. Lauvray, J. Kraiem, and M. Lemiti, “Electrical properties of boron, phosphorus and gallium co-doped silicon,” *Energy Procedia*, vol. 8, no. 0, pp. 349 – 354, 2011, <ce:title>Proceedings of the SiliconPV 2011 Conference (1st International Conference on Crystalline Silicon Photovoltaics)</ce:title>. [Online]. Available: http://www.sciencedirect.com/science/article/pii/S1876610211016572

[123] A. Herguth, G. Schubert, M. Kaes, and G. Hahn, “Investigations on the long time behavior of the metastable boron-oxygen complex in crystalline silicon,” *Progress in Photovoltaics: Research and Applications*, vol. 16, no. 2, pp. 135–140, 2008.

[124] F. Dannhäuser, J. Krausse, and K. Mayer, “Zum einfluss von temperprozessen auf widerstandsschwankungen in siliziumeinkristallen,” *Solid-State Electronics*, vol. 15, no. 12, pp. 1383 – 1384, 1972. [Online]. Available: http://www.sciencedirect.com/science/article/pii/0038110172901335

[125] J. Krausse, "Die abhängigkeit der trägerbeweglichkeit in silizium von der konzentration der freien ladungstrager - ii," *Solid-State Electronics*, vol. 15, no. 12, pp. 1377 – 1381, 1972. [Online]. Available: http://www.sciencedirect.com/science/article/pii/0038110172901323

[126] P. P. Altermatt, J. Schmidt, M. J. Kerr, G. Heiser, and A. G. Aberle, "Exciton-enhanced auger recombination in crystalline silicon under intermediate and high injection conditions," in *Proceedings of the 16th European Photovoltaic Solar Energy Conference, Glasgow, Wales*, 2000.

[127] F. Rougieux, P. Zheng, M. Thiboust, J. Tan, N. Grant, D. Macdonald, and A. Cuevas, "A contactless method for determining the carrier mobility sum in silicon wafers," *Photovoltaics, IEEE Journal of*, vol. 2, no. 1, pp. 41 –46, jan. 2012.

[128] S. W. Glunz, S. Rein, J. Knobloch, W. Wettling, and T. Abe, "Comparison of boron- and gallium-doped p-type czochralski silicon for photovoltaic application," *Progress in Photovoltaics: Research and Applications*, vol. 7, no. 6, pp. 463–469, 1999. [Online]. Available: http://dx.doi.org/10.1002/(SICI)1099-159X(199911/12)7:6<463::AID-PIP293>3.0.CO;2-H

[129] M. Dhamrin, K. Kamisako, T. Saitoh, T. Eguchi, T. Hirasawa, and I. Yamaga, "Effect of low segregation coefficient on ga-doped multicrystalline silicon solar cell performance," *Progress in Photovoltaics: Research and Applications*, vol. 13, no. 7, pp. 597–606, 2005. [Online]. Available: http://dx.doi.org/10.1002/pip.620

[130] V. Meemongkolkiat, K. Nakayashiki, A. Rohatgi, G. Crabtree, J. Nickerson, and T. L. Jester, "Resistivity and lifetime variation along commercially grown ga- and b-doped czochralski si ingots and its effect on light-induced degradation and performance of solar cells," *Progress in Photovoltaics: Research and Applications*, vol. 14, no. 2, pp. 125–134, 2006. [Online]. Available: http://dx.doi.org/10.1002/pip.659

[131] J. Schmidt and D. Macdonald, "Recombination activity of iron-gallium and iron-indium pairs in silicon," *Journal of Applied Physics*, vol. 97, no. 11, p. 113712, 2005. [Online]. Available: http://link.aip.org/link/?JAP/97/113712/1

[132] J. Schmidt, B. Lim, D. Walter, K. Bothe, S. Gatz, T. Dullweber, and P. P. Altermatt, "Impurity-related limitations of next-generation industrial silicon solar cells," *Photovoltaics, IEEE Journal of*, vol. PP, no. 99, pp. 1 –5, 2012.

[133] B. Lim, "Boron-oxygen-related recombination centers in crystalline silicon and the effects of dopant-compensation," Ph.D. dissertation, University of Hannover, 2012.

[134] D. Macdonald, A. Liu, A. Cuevas, B. Lim, and J. Schmidt, "The impact of dopant compensation on the boron-oxygen defect in p- and n-type crystalline silicon," *physica status solidi (a)*, vol. 208, no. 3, pp. 559–563, 2011. [Online]. Available: http://dx.doi.org/10.1002/pssa.201000146

[135] D. W. Palmer, K. Bothe, and J. Schmidt, "Kinetics of the electronically stimulated formation of a boron-oxygen complex in crystalline silicon," *Phys. Rev. B*, vol. 76, p. 035210, Jul 2007. [Online]. Available: http://link.aps.org/doi/10.1103/PhysRevB.76.035210

[136] K. Bothe, R. Hezel, and J. Schmidt, "Recombination-enhanced formation of the metastable boron–oxygen complex in crystalline silicon," *Applied Physics Letters*, vol. 83, no. 6, pp. 1125–1127, 2003. [Online]. Available: http://link.aip.org/link/?APL/83/1125/1

[137] S. Bernardini, D. Saynova, S. Binetti, and G. Coletti, "Light-induced degradation in compensated mc-si p-type solar cells," in *Proceedings 38th IEEE Photovoltaic Specialists Conference, Austin, Texas*, 2012.

[138] S. Glunz, S. Rein, W. Warta, J. Knobloch, and W. Wettling, "On the degradation of cz-silicon solar cells," in *Proceedings of the 2nd World Photovoltaic Solar Energy Conference, Vienna, Austria*, 1998.

[139] L. I. Murin, T. Hallberg, V. P. Markevich, and J. L. Lindström, "Experimental evidence of the oxygen dimer in silicon," *Phys. Rev. Lett.*, vol. 80, no. 1, pp. 93–96, Jan 1998.

[140] S. W. Glunz, S. Rein, J. Y. Lee, and W. Warta, "Minority carrier lifetime degradation in boron-doped czochralski silicon," *Journal of Applied Physics*, vol. 90, no. 5, pp. 2397–2404, 2001. [Online]. Available: http://link.aip.org/link/?JAP/90/2397/1

[141] K. Bothe, J. Schmidt, and R. Hezel, "Effective reduction of the metastable defect concentration in boron-doped czochralski silicon for solar cells," in *Proceedings of the 29th IEEE Photovoltaic Specialists Conference*, may 2002, pp. 194 – 197.

[142] A. Carvalho, P. Santos, J. Coutinho, R. Jones, M. J. Rayson, and P. R. Briddon, "Light induced degradation in b doped cz-si solar cells," *physica status solidi (a)*, vol. 209, no. 10, pp. 1894–1897, 2012. [Online]. Available: http://dx.doi.org/10.1002/pssa.201200196

[143] J. Bourgoin and J. Corbett, "A new mechanism for interstistitial migration," *Physics Letters A*, vol. 38, no. 2, pp. 135 – 137, 1972. [Online]. Available: http://www.sciencedirect.com/science/article/pii/0375960172905233

[144] J. Adey, R. Jones, D. W. Palmer, P. R. Briddon, and S. Öberg, "Degradation of boron-doped czochralski-grown silicon solar cells," *Phys. Rev. Lett.*, vol. 93, no. 5, p. 055504, Jul 2004.

[145] L. I. Murin, E. A. Tolkacheva, V. P. Markevich, A. R. Peaker, B. Hamilton, E. Monakhov, B. G. Svensson, J. L. Lindström, P. Santos, J. Coutinho, and A. Carvalho, "The oxygen dimer in si: Its relationship to the light-induced degradation of si solar cells?" *Applied Physics Letters*, vol. 98, no. 18, p. 182101, 2011. [Online]. Available: http://link.aip.org/link/?APL/98/182101/1

[146] V. V. Voronkov, R. J. Falster, J. Schmidt, K. Bothe, and A. Batunina, "Lifetime degradation in boron doped czochralski silicon," *ECS Transactions*, vol. 33, no. 11, pp. 103–112, 2010. [Online]. Available: http://ecst.ecsdl.org/content/33/11/103.abstract

[147] B. Lim, S. Hermann, K. Bothe, J. Schmidt, and R. Brendel, "Solar cells on low-resistivity boron-doped czochralski-grown silicon with stabilized efficiencies of 20162102, 2008. [Online]. Available: http://link.aip.org/link/?APL/93/162102/1

[148] B. Lim, A. Liu, D. Macdonald, K. Bothe, and J. Schmidt, "Impact of dopant compensation on the deactivation of boron-oxygen recombination centers in crystalline silicon," *Applied Physics Letters*, vol. 95, no. 23, p. 232109, 2009. [Online]. Available: http://link.aip.org/link/?APL/95/232109/1

[149] B. Lim, K. Bothe, and J. Schmidt, "Accelerated deactivation of the boron-oxygen-related recombination centre in crystalline silicon," *Semiconductor Science and Technology*, vol. 26, no. 9, p. 095009, 2011. [Online]. Available: http://stacks.iop.org/0268-1242/26/i=9/a=095009

[150] J. A. Giesecke and W. Warta, "Microsecond carrier lifetime measurements in silicon via quasi-steady-state photoluminescence," *Progress in Photovoltaics: Research and Applications*, vol. 20, no. 2, pp. 238–245, 2012. [Online]. Available: http://dx.doi.org/10.1002/pip.1128

[151] J. A. Giesecke, M. C. Schubert, and W. Warta, "Self-sufficient minority carrier lifetime in silicon from quasi-steady-state photoluminescence," *physica status solidi (a)*, pp. n/a–n/a, 2012. [Online]. Available: http://dx.doi.org/10.1002/pssa.201228383

[152] A. Cuevas and R. Sinton, "Detailed modelling of silicon solar cells," in *Proceedings of the 23rd European Photovoltaic Solar Energy Conference, Valencia, Spain*, W. Munich, Ed., 2008.

[153] P. Engelhart, D. Manger, B. Kloter, S. Hermann, A. Stekolnikov, S. Peters, H.-C. Ploigt, A. Eifler, C. Klenke, A. Mohr, G. Zimmermann, B. Barkenfelt, K. Suva, J. Wendt, T. Kaden, S. Rupp, D. Rychtarik, M. Fischer, and P. W. J.W. Müller, "Qantum - q-cells next generation high-power silicon cell & module concept," in *Proceedings of the 26th European Photovoltaic Solar Energy Conference, Hamburg, Germany, WIP Munich*, W. Munich, Ed., 2011.

[154] Z. Wang, P. Han, H. Lu, H. Qian, L. Chen, Q. Meng, N. Tang, F. Gao, Y. Jiang, J. Wu, W. Wu, H. Zhu, J. Ji, Z. Shi, A. Sugianto, L. Mai, B. Hallam, and S. Wenham, "Advanced perc and perl production cells with 20.3efficiency for standard commercial p-type silicon wafers," *Progress in Photovoltaics: Research and Applications*, vol. 20, no. 3, pp. 260–268, 2012. [Online]. Available: http://dx.doi.org/10.1002/pip.2178

List of publications

This thesis is based on the following publications

Journal papers

1. M. Forster, B. Dehestru, A. Thomas, E. Fourmond, R. Einhaus, A. Cuevas and M. Lemiti, «Compensation engineering for uniform n-type silicon ingots», *Solar Energy Materials and Solar Cells*, **111**, 146, (2013)

2. M. Forster, F. E. Rougieux, A. Cuevas, B. Dehestru, A. Thomas, E. Fourmond, and M. Lemiti, «Incomplete ionization and carrier mobility in compensated p-type and n-type silicon», *IEEE Journal of Photovoltaics*, **3**, 108, (2013)

3. A. Cuevas, M. Forster, F. E. Rougieux, D. Macdonald, «Compensation engineering for silicon solar cells», *Energy procedia*, **15**, 67-77, (2012)

4. M. Forster, A. Cuevas, E. Fourmond, F. E. Rougieux, and M. Lemiti, «Impact of incomplete ionization of dopants on the electrical properties of compensated p-type silicon», *Journal of Applied Physics*, **111**, 043701, (2012)

5. M. Forster, E. Fourmond, F. E. Rougieux, A. Cuevas, R. Gotoh, K. Fujiwara, S. Uda, and M. Lemiti, «Boron-oxygen defect in Czochralski-silicon co-doped with gallium and boron», *Applied Physics Letters*, **100**, 042110, (2012)

6. E. Fourmond, M. Forster, R. Einhaus, H. Lauvray, J. Kraiem, and M. Lemiti, «Electrical properties of B, P and Ga co-doped silicon» *Energy Procedia*, **8**, 349 (2011)

7. M. Forster, E. Fourmond, R. Einhaus, H. Lauvray, J. Kraiem, and M. Lemiti, «Ga co-doping in Cz-grown silicon ingots to overcome limitations of B and P compensated silicon feedstock for PV applications», *Physica status solidi c* , **8**, 678 (2011)

International conference and workshop papers

1. M. Forster, F. E. Rougieux, A. Cuevas, B. Dehestru, A. Thomas, E. Fourmond and M. Lemiti, «Incomplete ionization and carrier mobility in compensated p-type and n-type

silicon», *in Proceedings of the 38th IEEE Photovoltaic specialists Conference*, Austin, Texas, (2012)

2. M. Forster, B. Dehestru, R. Einhaus, E. Fourmond, and M. Lemiti, «Compensation engineering to improve the doping uniformity along n-type silicon ingots grown from UMG-Si», *in Proceedings of the 21st International Photovoltaic Science and Engineering Conference,* Fukuoka, Japan, (2011)

3. M. Forster, E. Fourmond, R. Einhaus, H. Lauvray, J. Kraiem, and M. Lemiti, «Doping engineering to increase the performance and material yield during crystallization of low-purity silicon for photovoltaic application», *Proceedings of the 3rd international forum on multidisciplinary education and research for energy science*, Ishigaki, Japan, (2010)

4. M. Forster, E. Fourmond, R. Einhaus, H. Lauvray, J. Kraiem, and M. Lemiti, «Doping engineering to increase the material yield during crystallization of B and P compensated silicon», *in Proceedings of the 25th European Photovoltaic Solar Energy Conference*, Valencia, Spain, (2010)

5. M. Forster, E. Fourmond, R. Einhaus, H. Lauvray, J. Kraiem, «Ga co-doping in Cz-grown silicon ingots to overcome limitations of B and P compensated silicon feedstock for PV applications», *in Proceedings of the 20th Workshop on Crystalline Silicon Solar Cells & Modules: Materials and Processes*, Breckenridge, Colorado, (2010)

Other publications by the author

1. A. Cuevas, F. E. Rougieux, and M. Forster, «Dopant Compensation for Photovoltaic Silicon: Challenges and Opportunities», *in Proceedings of the Korea-EU International Symposium on Photovoltaics*, Busan, Korea, (2012)

2. K. Tanaka, M. Tajima, M. Forster, H. Toyota, and A. Ogura, «Donor-acceptor pair luminescence in Si co-doped with B, P and Ga», *in Proceedings of the 6th International Symposium on Advanced Science and Technology of Silicon Materials*, Kona, Hawaii, (2012)

3. J. Kraiem, P. Papet, J. Degoulange, M. Forster, O. Nichiporuk, D. Grosset-Bourbange, F. Cocco, and R. Einhaus, “World class solar cell efficiency on n-type Cz UMG silicon wafers by heterojunction technology,” *in Proceedings of the 27th European Photovoltaic Solar Energy Conference*, Frankfurt, Germany, (2012)

4. R. Einhaus, J. Kraiem, J. Degoulange, O. Nichiporuk, M. Forster, P. Papet, Y. Andrault, D. Grosset-Bourbange, and F. Cocco, “19% heterojunction solar cells on Cz wafers from non-blended upgraded metallurgical silicon,” *in Proceedings of the 38th IEEE Photovoltaic Specialists Conference*, Austin, Texas, (2012)

5. S. Y. Lim, M. Forster, and D. Macdonald, “Estimation of solidification interface shapes in a boron-phosphorus compensated multicrystalline silicon ingot via photoluminescence imaging,” *in Proceedings of the 22nd Workshop on Crystalline Silicon Solar Cells and Modules: Materials and Processes*, Breckenridge, Colorado, (2012)

6. F. E. Rougieux, M. Forster, D. Macdonald, A. Cuevas, B. Lim, and J. Schmidt, “Recombination activity and impact of the boron-oxygen-related defect in compensated n-type silicon,” *in Proceedings of the 37th IEEE Photovoltaic Specialists Conference*, Seattle, Washington, (2011)

7. F. E. Rougieux, M. Forster, D. Macdonald, A. Cuevas, B. Lim, and J. Schmidt, «Recombination activity and impact of the boron-oxygen-related defect in compensated n-type Silicon», *IEEE Journal of Photovoltaics*, **1**, 54-58, (2011)

8. F. E. Rougieux, B. Lim, J. Schmidt, M. Forster, D. Macdonald, and A. Cuevas, “Influence of net doping, excess carrier density and annealing on the boron oxygen related defect density in compensated n-article silicon”, *Journal of Applied Physics*, **110**, 063708, (2011)

9. M. Forster, E. Fourmond, J. M. Lebrun, R. Einhaus, J. Kraiem, and M. Lemiti, «New method for grain size characterization of a multi-crystalline silicon ingot», *in Proceedings of the 24th European Photovoltaic Solar Energy Conference*, Hamburg, Germany, (2009)

Résumé étendu

Etude bibliographique

L'étude approfondie de la littérature traitant des propriétés électriques du Si compensé révèle que la compensation est susceptible d'influencer la performance des cellules solaires aux travers de deux aspects distincts. D'une part la recombinaison des porteurs de charges photogénérés et d'autre part leur transport. Dans le chapitre 1 de cette thèse, nous définissons les grandeurs essentielles pour comprendre la compensation et effectuons une revue de la littérature traitant de son effet sur les propriétés électriques du Si et de ses conséquences sur les caractéristiques des cellules solaires.

Définitions

Lorsque des impuretés introduisant des niveaux donneurs et accepteurs dans la bande interdite du Si sont présentes conjointement, le type de conductivité (n ou p) est définit par le type des impuretés majoritaires. Il est aussi communément accepté que la densité de porteurs majoritaires n_{maj} est égale à la différence entre les concentrations en impuretés majoritaires N_{maj} et minoritaires N_{min}, selon l'équation 1:

$$n_{\mathrm{maj}} = N_{\mathrm{maj}} - N_{\mathrm{min}} \tag{1}$$

L'équation 1 montre que la densité de porteurs majoritaires peut être réduite par l'ajout d'impuretés minoritaires. C'est le principe de la compensation de dopants. Nous définissons le Si compensé comme contenant une concentration en dopants minoritaires au moins égale à 3% de la concentration en dopants majoritaires, de manière à ce que la densité de porteurs majoritaires soit sensiblement (de façon détectable à l'aide des techniques de mesure les plus courantes tel que par résistivité 4-pointes ou par effet Hall) affectée par la présence de dopants minoritaires.

Pour quantifier la compensation, c'est à dire à quel point les concentrations en dopants minoritaires et majoritaires sont proches l'une de l'autre, nous introduisons les niveaux de

compensation R_C (équation 2) et K_C (équation 3) dont l'utilisation est pratique respectivement dans le cas de la compensation modérée pour R_C et dans le cas de la compensation extrême pour K_C.

$$R_C = \frac{N_{min}}{N_{maj}} \tag{2}$$

$$K_C = \frac{N_{maj} + N_{min}}{N_{maj} - N_{min}} \tag{3}$$

Recombinaison des porteurs de charges

Trois types de mécanismes de recombinaison interviennent dans le Si cristallin: les recombinaisons bandes à bandes radiatives et Auger et les recombinaisons au travers de niveaux intermédiaires introduits dans la bande interdite du Si par les impuretés et défauts cristallins (communément appelées recombinaisons SRH pour les initiales des inventeurs de la statistique permettant de les décrire Schokley, Read et Hall).

Les recombinaisons radiatives et Auger sont appelées recombinaisons intrinsèques, puisqu'elles ne nécéssitent pas la présence d'impuretés ou de défauts cristallins dans le Si. Ces recombinaisons intrinsèques ont été paramétrées par Kerr et Cuevas [24]. Ils proposent ainsi de décrire la durée de vie des porteurs dans le Si intrinsèque par l'équation 4.

$$\tau_{intrinsic} = \frac{1}{(n_0 + p_0 + \Delta n)(1.8 \times 10^{-24} n_0^{0.65} + 6 \times 10^{-25} p_0^{0.65} + 3 \times 10^{-27} \Delta n^{0.8} + 9 \times 10^{-15})} \tag{4}$$

Cette équation montre que la durée de vie intrinsèque augmente avec la diminution de la densité de porteurs majoritaires et peut donc être améliorée grâce à la compensation de dopants.

De la même manière, il est possible de montrer que la durée de vie SRH peut être augmenter par compensation grâce à deux effets décrits par Macdonald et Cuevas [25] grâce à un «effet de niveau d'injection» lorsque la durée de vie des porteurs présente une forte dépendance avec la densité de porteurs en excès ou à un «effet de niveau de Fermi» dans les cas des centres recombinants introduisant des niveaux d'énergie proche de la bande de valence ou de la bande de conduction.

L'étude des différents mécanismes de recombinaison montre donc que la durée de vie des porteurs augmente avec la densité de porteurs majoritaires et peut donc être améliorée par compensation. En cela, la théorie est en accord avec un grand nombre de résultats expérimentaux ayant été publiés au cours des dernières années [10, 13, 14, 15, 16].

Transport des porteurs de charges

Le capacité d'un type de porteurs charge à être transportée dans le Si est représentée par sa mobilité μ. Cette mobilité est affectée par l'interaction avec les phonons, les impuretés ion-

isées et les autres porteurs de charge. Dans le Si non compensé, la mobilité à température ambiante suit une fonction monotone de la concentration en dopants. De ce fait, la densité de porteurs majoritaires n_{maj} et la concentration en dopants N_{maj} peuvent être directement déterminés par une simple mesure de résistivité ρ selon l'équation 5:

$$\rho = \frac{1}{n_{\mathrm{maj}} \times q \times \mu_{\mathrm{maj}}} = \frac{1}{N_{\mathrm{maj}} \times q \times \mu_{\mathrm{maj}}(N_{\mathrm{maj}})} \tag{5}$$

Dans le Si non compensé, en revanche, la mobilité dépend de la concentration en impuretés majoritaires et minoritaires et la résistivité suit la relation:

$$\rho = \frac{1}{n_{\mathrm{maj}} \times q \times \mu_{\mathrm{maj}}} = \frac{1}{(N_{\mathrm{maj}} - N_{\mathrm{min}}) \times q \times \mu_{\mathrm{maj}}(N_{\mathrm{maj}}, N_{\mathrm{min}})} \tag{6}$$

Il n'existe donc plus de relation non ambigüe entre la résistivité et la densité de porteurs majoritaires ou les concentrations en dopants. En effet, à une valeur de résistivité peut correspondre une infinité de couples de valeurs pour les concentrations en dopants majoritaires et minoritaires. La résistivité n'est donc pas une grandeur fiable dans le Si compensé pour juger du caractère approprié du dopage pour une application donnée.

De nombreux modèles permettent de calculer la mobilité des porteurs en fonction des concentrations en dopants [62, 67, 68, 69, 57, 56]. Parmi eux, le modèle de Klaassen est à priori le plus adapté au Si compensé, puisqu'il distingue les interactions répulsives des interactions attractives, les interactions avec des charges fixes des interactions avec des charges mobiles et prend en compte l'effet d'écrantage des charges les unes des autres. Malgré cela, le modèle de Klaassen, de même que tous les autres modèles disponibles, surestime systématiquement la mobilité des porteurs majoritaires et minoritaires dans le Si compensé [10, 46, 70, 71, 14, 72, 73, 74, 75, 76, 77]. Il a également éta montré que cet écart entre modèles et valeurs expérimentales augmente avec le niveau de compensation. Deux explications ont été proposées pour cette réduction de la mobilité. La première est l'existence d'un mécanisme de diffusion des porteurs de charge spécifique au Si compensé [70]. La deuxième est la mauvaise prise en compte de la diminution de l'écrantage des charges fixes par les charges mobiles dans le Si compensé [46, 74, 77, 70]. Ces propositions seront discutées aux vues de nos résultats expérimentaux sur la dépendance de la mobilité avec la température dans le Si compensé.

Cellules solaires à base de Si compensé

Courant de court-circuit Diverses études expérimentales montrent que la longueur de diffusion des porteurs minoritaires L_{min} (7) augmentent avec la compensation [11, 79].

$$L_{\mathrm{min}} = \sqrt{\tau_{\mathrm{eff}} \times D_{\mathrm{min}}} = \sqrt{\tau_{\mathrm{eff}} \times \mu_{\mathrm{min}} \times \frac{kT}{q}} \tag{7}$$

Ceci suggère que la diminution de la mobilité des porteurs minoritaires due à la compensation est largement contrebalancée par l'augmentation de la durée de vie liée à la diminution

de la densité de porteurs majoritaires. En conséquence, la compensation a généralement un effet positif sur le courant de court-circuit des cellules solaires.

Tension de circuit ouvert La tension de circuit ouvert V_{oc} d'une cellule solaire s'exprime de la façon suivante:

$$V_{oc} = kT \times \ln\left(\frac{(n_0 + \Delta n) \times (p_0 + \Delta n)}{n_i^2}\right) \approx kT \times \ln\left(\frac{(n_{maj} + \Delta n) \times \Delta n}{n_i^2}\right) \tag{8}$$

Ainsi, la densité de porteurs majoritaires influence la tension de circuit ouvert de deux manières:

1. D'une part en intervenant directement dans l'expression de la tension de circuit ouvert. A densité de porteurs en excès Δn constante, la tension de circuit ouvert augmente avec la densité de porteurs majoritaires.

2. D'autre part en faisant varier la densité de porteurs en excès au travers de la durée de vie. Plus la densité de porteurs est grande, plus la durée de vie est faible et donc plus la densité de porteurs en excès est faible, ce qui a pour effet de réduire la tension de circuit ouvert.

La compensation a donc un effet ambivalent sur la tension de circuit ouvert et la densité de porteurs optimale dépend des mécanismes de recombinaison dominants et de la structure de la cellule utilisée.

Facteur de forme Le facteur de forme est également affecté par la densité de porteurs majoritaires, particulièrement lorsque la durée de vie présente une forte dépendance avec la densité de porteurs en excès à cause d'un «effet de niveau d'injection» similaire à celui impactant la durée de vie. De même que pour la tension de circuit ouvert, la densité de porteurs optimale pour le facteur de forme dépend des mécanismes de recombinaison dominants et de la structure de la cellule utilisée.

Rendement de conversion Le rendement de conversion est le produit des 3 caractéristiques mentionées ci-dessus divisé par la puissance lumineuse incidente. Puisque ces 3 caractéristiques dépendent de la densité de porteurs majoritaires, cette grandeur a une influence importante sur le rendement de conversion des cellules. La densité de porteurs optimales doit donc être trouvée pour maximiser la performance d'une cellule en fonction des mécanismes de recombinaison dominants et de la structure utilisée. Dans le Si purifié par voie métallurgique, les concentrations en dopants sont généralement supérieures à la densité de porteurs majoritaires optimales. Comme nous l'avons mentionné précédemment, la densité de porteurs majoritaires peut cependant être ajustée par compensation. C'est ainsi qu'il a été observé une augmentation du rendement de conversion avec le niveau

de compensation dans des cellules réalisées à partir de Si purifié par voie métallurgique [82].

En conclusion du premier chapitre sur l'état de l'art, il apparaît que la densité de porteurs majoritaires dans la base d'une cellule solaire a une très forte influence sur sa performance. Lorsque la concentration en dopants majoritaires est supérieure à la densité de porteurs optimales, il est possible d'ajuster cette dernière par compensation. Cette thèse se propose d'étudier comment appliquer se principe dans la pratique et d'approfondir la compréhension des propriétés fondamentales du matériau et des cellules solaires liées à la compensation.

Ingénierie de compensation pour contrôler le dopage net le long de lingots de silicium

Dans le chapitre 2, nous étudions dans un premier temps le phénomène de ségrégation des impuretés lors de la solidification directionelle de lingots de Si. Nous exposons la tendance qu'ont la plupart des impuretés à s'accumuler dans la phase liquide pendant la cristallisation, donnant lieu à une augmentation de leur concentration d'une extrémité à l'autre d'un lingot. Cette augmentation de la concentration en impureté est d'autant plus importante que l'impureté en question présente un coefficient de ségrégation faible par rapport à 1.

Les deux dopants majoritairement présents dans le Si UMG présentent des coefficients de ségrégation différents. Le coefficient de ségrégation du B est égale à 0,8 et est donc très proche de 1. Par conséquent, la concentration en B varie très peu le long d'un lingot de Si. Le P, en revanche, présente un coefficient de ségrégation de 0,35 et sa concentration varie donc significativement le long d'un lingot de Si. Cette différence de distribution des dopants de type p et n présents conjointement dans le Si UMG engendre une forte variation du dopage net le long des lingots compensés de type p comme de type n (Figure 8). Cette variation peut aller, lorque le début du lingot est de type p, jusqu'à une inversion de type de p à n. Il est donc particulièrement difficile de maintenir le dopage net à une valeur optimale pour la fabrication de cellules sur toute la longueur d'un lingot cristallisé à partir de Si UMG. Ce contrôle ne peut le plus souvent pas se faire en rajoutant du B ou du P. Dans le cas d'un lingot de type p, lorsqu'on ajoute du P pendant la cristallisation pour diminuer le dopage net, on diminue également la fraction du lingot de type p et donc le rendement matière. A l'inverse, si l'on ajoute du B pour augmenter le rendement matière, on augmente également le dopage net en début de cristallisation, ce qui n'est généralement pas souhaitable pour la performance des cellules.

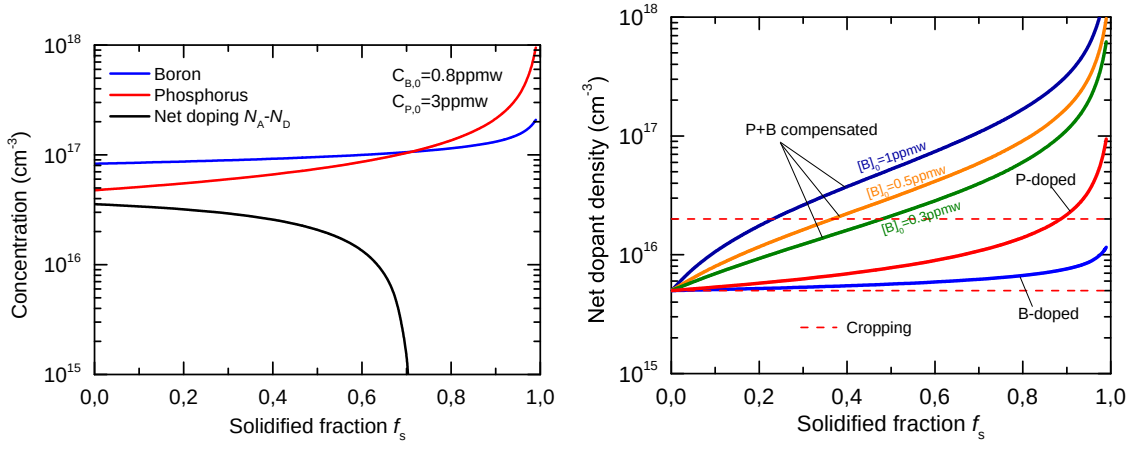

Figure 8: (a) Variation des concentrations en B et P et du dopage net dans un lingot compensé majoritairement de type p. (b) Variation du dopage net le long de lingots non compensés dopés simplement au B ou simplement au P et le long de lingots de type n compensés.

Cet effet impose des contraintes importantes sur les tolérances en B et P dans le Si UMG illustrées sur la Figure 9. Par exemple, pour obtenir un lingot au moins à 90% de type p avec un dopage net maximum de $1 \times 10^{16}\text{cm}^{-3}$, le point orange sur la Figure 9 indique que les concentrations maximales que l'on peut tolérer dans le Si sont $[\text{B}]_0 = 1.9 \times 10^{16}\text{cm}^{-3}$ (0.15ppmw) et $[\text{P}]_0 = 1.5 \times 10^{16}\text{cm}^{-3}$ (0.33ppmw).

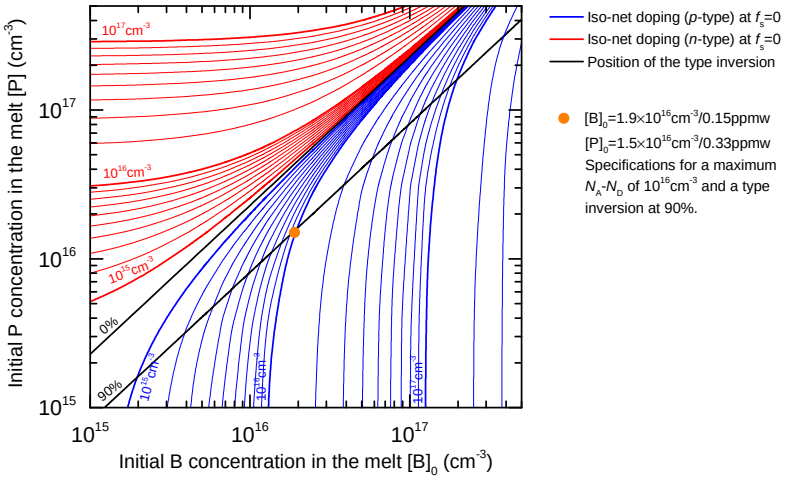

Figure 9: Abaque permettant d'évaluer le rendement matière et le dopage net maximum dans des lingots de Si compensé.

Pour résoudre ce problème, nous proposons dans le chapitre 2 d'ajouter du Ga pendant la cristallisation. Le Ga est un dopant de type p avec un très faible coefficient de ségrégation égal à 8×10^{-3}. Cela signifie que la concentration en Ga varie de façon très importante le long d'un lingot de Si. L'idée du co-dopage au Ga est d'utiliser ces propriétés avantageuses (type p et très faible coefficient de ségrégation) pour compenser l'augmentation de la concentration en P le long des lingots de Si.

Nous montrons que cette technique est efficace d'une part pour la réalisation de lingots intégralement de type p avec un dopage net relativement faible, malgré de fortes concentrations initiales en B et P ($[\text{B}]_0 = 1.5$ppmw et $[\text{P}]_0 = 10$ppmw dans l'exemple présenté sur la Figure 10a). D'autre part, elle permet d'obtenir des lingots de Si de type n avec une faible variation de dopage net malgré la présence initiale de B et P en concentrations importantes ($[\text{B}]_0 = 0.5$ppmw et $[\text{P}]_0 = 5.6$ppmw dans l'exemple présenté sur la Figure 10b).

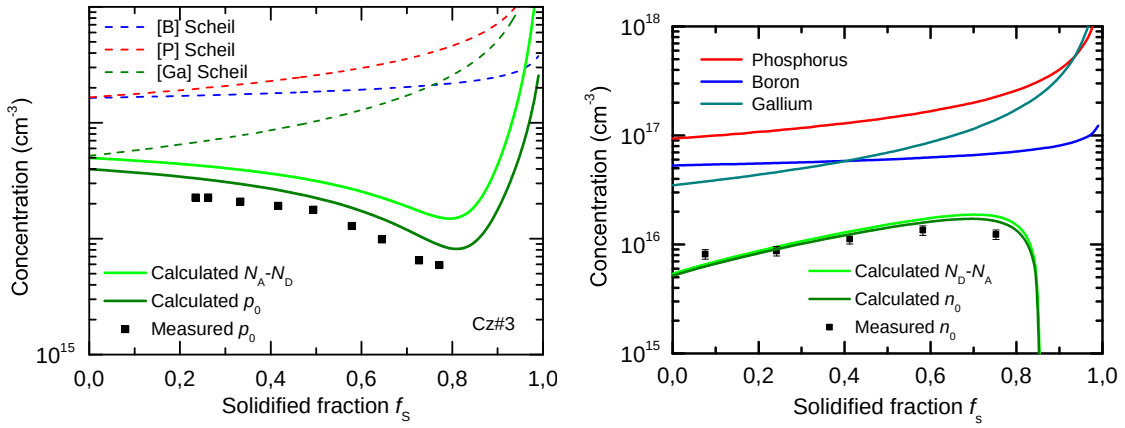

(a) (b)

Figure 10: Variation des concentrations en B, P et Ga le long d'un lingot co-dopé de type p (a) et un lingot co-dopé de type n (b).

En permettant de contrôler la valeur du dopage net et de la maintenir uniforme le long des lingots de Si, le co-dopage au Ga autorise donc en principe de tolérer des concentrations en B et P dans le Si UMG plus élevée tout en conservant un rendement matière important et de bonnes performances cellules. Ceci est cependant sous réserve que les propriétés électriques du Si et des cellules solaires sont principalement déterminées par le dopage net et que le Ga n'a pas d'effet néfaste particulier. Pour répondre à ces questions, nous étudions dans les 3 prochains chapitres (3, 4 et 5) les propriétés électriques et les performances cellules du Si co-dopé au B, P et Ga .

Concentration, transport et recombinaison des porteurs de charges dans le silicium compensé

Dans le chapitre 3, nous étudions les propriétés fondamentales du Si co-dopé au B, P et Ga relatives à la densité, la mobilité et la durée de vie des porteurs.

Densité de porteurs majoritaires

Tout d'abord, une analyse théorique de l'ionisation incomplète des dopants dans le Si permet d'identifier les facteurs qui rendent ce phénomène influent vis-à-vis de la densité de porteurs majoritaires. Ces facteurs, illustré sur la Figure 11 sont (1) la concentration en dopant majoritaire, (2) son énergie d'ionisation, (3) le type de conductivité et (4) le niveau de compensation:

1. Dans la gamme de concentration $10^{15} - 10^{18}\text{cm}^{-3}$, c'est à dire pour des concentrations inférieures à la transition de Mott, l'impact de l'ionisation incomplète sur la densité de porteurs majoritaires augmente avec la concentration en dopant majoritaire.

2. Plus l'énergie d'ionisation du dopant majoritaire est importante, plus l'impact de l'ionisation incomplète sur la densité de porteurs est fort.

3. L'ionisation incomplète a un impact plus important dans le Si de type p que dans le Si de type n, dû à la quadruple dégenerescence des niveaux accepteurs contre la double dégenerescence seulement des niveaux donneurs.

4. Finalement, l'impact de l'ionisation incomplète augmente légèrement dans le Si compensé, par rapport au Si non compensé.

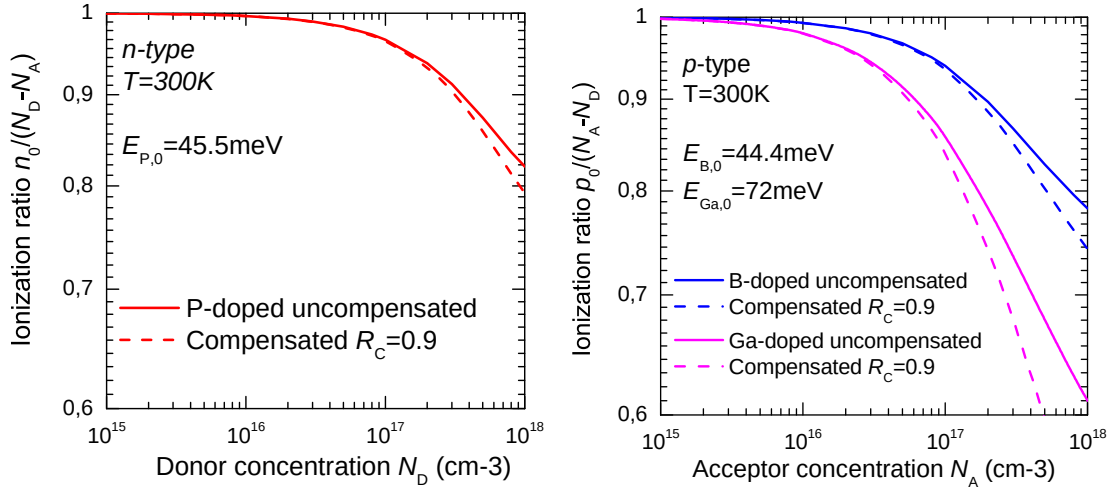

(a) (b)

Figure 11: Rapport densité de porteurs majoritaires sur dopage net en fonction de la concentration en dopant majoritaire et du niveau de compensation dans le Si de type n (a) et de type p (b).

A partir de ces graphiques, nous pouvons déduire que l'ionisation incomplète est à prendre en compte pour un calcul précis de la densité de porteurs majoritaires dès lors que le Si contient une concentration supérieure à $5 \times 10^{16}\text{cm}^{-3}$ en B ou $2 \times 10^{16}\text{cm}^{-3}$ en Ga dans le type p ou une concentration supérieure à 10^{17}cm^{-3} en P dans le type n. Cette étude montre donc qu'on ne peut pas dans le cas général considérer que la densité de porteurs majoritaires est strictement égale au dopage net.

Des mesures d'effet Hall montrent la densité de porteurs ne varie pas autour de la température ambiante dans du Si non compensé de type p et n avec un dopage proche de 10^{16}cm^{-3} (dopage typique pour les cellules solaires). Ceci montre que le régime de saturation des porteurs est atteint à température ambiante ou autrement dit qu'il n'y a pas d'ionisation incomplète. Dans des échantillons de Si compensés avec le même dopage net proche de 10^{16}cm^{-3} mais des concentrations totales en dopants plus importantes, la densité de porteurs varient fortement autour de la température ambiante, montrant que l'ionisation incomplète n'est pas négligeable à cette température. Nos résultats expérimentaux confirment donc la théorie présentée ci-dessu et montrent que, à dopage net constant, l'ionisation incomplète a un impact plus important sur la densité de porteurs majoritaires dans le Si compensé que dans le Si non compensé, principalement à cause de la plus forte concentration en dopants majoritaires dans le Si compensé.

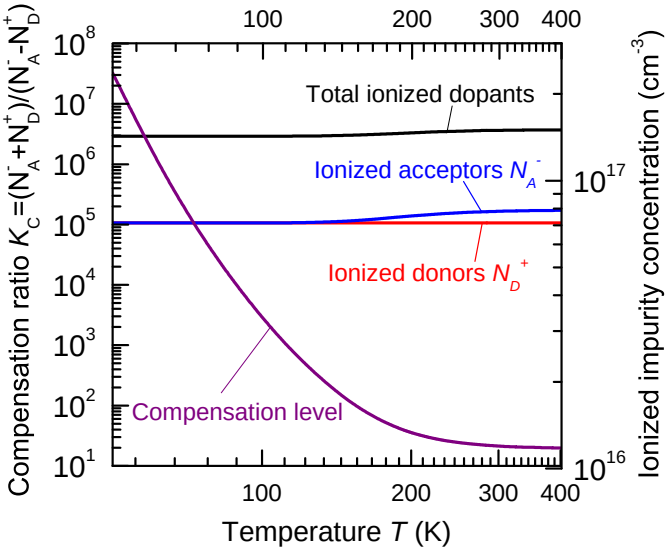

Figure 12: Variation des concentrations en accepteurs et donneurs et du niveau de compensation avec la température.

D'autre part, les mesures d'effet Hall montrent qu'à très faible température, la densité de porteurs décroît de plusieurs ordres de grandeur par rapport à sa valeur à température ambiante. Ceci s'explique de la manière suivante. Lorsqu'on baisse la température, la concentration en dopants majoritaires ionisés diminiue alors que la concentration en dopants minoritaires ionisés reste constante. Pour satisfaire l'équation de Poisson, la concentration en dopants majoritaires ionisés ne peut cependant pas décroître en dessous de la concentration en dopants minoritaires. Puiqu'en baissant la température, la concentration en dopants majoritaires ionisés se rapproche donc de la concentration en dopants minoritaires

la densité de porteurs majoritaires diminue. Puisque la concentration totale en dopants ionisés varie peu (la concentration en dopants majoritaires ionisés sature à la valeur de la concentration en minoritaires), la baisse de température entraîne donc une augmentation du niveau de compensation jusqu'à des valeurs extrêmes (Figure 12).

Mobilité des porteurs de charges dans le silicium compensé

Nous confirmons la réduction observée précédemment de la mobilité des porteurs majoritaires et minoritaires par rapport au modèle de Klaassen. L'écart entre mobilité expérimentale et théorique suit une relation simple avec le niveau de compensation (Figure 13), qui ne semble pas dépendre de la concentration totale en dopant.

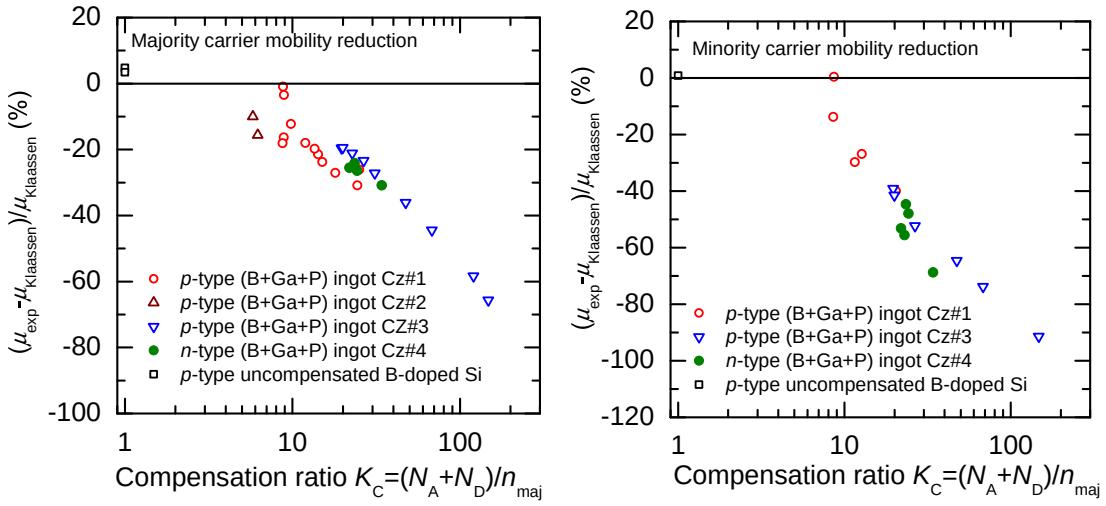

Figure 13: Ecart relatif de la mobilité des porteurs majoritaires (a) et minoritaires (b) au modèle de Klaassen en fonction du niveau de compensation.

Pour permettre un calcul précis de la mobilité dans le Si compensé, nous introduisons un préfacteur permettant de corriger la valeur donnée par le modèle de Klaassen. Se facteur correctif s'exprime en fonction du niveau de compensation de la manière suivante:

$$C = \frac{1}{1 + \left[(K_C - 1)/K_{C,ref}\right]^{\gamma}} \tag{9}$$

Type of carrier	$K_{C,ref}$	γ
Majority	74	0.89
Minority	24	1.43

Table 6: Constantes utilisées pour le calcul du préfacteur correctif.

L'étude de la dépendance en température de la mobilité des porteurs majoritaires montre que l'écart à Klaassen varie peu avec la température. Comme nous l'avons vu, le niveau

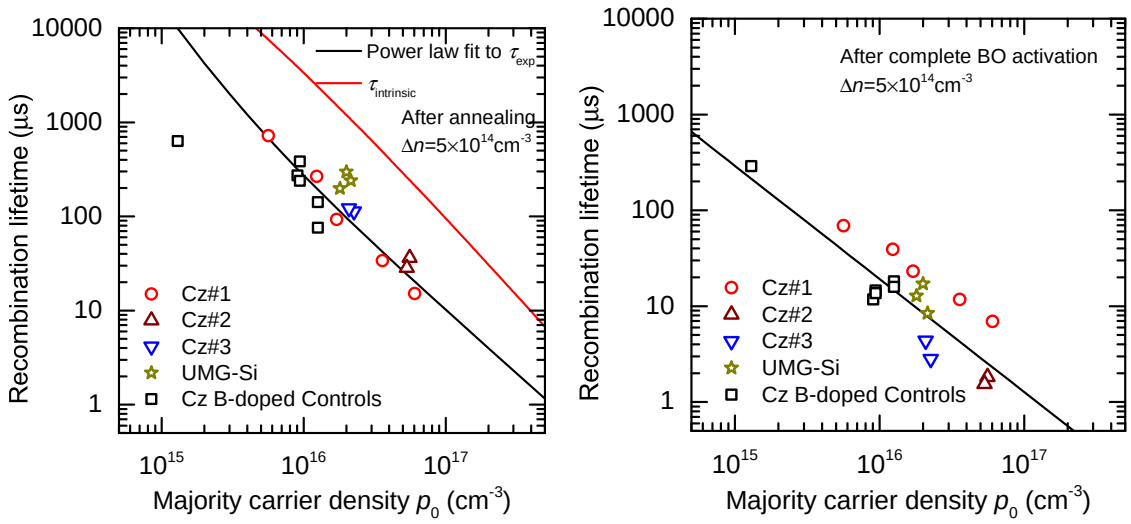

Figure 14: Variation de la durée de vie avec la densité de porteurs majoritaires avant (a) et après (b) dégradation sous éclairement.

de compensation augmente jusqu'à des valeurs extrême à basse température. Ceci suggère que la réduction observée ne peut pas s'expliquer par un mécanisme de diffusion des porteurs spécifique à la compensation qui entraînerai une forte chute de la mobilité dans le Si compensé à basse température. De la même manière, on peut montrer que si le désécrantage des charges fixes par les charges mobiles était responsable de l'écart entre le modèle de Klaassen et les mobilité expérimentales, cet écart devrait augmenter à basse température, ce qui n'est pas systématiquement le cas. Une mauvaise prise en compte de l'écrantage des charges les unes des autres par le modèle de Klaassen ne peut donc à elle seule expliquer le désaccord entre expérience et théorie.

Recombinaison des porteurs de charges dans le silicium compensé

Avant dégradation sous éclairement, nous montrons que la durée de vie présente une forte dépendance avec la densité de porteurs majoritaires (Figure 15). Cette dépendance est la même que dans le Si non compensé et ne dépend pas de la concentration totale en dopants. Ceci suggère que les dopants, même présents en fortes concentrations, n'agissent pas comme des centres de recombinaisons importants. Nous confirmons ainsi que la durée de vie peut être efficacement augmenter par compensation. Nous confirmons également, en combinant nos mesures de mobilité des porteurs minoritaires et de durée de vie, que l'effet positif de la compensation sur la durée de vie prend le pas sur l'effet négatif sur la mobilité et que la longueur de diffusion des porteurs minoritaires augmente donc avec la compensation.

Après dégradation, nous observons une perte de corrélation entre la durée de vie et la densité de porteurs majoritaires (Figure 15). Ce résultat est difficile à réconcilier avec la dépendance présumée de la densité de défauts bore-oxygène avec la densité de porteurs

majoritaires [45, 46, 47, 48, 44]. Pour mieux comprendre ce résultat surpenant, le chapitre suivant (chapitre 4) se focalise sur l'étude des caractéristiques du défaut bore-oxygène dans le Si compensé.

Le défaut bore-oxygène

Dans le chapitre 4, nous étudions la densité, la cinétique de formation et l'activité recombinante du défaut bore-oxygène dans une série d'échantillons présentant une large gamme de niveaux de dopage et de compensation. Cette étude a pour but de clarifier la dépendance de la densité de défaut avec la concentration totale en bore ou avec le dopage net et d'améliorer la compréhension de la composition du défaut et du mécanisme de dégradation.

Densité de défauts

L'étude de la densité de défauts bore-oxygène par des mesures de durée de vie des porteurs de charges montre que celle-ci est généralement proportionelle à la concentration totale en B et ne présente pas de dépendance évidente avec la densité de porteurs majoritaires (Figure 15). Ce résultat contredit un certain nombre de publications [45, 46, 47, 48, 44] présentant la densité de défauts bore-oxygène comme étant proportionelle dans le Si compensé à la densité de porteurs majoritaires. Dans le chapitre 4, nous discutons les sources d'erreur pouvant expliquer cette contradiction avec nos résultats.

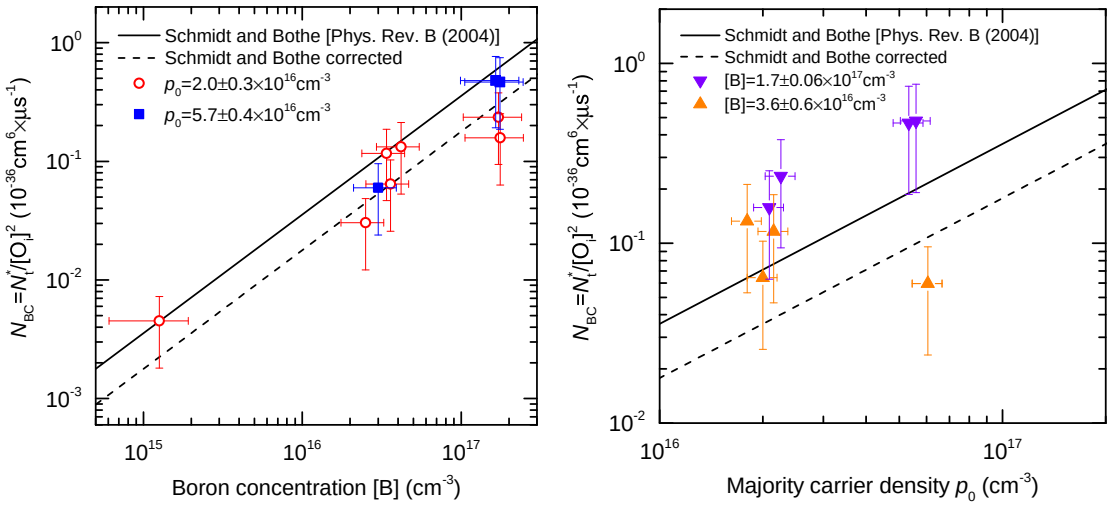

Figure 15: Variation de la densité de défauts bore-oxygène en fonction de la concentration total en B (a) ou de la densité de porteurs majoritaires (b).

Cette dépendance avec la concentration totale en B prouve l'implication du bore substitutionnel dans le complexe responsable de la dégradation et tend à invalider la proposition faite par Voronkov et Falster [49] que le complexe est formé à partir d'un atome de bore interstitiel. Plus généralement, elle montre que la dégradation sous éclairement ne peut pas être minimisée par compensation puisque la densité de défauts dépend de la concentration totale en B.

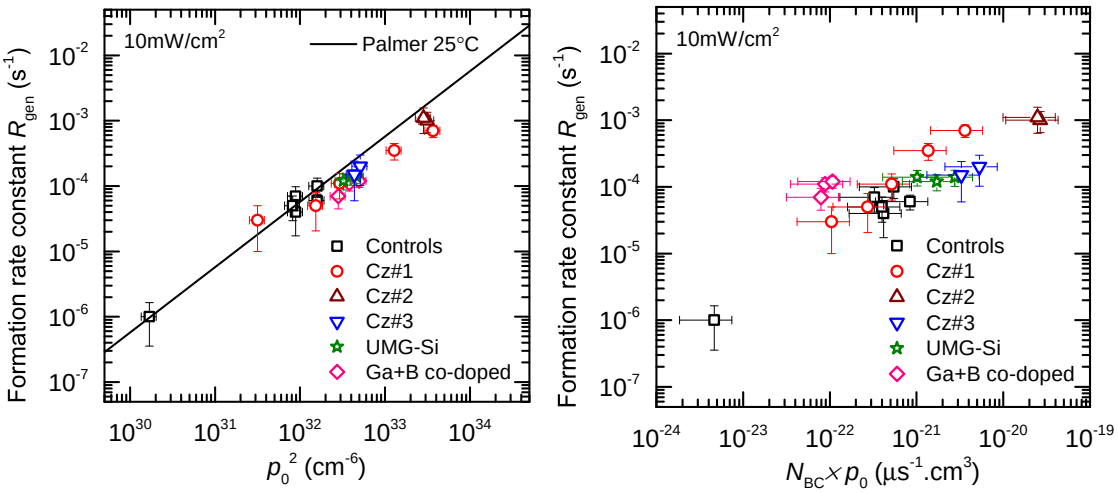

Figure 16: Taux de formation ou d'activation du défaut bore-oxygène sous éclairement en fonction du carré de la densité de trous libres ou du produit de la densité de défauts par la densité de trous libres.

Cinétique de dégradation

L'étude de la cinétique de la dégradation montre que dans le Si de type p comme dans le Si de type n, le taux de formation ou activation du défaut est proportionnel au carré de la densité de trous libres. En mettant en relation ce résultat avec les modèles [135, 49] proposés dans la littérature pour expliquer la dégradation, nous suggérons que celle-ci procède non pas par la formation du complexe bore-oxygène mais par l'activation d'un défaut préexistant qui passe d'une configuration inactive à une configuration très recombinante sous injection de porteurs de charges.

Caractéristiques SRH

L'étude de la dépendance de la durée de vie liée au défaut bore-oxygène montre que celle-ci ne peut être fittée en considérant dans la statistique SRH un simple défaut profond. Pour fitter toutes les courbes, il est nécéssaire d'ajouter dans certains cas un centre recombinant supplémentaire avec un niveau superficiel. Ce niveau supplémentaire apparaît dans certains échantillons de façon aléatoire et empêche de déterminer précisément le rapport de section de capture du défaut bore-oxygène pour les électrons et pour les trous (Figure 17).

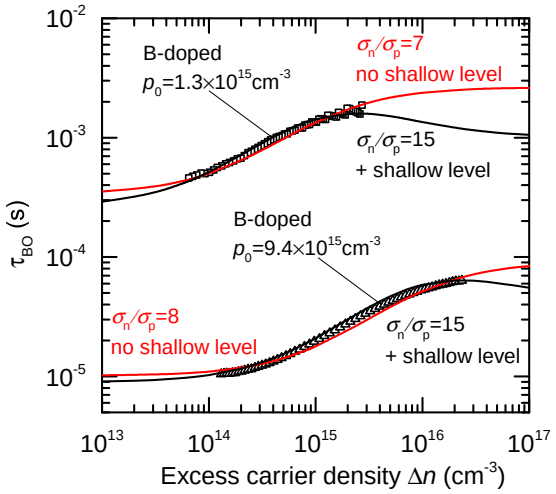

Figure 17: Dépendance de la durée de vie liée au défaut bore-oxygène en fonction de la densité de porteurs en excès.

De la même manière, nous montrons que les mesures de dépendance de la durée de vie en température ne sont à priori pas valable pour l'étude du défaut bore-oxygène à cause du caractère métastable de celui-ci, qui se dissocie à des température supérieures à 100°C.

Nous suggérons qu'un travail supplémentaire doit donc être dédié à la détermination des caractéristiques SRH du défaut bore-oxygène. Ceci permettrait en autre de déterminer les densité de défauts par des mesures de durée de vie avec plus de confiance. Nous proposons par exemple d'utiliser une analyse de photoluminescence, couplée avec la mesure de durée de vie par photoconductance, ce qui permet de déterminer la durée de vie des porteurs de charge sur une gamme plus large de niveau d'injection.

Application de l'ingénierie de compensation aux cellules solaires en silicium purifié par voie métallurgique

Dans le chapitre 5, nous appliquons le co-dopage au gallium à la cristallisation de lingots de Si à partir d'une charge de Si UMG. Des cellules solaires sont fabriquées avec le matériau résultant et leur performance est mesurée, modélisée et analysée pour être mise en relation avec la compensation et le co-dopage au Ga.

Pour cette étude, nous cristallisons deux lingots Cz à partir de la même charge de Si UMG contenant des concentrations en B et P estimée respectivement à 0.25ppmw et 0.6ppmw. L'un des lingots est cristallisé sans ajout de dopants tandis ce que l'autre est co-dopé avec du P pour diminuer le dopage net et avec du Ga pour maintenir une conductivité de type sur toute la hauteur du lingot. Ceci résulte en une résistivité plus élevée dans le lingot co-dopé que dans le lingot non co-dopé (Figure 18). Le lingot co-dopé est intégralement de type p alors que le lingot non co-dopé présente une inversion de type à 85% de sa hauteur.

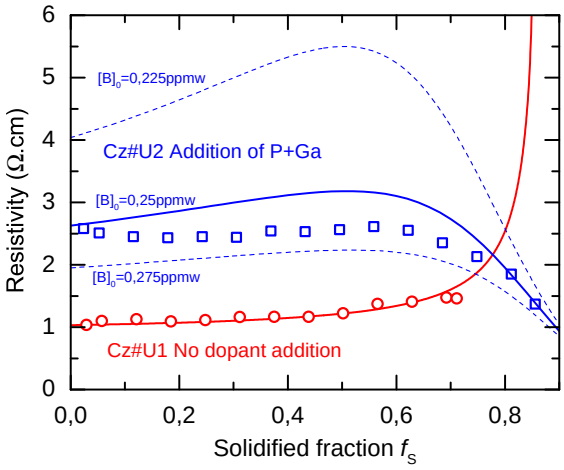

Figure 18: Mesure et calcul de la résistivité le long de lingots cristallisés à partir du même Si UMG l'un sans co-dopage (rouge) et l'autre avec (bleu).

Des cellules sont fabriquées avec des plaquettes découpées dans ces deux lingots ainsi qu'avec des plaquettes de Si de grade électronique (EG) pour comparaison. Les caractéristiques I-V de ces cellules sont mesurées et modélisées à l'aide du logiciel de simulation QSS-Model.

La Figure 19 montre que la tension de circuit ouvert est légèrement plus importante dans le lingot non co-dopé que dans le lingot co-dopé, principalement à cause de la plus forte densité de porteurs majoritaires dans le lingot non co-dopé. La différence est cependant très faible car la diminution de la densité de porteurs majoritaires dans le lingot co-dopé est contrebalancée par une plus grande durée de vie des porteurs de charges.. Il est également à noter que la tension de circuit ouvert est semblable dans les deux lingots en Si UMG et dans les plaquettes de référence en Si EG.

Après dégradation sous éclairement, la modélisation donne une tension de circuit ouvert beaucoup plus faible dans les cellules à base de Si UMG que dans les cellules à base de Si

EG, à cause de la plus forte concentration en B dans le Si EG. On remarque également que, puisqu'il n'y a plus d'effet positif de la compensation sur la durée de vie après dégradation, la tension de circuit ouvert est plus faible dans le lingot co-dopé que dans le non co-dopé.

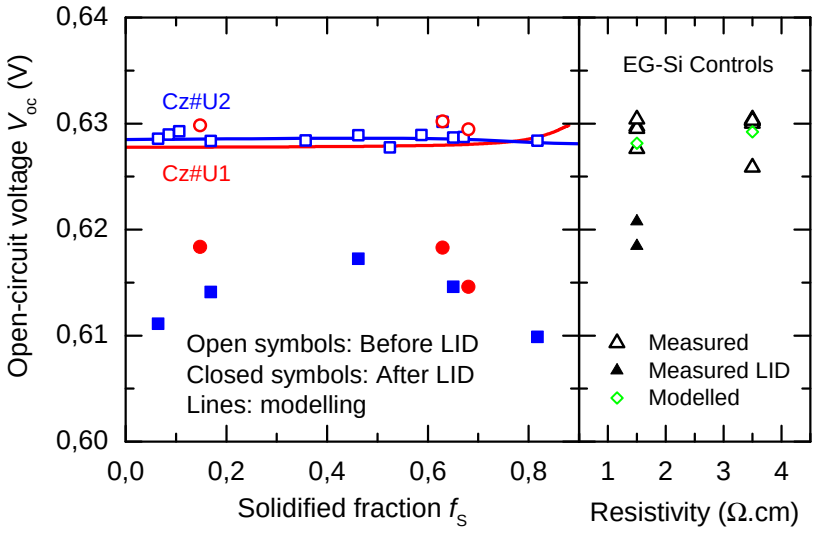

Figure 19: Variation de la tension de circuit ouvert le long des lingots de Si UMG co-dopé et non co-dopé et comparaison avec des cellules en Si EG.

La Figure 20 montre que le courant de court-circuit est légèrement plus important dans les cellules faites à partir de Si UMG co-dopé par rapport aux Si UMG non co-dopé. Ce résultat confirme l'effet positif de la compensation sur la longueur de diffusion des porteurs minoritaires. Encore une fois, le courant de court-circuit est similaires dans les deux lingots de Si UMG et dans les cellules de Si EG.

Après dégradation, le courant de court-circuit est plus faible dans les cellules de Si UMG que EG et plus faible dans le Si UMG co-dopé que dans le Si UMG non co-dopé. Ceci s'explique par les mêmes raisons que les observations faites sur la tension de circuit ouvert après dégradation.

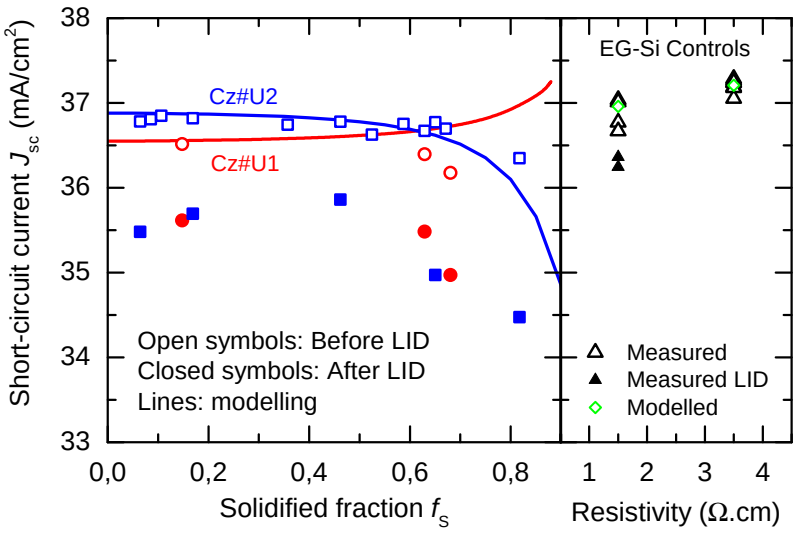

Figure 20: Variation du courant de court-circuit le long des lingots de Si UMG co-dopé et non co-dopé et comparaison avec des cellules en Si EG.

La Figure 21 montre que le rendement est similaire dans les cellules provenant du lingot co-dopé que dans les cellules provenant du lingot non co-dopé. Ceci montre qu'il est possible de tolérer, grâce à l'ajout de Ga, des concentrations en P plus importantes dans le Si UMG sans donner lieu à des chutes de rendement matière ou de performance cellules avant dégradation. Les performances cellules sont quasiment identiques dans le Si UMG et dans le Si EG.

Après dégradation la performance des cellules UMG diminue plus que celle des cellules EG, à cause de la plus forte concentration en B dans l'UMG. Puisque la compensation n'apporte plus un gain en durée de vie après dégradation, le rendement des cellules en Si UMG co-dopé est plus faible que celui dans les cellules en Si UMG non co-dopé.

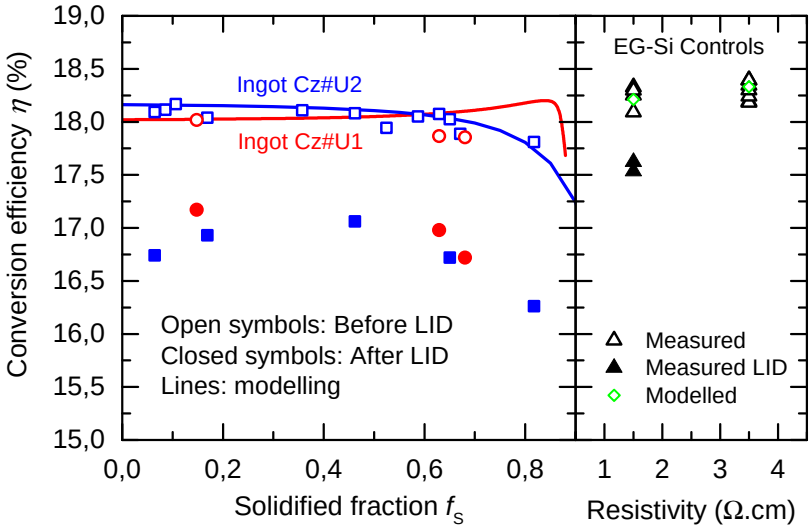

Figure 21: Variation du rendement de conversion le long des lingots de Si UMG co-dopé et non co-dopé et comparaison avec des cellules en Si EG.